N°d'ordre NNT : 2023ISAL0006

THESE de DOCTORAT DE L'INSA LYON, membre de l'Université de Lyon

Ecole Doctorale N° 34
Ecole Doctorale Matériaux de Lyon

Spécialité/ discipline de doctorat :
Matériaux

Soutenue publiquement le 24/01/2023, par :
Héloïse Willeman

Multi-scale characterization of deformation mechanisms of poly-ether-ether-ketone (PEEK) under tensile stretching

Devant le jury composé de :

Noëlle BILLON	Professeure	CEMEF – Mines ParisTech	Rapporteure
Pierre-Antoine ALBOUY	DR CNRS	Université Paris Saclay	Rapporteur
Valérie GAUCHER	Professeure	Université de Lille	Examinatrice
Leon GOVAERT	Professeur	TuEindhoven	Examinateur
Paul SOTTA	Professeur	INSA Lyon	Directeur de thèse
Olivier LAME	Professeur	INSA Lyon	Co-directeur de thèse
Jérôme BIKARD	Ingénieur de recherche	Solvay Materials	Encadrant industriel
Renaud Rinaldi	Maître de conférences	INSA Lyon	Invité
Coen Clarijs	Ingénieur de recherche	Solvay Materials	Invité

Cette thèse est accessible à l'adresse : https://theses.insa-lyon.fr/publication/2023ISAL0006/these.pdf
© [H. Willeman], [2023], INSA Lyon, tous droits réservés

Cette thèse est accessible à l'adresse : https://theses.insa-lyon.fr/publication/2023ISAL0006/these.pdf
© [H. Willeman], [2023], INSA Lyon, tous droits réservés

INSTITUT NATIONAL DES SCIENCES APPLIQUÉES LYON

Département de la Formation par la Recherche et des Études Doctorales (**FEDORA**)

Bâtiment INSA direction, 1er étage
37, av. J. Capelle
69621 Villeurbanne Cédex
fedora@insa-lyon.fr

Référence : TH0934_WILLEMAN

L'INSA Lyon a mis en place une procédure de contrôle systématique via un outil de détection de similitudes (logiciel Compilatio). Après le dépôt du manuscrit de thèse, celui-ci est analysé par l'outil. Pour tout taux de similarité supérieur à 10%, le manuscrit est vérifié par l'équipe de FEDORA. Il s'agit notamment d'exclure les auto-citations, à condition qu'elles soient correctement référencées avec citation expresse dans le manuscrit.

Par ce document, il est attesté que ce manuscrit, dans la forme communiquée par la personne doctorante à l'INSA Lyon, satisfait aux exigences de l'Etablissement concernant le taux maximal de similitude admissible.

Cette thèse est accessible à l'adresse : https://theses.insa-lyon.fr/publication/2023ISAL0006/these.pdf
© [H. Willeman], [2023], INSA Lyon, tous droits réservés

Département FEDORA – INSA Lyon - Ecoles Doctorales

SIGLE	ECOLE DOCTORALE	NOM ET COORDONNEES DU RESPONSABLE
CHIMIE	**CHIMIE DE LYON** **https://www.edchimie-lyon.fr** Sec. : Renée EL MELHEM Bât. Blaise PASCAL, 3e étage secretariat@edchimie-lyon.fr	**M. Stéphane DANIELE** C2P2-CPE LYON-UMR 5265 Bâtiment F308, BP 2077 43 Boulevard du 11 novembre 1918 69616 Villeurbanne **directeur@edchimie-lyon.fr**
E.E.A.	**ÉLECTRONIQUE, ÉLECTROTECHNIQUE, AUTOMATIQUE** **https://edeea.universite-lyon.fr** Sec. : Stéphanie CAUVIN Bâtiment Direction INSA Lyon Tél : 04.72.43.71.70 secretariat.edeea@insa-lyon.fr	**M. Philippe DELACHARTRE** INSA LYON Laboratoire CREATIS Bâtiment Blaise Pascal, 7 avenue Jean Capelle 69621 Villeurbanne CEDEX Tél : 04.72.43.88.63 **philippe.delachartre@insa-lyon.fr**
E2M2	**ÉVOLUTION, ÉCOSYSTÈME, MICROBIOLOGIE, MODÉLISATION** **http://e2m2.universite-lyon.fr** Sec. : Bénédicte LANZA Bât. Atrium, UCB Lyon 1 Tél : 04.72.44.83.62 secretariat.e2m2@univ-lyon1.fr	**Mme Sandrine CHARLES** Université Claude Bernard Lyon 1 UFR Biosciences Bâtiment Mendel 43, boulevard du 11 Novembre 1918 69622 Villeurbanne CEDEX **sandrine.charles@univ-lyon1.fr**
EDISS	**INTERDISCIPLINAIRE SCIENCES-SANTÉ** **http://ediss.universite-lyon.fr** Sec. : Bénédicte LANZA Bât. Atrium, UCB Lyon 1 Tél : 04.72.44.83.62 secretariat.ediss@univ-lyon1.fr	**Mme Sylvie RICARD-BLUM** Institut de Chimie et Biochimie Moléculaires et Supramoléculaires (ICBMS) - UMR 5246 CNRS - Université Lyon 1 Bâtiment Raulin - 2ème étage Nord 43 Boulevard du 11 novembre 1918 69622 Villeurbanne Cedex Tél : +33(0)4 72 44 82 32 **sylvie.ricard-blum@univ-lyon1.fr**
INFOMATHS	**INFORMATIQUE ET MATHÉMATIQUES** **http://edinfomaths.universite-lyon.fr** Sec. : Renée EL MELHEM Bât. Blaise PASCAL, 3e étage Tél : 04.72.43.80.46 infomaths@univ-lyon1.fr	**M. Hamamache KHEDDOUCI** Université Claude Bernard Lyon 1 Bât. Nautibus 43, Boulevard du 11 novembre 1918 69 622 Villeurbanne Cedex France Tél : 04.72.44.83.69 **hamamache.kheddouci@univ-lyon1.fr**
Matériaux	**MATÉRIAUX DE LYON** **http://ed34.universite-lyon.fr** Sec. : Yann DE ORDENANA Tél : 04.72.18.62.44 yann.de-ordenana@ec-lyon.fr	**M. Stéphane BENAYOUN** Ecole Centrale de Lyon Laboratoire LTDS 36 avenue Guy de Collongue 69134 Ecully CEDEX Tél : 04.72.18.64.37 **stephane.benayoun@ec-lyon.fr**
MEGA	**MÉCANIQUE, ÉNERGÉTIQUE, GÉNIE CIVIL, ACOUSTIQUE** **http://edmega.universite-lyon.fr** Sec. : Stéphanie CAUVIN Tél : 04.72.43.71.70 Bâtiment Direction INSA Lyon mega@insa-lyon.fr	**M. Jocelyn BONJOUR** INSA Lyon Laboratoire CETHIL Bâtiment Sadi-Carnot 9, rue de la Physique 69621 Villeurbanne CEDEX **jocelyn.bonjour@insa-lyon.fr**
ScSo	**ScSo*** **https://edsciencessociales.universite-lyon.fr** Sec. : Mélina FAVETON INSA : J.Y. TOUSSAINT Tél : 04.78.69.77.79 melina.faveton@univ-lyon2.fr	**M. Bruno MILLY** Université Lumière Lyon 2 86 Rue Pasteur 69365 Lyon CEDEX 07 **bruno.milly@univ-lyon2.fr**

*ScSo : Histoire, Géographie, Aménagement, Urbanisme, Archéologie, Science politique, Sociologie, Anthropologie

Cette thèse est accessible à l'adresse : https://theses.insa-lyon.fr/publication/2023ISAL0006/these.pdf
© [H. Willeman], [2023], INSA Lyon, tous droits réservés

Remerciements

Avant le déroulé de ce manuscrit, je tiens d'abord à remercier les nombreuses personnes qui ont grandement contribué à ce travail de thèse. Trois ans riches en évènements, challenges avant un aboutissement final. Une aventure plus complète que ce que j'aurais pu imaginer le jour de son commencement.

Je remercie en premier lieu Florence Clément et Didier Long, directrice et directeur adjoint du Laboratoire des Polymères & Matériaux Avancés (LPMA) dans lequel j'ai débuté cette thèse, qui m'ont offert l'opportunité d'effectuer ce travail au sein de leur équipe. Cette expérience a été très enrichissante, personnellement et professionnellement.

Mes plus sincères et profonds remerciements vont ensuite à Paul Sotta, mon directeur de thèse. Paul, merci infiniment pour tout ce que tu m'as apporté : merci de m'avoir transmis ton expertise sur les rayons X et leur utilité pour l'étude des matériaux polymères, pour ton soutien et ton temps précieux que tu as toujours pris lorsque j'en avais besoin. Je tacherai de me souvenir et de m'inspirer pendant toute ma carrière de ta rigueur scientifique. Un grand merci à Olivier Lame, co-directeur de thèse pour ton suivi et nos discussions à se tirer les cheveux sur l'orientation possible des empilements lamellaires du PEEK. Je remercie Jérôme, encadrant Solvay pour son expertise méca et son suivi pendant le projet.

Je remercie vivement l'ensemble des membres du jury, Valérie Gaucher et Leon Govaert ainsi que les rapporteurs Noëlle Billon et Pierre-Antoine Albouy qui ont accepté de prendre le temps d'évaluer ce travail. Merci à Renaud Rinaldi et Coen Clarijs d'avoir accepté d'assister à la soutenance. Merci à tous pour nos échanges intéressants lors de la soutenance de thèse.

Une des particularités de ce travail a été la chance de réaliser des expériences à deux reprises dans des établissements hors du commun, les Synchrotron SOLEIL à Saclay et l'ESRF à Grenoble. Pour cela, je remercie pour leur accueil et leur support lors de l'installation des équipements, de la réalisation des expériences et le traitement des données ; Javier Perez de SOLEIL et Isabelle Morfin et Nils Blanc de l'ESRF. Je remercie aussi particulièrement Renaud Rinaldi, merci pour ton aide, tes conseils précieux et ta bonne humeur lors de ce week-end prolongé de Pâques passé à étirer mes échantillons.

J'ai eu la chance durant ces trois ans de thèse de travailler aux côtés d'une grande équipe sur le centre de recherche RICL de Solvay. Merci Sylvie, Violaine, Sandrine, Christiane, Tiffany, Olivier, Thibaut, Vincent, Thierry, Fabrice, Olivier, Robert, Michel ; Baptiste, Clémence et Pauline au labo microscopie. Votre accueil, votre bienveillance et votre bonne humeur, tant au labo qu'à la salle café ou en terrasse, contribue grandement au bien-être des thésards. Merci à Rabih pour mes premiers pas chez Solvay et de m'avoir donné le gout de la recherche. Merci à Lise pour ta bienveillance envers les thésards. Merci aussi à Olivier, Mathieu, Denis, Pierre-Yves & Anthony.

Plus particulièrement, je voudrais maintenant remercier l'ensemble des thésards avec qui j'ai pu partager cette aventure. La cohésion entre nous n'a fait que renforcer cette bonne ambiance de labo par des vraies amitiés ! Merci aux mamans, Agathe et Rita. Merci Stéphanie, pours les discussions dans la navette et le pied chez Nexans. Merci à Eléonore d'avoir été une guide et une amie depuis le début. Merci à Julien Merci à Nicolas, soleil du LPMA qui nous réconfortaient avec de délicieuses crêpes. Merci à mes deux dernières compères avec qui j'ai pu partager le plus de bon moments comme le DYFP et d'avoir fini dans le meilleur bureau, merci Mélissa d'avoir été l'oreille attentive et merci Anne d'avoir suivi si passionnément ma vie de famille, j'espère que tu trouveras ton chalet en montagne. Je remercie aussi les nombreux stagiaires qui ont participé à la bonne ambiance du laboratoire, Alexandre, Océane, et

Cette thèse est accessible à l'adresse : https://theses.insa-lyon.fr/publication/2023ISAL0006/these.pdf
© [H. Willeman], [2023], INSA Lyon, tous droits réservés

surtout je remercie vivement Julie pour tout le travail que tu as fait pour moi, c'était un plaisir de travailler ensemble ! Merci aussi à Franceso, Agathe V, Jessica, Ludovic, Illan.

Je voudrais aussi remercier les équipes de Nexans avec qui j'ai eu de la chance de travailler lors de la fin de rédaction de ce manuscrit.

Je remercie aussi toute la team Jacka7 qui est toujours là aujourd'hui, ainsi que ses associés pour ces week-ends réunions. Spéciale dédicace à Cécé qui a suivi cette thèse du début à la fin. A nos sessions débrief sportives, pourvu qu'elles durent.

Je remercie énormément ma famille pour leur soutien inconditionnel, le plus grand des support system, mon préféré. Papa, Maman, Théo, Nathalie & Henri.

Et enfin, je remercie Kévin pour le soutien et l'amour quotidien. *Téléguidée par tes pouvoirs, auprès de toi chaque jour est victoire.*

Cette thèse est accessible à l'adresse : https://theses.insa-lyon.fr/publication/2023ISAL0006/these.pdf
© [H. Willeman], [2023], INSA Lyon, tous droits réservés

Abstract

The aim of this PhD work is accessing the microscopic deformation mechanisms of bulk poly-ether-ether-ketone (PEEK) under tensile stretching. Beforehand, the thermal and mechanical properties of two commercial grades of PEEK were characterized. Tensile specimens were then compression-molded to obtain morphologies as isotropic as possible and characterized below and above the glass transition temperature. Deformations at the scales of lamellar stacks and of the crystalline unit cell have been characterized by small and wide-angle X-ray scattering (SAXS and WAXS) performed in-situ during tensile tests. Simultaneously, the strain field within the samples was followed by digital image correlation (DIC) in order to compare microscopic and macroscopic strains. At both temperatures, lamellae tend to orient perpendicular to the tensile direction (TD). This orientation mechanism (which we denote as 'Chain Network model') is driven by the amorphous chains which transmit the stress between adjacent lamellae. The tensile strain in lamellar stacks perpendicular to TD is lower than the macroscopic tensile strain, which must be compensated by increased shear in inclined stacks. Some differences of behavior have been observed depending on the test temperature, especially at high deformation. A highly oriented morphology is ultimately obtained in all cases. However, the central scattering profiles changes with testing temperatures. Below T_g, the presence of small entities randomly oriented is indicated. Above T_g, the material is fibrillar and contains cavities.

KEYWORDS : PEEK, in-situ tensile test, SAXS, WAXS, semi-crystalline

Résumé

L'objectif de cette thèse est d'établir le scénario multi-échelles de déformation du PEEK lorsqu'il est sollicité en traction uniaxiale. Préalablement à la mise en œuvre d'échantillons de deux grades commerciaux de PEEK, les propriétés thermiques et mécaniques de ces matériaux ont été caractérisées. La température d'oubli thermodynamique ainsi que la sensibilité aux vitesses de refroidissement ont été établies. Des éprouvettes de traction ont été obtenues à partir de plaques thermocompressées, procédé choisi pour obtenir des morphologies les plus isotropes possibles. Les propriétés mécaniques en traction ont ensuite été caractérisées au-dessus et au-dessous de la transition vitreuse de la phase amorphe (Tg). Grâce à un dispositif expérimental fabriqué sur mesure, des essais de traction à deux températures distinctes au-dessous et au-dessus de T_g ont été suivis par diffusion des rayons X aux petits (SAXS) et grands angles (WAXS) pour caractériser les déformations à l'échelle des empilements lamellaires et à l'échelle de la maille cristalline. Simultanément, le champ de déformation a été mesurée par corrélation d'images (DIC) afin de comparer la déformation macroscopique et microscopique. Pour les deux températures, les lamelles tendent à s'orienter perpendiculairement à la direction de traction (TD). Ce mécanisme d'orientation local (que nous appelons « modèle de réseau de chaînes ») est induit par la transmission des contraintes par les chaînes amorphes reliant les lamelles cristallines adjacentes. Au-dessus de T_g, l'allongement local est plus faible que l'allongement macroscopique dans les lamelles perpendiculaire à TD, ce qui implique que les lamelles inclinées doivent être cisaillées. L'évolution de la distribution d'orientation des lamelles appuie ce résultat. Une morphologie fortement orientée est finalement obtenue quelle que soit la température. Cependant, le profil d'endommagement est différent. En-dessous de T_g, le profil de diffusion centrale indique l'existence de petites entités (lamelles ou crystallites) orientées aléatoirement. A hautes température, le matériau est fibrillaire et présente des cavités.

MOTS-CLES : PEEK, traction in-situ, SAXS, WAXS, semi-cristallin

Cette thèse est accessible à l'adresse : https://theses.insa-lyon.fr/publication/2023ISAL0006/these.pdf
© [H. Willeman], [2023], INSA Lyon, tous droits réservés

Table of contents

Remerciements **5**

Abstract **7**

Table of contents **8**

Introduction **12**

Chapter I. State of the art: Deformation mechanisms in semi crystalline polymers and properties of PEEK **14**

I. Introduction **15**

II. PEEK, a high performances semi crystalline polymer **15**

1. Molecular structure 15
2. Stability and degradation 16
3. Crystallographic structure 18
4. Lamellar and spherulitic structure 20

III. Deformation mechanisms in semi crystalline polymers **23**

1. Elastic behavior 23
2. Plastic behavior 23
   a. Cavitation 24
   b. Crazing 25
   c. Shear bands 26
   d. Fibrillar structure 26
3. In situ X-rays scattering studies 27

IV. Properties of PEEK **29**

1. Relaxations 29
2. Mechanical properties 30
   a. Influence of temperature and strain rate 31
   b. Influence of molecular weight 32
   c. Fatigue behavior 32
3. Physical ageing in PEEK 33
4. Crystallization 35
   a. Double melting behavior 35
   b. Multiple melting peaks 37
   c. Thermal treatments and memory effects 38
   d. Models of polymer crystallization 39
   e. Crystallization kinetics in PEEK 41

Cette thèse est accessible à l'adresse : https://theses.insa-lyon.fr/publication/2023ISAL0006/these.pdf
© [H. Willeman], [2023], INSA Lyon, tous droits réservés

f. Effect of stretching on crystallization 44
V. Objectives of the research 45
Chapter II. Materials and methods 46
I. Introduction 47
II. Materials and processing 47
1. Materials 47
2. Degradability: TGA and IR study 47
3. Processing: compression molding 48
III. Mechanical properties 49
1. Tensile tests 49
2. Digital Image Correlation (DIC) 49
3. DMA 50
IV. Microstructural analysis 51
1. Cross-polarized optical microscopy 51
a. Morphology study 51
b. Crystallization kinetics 51
2. Differential Scanning Calorimetry (DSC) 51
a. Lamella thickness 52
b. Crystallization kinetics 53
c. Physical ageing 53
V. X-ray Scattering 54
1. Small Angle X-ray Scattering (SAXS) 54
2. Wide Angle X-ray Scattering (WAXS) 60
3. Case of anisotropic system 63
4. In situ SAXS/WAXS tensile tests 64
Chapter III. General, thermal and mechanical properties of PEEK 68
I. Crystallization 69
1. Memory effects 69
2. Crystallization kinetics 73
a. Isothermal crystallization 73
b. Cold-crystallization 76
c. TTT diagram 77
II. Compression molding 79
1. Crystallinity 79
2. Spherulite morphology 79
3. Thermal stability 80

Cette thèse est accessible à l'adresse : https://theses.insa-lyon.fr/publication/2023ISAL0006/these.pdf
© [H. Willeman], [2023], INSA Lyon, tous droits réservés

III. Mechanical properties under tensile stretching 82
1. DMA 82
2. Tensile tests 83
a. Influence of the PEEK grade (molecular weight) 83
b. Influence of processing conditions 84
c. Influence of temperature 84
d. Influence of strain rate 85
3. Strain localization 86
IV. Physical ageing 88
1. DSC 88
2. DMA 89
3. Tensile tests 90
4. A tentative model for the effect of ageing on the thermo-mechanical response of PEEK 91
V. Conclusion 92
Chapter IV. Study of the microscopic strain: elastic regime 93
I. Introduction 94
II. Elastic strain regime at the scale of lamellar stacks 97
1. SAXS protocol 97
2. Local strain in HORI lamellar stacks 99
3. Local strain as a function of orientation 102
a. Tensile tests at T = 23°C, $T < Tg$ 103
b. Tensile tests at T = 170°C, $T > Tg$ 106
4. Orientation distribution of lamellar stacks 108
a. Discussion 112
III. Elastic strain regime at the scale of crystal unit cell, by WAXS 113
1. WAXS protocol 113
2. Local strain at the scale of crystal planes 114
3. Local strain as a function of orientation 116
4. Orientation distribution of crystal planes 119
IV. Discussions: deformation mechanisms in the elastic pre-yield regime 121
1. SAXS experiments 121
a. Local strain within lamellar stacks 121
b. Lamellar stacks orientation 122
2. Models 124
a. Chain network (CN) model 124
b. Rigid lamella (RL) model 125

Cette thèse est accessible à l'adresse : https://theses.insa-lyon.fr/publication/2023ISAL0006/these.pdf
© [H. Willeman], [2023], INSA Lyon, tous droits réservés

3. Conclusion 126
V. Conclusion 127
Chapter V. Microscopic strain study: plastic regime 128
I. Introduction 129
II. Deformation in the plastic regime 129
1. Tensile tests at room temperature, $T < T_g$ 129
2. Tensile tests at 170°C, $T > T_g$ 132
III. Deformation at the scale of crystal planes in the plastic regime 133
1. Local strain at the scale of crystal planes, WAXS 133
a. Tensile tests at room temperature, $T < T_g$ 133
b. Tensile tests at T=170°C, $T > T_g$ 135
2. Orientation distributions at room temperature and at T=170°C 136
IV. Deformation at the scale of lamellae stacks in the plastic regime 141
1. Local strain at the scale of lamellar stacks, SAXS 141
a. Tensile tests at room temperature, $T < T_g$ 141
b. Tensile tests at T=170°C, $T > T_g$ 142
2. Orientation distribution 144
V. Central scattering: damage mechanisms 147
1. Tensile tests at T=23°C, $T < T_g$ 147
2. Tensile tests at T=170°C, $T > T_g$ 150
VI. Proposed mechanisms of deformation in PEEK 153
1. Below glass transition temperature 153
2. Above glass transition temperature 154
Conclusion 157
References 159
Résumé en français 168
FOLIO ADMINISTRATIF 171

Cette thèse est accessible à l'adresse : https://theses.insa-lyon.fr/publication/2023ISAL0006/these.pdf
© [H. Willeman], [2023], INSA Lyon, tous droits réservés

Introduction

Polyethertherketone (PEEK) is a semi-crystalline thermoplastic polymer with very high mechanical performances, resistance to solvents and melting temperature. It is increasingly used in high performance applications such as composites in the aerospace field and 3D printing. Due to its exceptional chemical resistance, it can withstand sterilization and is suitable for medical applications (implants, surgical devices). To potentially predict and enhance the material lifetime and its mechanical properties, it is essential to fully understand the PEEK properties at a microscopic scale, in relation to its structure, itself driven by process conditions. This is a multiscale problem, as semi-crystalline polymers generally have a hierarchical structure/morphology (from the crystal unit cell to lamella stacks to large scale spherulites). As for other semi-crystalline thermoplastic polymers, processing conditions from the molten state have a strong impact on PEEK properties, essentially related to crystallization conditions during the process. While thermal and mechanical properties in relation to crystallization conditions have been already studied quite in details in the literature, the relationships between the mechanical response and the microscopic multiscale structure have not been extensively and comprehensively studied yet.

The aim of this study is to obtain a full description of the multiscale mechanical response of bulk PEEK samples by performing in situ, real-time small-angle and wide-angle X-ray scattering (SAXS and WAXS) experiments during tensile stretching, both below and beyond the yield stress (elastic and plastic regimes) up to the development of a highly oriented morphology or up to failure. This analysis is of prior importance in the aim to develop a micromechanical model (based on physical description) for understanding the short-term mechanical performances, predicting the long-term mechanical behavior and evaluate the lifetime of materials and systems based on PEEK matrices (including composites).

In situ, real-time SAXS and WAXS experiments provide information on the local deformation mechanisms like the stress and strain distributions at the scales of lamellar stacks and crystal unit cells, lamella rotation, reorganization mechanisms. Damage mechanisms like cavitation can also be investigated along the whole stretching process. Depending on the testing temperature (either below or above the glass transition temperature T_g), the amorphous phase may be either rigid (glassy) or soft (rubbery). However, the coupling between crystalline and amorphous phases at the scale of lamellar stacks may drastically impact the micromechanical response of the amorphous phase. This may affect the transfer of local stress between phases and consequently the overall mechanical behavior of the material. This approach, based on advanced analysis tools that we have developed, has been applied to polyamides (PA6, PhD thesis of C. Millot, 2015) and polyolefins (PE, PhD of H. Guo, 2021 and of S. Humbert 2009, and PE and PP, PhD of B. Xiong, 2014).

This manuscript is divided into five chapters. The first chapter presents a literature review of PEEK. It consists in a presentation of the structure of semi crystalline PEEK and of the properties of this polymer. The mechanical properties, physical ageing and the crystallization behavior of PEEK are discussed. The mechanisms of deformation usually encountered in semi-crystalline polymers are presented as well. This review allowed us to define a strategy in order to achieve our objective on the understanding of deformation mechanisms in PEEK.

In the second chapter, an overall description of the techniques used for the physico-chemical and microstructural analyses as well as the mechanical investigations is reported.

The third chapter presents the thermal and mechanical characterization of PEEK samples as well as the sample processing and characterization prior to in situ tensile tests. The results on the influence of

Cette thèse est accessible à l'adresse : https://theses.insa-lyon.fr/publication/2023ISAL0006/these.pdf
© [H. Willeman], [2023], INSA Lyon, tous droits réservés

process parameters such as the cooling rate or the temperature of crystallization on the overall crystallization behavior and on the morphology are presented. The elaboration process of tensile specimens by compression molding is then described. The mechanical properties of these samples, depending on the process parameters, are then discussed. Lastly, the effect of physical ageing is investigated.

The presentation of the results of tensile tests combined with in-situ, real time X-ray scattering is then divided into two parts: the pre-yield (elastic) and the post-yield (plastic) strain regimes, presented in chapter IV and chapter V respectively. In these chapters, the mechanical response of PEEK samples at various scales and at two distinct temperatures (one below and another one above T_g) is described. The microscopic deformation at the scale of lamellar stacks and crystal planes is analyzed and compared with the macroscopic deformation. The evolution of orientation distribution is discussed in order to determine the deformation scenario leading to plasticity and failure of the polymer.

As a general conclusion, the main results obtained on the mechanisms of deformation in PEEK is summarized. Then, the perspectives of this project conclude the present work.

Cette thèse est accessible à l'adresse : https://theses.insa-lyon.fr/publication/2023ISAL0006/these.pdf
© [H. Willeman], [2023], INSA Lyon, tous droits réservés

Chapter I. State of the art: Deformation mechanisms in semi crystalline polymers and properties of PEEK

I. Introduction 15
II. PEEK, a high performances semi crystalline polymer 15
1. Molecular structure 15
2. Stability and degradation 16
3. Crystallographic structure 18
4. Lamellar and spherulitic structure 20
III. Deformation mechanisms in semi crystalline polymers 23
1. Elastic behavior 23
2. Plastic behavior 23
3. In situ X-rays scattering studies 27
IV. Properties of PEEK 29
1. Relaxations 29
2. Mechanical properties 30
3. Physical ageing in PEEK 33
4. Crystallization 35
V. Objectives of the research 45

Cette thèse est accessible à l'adresse : https://theses.insa-lyon.fr/publication/2023ISAL0006/these.pdf
© [H. Willeman], [2023], INSA Lyon, tous droits réservés

I. Introduction

High performance thermoplastic polymers are increasingly replacing traditional materials like metals in different fields of application such as aeronautics, medical devices or smart devices. Often used as a matrix for composites, the major advantage of these polymers is the combination of high mechanical properties or thermal resistance with lightweight. In the context of sustainability and carbon dioxide emission reduction, the use of these polymers is thus of great interest. This work will focus on investigating fundamental properties of poly-ether-ether-ketone (PEEK) in order to provide a set of data which may potentially be used to feed simulations of the mechanical behavior. The ultimate objective will be to predict long-term mechanical performances and lifetime of the polymer.

Poly(aryl-ether-ketone) (PAEKs) is a high-performance polymer family which demonstrates high thermo-mechanical properties. Poly(ether-ether-ketone) or PEEK today represents the biggest part of the PAEKs market. It was first introduced by ICI[1] then bought by Victrex in 1992 and was studied by a number of academic groups. Today, as the interest in this polymer rises, to fulfill the need of high-performance applications, other suppliers like Solvay produce several grades of PEEK with different molecular weights. The first synthesis of PEEK was carried out by Imperial Chemical Industries (ICI) in 1978. Patents from ICI mention that the polymer may be synthetized by condensation of hydroquinone, 4,4'-difluorobenzophenone and an alkali metal carbonate or bicarbonate in the presence of an aromatic solvent (diphenyl sulphone) from 150°C to final temperature 320°C.[1]

The objective of this chapter is to present a summarized bibliographic review of the main parameters which govern the structure, mechanical behavior and deformation mechanisms in semi crystalline polymers, especially in PEEK. The general structure and properties of this high-performance thermoplastic polymer will be introduced, with an emphasis on the influence of the crystallization conditions on the structure and then on the mechanical properties. Deformation mechanisms in semi crystalline polymers will also be reviewed in a general way.

II. PEEK, a high performances semi crystalline polymer

1. Molecular structure

PEEK consists of aromatic rings linked with ether and ketone groups. One repeat unit includes two ether and one ketone groups (Figure 1). The structure of the PEEK monomer results in a combination of high-performance characteristics. Aryl groups provide high modulus, thermal stability, and flame retardancy. Ether linkages provide toughness and ductility. Ketones provide long term thermal oxidative resistance. Due to its quasi-linear and aromatic structure, PEEK has thus excellent mechanical properties, temperature and chemical resistance. PEEK is not dissolved by any usual organic solvent at room temperature.

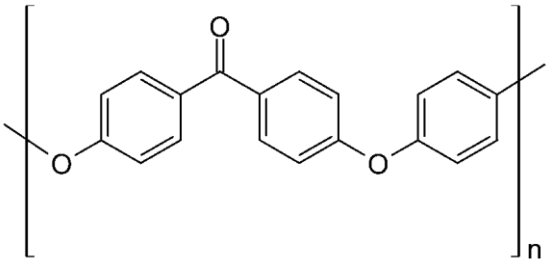


Figure 1. Chemical structure of PEEK

Cette thèse est accessible à l'adresse : https://theses.insa-lyon.fr/publication/2023ISAL0006/these.pdf
© [H. Willeman], [2023], INSA Lyon, tous droits réservés

2. Stability and degradation

Detailed rheological characterization by White et al.[2] has revealed that several grades of PEEK exhibit relaxation behavior characteristic of a long-chain branched structure. The molecular weight dependence of the zero-shear viscosity for several linear-chain PAEKs polymers indicates that PEEK chains are quite rigid in the melt. [2] However, due to insolubility of PEEK in organic solvents, the Kuhn length was not measured directly. Only data for Me-PEEK are reported. Estimations indicate that the rigidity should be comparable to other semi-aromatic polymers. [3] The potentially branched PEEKs are most susceptible to oxidation in air, but exhibit much greater stability in nitrogen. [4] This means that degradation of the polymer may potentially happen in the processing steps.

The thermal stability and degradation of PEEK were studied by thermogravimetry. As depicted in Figure 2, the onset decomposition temperatures are approximately 550°C under nitrogen and 500°C under air which results in a mass loss of about 60% of the material at 1000°C under nitrogen and full decomposition under air. [4]

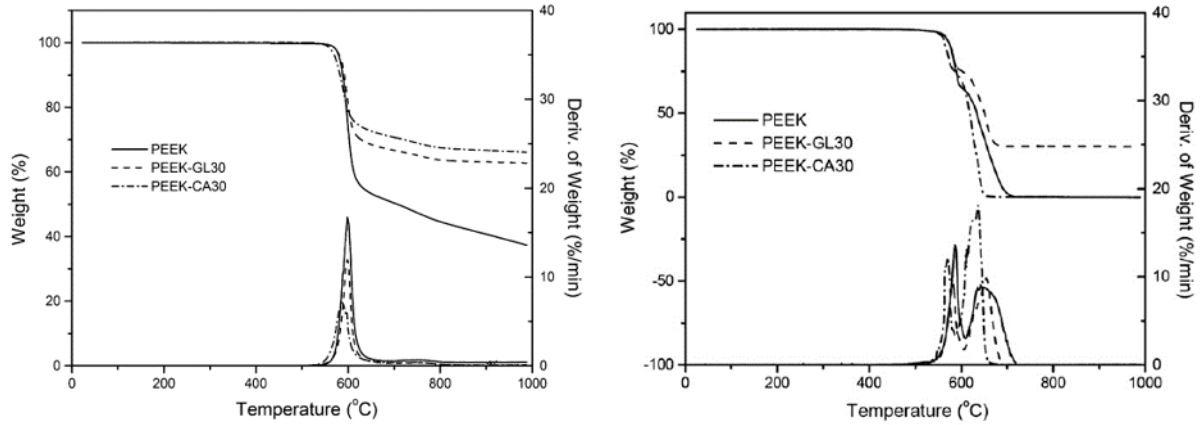


Figure 2. Thermal decomposition of PEEK and its glass (GL30) and carbon (CA30) fibre composites at a heating rate of 10°C.min^{-1} under nitrogen (left) and under air (right) [4]

The main products of decomposition are phenols[5]. Combining pyrolysis/gas chromatography/mass spectrometry (Py/GC/MS), other decomposition products such as carbon monoxide and dioxide and benzene were identified along pyrolysis, as shown in Figure 3. [6] The degradation of PEEK is initiated by selective cleavage at chain ends and chain branching to produce phenols.

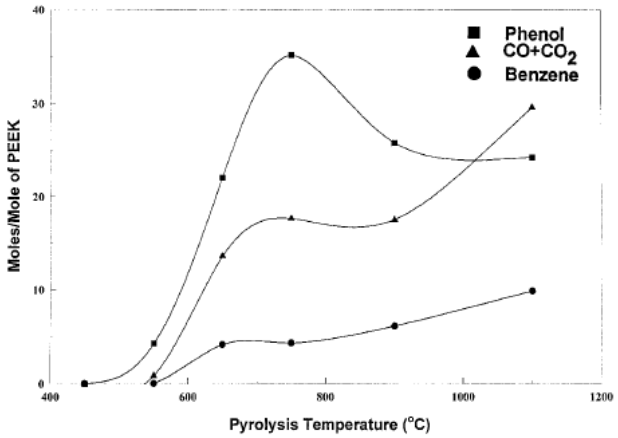


Figure 3. The Combining pyrolysis/gas chromatography/mass spectrometry (Py/GC/MS) evolution profiles of (a) phenol, CO + CO2, and benzene [6]

Cette thèse est accessible à l'adresse : https://theses.insa-lyon.fr/publication/2023ISAL0006/these.pdf
© [H. Willeman], [2023], INSA Lyon, tous droits réservés

The stability of PEEK in solution has been investigated by Bishop et al. [7] The PEEK solubility at room temperature being restricted to a few strong acids, sulfuric and chlorosulfonic acids were used. Chemical modifications were followed by static and dynamic light scattering, absorption spectroscopy, and viscosimetry. The conclusions were that protonation and chemical modification of the dissolved polymer must be taken in account when characterizing the polymer, as it will depend on the chosen solvent. Figure 4 presents a summary of room temperature solubility of PEEK for several solvents. [7]

solvent	solubility
94.9% H_2SO_4	complete
89.9% H_2SO_4	nearly complete
84.8% H_2SO_4	partial
79.6% H_2SO_4	negligible
CH_3SO_3H	complete
CF_3CO_2H	negligible
poly(phosphoric acid) (100 °C)	slight/partial

Figure 4. Solubility of PEEK at 25°C [7]

A branching mechanism leading to crosslinking has been observed in PEEK in melt processing conditions by Jonas and Legras. [8] The evolution of M_w and M_z with holding time in air measured by gel permeation chromatography (GPC) is presented in Figure 5. In air, the branching mechanism in the melt is rapid already from 385°C, as M_z increases by 10% after t_{hold}= 15min and up to 30% after 15min at T_{hold}= 400°C. For the polymer sealed under low vacuum conditions, the branching mechanism is slow and M_w can be considered to be constant up to 400°C over 40min.

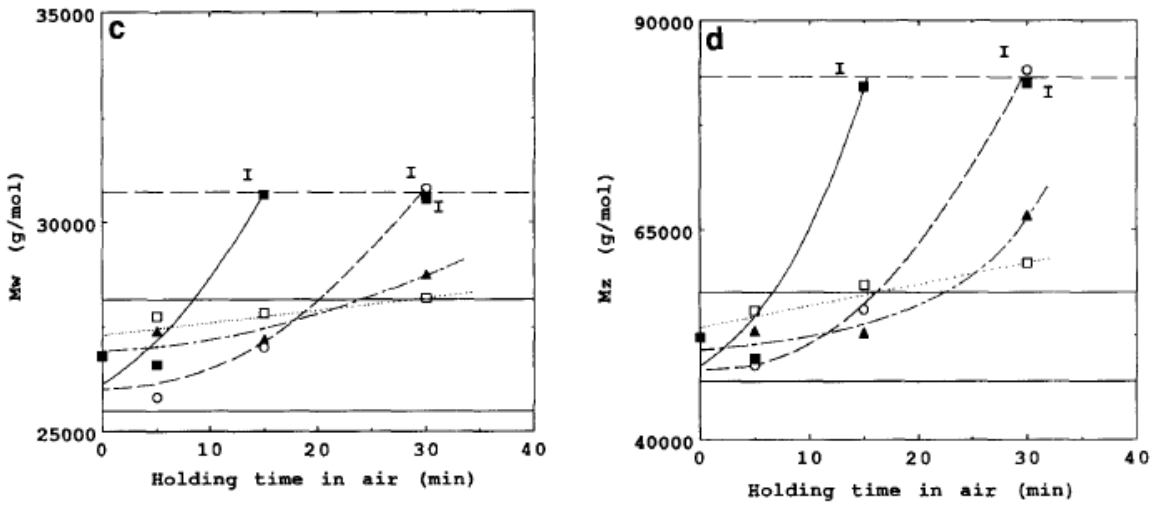


Figure 5. Mw and Mz as a function of the holding time in the molten state in air ((c) and (d)). When an insoluble fraction appears in the solution, the symbol I is drawn near the relevant point. The solid lines represent the estimated maximum uncertainly interval around the mean values for the as-received polymer. The melt holding temperatures are: □ ,385°C; ▲, 400°C; O, 420°C; ■, 440°c [8]

Cette thèse est accessible à l'adresse : https://theses.insa-lyon.fr/publication/2023ISAL0006/these.pdf
© [H. Willeman], [2023], INSA Lyon, tous droits réservés

3. Crystallographic structure

Crystallization in semi crystalline polymers leads to a multiscale, hierarchical organization of the material, with various relevant entities, from the smallest to largest scale: crystalline unit cells, crystalline lamellae and spherulites.

PEEK crystallizes in an orthorhombic structure, following the Pbcn group symmetry with two chains and four monomers per unit cell. The polymer backbone is aligned along the c-axis. Unit cell parameters of PEEK have been determined by Wakelyn[9]: a=7.88 Å b=5.94 Å c= 30.50 Å. These parameters lead to a crystal density of 1.4 $g.cm^{-3}$. For fully amorphous PEEK, the density is equal to 1.26 $g.cm^{-3}$ at room temperature [10]. However, the cell parameters and thus the crystal density are dependent on crystallization temperature[11] [12]. When amorphous films of PEEK were annealed at temperatures T_a ranging from 189 to 323°C, the unit cell parameters changed with crystallization temperature as indicated in Table 1 and thus the crystal density increased from 1.367 to 1.412 $g.cm^{-3}$. An increasing degree of disorder in the packing of the molecular chains as T_a decreases is the hypothesis put forward by Hay et al to explain this observation [12].

Table 1. PEEK - crystallization temperature dependence of unit cell parameters, after Wakelyn [11]

T_a (°C)	a (nm)	b (nm)	c (nm)	density ($g.cm^{-3}$)
189	0.7843	0.5937	3.0074	1.3665
216	0.7844	0.5912	3.0138	1.3692
241	0.7845	0.5906	2.9858	1.3833
264	0.7787	0.5855	3.0210	1.3893
282	0.7769	0.5857	3.0376	1.3845
306	0.7741	0.5848	3.0050	1.4067
323	0.7733	0.5844	3.0013	1.4109

The main diffraction peaks obtained by WAXS by Wakelyn [9] are shown in Figure 6. They are indexed as (110), (113) ,(200) and (213) at the diffraction angles 2θ approximately 18.7°, 20.7°, 22.6° and 28.6° respectively.

Cette thèse est accessible à l'adresse : https://theses.insa-lyon.fr/publication/2023ISAL0006/these.pdf
© [H. Willeman], [2023], INSA Lyon, tous droits réservés

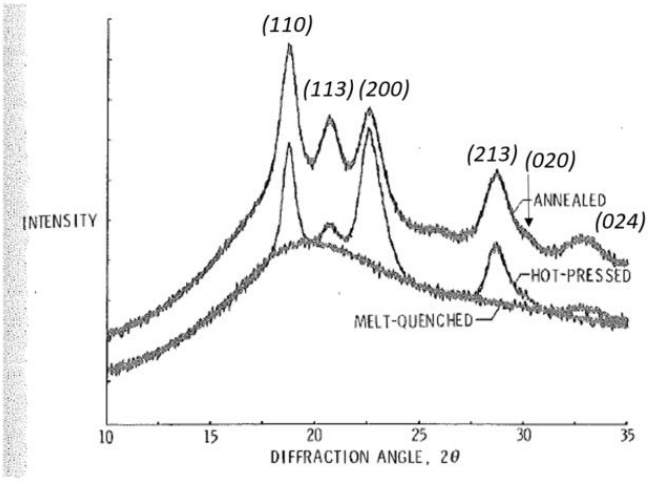


Figure 6. Diffractogram of annealed, hot-pressed and quenched PEEK [9]

In Figure 7 is represented the crystallographic structure of PEEK. It is two structural unit long along $\vec{c}$ and with (110) planes having the largest signature on diffractograms (the most dense planes). Only one crystal structure of PEEK has been reported in the literature, with variable cell parameters however (see Table 1).

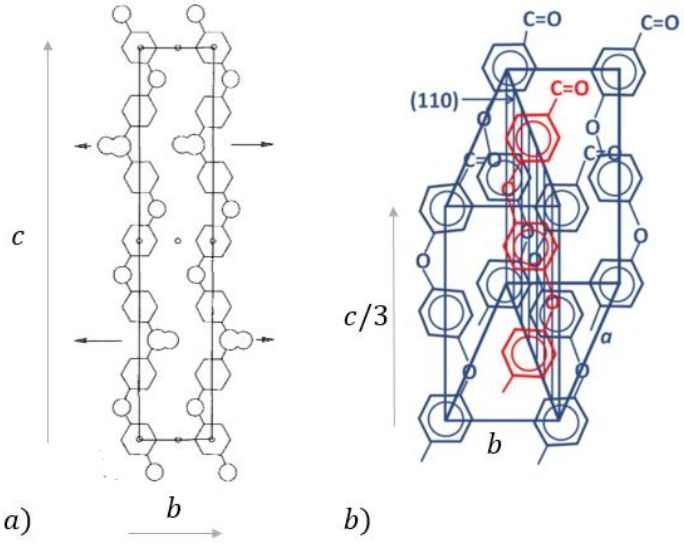


Figure 7. Crystallographic structure of PEEK (100) (left) and (110) (right) planes [9] [13]

Lovinger, who studied the morphology of solution-crystallized single crystals and spherulites of PEEK, has shown that when crystallized in solution, spherulites appears as very narrow lamellar branches that grows along the $\vec{b}$ axis in the radial direction [14] [15]. PEEK crystals crystallized in solution are seen in Figure 8. The long axis of the needle-shaped crystals corresponds to the $\vec{b}$ axis of the unit cell, while their transverse direction corresponds to the $\vec{a}$ axis and the thickness direction to the molecular $\vec{c}$ axis.

Cette thèse est accessible à l'adresse : https://theses.insa-lyon.fr/publication/2023ISAL0006/these.pdf
© [H. Willeman], [2023], INSA Lyon, tous droits réservés

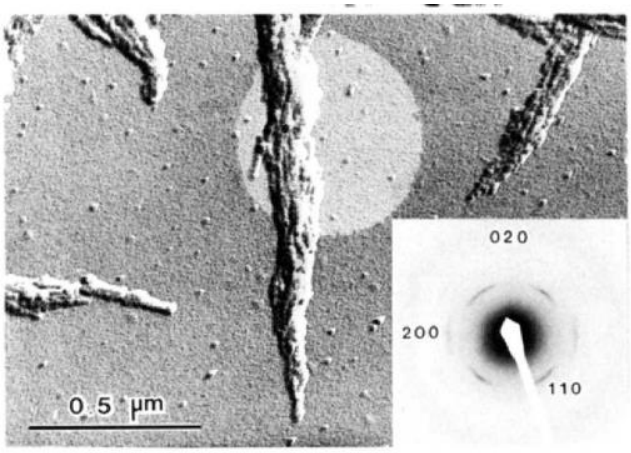


Figure 8. Electron-microscopic appearance of PEEK single crystals grown from a 0.01% solution in α-chloronaphthalene at 205 °C. The electron-diffraction patterns originate from the circled areas of the micrographs and are shown in correct orientation. [14]

The crystallinity index of PEEK may be assessed using several techniques such as DSC or infrared spectroscopy. [16], [17] However, due to recrystallization processes during the heating ramp in DSC, this technique may not be reliable to determine the initial crystallinity of a PEEK sample. Using infrared spectroscopy, Jonas et al. put in evidence the presence of 'crystallinity sensitive' absorption bands at 947 and 965 cm^{-1} that can be used to evaluate the crystallinity of a sample.

4. Lamellar and spherulitic structure

During crystallization, polymer chains organize and form crystalline unit cells. These crystalline unit cells are constituent units of lamellae, whose thickness L_c varies typically between 4 and 40 nm in semi-crystalline polymers in general. A characteristic parameter of semi-crystalline polymers is the long period L_p, depicted in Figure 9, which is the one -dimensional periodic characteristic of lamellar structure equal to the sum of the crystal lamellar thickness (L_c), and the interlamellar amorphous layer thickness (L_a).

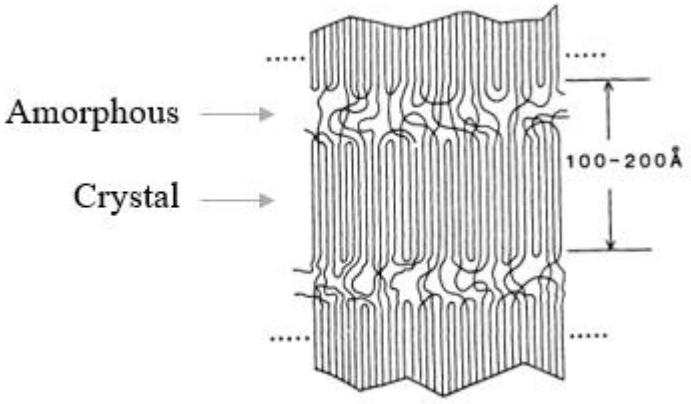


Figure 9. Schematic diagram of lamellar stacking in a semi-crystalline polymer[18]

At a larger scale, spherulites are the preferential crystalline structures adopted by semi crystalline polymers during crystallization. The radius of these entities is generally between 1 and 100µm. Crystalline lamellae radially grow from a unique nucleus, separated by interlamellar amorphous phase as schematized in Figure 10. Secondary crystallization may occur in between lamellae. The periodicity of lamellae stacking is around 10 nm but the length of lamellae can reach a few micrometers (similar to the spherulite radius). When spherulites grow from the molten state, especially for non-controlled

Cette thèse est accessible à l'adresse : https://theses.insa-lyon.fr/publication/2023ISAL0006/these.pdf
© [H. Willeman], [2023], INSA Lyon, tous droits réservés

crystallization conditions, they can lack perfection and grow on each other, giving a fragmented and segmented appearance.

The spherulite sizes strongly depend on parameters such as thermal history or molecular weight. [19][20] The influence of molecular weight of PEEK on the spherulite size has been studied by Schultz and Chu. [21] They concluded that the average spherulite size was smaller for the material of higher molecular weight.

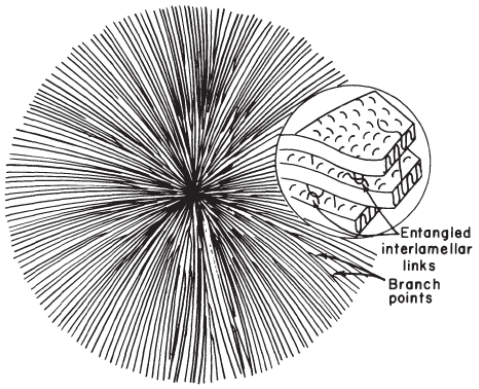


Figure 10. Polymer spherulite with chain folded lamellae[22]

The lamellar structure in PEEK has been successfully observed at different scales. At the lamella scale, scanning electron microscopy (SEM) is used with permanganic etching preparation technique proposed by Olley, Basset and Blundell in 1985 (Figure 11).[23]

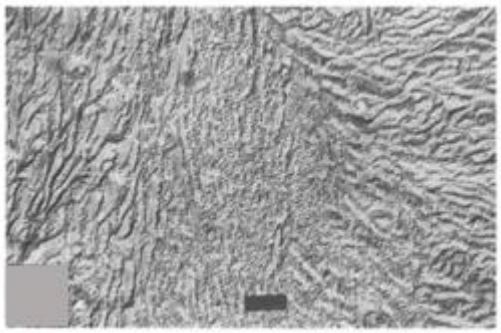


Figure 11. Electron micrographs of replicas of PEEK at high magnification, showing lamellar details. The PEEK sample was etched with sulphuric acid-phosphoric acid and water mixture. Scale bar = 100 nm [23]

At a larger scale, the spherulitic structure can be observed via crossed polarizer optical microscopy because of the birefringence of the crystalline phase [10] [24] [25]. Figure 12 gives an example of spherulite observation by optical microscopy.

Cette thèse est accessible à l'adresse : https://theses.insa-lyon.fr/publication/2023ISAL0006/these.pdf
© [H. Willeman], [2023], INSA Lyon, tous droits réservés

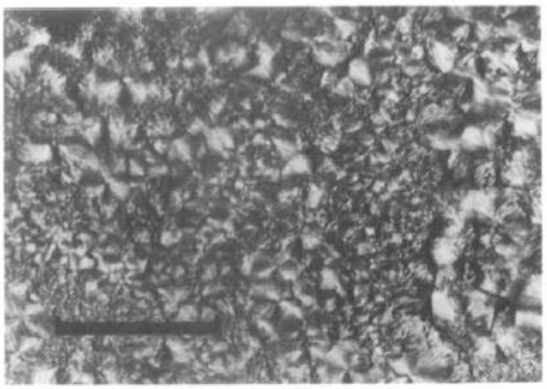


Figure 12. Polarized light micrograph of a section cut from a sample crystallized isothermally at 287°C. Scale bar =100 µm [10]

Recently, other unusual crystalline morphologies of PEEK consisting of granular blocks have been described by Wang et al. and are presented in Figure 13 [26]. This study has revealed a new hierarchical spherulitic crystal structure, different from the usual morphology with lamellae that grows in a radial direction to form spherulites, composed of small primary crystal blocks, secondary structures and large granular crystal blocks. These structures are independent of the process as they were found both in laser-sintered samples and in samples crystallized from the melt.

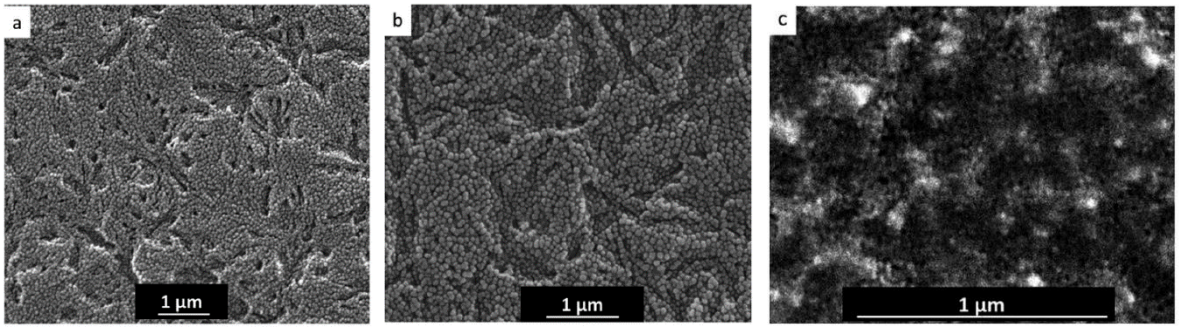


Figure 13. Crystal morphology of melt crystallized PEEK, imaged with SEM. (a) low magnification image showing the spherulitic structure and the granular crystal blocks. (b) high magnification image showing the granular crystal blocks (c) high magnification images taken from etched sample showing small primary crystals. [26]

Cette thèse est accessible à l'adresse : https://theses.insa-lyon.fr/publication/2023ISAL0006/these.pdf
© [H. Willeman], [2023], INSA Lyon, tous droits réservés

III. Deformation mechanisms in semi crystalline polymers

1. Elastic behavior

At low deformation corresponding to the elastic regime, Bowden and Young in 1974 assume that mostly only the amorphous phase deforms.[27] They have studied deformation mechanisms in semi crystalline polymers by using small and wide angle X-ray diffraction. In a semi-crystalline material with local lamellar structure, the main deformation mechanisms under tensile stress are schematized in Figure 14.

Interlamellar shear consists in the slip of crystal lamellae parallel to each other where the amorphous phase in between undergoes simple shear stress. This mechanism is more likely to happen above the glass transition when the amorphous phase is in a rubbery state, so that shear can happen at relatively low stress. The reversibility of this mechanism is related to tie molecules, which are able to extend upon deformation and relax with unloading.

Interlamellar separation is induced by a tensile or compressive stress component parallel to the normal to the lamellae surface.

Stack rotation occurs only for lamellae in a stack free to rotate under the action of the applied stress. It requires that the stack is surrounded by some amorphous phase that can accommodate the deformation.

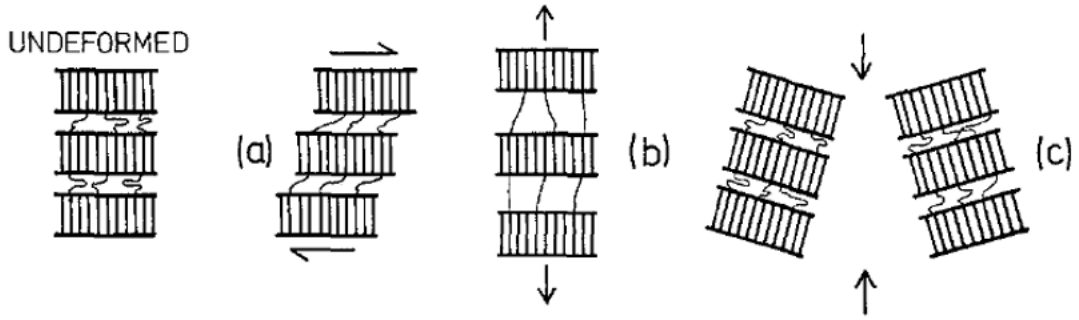


Figure 14. Deformation mechanisms in the amorphous phase. (a) Interlamellar shear (b) Interlamella separation (c) Stack rotation [27]

2. Plastic behavior

The plastic deformation of polymer crystals, like the plastic deformation of crystals of other materials, is generally expected to be crystallographic in nature without destroying the crystalline order. Only at larger deformation, the macroscopic deformation is often associated with localization phenomena such as necking, cavitation or crazing where crystal order may break down. During this process, the material will transition from a lamellar to a fibrillar structure.

At the macroscopic scale, the appearance of necking in a semi crystalline polymer is described by Strobl and represented in Figure 15. [28] During stretching, when the polymer reaches the yield point, visible flow sets in at some point of the sample and is accompanied by a drop in the load. The lateral dimensions of the sample narrow and finally a neck is formed, with a smaller cross-section area. A shoulder with a continuous profile develops between the original part of the sample and the neck. Further extension is achieved by the propagation of the neck i. e. an increase of the neck length over the sample. The external force that has to be applied during this cold-drawing process remains constant as long as the neck length increases.

Cette thèse est accessible à l'adresse : https://theses.insa-lyon.fr/publication/2023ISAL0006/these.pdf
© [H. Willeman], [2023], INSA Lyon, tous droits réservés

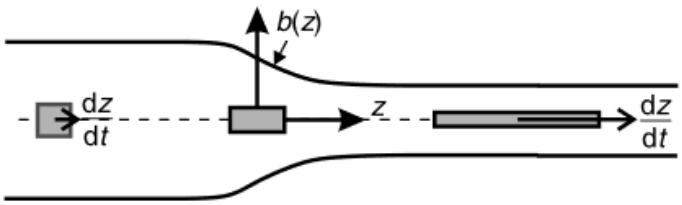


Figure 15. States of deformation of a volume element passed over by a shoulder with the profile b(z), and the velocity dz/dt relative to the shoulder [28]

Plastic deformation involves deformation of the crystalline phase via several mechanisms such as crystal shear, slip in the chain direction, and phase transformation. The slip mechanism is the most important as it can produce large plastic strain while preserving the crystalline order to a large extent. A slip system in a crystal is the combination of a slip direction and a slip plane containing that direction. (Figure 16) The slip mechanism produces a simple shear deformation of the crystal localized in the slip plane. In polymer crystals, slip planes are restricted to planes containing the chain direction. Two types of slip can occur: chain slip, along the chains, and transverse slip, perpendicular to the chains. The slip plane is the crystallographic plane parallel to the slip direction.

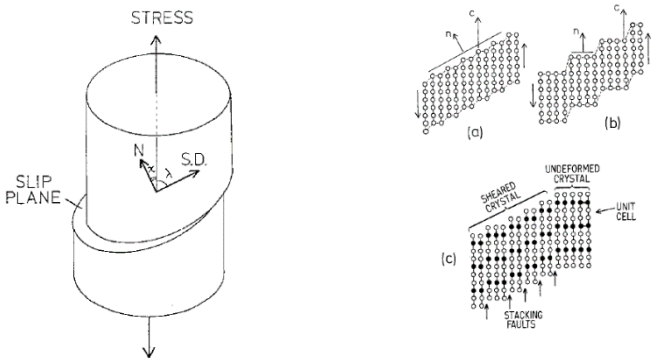


Figure 16. Slip under uniaxial tensile stress[27]

a. Cavitation

Cavitation is one of the micro-mechanisms of plastic deformation of semi-crystalline polymers during tensile loading. This phenomenon consisting in the formation of nano or micro voids is also considered to be a damaging process because it affects the plastic yield and the failure of the material. Cavitation phenomena decompose in three steps: nucleation, growth and coalescence. Whitening of the sample during tensile test near the yield point is one hint of cavitation phenomena. During these tests, cavitation begins in the amorphous phase, between the crystalline lamellae perpendicular to the stress axis.[29]

Pawlak and Galeski studied the role of cavitation and crystal plasticity into plastic deformation of semi crystalline polymers. Cavitation occurs in polymers with crystals of high plastic resistance, while plastic deformation of crystals occurs in polymers with crystals of lower plastic resistance. Using electron microscopy, Galeski was able to localize cavities in the interlamellar and interspherulitic amorphous phase and elaborate a scenario of cavities formation schematized in Figure 17. [30] Small-angle X-ray scattering (SAXS) can be used for the detection of voids. [29]

Cette thèse est accessible à l'adresse : https://theses.insa-lyon.fr/publication/2023ISAL0006/these.pdf
© [H. Willeman], [2023], INSA Lyon, tous droits réservés

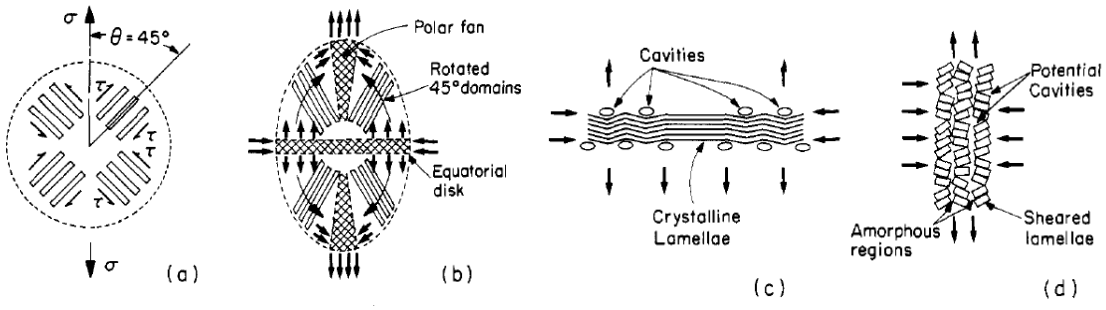


Figure 17. Steps of cavities formation into equatorial regions of spherulites: a) Initial undeformed state; b) Rotations due to simple shear; c) Kink of underformed lamellae in equatorial regions; d) Instabilities due to chain slip for lamellae in polar regions [30]

b. Crazing

Crazing in semi crystalline polymers has been described by Narisawa[31], Friedrich[32] or Kausch[33]. The formation of voids in a homogeneous material happens mostly on heterogeneities in zones of stress concentration. It is a thermally activated mechanism. Voids appears in between macromecules without breaking chains. The initiation kinetics of crazes is faster when the stress is higher. After the initiation step and stabilization of craze density, crazes grow perpendicular to the stress direction. They are composed of two decohesive surfaces which are interconnected by fibrils between which micro voids develop. The Friedrich's model of craze initiation and propagation is displayed on Figure 18.

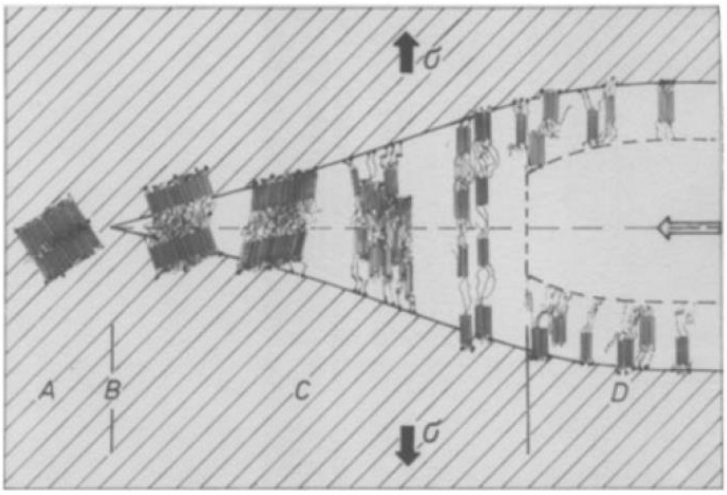


Figure 18. Model of craze initiation and propagation in a semi-crystalline polymer: A. elastically strained region, B. region of void nucleation and fibril formation, C. craze growth due to fibril extension and continued fibrillation, D. transformation of craze into crack [32]

Observation of the crazing phenomenon usually combine X-ray diffraction and microscopy techniques (SAXS, optical microscopy (see Figure 19), transmission electron microscopy (TEM).

Cette thèse est accessible à l'adresse : https://theses.insa-lyon.fr/publication/2023ISAL0006/these.pdf
© [H. Willeman], [2023], INSA Lyon, tous droits réservés

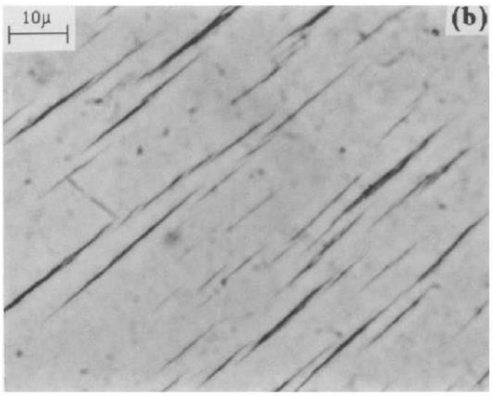


Figure 19. Optical micrograph of crazing in PEEK without crossed polarizer[34]

c. Shear bands

The formation of localized deformation zones such as shear bands is often observed in metals and semi-crystalline polymers. They are based on a slip phenomenon. No void is created in the material by the formation of shear bands, unlike for cavities. Shear bands can be observed by cross-polarized optical microscopy in the maximum shear direction, which is 45° from the stress direction for uniaxial stress. Shear bands are most often observed under compressive loading.

A review by Friedrich indicates that the shear band direction in semi crystalline polymers is between 35° and 42°.[32] Figure 20 shows an example of shear bands in HPDE. According to Bowden and Young, shears bands are mostly localized in spherulites at 45° from tensile direction.

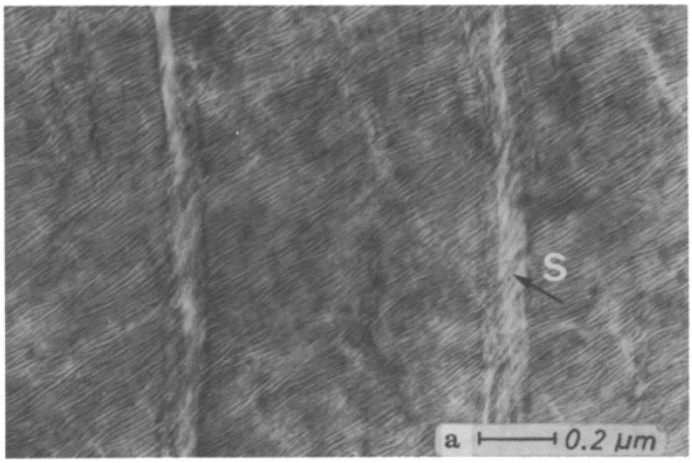


Figure 20. Shear bands (S) in the compressive region of a HDPE-bend specimen. The axis of the compressive stress is perpendicular to the direction of the lamellae [32]

d. Fibrillar structure

At high deformations, the material undergoes crystal fragmentation, the crystallites orient along the stress and can form new crystals. This reorganization is enabled by crystal shear and stack rotation along the tensile direction. The initially isotropic spherulitic structure changes into a microfibrillar oriented structure. This final structure is usually accompanied by high localization of plastic deformation in a local necking zone whose section is reduced.

Cette thèse est accessible à l'adresse : https://theses.insa-lyon.fr/publication/2023ISAL0006/these.pdf
© [H. Willeman], [2023], INSA Lyon, tous droits réservés

Peterlin has studied the fibrillar evolution of the crystalline structure at large elongation. [35] The final structure is characterized by the nearly perfect orientation of the crystallized chains along the fibre axis and by a high longitudinal elastic modulus and tensile strength. Crystal lamellae are perpendicular or at a finite angle to the fiber axis.

Microfibrilles are approximately a dozen of micrometers long and the lateral size is a few nanometers. The elastic modulus of the polymer chains is higher than the bulk elastic modulus. Two types of amorphous phase are present: one localized in between crystallites within a microfibrille and one localized in between microfibrilles.

In a study by Schultz on the influence of microstructure on failure of semi crystalline polymers, a map of break modes as a function of strain rate or temperature has been established (Figure 21) [36]. Three regions are described: the intercrystalline fracture at low temperature, the interspherulitic fracture at intermediate temperature, and the semibrittle and ductile failure at higher temperatures. The parallel lines separating the three domains are intended to illustrate that the transitions are sensitive to various elements of the microstructure. It is hazardous to discuss the influence of one parameter at a time as they are interdependent.

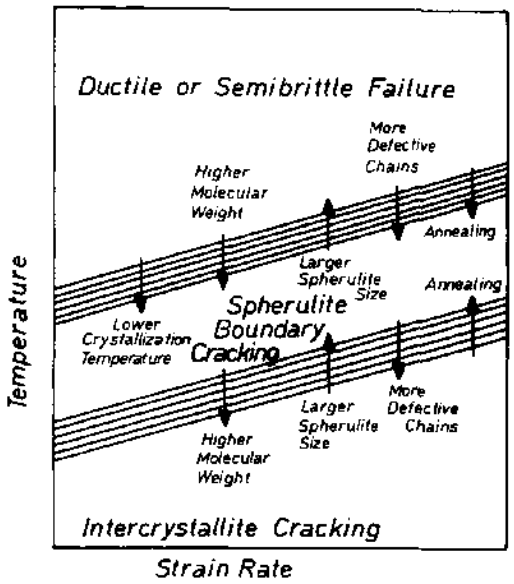


Figure 21. Schematic temperature-strain rate failure map [36]

3. In situ X-rays scattering studies

To access the structural evolution of a polymer in real time, in situ X-ray scattering studies have been most often carried out using Synchrotron radiation. This technique has been more recently used to study deformation processes of semi crystalline polymers under tensile stretching. However, no study has focused on PEEK so far.

Polyolefin have been widely studied using this technique. [37]–[40] In 1995, Butler et al. compared deformation mechanisms of LLDPE and HDPE. [37] Combination of SAXS and WAXS allowed to notice the correspondence between the onset of cavitation and a martensitic transformation of the polymer. The yielding behavior and the influence of stress transmitters and crystallinity were investigated by Humbert et al. [41], [42] Cavitation in HDPE was also studied by Schneider et al. [40] Investigations on polypropylene were carried out by Schneider et al. [43] [44]

Cette thèse est accessible à l'adresse : https://theses.insa-lyon.fr/publication/2023ISAL0006/these.pdf
© [H. Willeman], [2023], INSA Lyon, tous droits réservés

More recently, Xiong et al. [38] and Hang et al. [39] have studied the intraspherulitic deformation of PE for oligocyclic or tensile stretching using this technique. The polar and equatorial strains in the spherulites can be compared.

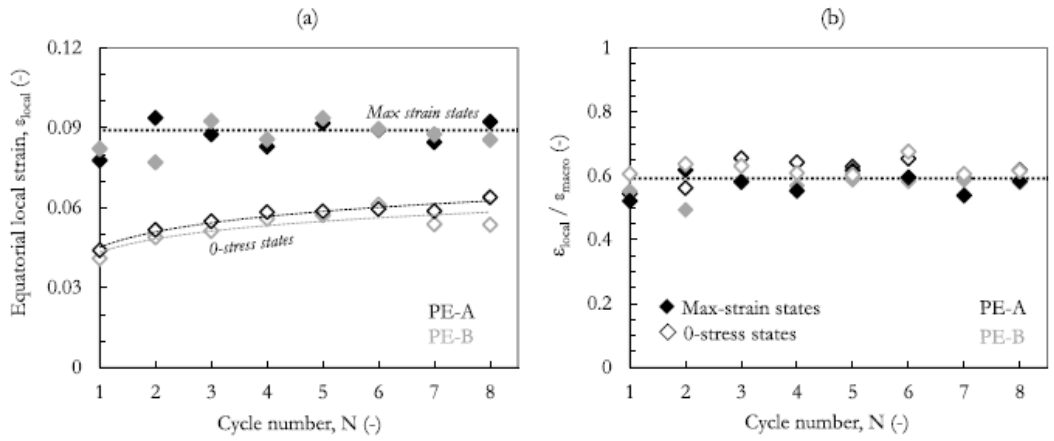


Figure 22. (a) Local strain at maximum-strain and minimum-stress states. (b) Plot of the ratio $\varepsilon_{local}/\varepsilon_{macro}$ as a function of cycle number (quenched samples) [39]

In Figure 22, the equatorial local strain in two types of PE is shown as a function of the number of cycles. The ratio between the local and global microscopic and macroscopic strains is also followed along loading. It is found to be nearly constant, equal to 0.6, which indicates that heterogeneity exists at the microscopic scale as the equatorial region of the spherulites is less deformed than other regions along the macroscopic loading direction.

Polyamides were studied by Paolucci et al. [45] and by Millot et al. [46]. Using in situ X-ray scattering during tensile tests, Paolucci et al. concluded that cavitation processes are different depending on the type of processing (sintering or molding).

Our project on PEEK closely follows the approach of Millot et al on polyamides. Analysis of SAXS and WAXS data during tensile tests allows to determine and compare the deformations at different scales, including the macroscopic and microscopic (lamellar stacks and crystal planes) scales, as depicted in Figure 23.

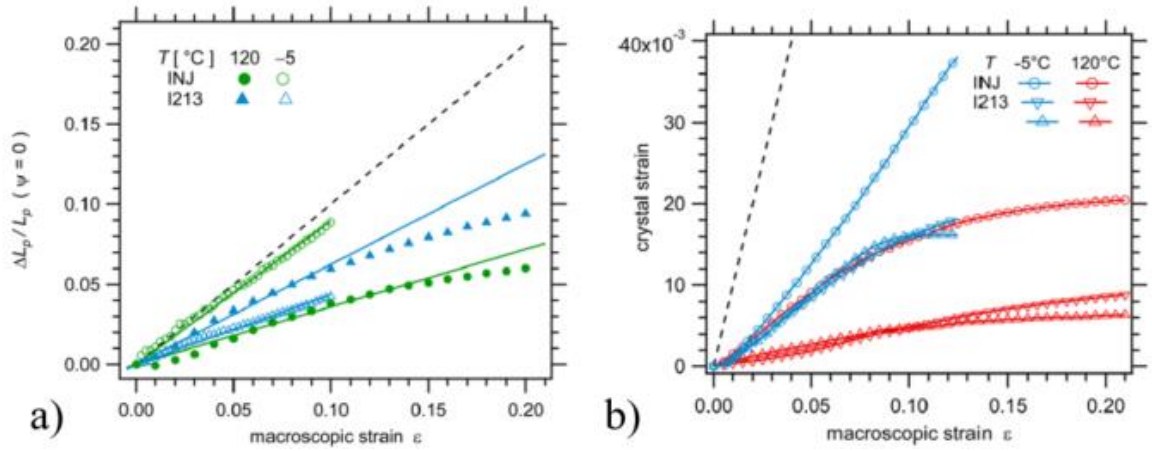


Figure 23. a) Local strain of the lamella stacks along the tensile direction TD, ΔLp/Lp (ψ = 0), as a function of the macroscopic strain, ε, for samples I213 (isothermally crystallized) and INJ (injected) stretched at T = −5 °C and T = 120 °C. The dashed line corresponds to ΔLp/Lp = ε macro; full lines are linear fits of the experimental data in the range 0 < ε < 0.10 b) Crystal strain given by the relative variation of lattice spacing along SD for INJ and I213 samples stretched at T = −5 °C and T = 120 °C. [46]

Cette thèse est accessible à l'adresse : https://theses.insa-lyon.fr/publication/2023ISAL0006/these.pdf
© [H. Willeman], [2023], INSA Lyon, tous droits réservés

Analogies between PEEK and PET have been made in the literature as they present somehow similar crystallization behavior [10], [47]. In situ X-ray scattering studies on PET is thus interesting, such as the work of Forestier et al. [48], [49] on PET following the evolution of the crystalline structure by formation of mesophase in the polymer under tensile stretching.

IV. Properties of PEEK

As a semi crystalline polymer, the PEEK properties will strongly depend on its structure at every scale mentioned in the previous part. In this section, the relaxation processes and mechanical properties of PEEK will be reviewed as well as various aspects of the crystallization process such as double melting behavior or crystallization kinetics.

1. Relaxations

To characterize a polymer, mechanical relaxations can be studied using dynamic mechanical analysis (DMA). The α-relaxation process corresponds to the glass transition phenomenon. This main relaxation that occurs in PEEK around 150°C has been extensively characterized, as displayed on Figure 24. This relaxation is due to large scale motions of the macromolecular chains and greatly impacts the mechanical properties of the material.

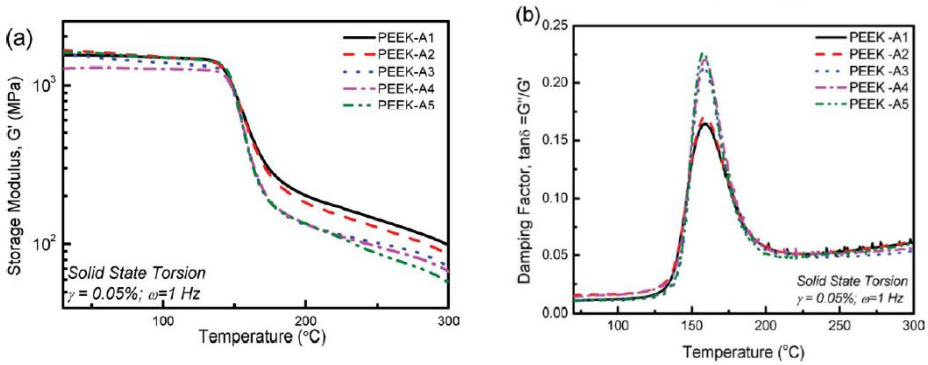


Figure 24. Solid state viscoelastic properties of various grades of PEEK (with different crystallinity indices); (a) storage modulus and b) loss factor, during a temperature ramp from 30°C to 300°C at a rate of 3°C/min [2]

The β relaxation occurs at lower temperatures, and corresponds to local chain movements. Depending on the thermal history of PEEK samples, relaxations at low temperatures are observed around -70° or -100°C. For amorphous PEEK, Krishnaswamy and Kalika[50] observed a relaxation at -70°C (Figure 25).

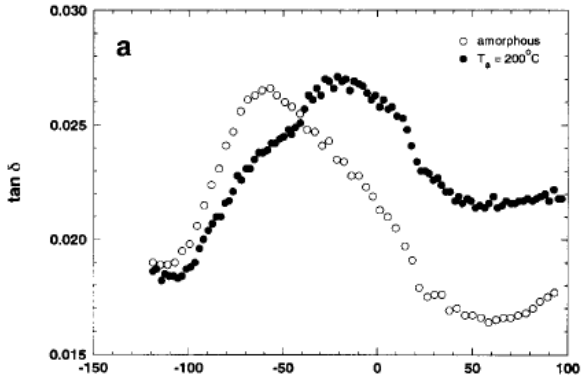


Figure 25. Dynamic mechanical loss factor (tan δ) versus temperature (°C) at 5 Hz, sub-glass (β) relaxation for amorphous (o) and cold-crystallized PEEK (•) Tc=200°C [50]

Cette thèse est accessible à l'adresse : https://theses.insa-lyon.fr/publication/2023ISAL0006/these.pdf
© [H. Willeman], [2023], INSA Lyon, tous droits réservés

Sasuga and Hagiwara[51] observed a broad relaxation mode near -90°C: it was associated to oscillations of phenyl groups. Mourgues-Martin presented complementary data obtained by dielectric spectroscopy.[52] The technique of thermally stimulated current revealed the bimodal behavior of the low temperature relaxation mode. The lower temperature contribution at -110 °C was associated with the local mobility of phenyl groups in the amorphous phase and the higher temperature one at -75 °C was attributed to localized movements in the so-called rigid amorphous phase, located at the interface between the amorphous and crystal phases, which has a constrained mobility.

Starkweather and Avakian compared the data on the β-relaxation of phenylene polymers obtained by dielectric and mechanical measurements. [53] They have shown that the maximum value of tanδ was larger in the mechanical data, the activation energy was larger, and the peak occurred at a higher temperature and a lower frequency than in the dielectric data.

2. Mechanical properties

Figure 26 represents the general mechanical behavior of a semi-crystalline polymer under tensile stress. This curve can be divided into four domains:

I: An elastic response is observed at low stresses. The deformation is reversible and proportional to the stress, it follows Hooke's law: $\sigma = E \cdot \varepsilon$ The slope E of the curve in the initial elastic domain is the Young's modulus.

II: The stress reaches a maximum, called plasticity threshold or yield stress and noted σ_y. The yield point is the limit between elastic and plastic strain. At this stage, if the polymer localizes the deformation, macroscopic necking can start in the sample. Two phases with different draw ratio coexist.

III: This domain is called the stress plateau or the plastic (flow) regime. The stress does not depend on the deformation. It corresponds to the propagation of the necking phenomenon over the whole sample length, with the phase with higher draw ratio increasing progressively.

IV: At higher deformation levels, the stress might increase again before failure of the sample. This phenomenon is called strain hardening.

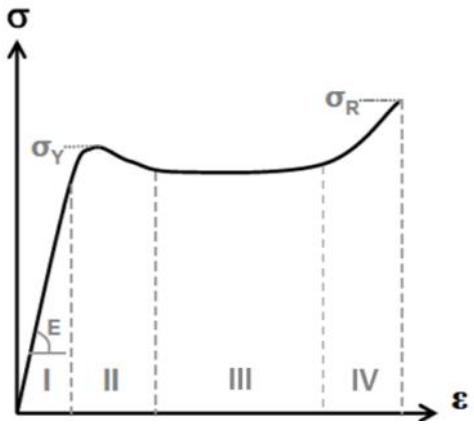


Figure 26. Nominal stress-strain curve for a semi crystalline polymer

In general, many parameters can influence the mechanical response of a polymer material: temperature, strain rate, type of loading, humidity…

The general mechanical properties found in the literature are listed in Table 2 below:

Cette thèse est accessible à l'adresse : https://theses.insa-lyon.fr/publication/2023ISAL0006/these.pdf
© [H. Willeman], [2023], INSA Lyon, tous droits réservés

Table 2. General properties of PEEK at room T [54]

Young's Modulus (GPa)	3.4 – 3.7
Tensile strength (MPa)	90 - 100
Elongation at break (%)	20

a. Influence of temperature and strain rate

The influence of temperature and strain rate on the macroscopic mechanical behavior of PEEK has been investigated by several authors. [55]–[57] In Figure 27 are represented stress strain curves for three temperatures, below, at and above the glass transition temperature from the work of Barba [55].

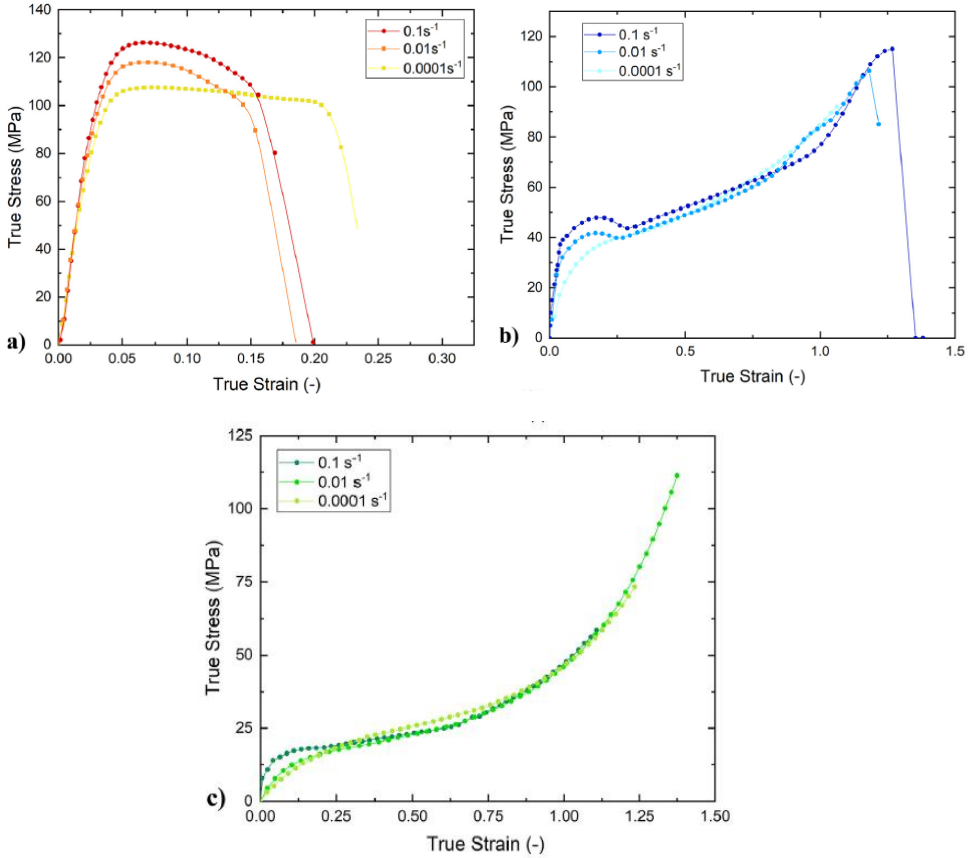


Figure 27. Experimental stress-strain curves of PEEK under tensile deformation at dif ferent strain rates at: (a) 20 °C; (b) 150 °C; (c) 240 °C. [55]

Below T_g, an initial linear elastic response is followed by the yielding of the material. The yield stress value increases as the strain rate increases; as it is generally reported. [58] Beyond yield, a drop of the macroscopic stress occurs at the two highest strain rates. Barba explains this phenomenon by adiabatic heating resulting from dissipation, leading to global thermal softening as deformation and thus heat localizes. Finally, the material breaks abruptly. The elongation at break is smaller for the higher strain rates. At T_g (150°C), a drop in yield stress from about 100 MPa at 20°C to 40 MPa at 150°C and a softening phase after yielding is observed. The yield stress value increases as the strain rate increases. Finally, the material hardens in the final stage of the strain-stress curves before rupture occurs. Above glass transition, the amorphous phase is in the rubbery state, the mechanical behavior is then expected to be very different. No decrease of the stress is observed for any strain rate. The mechanical behavior

Cette thèse est accessible à l'adresse : https://theses.insa-lyon.fr/publication/2023ISAL0006/these.pdf
© [H. Willeman], [2023], INSA Lyon, tous droits réservés

is composed of two different loading regions with a smooth transition: the initial elastic region, dependent on the strain rate, and a hardening region up to failure. The rate dependence is less pronounced than for other test temperatures.

The effects of strain rate and temperature on fracture morphology of PEEK have been investigated by Chen et al. [56] Hot tensile fracture was the main focus of the study: three test temperatures below and close to T_g were chosen (100, 140 and 150°C) and the strain rate ranged between 0.01 s^{-1} and 1 s^{-1}. For each test conditions, the morphology of fractured surfaces has been characterized by SEM. These observations suggest that fracture morphology does not depend on strain rate but is temperature dependent. Examples of failure morphology are presented in Figure 28.

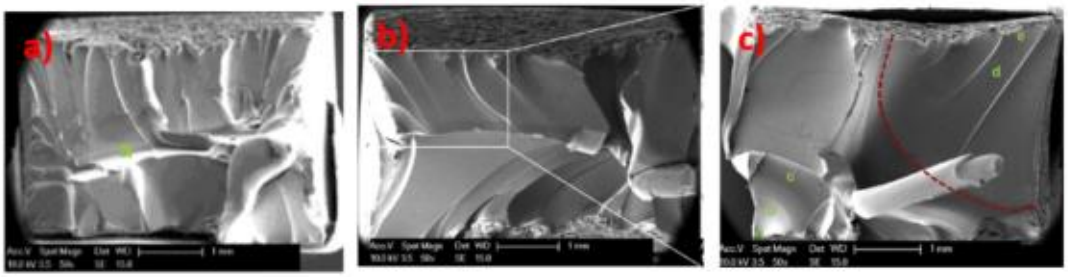


Figure 28. SEM fractograph at the strain rate of 0.1 s^{-1}. And at the temperature of a) 100°C, b) 140°C and c) 150°C [56]

b. Influence of molecular weight

The influence of molecular weight on mechanical properties of PEEK grades have been characterized using several methods such as tensile or compression tests and Izod impact resistance tests. [59] [60] [61] Corresponding stress-strain curves are represented in Figure 29. The KT820 and KT880 grades were compared. KT820, with higher molecular weight, exhibited lower strength, lower ductility, and greater impact resistance when compared to KT880.

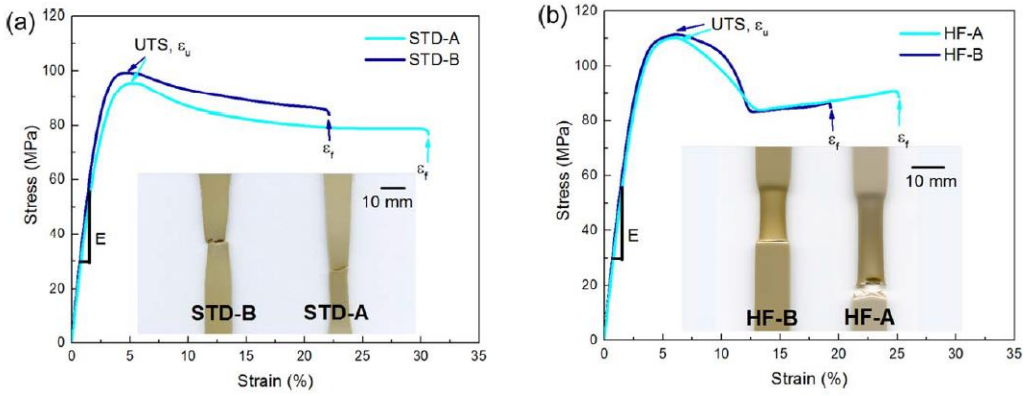


Figure 29. Nominal stress-strain curves of standard (STD) and high melt flow (HF) commercial grades of PEEK (STDA=KT820 and HFA=KT880) [60]

c. Fatigue behavior

The long term performances of PEEK have been widely studied, especially for PEEK-based composites. [62]–[65] In the study of Pastukhov et al. [58], the time to failure in PEEK is characterized by an apparent endurance (fatigue) limit due to the evolution of yield stress with test conditions, temperature and stress specifically as shown on Figure 30. Combination of the yield stress evolution with a previously developed model by Pastukhov and Govaert [66] for plasticity-controlled failure allows

Cette thèse est accessible à l'adresse : https://theses.insa-lyon.fr/publication/2023ISAL0006/these.pdf
© [H. Willeman], [2023], INSA Lyon, tous droits réservés

predicting the time-to-failure of the polymer under both static and cyclic loadings and quantitative determination of the apparent endurance limit.

Fractography of PEEK samples submitted to fatigue tests were carried out by Shrestha et al. [67] The analysis shows two fatigue stages observed on the fracture surface of PEEK specimens characterized by crack initiation and slow crack growth. Moreover, two types of inclusions, namely unmelted particles and void-like defects, were found responsible for crack initiation.

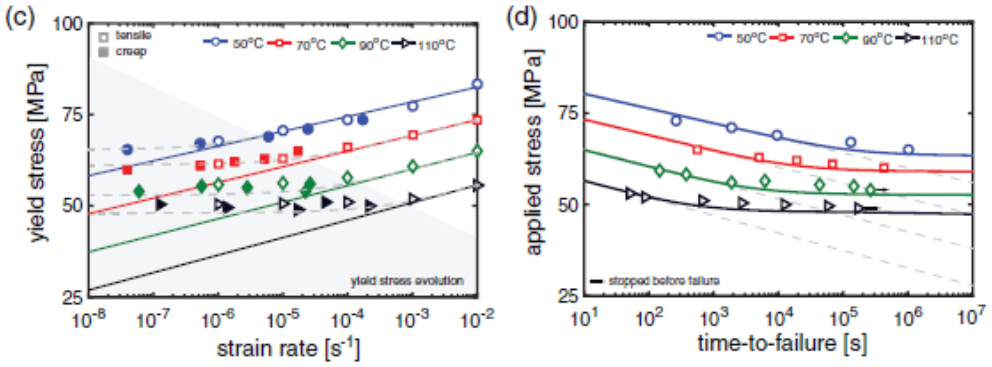


Figure 30. c) Yield stresses versus logarithm of strain rate both from tensile tests (open markers) and creep tests (filled markers) and (d) applied stresses in creep loading versus logarithm of time-to-failure. [58]

3. Physical ageing in PEEK

When an amorphous or semi crystalline polymer is cooled quickly from an equilibrium state above the glass transition temperature T_g down to below T_g, the viscosity increases, which causes a decrease in chain mobility and does not allow the macromolecular system to reach thermodynamic equilibrium. The material will thus be in a metastable state, with larger free volume than at the equilibrium. If the material is then kept at a temperature close to T_g (usually between Tg-50°C and T_g) for a long period of time, it will tend to reach a more stable state through slow molecular reorganization. This phenomenon is called physical ageing. It is different from chemical ageing during which the chemical structure of the polymer is irreversibly modified.

To achieve physical ageing, a material is kept at an ageing temperature for a period of time t. As we can see in Figure 31, the further the ageing temperature is from T_g, the more the material will have the possibility to age, i.e. to decrease its enthalpy (or volume). However, as the material is at a rather low temperature, the mobility of the macromolecules will be limited, so it may take a very long (geological) time for the material to reorganize to reach a hypothetical equilibrium state. If, on the other hand, the ageing temperature is close to T_g, the material will have a more limited possibility to age, but being close to T_g, the mobility of the chains may remain quite high and allow the material to reach equilibrium in a relatively short time. The choice of the ageing temperature is therefore a compromise between the material's ability to age and the time required for the material to reach its equilibrium state.

The enthalpy $\Delta H = H_0 - H_{aged}$ lost during physical ageing by the material is directly accessible during a DSC scan. What is measured in DSC is the heat capacity $C_p(T) = \frac{\partial \Delta H}{\partial T}$.

From Figure 31 that describes the DSC experiment, the enthalpy gain from A to B corresponds to the enthalpy gained during aging, or also to the gain in density (lower volume) that corresponds to a state closer to or at equilibrium, if enough time is given to the sample to reach its equilibrium. The enthalpy gain between points A and B is calculated as the area in between the two heat capacity curves

Cette thèse est accessible à l'adresse : https://theses.insa-lyon.fr/publication/2023ISAL0006/these.pdf
© [H. Willeman], [2023], INSA Lyon, tous droits réservés

corresponding to the heating cycles from points A and B. For the unaged sample, the enthalpy variation in the glass transition is given by equation (1), where $H_A$corresponds to the enthalpy of the glass at the point A at the aging temperature T_a and H_M corresponds to the enthalpy at a given temperature $T_M > T_g$. The same equation can be written for the enthalpy variation in the glass transition for the aged sample, as presented in equation (2), where H_B represents the enthalpy of the aged sample at point B, after an aging step at temperature T_a.

$$H_M - H_A = \int_{T_a}^{T_M} C_p^A(T)dT \quad (1)$$

$$H_M - H_B = \int_{T_a}^{T_M} C_p^B(T)dT \quad (2)$$

The enthalpy lost by the material during physical ageing is thus equal to the integral of the difference of the two curves as explained in equation (3), and will be called the "overshoot area". The overshoot appears as an endothermic peak (Figure 31b).

$$\Delta H_{ageing} = H_A - H_B = \int_{T_a}^{T_M} \left(C_p^B(T) - C_p^A(T)\right) dT \quad (3)$$

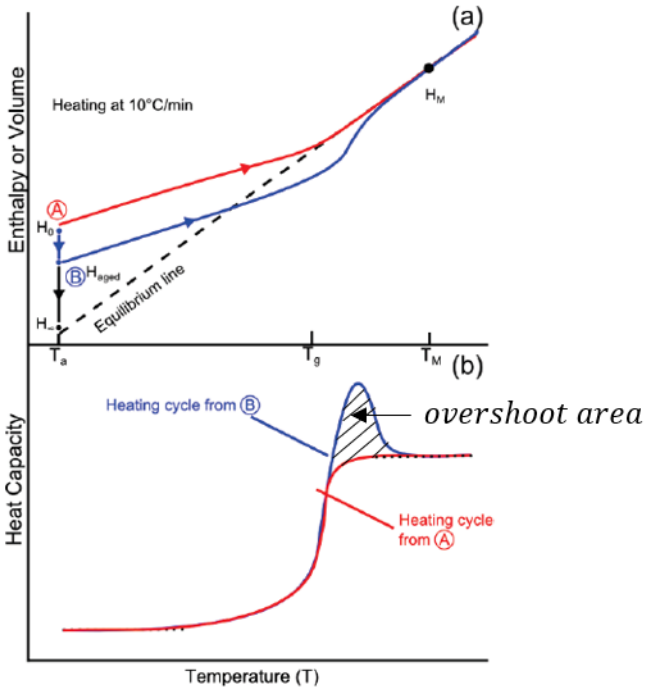


Figure 31. Schematic representation of (a) enthalpy or volume as a function of temperature and (b) heat capacity as a function of temperature, obtained as the derivative of enthalpy [68]

The effects of physical ageing on amorphous PEEK were studied by few authors [69]–[73]. In the work of Kemmish and Hay, physical ageing was studied by DSC [69]. Heating through glass transition temperature, the thermograms exhibited marked endothermic peaks as depicted in Figure 32. These peaks are characteristic of physical ageing as discussed above. As regards the mechanical properties of aged samples, ageing in PEEK is accompanied by an increased tensile yield stress and drawing stress, more localized yielding and a decrease in impact strength. [69]

Cette thèse est accessible à l'adresse : https://theses.insa-lyon.fr/publication/2023ISAL0006/these.pdf
© [H. Willeman], [2023], INSA Lyon, tous droits réservés

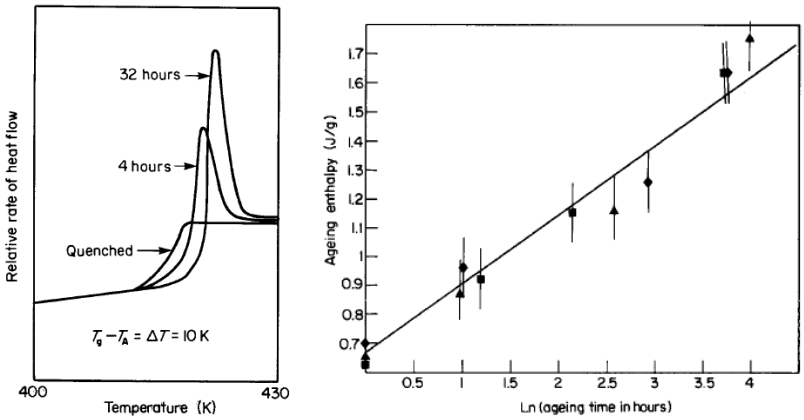


Figure 32. Heat capacity curves of PEEK samples aged at a temperature T (ΔT=Tg-T=10K), for different durations [69]

D'amore et al. used creep and DMA to monitor physical ageing in PEEK. [72], [73] By following the creep compliance, they observe an increase of stiffness with ageing time.

4. Crystallization

At every scale of the material (the crystalline lattice, crystallites, lamellar stacks and spherulites) crystallization involves an evolution of the microstructure. Crystallization from the melt in polymers is defined by the transition of an amorphous viscoelastic liquid into a crystal. Two phases coexist in semi crystalline polymers: the amorphous phase defined by entangled chains and the crystalline phase defined by a long-range order characterized by the crystalline cell periodically repeated in the material. Below the glass transition temperature T_g, the polymer cannot crystallize as it has no large-scale mobility.

Differential scanning calorimetry (DSC) allows determining the glass transition, the melting and the crystallization temperatures as presented in Figure 33. For PEEK, the glass transition temperature is 150°C, the melting temperature is about 340°C and crystallization occurs typically between 280 and 300°C for non-isothermal crystallization from the melt.

In this section, the influence of the thermal history and double melting behavior as well as memory effects in PEEK will be described, followed by a description of established models of polymer crystallization.

a. Double melting behavior

Double melting behavior of PEEK has been noted by many authors since the 1980s. The origin of these double peaks remains a matter of debate. For some authors, the double melting peak is explained by the growth of two different crystal populations during isothermal crystallization[74]·[75]. For other authors, this phenomenon is due to a reorganization during the heating cycle[76]. Figure 33 shows an example of a DSC study on melting behavior of PEEK which reveals double melting behavior depending on process conditions. [77] A melting peak at a temperature slightly above the crystallization temperature is present besides the main melting peak.

Cette thèse est accessible à l'adresse : https://theses.insa-lyon.fr/publication/2023ISAL0006/these.pdf
© [H. Willeman], [2023], INSA Lyon, tous droits réservés

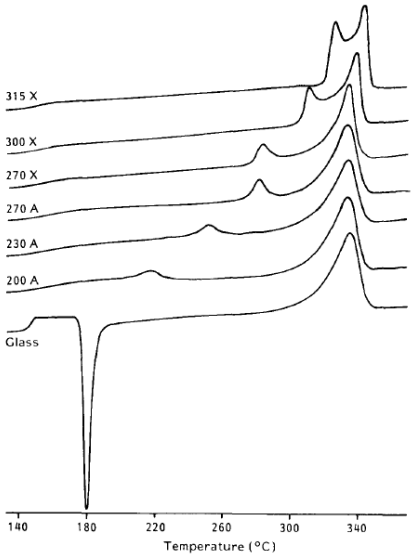


Figure 33. Melting endotherms of PEEK specimens: (200A, 230A, 270A) annealed from the glass for 1 h at the indicated temperature; (270X, 300X, 315X) crystallized (X) from the melt for 1 h at 270 and 300°C, and 4 h at 315°C. [77] The exotherm of the glassy sample shows a cold-crystallization peak at about 180°C.

X-ray scattering techniques combined with DSC have been used by Fougnies et al. in order to investigate the double melting behavior of PEEK. [78], [79] They noted a difference between samples crystallized from the glassy state below and above 315°C. For annealing at temperatures below 315°C, double melting behavior can be attributed to a melting-recrystallization process of a single population of crystals, as structural parameters of reorganized lamellae are similar above annealing temperature. When annealing at temperatures corresponding to the second melting point region (340 °C), the resulting sample contains two populations of lamellae with a melting behavior very different from that of the samples prepared at lower temperatures.

Flash differential scanning calorimetry (FDSC) enables obtaining a more precise description of this double melting behavior of PEEK. The extremely fast achievable heating and cooling rates allow dismissing the hypothesis of reorganization during the heating cycle.

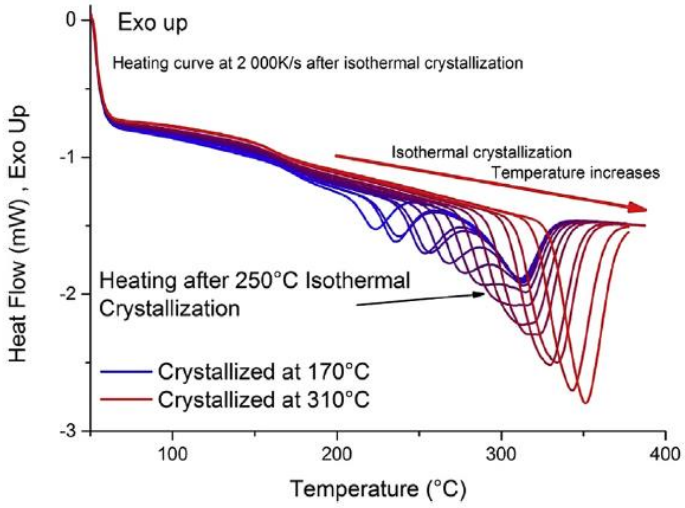


Figure 34. Heating curves of the PEEK at 2 000 K/s after complete isothermal crystallization at different temperatures in the range in between 170 °C and 310 °C [80]

Cette thèse est accessible à l'adresse : https://theses.insa-lyon.fr/publication/2023ISAL0006/these.pdf
© [H. Willeman], [2023], INSA Lyon, tous droits réservés

Tardif et al.[80] studied isothermal crystallization of PEEK from 170 to 310°C with this method (Figure 34). The melting behavior of the polymer changes for isothermal crystallization temperature around 250 C. Below this temperature, the melting peak is a double peak. The first part of the peak at lower temperature shifts upwards with crystallization temperature. The higher this temperature is, the higher will start the melting process. For crystallization above 250°C, the lower melting peak merges with the main melting peak around 330-350°C.

b. Multiple melting peaks

The evolution of the crystalline structure with crystallization temperature have been studied for different purposes. [75], [81]–[84] In the study of Hsiao et al, the final value of the long period was found to increase with crystallization temperature, e.g. the final value of L_p at 230°C was 14.7 nm, and at 310°C was 15.9 nm.

Figure 35 shows the results of the study of Krueger and Zachmann who investigated PEEK melting and crystallization processes using X-ray scattering techniques and DSC to follow the structural evolution of the polymer. [75]Multiple melting peaks are observed by DSC during heating of PEEK samples which were previously crystallized at different temperatures successively ($T_{c,1}$ = 302°C, $T_{c,2}$ = 272°C) by cooling from the melt. Structural changes can be highlighted by comparing the evolution of the degree of crystallinity with increasing temperature, measured by DSC or WAXS, with the change of long period L_p and scattering power Q derived from SAXS. They concluded that the multiple melting peaks arise from melting of crystals with different thicknesses which were formed during the different crystallization steps within already existing lamellae stacks.

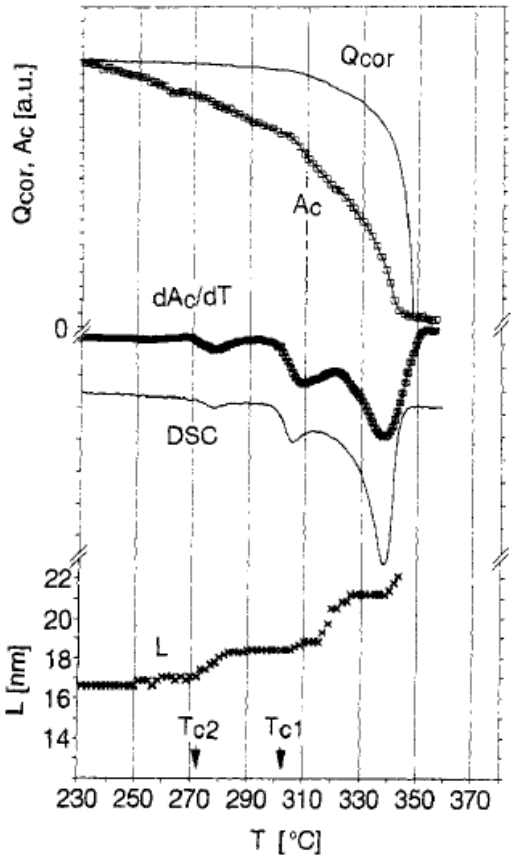


Figure 35. Corrected SAXS power (Qcor, integral intensity of the crystal reflections Ac, Ac differentiated with respect to T, and long period L as a function of temperature during heating (5 °C/min) of a PEEK sample. The DSC curve is also presented. The two temperatures of crystallization are indicated by the arrows. [75]

Cette thèse est accessible à l'adresse : https://theses.insa-lyon.fr/publication/2023ISAL0006/these.pdf
© [H. Willeman], [2023], INSA Lyon, tous droits réservés

c. Thermal treatments and memory effects

A so-called "crystalline memory effect" is often observed in polymers. Memory effects reflect the thermal history of the sample. A given temperature above the bulk melting point has to be reached in order to erase any influence of thermal history on the subsequent crystallization of a sample. This temperature is generally called the thermodynamic melting point. When studying crystallization, it is of great importance to know the temperature to melt the polymer in order to erase thermal history effects. Several thermodynamic melting point values for PEEK have been reported, ranging between T_m^∞ = 385°C and 395°C [85] [86] [10].

Thermal history effects include differences in crystallization kinetics as described by Lee and Porter.[87] Isothermal crystallization at 315°C was studied from different melt temperatures.

In Figure 36, as the temperature in the melt was increased, crystallization exotherms on cooling shifted to lower temperatures. As the holding time in the melt was increased, the isothermal crystallization curves shifted to longer time. These observations may indicate that small residual crystalline regions or nuclei may still exist after the melting step.

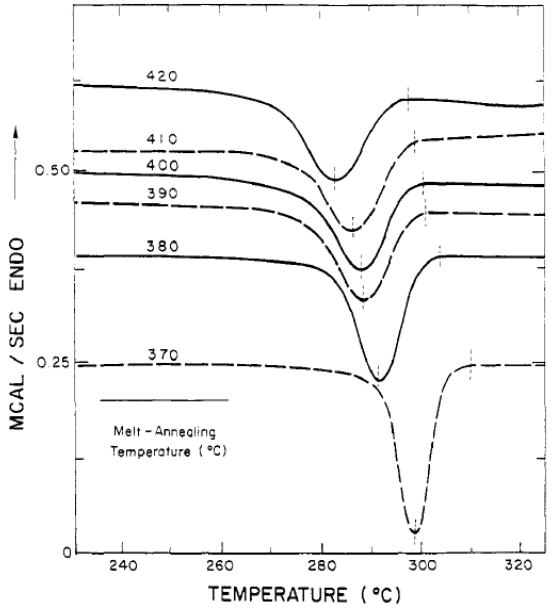


Figure 36. DSC cooling curves (-10 °C/min) for powder I after melting at various temperatures (370-420 °C) for 30 min. [87]

The influence of the crystallization temperature on melting has been studied by Choe and Lee in the case of non-isothermal crystallization [85]. The lower the crystallization temperature is, the lower the melting temperature of the crystals will be as shown on Figure 37. The intersection between melting and crystallization temperature lines indicates a value of $T_m^\infty = 385°C$.

Cette thèse est accessible à l'adresse : https://theses.insa-lyon.fr/publication/2023ISAL0006/these.pdf
© [H. Willeman], [2023], INSA Lyon, tous droits réservés

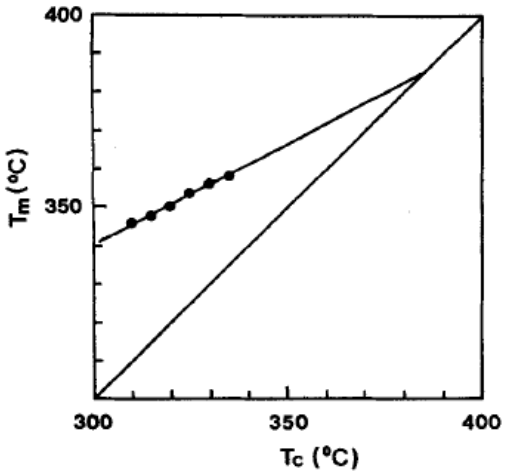


Figure 37. Observed melting point, T_m , as a function of crystallization temperature, T_c for PEEK [85]

d. Models of polymer crystallization

To describe the crystallization of polymer chains from the molten state, two mechanisms are involved in the phase transition from a metastable liquid into a crystal: nucleation and growth. Regarding kinetic aspects, two types of crystallization experiments are reported: isothermal and non-isothermal crystallizations (constant cooling rate). Isothermal crystallization is in principle easier to analyze quantitatively.

When a polymer in the molten state is cooled at a temperature T below its equilibrium melting temperature T_m^0, crystal nuclei may appear. Indeed, below T_m^0, the crystal phase is the stable phase. However, the appearance of a crystal within the molten phase creates an interface, which has an energy cost related to the interfacial tension between the amorphous and crystal phases. As a result of this energy balance, a crystal nucleus needs to reach a critical size r_{crit} to be stable and able to grow, otherwise it shall dissolve back in the melt.

The classical expression for the critical radius r_{crit} (assuming isotropic phases, thus a spherical nucleus) is: [88]

$$r_{crit} = \frac{2\,\gamma\,T_m^0}{\Delta H_m \Delta T} \tag{4}$$

where $\Delta H_m$is the heat of melting, T_m^0 the equilibrium melting temperature, γ the interfacial tension between the amorphous and crystal phases, $\Delta T = T_m^0 - T$ the undercooling.

Nucleation (i.e. the generation of a nucleus of the critical size r_{crit}) is associated with a nucleation barrier:

$$H = \frac{16\pi}{3}\frac{\gamma^3\,T_m^0}{{\Delta H_m}^2\,\Delta T^2} \tag{5}$$

And the nucleation rate (number of nuclei nucleated per second and per unit volume) is given by:

$$R = R_0\,exp\left(-\frac{H}{k_B T}\right) \tag{6}$$

Thus, the nucleation rate essentially depends on the undercooling ΔT. The larger the undercooling, the smaller the critical size and the faster the nucleation.

Cette thèse est accessible à l'adresse : https://theses.insa-lyon.fr/publication/2023ISAL0006/these.pdf
© [H. Willeman], [2023], INSA Lyon, tous droits réservés

This explains the very steep acceleration of the crystallization kinetics as the crystallization temperature is decreased.

Other environmental parameters can influence the nucleation process such as the presence of impurities and nucleating agents due to process and formulation of the polymer or the application of pressure in the case of strain-induced crystallization.

Indeed, two mechanisms of primary nucleation can be observed: if nuclei appear at the surface of external bodies in the liquid polymer such as impurities or cavities, we are talking about heterogeneous nucleation. If nuclei appear directly in the melted polymer, the nucleation process is called homogeneous. Secondary nucleation concerns nuclei that form from the contact with preexisting nuclei. When the rate of nucleation is constant, nucleation is qualified as sporadic.

On the other hand, when the crystallization temperature is decreased further and becomes close to the glass transition temperature, the mobility of the chains decreases drastically and the crystallization kinetics become increasingly slower. Hence the general slope of the curve crystallization time vs temperature is presented in Figure 38.

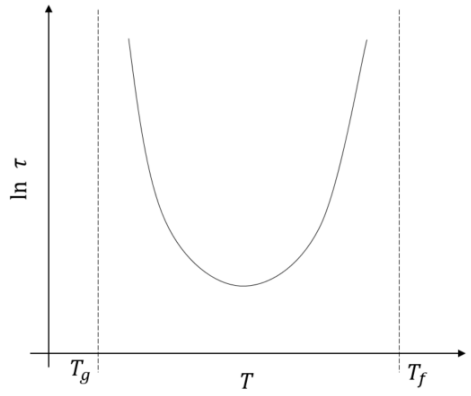


Figure 38. General shape of the curve of crystallization time of a polymer vs temperature. Such a diagram is often called a TTT (Time-Temperature-Transformation) diagram.

The development of spherulites and the kinetics related to crystallization can be described using crystallization kinetics theories. The most used model have been established by Evans and Avrami[89] for isothermal crystallization and by Ozawa[90] for non-isothermal crystallization .

Avrami's model is often used to describe isothermal crystallization. The fraction of the crystalline phase, α(t) as a function of time, t, can be described by the following equation :

$$\alpha\,(t) = 1 - exp(-Kt^n) \qquad (7)$$

This model is based on different assumptions: the nuclei have to appear randomly; the growth rate must be the same for all directions and the growth rate is supposed constant.

Table 3. Avrami exponent

	n	
Nucleation	Homogeneous	Heterogeneous
3D growth	4	$3 \leq n \leq 4$
2D growth	3	$2 \leq n \leq 3$
1D growth	2	$1 \leq n \leq 2$

Cette thèse est accessible à l'adresse : https://theses.insa-lyon.fr/publication/2023ISAL0006/these.pdf
© [H. Willeman], [2023], INSA Lyon, tous droits réservés

The Avrami model provides information about the crystallization mechanisms, the value of the coefficient n depends on the type of nucleation and the growth geometry, n being supposed an integer from 1 to 4. The link between the value of n and the crystallization mechanisms is given in Table 3.

Lamellar growth can be described using the Hoffman-Lauritzen theory in which crystal growth is assumed to occur by successive attachment of polymer stems to crystallites. [91] This theory is based on a lateral growth, surface-nucleation controlled process to describe the growth rates of polymer lamellar crystals. The Hoffman-Lauritzen theory predicts three growth regimes described in Figure 39:

- At low undercooling ΔT, regime I takes place when the growth from a single nucleus covers the entire growth plane L as shown in Figure 39.a.
- At intermediate ΔT, the lateral growth rate g is comparable to or smaller than the nucleation rate *i*. In this case, the second regime applies: further nuclei are deposited before the first layer is fully formed as shown in Figure 39.b.
- At high ΔT, the multiple nucleation of stems is so prolific that the spreading rate is irrelevant, *i* >> *g*, as sketched in Figure 39.c.

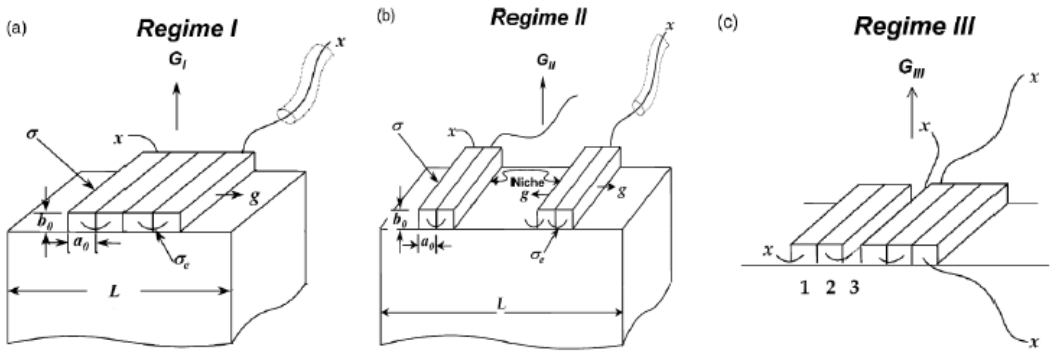


Figure 39. Schematic drawings of how polymer crystal growth takes place in different regimes: (a) regime I; (b) regime II; and (c) regime III [92]

e. Crystallization kinetics in PEEK

Isothermal crystallization has been investigated for PEEK by many authors [93] [94] [95] [96]. DSC studies allows following the kinetics of crystallization for a given isotherm temperature and determining the evolution of relative crystallinity with holding time (Figure 40).

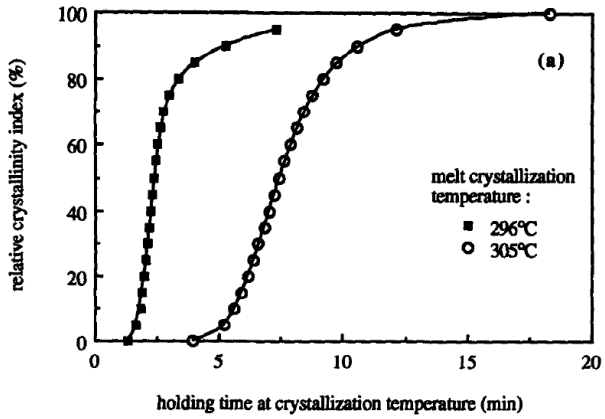


Figure 40. Changes in the relative crystallinity indices with the holding time at different crystallization temperatures [94]

Cette thèse est accessible à l'adresse : https://theses.insa-lyon.fr/publication/2023ISAL0006/these.pdf
© [H. Willeman], [2023], INSA Lyon, tous droits réservés

The half times of crystallization obtained via these experiments allow establishing a TTT diagram [25] [94] . Figure 41 shows a compilation of measurements of the crystallization half times of PEEK for different isothermal crystallization temperatures from different sources. [80] [97] [98]

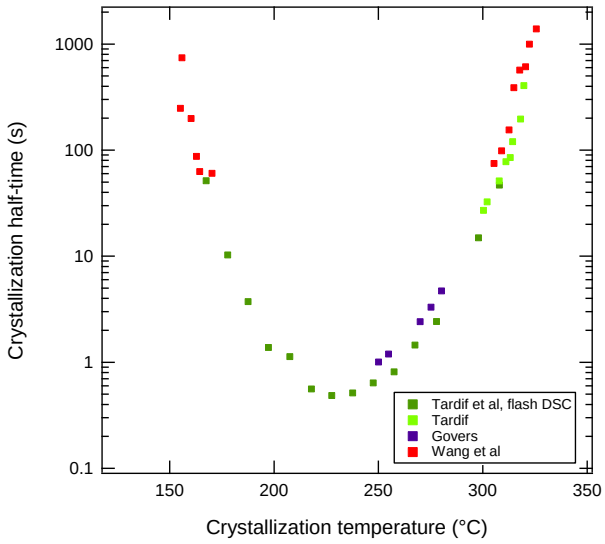


Figure 41. TTT diagram of PEEK compiling literature data [80] [97] [98]

Cold crystallization of PEEK can also be monitored in a more indirect way using DMA and dielectric spectroscopy. [47] The Avrami's approach is applied to the time evolution of the normalized moduli or dielectric constant. Similar Avrami's coefficients around 3 were obtained from dielectric and DSC analysis. Another result specific to PEEK is the presence of a secondary crystallization with different growth kinetics as presented in Figure 42. [96]

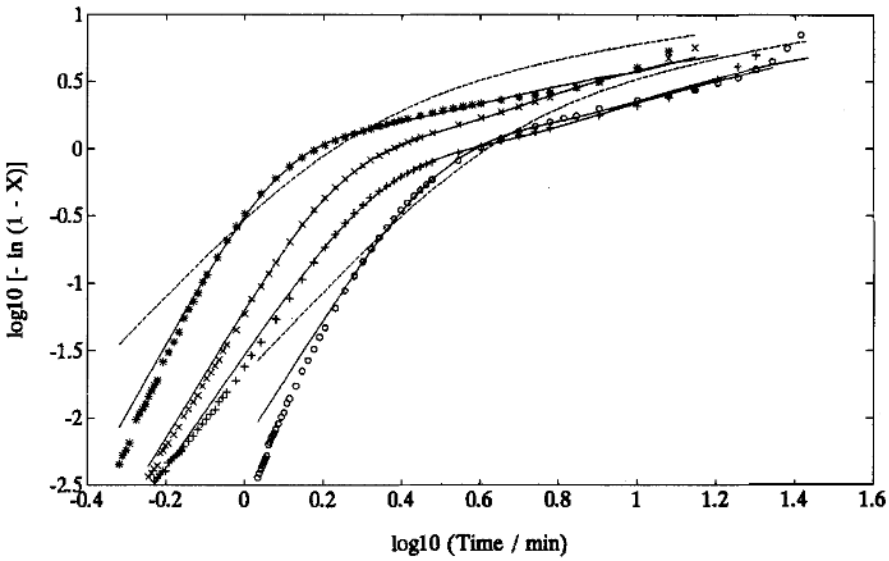


*Figure 42. Isothermal crystallization of PEEK (o 315°C, + 312°C, x 310°C, * 307°C) --- two-parameter, single Tobin's model; -- five-parameter, Tobin based, modified Hillier's model) [96]*

The spherulitic structure in PEEK can be observed with optical or electron microscopy. Few studies have shown the observation of spherulite growth using a heating stage and optical microscopy as shown in Figure 43 [24] [99]. At the early stage of crystallization (first image), nucleation can be observed and the growth rate of spherulite radii can be measured. In this case, growth is two-dimensional.

Cette thèse est accessible à l'adresse : https://theses.insa-lyon.fr/publication/2023ISAL0006/these.pdf
© [H. Willeman], [2023], INSA Lyon, tous droits réservés

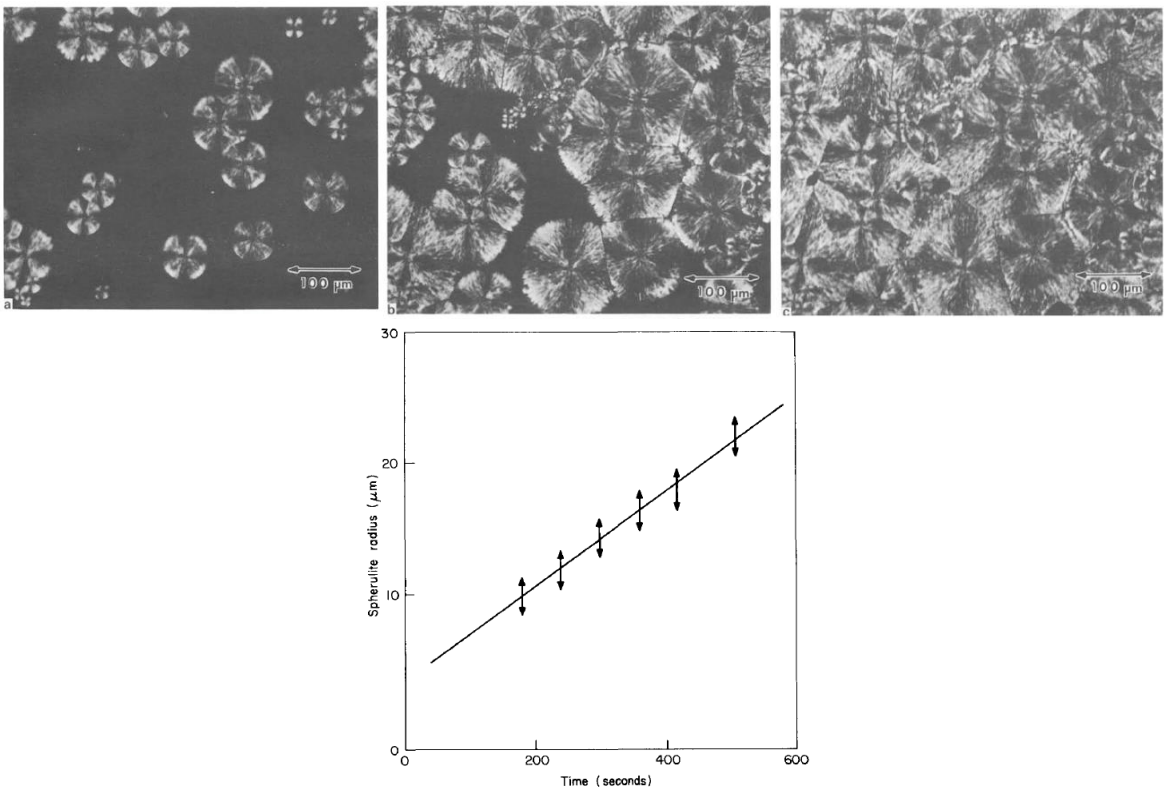


Figure 43. Nucleation and growth of PEEK spherulites, melt conditions--5 min at 420°C, crystallization temperature 320°C. Photographs taken at 320°C between cross polarizers after 8 min, 16 min and 24 min from left to right [24]

The influence of the molecular weight on crystallization and growth rate has been studied by Deslandes et al. [100] [101] By recording the growth rates in PEEK grades of different molecular weights, at several crystallization temperatures, the authors could relate the growth rate G to the molecular weight by an equation of the form:

$$log\, G(T_c) = log\, A(T_c) + B(T_c)\, log\, M_n \qquad (8)$$

Where A and B are functions of the crystallization temperature and G is the spherulite growth rate. These results for several crystallization temperatures are displayed in Figure 44. A significant decrease in spherulitic growth rate as the molecular weight increases is observed. This is related to the lower chain mobility as the molecular weight increases. Also, as expected, the growth rate increases as the crystallization temperature decreases.

Cette thèse est accessible à l'adresse : https://theses.insa-lyon.fr/publication/2023ISAL0006/these.pdf
© [H. Willeman], [2023], INSA Lyon, tous droits réservés

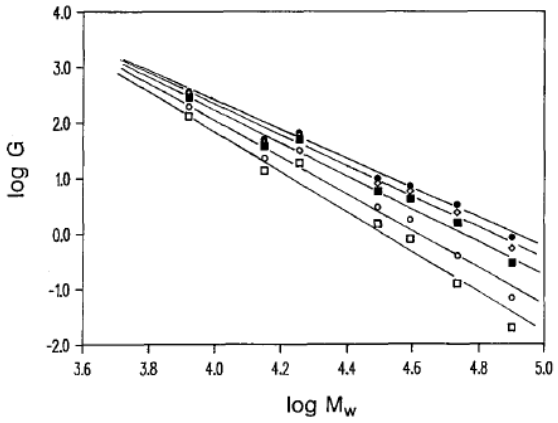


Figure 44. Log-log plot showing the change in crystal growth rate ($\mu m.s^{-1}$) as a function of molecular weight for different temperatures from bottom to top curves:295, 291, 287, 283 and 279°C [100]

f. Effect of stretching on crystallization

Flow induced crystallization in PEEK was investigated by Chien and Weiss but also recently by Seo et al. [102]–[104] Usually, when processing a polymer in the molten state under large amplitude flow, the nucleation rate can be accelerated. This leads to anisotropic morphologies of the polymer. The dynamic response to shear flow induced crystallization was followed by rheology and final structures were determined by SAXS and WAXS.

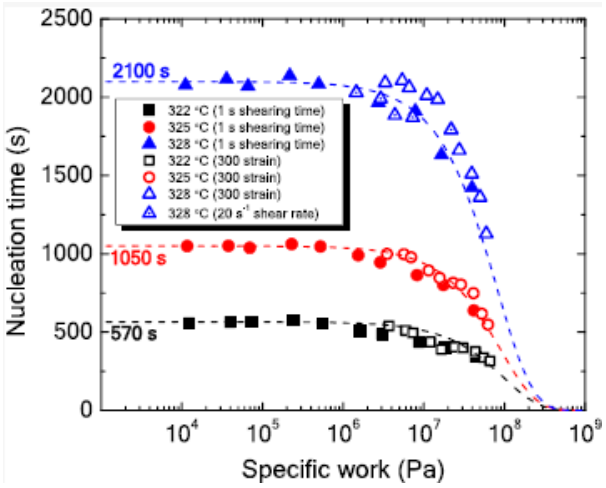


Figure 45. Nucleation time of PEEK 450G as a function of the specific work at three crystallization temperatures, Tc = 322 (black), 325 (red), and 328 °C (blue) [103]

As described in Figure 45, when using a constant shearing time, the nucleation rate increases with shear rate and when using a constant shear rate, the nucleation rate increases with shearing time.

SAXS patterns on Figure 46 illustrate qualitatively the influence of shear on the orientation of lamellar stacks. For short shearing time (1 or 10s), circular patterns indicate a random distribution of lamellae stacks orientations. For longer shearing times (60 or 230s) corresponding to large final strain, the intensity concentrates in the pole of the pattern which reflects the orientation of lamella along the shear direction.

Cette thèse est accessible à l'adresse : https://theses.insa-lyon.fr/publication/2023ISAL0006/these.pdf
© [H. Willeman], [2023], INSA Lyon, tous droits réservés

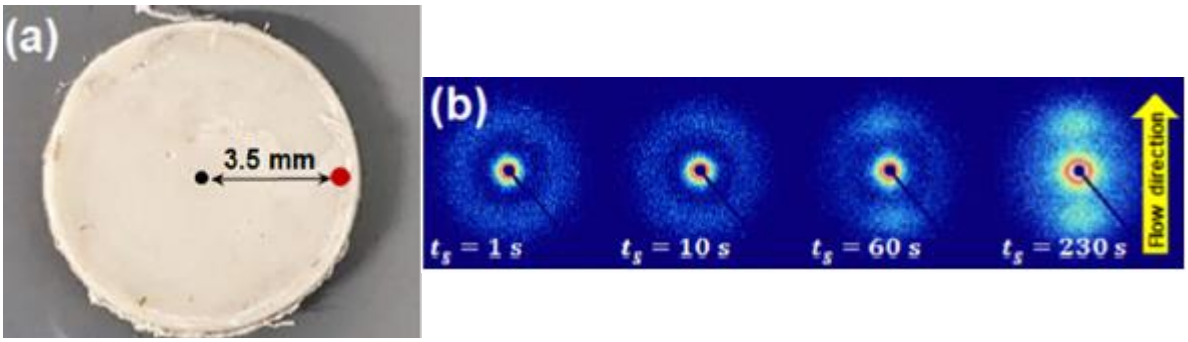


Figure 46. (a) Representative sheared PEEK 450G disk, (b) ex situ two-dimensional SAXS patterns from four sheared PEEK 450G disks. The sheared PEEK 450G disks are fabricated by crystallizing at Tc =328 °C for an hour after shearing at $\dot{\gamma}$= 20 s−1 at the perimeter of parallel plates for shearing times of ts = 1, 10, 60, and 230 s at Ts = 328 °C using 8 mm parallel plates. The SAXS patterns are obtained at 3.5 mm (red dot) on the right-hand side from the center (black dot). The corresponding shear rate at 3.5 mm is $\dot{\gamma}$ = 17.5 s−1. [104]

V. Objectives of the research

This current research work is financed by Solvay, an industrial group that focus on high performances polymers for high demanding applications such as aeronautics. PolyEtherEtherKetone (PEEK) is a polymer of great interest nowadays, especially for lightweight demanding applications. Fundamental knowledge on these polymers and especially their mechanical properties is essential. Proposed approach for this research on PEEK is an extension of a previous PhD thesis on deformation mechanisms in PA6,6. [46]

Firstly, characterizing the process of crystallization of PEEK polymer and its kinetics shall allow better control of the process-structure relationship as structure of semi-crystalline polymer is highly dependent of process conditions. General mechanical properties of PEEK will also be presented.

During this project, we shall then perform in situ, real-time SAXS and WAXS on a high-performance semi-crystalline polymer (PEEK) during tensile stretching up to failure in order to investigate the structural evolution and quantitatively describe microscopic deformation processes. Those are likely to crucially depend on the contrast in modulus between amorphous and crystalline domains. The strategy we have adopted to change this parameter is to perform tensile tests at two distinct temperatures, one above (170°C) and one below (23°C) the glass transition temperature. This can be determined by combined, simultaneous measurements of tensile deformations at different scales (crystal lattice planes and lamellar stacks) obtained from SAXS and WAXS. Ultimately our aim is to develop a fundamental multiscale, micromechanical model and to feed it with physically based processes and parameters, in order to predict long-term mechanical performances and lifetime of PEEK.

Cette thèse est accessible à l'adresse : https://theses.insa-lyon.fr/publication/2023ISAL0006/these.pdf
© [H. Willeman], [2023], INSA Lyon, tous droits réservés

Chapter II. Materials and methods

I. Introduction 47
II. Materials and processing 47
1. Materials 47
2. Degradability: TGA and IR study 47
3. Processing: compression molding 48
III. Mechanical properties 49
1. Tensile tests 49
2. Digital Image Correlation (DIC) 49
3. DMA 50
IV. Microstructural analysis 51
1. Cross-polarized optical microscopy 51
2. Differential Scanning Calorimetry (DSC) 51
V. X-ray Scattering 54
1. Small Angle X-ray Scattering (SAXS) 54
2. Wide Angle X-ray Scattering (WAXS) 60
3. Case of anisotropic system 63
4. In situ SAXS/WAXS tensile tests 64

Cette thèse est accessible à l'adresse : https://theses.insa-lyon.fr/publication/2023ISAL0006/these.pdf
© [H. Willeman], [2023], INSA Lyon, tous droits réservés

I. Introduction

The techniques used to investigate the properties of PEEK samples will be described in this chapter. Two grades of PEEK referred to as commercial names KT820 and KT880, corresponding to different molecular masses are presented. To obtain samples with isotropic morphology (or as isotropic as possible), the polymers were processed by compression molding. The techniques used to characterize the mechanical behavior of the polymer are then described. Then, the techniques used for the microstructural analysis are listed. Several techniques have been combined for determining the microstructural state of the material during tensile deformation.

II. Materials and processing

1. Materials

Two grades of PEEK pellets were provided by Solvay from the KetaSpire line in the form of pellets, KT820 and KT880 with respectively high and low molecular weight, thus respectively low and high melt flow indices. KetaSpire® PEEK is produced using nucleophilic displacement copolymerization of hydroquinone and 4,4'-difluorobenzophenone. These pellets are formulated polymers with 0.01% calcium stearate as a lubricant in injection process. [105], [106, p. 88] These commercial grades of PEEK have been extensively characterized by Garcia-Leiner[60] et al. The values of molecular weight for both grades are reported in Table 1 below:

Table 1. Molecular weight distribution of PEEK grades

	Mn ($g.mol^{-1}$)	Mw ($g.mol^{-1}$)
KT820	51900 ± 300	107300 ± 600
KT880	40000 ± 400	80000 ± 1700

Actually, the molecular weights are not largely different. Both are above the entanglement molecular weight.

2. Degradability: TGA and IR study

The thermal stability and degradation of both polymer grades have been studied by Thermogravimetric Analysis (TGA). TGA consists in monitoring the mass of a sample being exposed to a temperature ramp which can induce weight losses due to material degradation, chemical desorption or molecule vaporization. The sample is introduced in an aluminum cell placed on a nanobalance in an oven that imposes the temperature program. TGA measurements were performed on Netzsch TG 209 F1 Libra™. The temperature program used for the analysis of polymer degradation in the molten state consists in a heating step from 20 to 380°C at 10°C/minute followed by an isotherm of 30 minutes. A simple ramp from 20 to 600°C was also used to determine degradation temperatures.

The degradation of the polymer during the process was investigated via IR study of hot molded samples. Fourier-Transformed Infrared Spectroscopy (FTIR) is a characterization technique which allows identifying chemical functions present in the analyzed sample. The technique is based on the absorption of infrared radiations coupled to vibrations of the chemical bonds in the polymer structure. The wavelengths of the absorbed radiations depend on the type of chemical bonds, on the way they vibrate (rotational, stretching...), on the atoms involved, and on their chemical environment.

Cette thèse est accessible à l'adresse : https://theses.insa-lyon.fr/publication/2023ISAL0006/these.pdf
© [H. Willeman], [2023], INSA Lyon, tous droits réservés

3. Processing: compression molding

Injection is the most commonly used process to mold thermoplastic polymers. However, injection leads to oriented microstructures. The objective of the study being in situ SWAXS tensile tests to study the evolution of the PEEK microstructure (including local orientation processes), initial isotropic samples are needed. Compression molding is then a more appropriate process to obtain sample structures as isotropic as possible.

The polymer pellets provided by Solvay were used as received. They were hot-pressed, from room temperature to a chosen melting temperature between 380 and 420°C, which is high enough to erase the thermal history. They were then cooled down and crystallized in the form of about 450 × 500 × 2 mm^3 thick plaques. The pressure and temperature cycles used for compression molding of PEEK sheets is depicted in Figure 47. The polymer was melted above the melting temperature at 380, 400 and 420°C. These temperatures are close to or above the so-called equilibrium (extrapolated) melting temperature (see Figure 37) . The duration in the melt was set to 10min. The applied pressure was 15 bar and the heating and cooling rates were set to 20°C.min^{-1}.

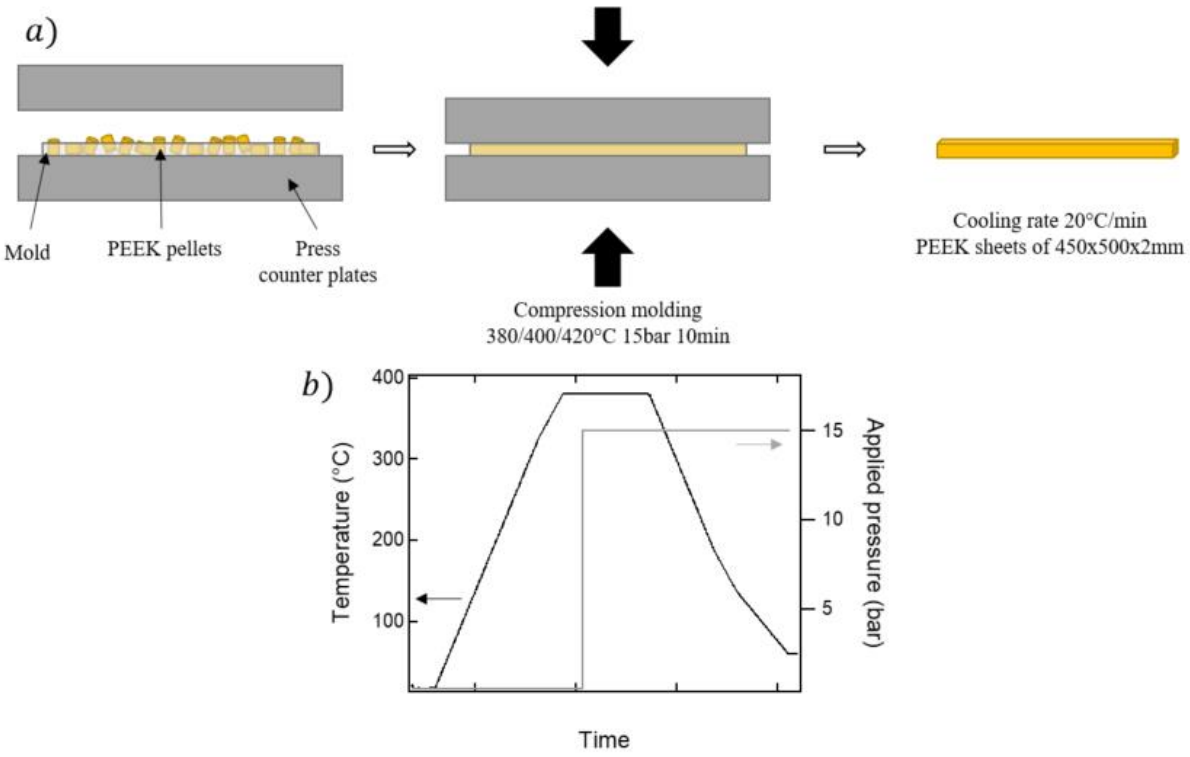


Figure 47. a) PEEK sheets compression molding process b) temperature and pressure cycle

The processing conditions lead to six different samples types: the two PEEK grades were processed using three different molten state temperature (380,400,420°C). H-shaped (ISO527) and bone-shaped (Figure 68) test samples were then machined in the plaques for the tensile test experiments.

Cette thèse est accessible à l'adresse : https://theses.insa-lyon.fr/publication/2023ISAL0006/these.pdf
© [H. Willeman], [2023], INSA Lyon, tous droits réservés

III. Mechanical properties

1. Tensile tests

To investigate the macroscopic mechanical properties of a polymer, the sample is uniaxially stretched to record its stress-strain behavior. In this study, two systems were used in order to access the global mechanical behavior of the samples.

Tensile tests were led on a Zwick/Roell Z020 universal testing machine equipped with a 50 kN load cell, a thermally controlled chamber and a non-contact extensometer. Alternatively, the tensile tests were led on a home-made tensile device in the context of in situ tensile test experiments at Synchrotron. The deformation of the sample was imposed by a constant crosshead displacement.

The nominal stress σ_n is defined by the ratio between the applied force and the initial cross-section of the sample S_0 :

$$\sigma_n = \frac{F}{S_0} \tag{9}$$

The nominal strain ε_n is expressed as equation (10) as a function of the initial length of the sample:

$$\varepsilon_n = \frac{\Delta L}{L_0} = \frac{L - L_0}{L_0} \tag{10}$$

To investigate the temperature dependence of the mechanical behavior, tests have been carried out at different temperatures below and above the glass transition temperature to vary the state of the amorphous phase (glassy or rubbery). Several strain rates were used during tensile tests: 10^{-4}, 10^{-3} and 10^{-2} s^{-1}.

2. Digital Image Correlation (DIC)

Digital Image Correlation (DIC) is an optical method which measures the deformation on an object surface by following a speckle created on the sample using spray-paint. The method tracks the changes in grey value pattern in small neighbourhoods called subsets (indicated in Figure 48 below) during deformation.

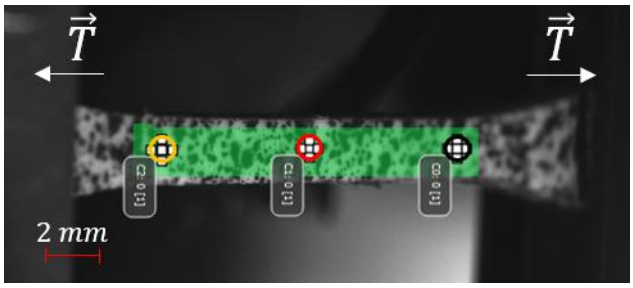


Figure 48. Image correlation of a speckled PEEK tensile samples using Vic-2D software

Image correlation and strain calculation were led on the Vic-2D software. The true strain field within subsets can be calculated. It is defined by the following equation:

$$\varepsilon = \int_{L_0}^{L} \frac{dL}{L} = ln\frac{L}{L_0} \tag{11}$$

In order to compare the values of deformation obtained by DIC to microscopic strains obtained by SAXS and WAXS, the nominal strain (equation (10)) was chosen as the output of the strain calculation.

Cette thèse est accessible à l'adresse : https://theses.insa-lyon.fr/publication/2023ISAL0006/these.pdf
© [H. Willeman], [2023], INSA Lyon, tous droits réservés

3. DMA

DMA (Dynamic Mechanical Analysis) allows characterizing the viscoelastic behavior of a material and the relaxation processes (molecular motions) which occur depending on temperature. The main relaxation process is associated to the glass transition. A small amplitude sinusoidal strain expressed by the equation below is applied to the specimen.

$$\varepsilon(t) = \varepsilon_0 \, sin(\omega t) \tag{12}$$

The temperature of the test or frequency of the applied strain can be varied. The measured stress can be decomposed in two parts, one in-phase with the strain and one in-phase with the strain rate, as described below:

$$\sigma(t) = \varepsilon_0 \, [E' \, sin(\omega t) + E'' \, cos(\omega t)] \tag{13}$$

The first part gives the storage modulus (E' for stretching, G' for shear), it corresponds to the part of the applied mechanical energy which is elastically returned by the material. The second part gives the loss modulus (E'' or G'') related to the viscous response of the material. (The viscosity is $\frac{G''}{\omega}$). The measured stress can be written equivalently as:

$$\sigma(t) = \varepsilon_0 \, |E^*| \, sin(\omega t + \delta) \tag{14}$$

Which gives $E' = |E^*| cos\delta$ and $E'' = |E^*| sin\delta$ and the complex modulus $|E^*| = \sqrt{E'^2 + E''^2}$. The phase shift δ between the applied strain and the measured stress is called the loss angle and corresponds to the loss factor $tan\delta = \frac{E''}{E'}$.

Typically, when a given relaxation occurs, at a given temperature, there is a small drop in E' for secondary relaxations, while for the main relaxation (often denoted α) a large drop of about 1 or 2 decades in E' is observed. Concomitantly, a peak is observed in E'' and $\tan\delta$.DMA analysis allows observing the relaxations occurring in the material at different frequencies and temperatures, it is then possible to obtain the activation energies of these relaxations by using Arrhenius or Vogel-Fulcher-Tammann models.

In this study, specimens of 2x10x35 mm^3 cut from PEEK hot-molded sheets were placed in a RSA G2 equipment using a three-point bending geometry, in which a sample is placed between two supports and the mechanical deformation is applied by a cantilever located at the middle of the sample. Figure 49 shows the storage and loss moduli as a function of temperature, measured at a frequency of 1 Hz.

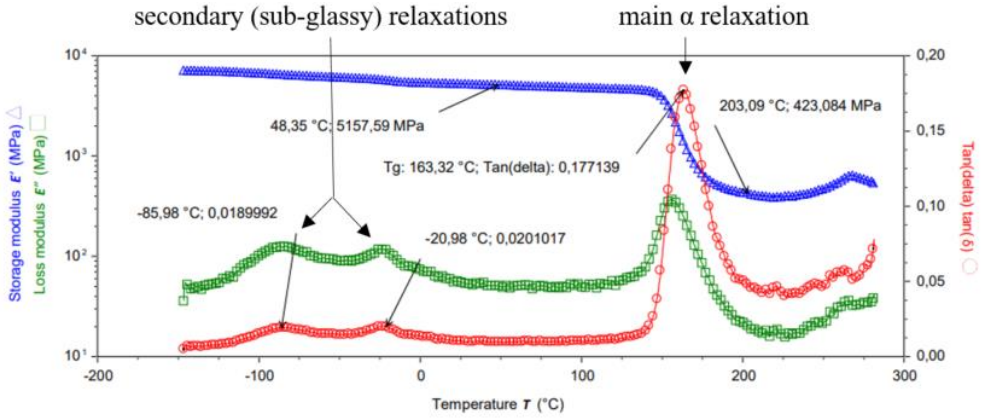


Figure 49. Storage and loss moduli of PEEK KT820 as a function of temperature measured by DMA (3-points bending geometry, frequency: 1Hz)

Cette thèse est accessible à l'adresse : https://theses.insa-lyon.fr/publication/2023ISAL0006/these.pdf
© [H. Willeman], [2023], INSA Lyon, tous droits réservés

IV. Microstructural analysis

The microstructural characterization of processed PEEK is of key importance in this work. Several scales of observation are concerned including spherulites, lamellae stacks, and crystal planes. In order to access these different levels of microstructure, several techniques are needed and will be described in this part. X-ray scattering will be described in a separate section.

1. Cross-polarized optical microscopy

The aim of optical microscopy is to characterize the global crystalline microstructure at scales from a few micrometers to millimeters. In a semi crystalline polymer, spherulites are the characteristic entities observable with this technique. It is based on the interaction of anisotropic microscopic objects (crystalline lamellae) with the polarized light. As a result of local anisotropy, spherulites are birefringent objects while the amorphous polymer is isotropic. With cross-polarizers, the amorphous polymer appears dark while spherulites are visible. The crystalline morphology can then be analyzed in terms of the distribution and sizes of spherulites in the polymer.

a. Morphology study

Cross-polarized optical microscopy was performed on compression molded samples. Sections 1 µm thick were cut out at room temperature by using a Leica microtome equipped with a diamond knife. The sections were placed on a glass slide, sealed in paraffin and analyzed in transmission mode. The size and number of spherulites were measured depending on the process conditions.

b. Crystallization kinetics

The crystallization kinetics of PEEK were investigated using a hot stage Linkam LTS420 combined with cross polarized optical microscopy. This in situ technique allows observing in real time the crystallization of thin films of polymers from the melt, including the nucleation type and growth rate of spherulites.

2. Differential Scanning Calorimetry (DSC)

DSC (Differential Scanning Calorimetry) is based on the measurement of the enthalpy variation. It consists in applying a temperature ramp on two pans, one with the sample and one empty as reference, and recording the energy that have to be provided to keep both pans at the same temperature. This technique is commonly used to determine the characteristic temperatures of the polymer (glass transition, melting and crystallization temperatures) but also the crystallinity index and crystallization kinetics. The thermal history of the sample can also be investigated in order to identify the temperature that allows the material to erase the memory of all previous treatments.

A TA Instruments Q2000 calorimeter in the standard mode and the Universal Analysis software were used to acquire and process thermograms. For each experiment, non-hermetic aluminum pans were filled with 5-10 mg of polymer sample. Thermal measurements were performed at a heating/cooling rate of 10°C/min. A Rapid Cooling System (RCS) with a nitrogen gas flow of 50 mL/min was used. Samples were heated from 35 to 380°C, then cooled down to 35°C and finally heated again to 380°C. The glass transition, melting and crystallization temperatures were measured from the second heating cycle as the first cycle is used to erase the thermal history. However, it is important to realize that the initial crystallinity index of a sample is not measured in this way.

Crystallization and melting are first order transitions, characterized by absorption or release of latent heat. An example of a PEEK thermogram is represented in Figure 50.

Cette thèse est accessible à l'adresse : https://theses.insa-lyon.fr/publication/2023ISAL0006/these.pdf
© [H. Willeman], [2023], INSA Lyon, tous droits réservés

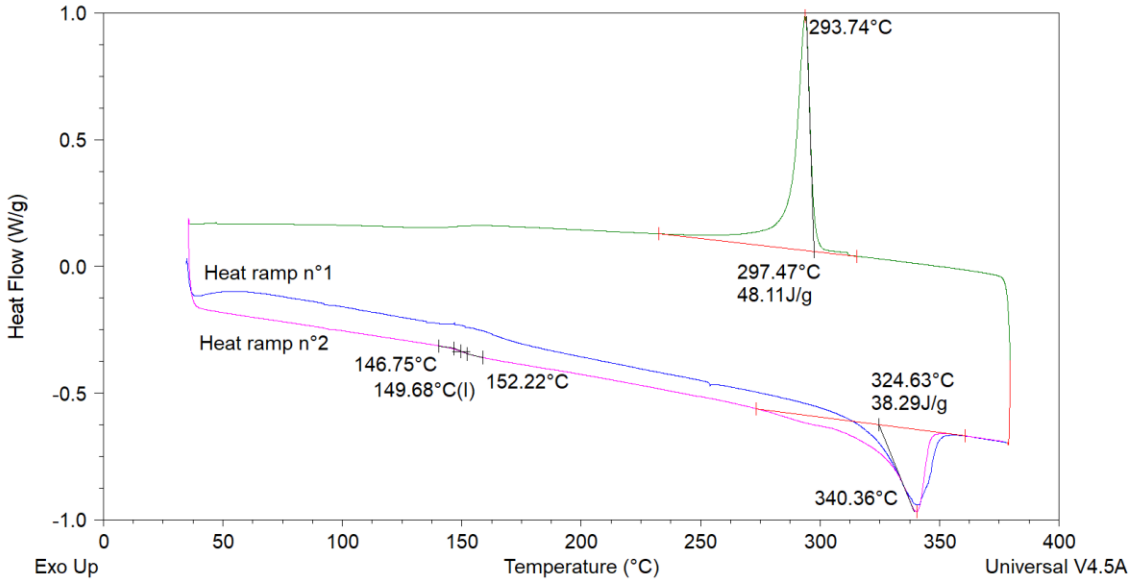


Figure 50. DSC thermogram of a PEEK KT820 pellet and integrated glass transition, melting and crystallization peaks

From these experiments, the crystallinity of a polymer can be calculated by integrating the endothermic melting peak that leads to the following relation (15). χ_c is defined here as a mass fraction.

$$\chi_c = \frac{\Delta Hf}{\Delta Hf_\infty} \tag{15}$$

where ΔHf is the integrated melting enthalpy of the material and $\Delta Hf_\infty$is the specific melting enthalpy of an infinite perfect crystal. According to the study of Blundell and Osborn[10], ΔHf_∞(PEEK) is about 130 J.g^{-1}. In order to ensure coherent measurements and comparisons, the integration limits of the melting endotherm were set between 270 and 360°C.

For polymers with a melting temperature more than 100°C higher than the crystallization temperature, in order to give more precision to the calculated crystallinity of the material, the temperature dependence of the heat capacity has to be considered. In 1993, Séguéla[107] gave expressions of heat capacities and melting enthalpy of PEEK based on Wunderlich and Cheng's work.[108]

$$C_{p,l} = 1.0700 + 0.001722T\ (J.g^{-1}.K^{-1}) \tag{16}$$

$$C_{p,s} = 0.0891 + 0.003412T\ (J.g^{-1}.K^{-1}) \tag{17}$$

Where $C_{p,l}$ is the heat capacity in the liquid (amorphous) phase and $C_{p,s}$ that in the solid (semi-crystalline) phase. The temperature dependence of the melting enthalpy follows the relation (18):

$$\Delta H_f(PEEK) = -118.90 + 0.9809T - 0.000845T^2\ (J.g^{-1}) \tag{18}$$

a. Lamella thickness

The thickness of crystalline lamellae, l_c, can be accessed with the measurement of the melting temperature, according to the Gibbs-Thomson relation:

$$T_m = T_{m,0}\left(1 - \frac{2\gamma_e}{\Delta Hf_\infty \rho_c\, l_c}\right) \tag{19}$$

Cette thèse est accessible à l'adresse : https://theses.insa-lyon.fr/publication/2023ISAL0006/these.pdf
© [H. Willeman], [2023], INSA Lyon, tous droits réservés

Where T_m is the melting temperature, $T_{m,0}$ the equilibrium melting temperature, it would be the melting temperature of a lamella with infinite thickness ($T_{m,0}$=395°C [10]), $\Delta H_{f,\infty}$ the corresponding enthalpy, ρ_c the density of PEEK crystal (1.4 g.cm^{-3} [10]),γ_e the surface energy of the crystalline lamellae in contact with the amorphous phase and l_c the thickness of crystalline lamellae.

b. Crystallization kinetics

The crystallization kinetics of PEEK has been studied using temperature cycles as displayed on the red curve in Figure 51. The blue curve is the corresponding heat flow. The evolution of the relative crystallinity with time is measured during the isothermal crystallization step. The isothermal crystallization temperature was varied from 308 to 322°C for the KT820 grade and from 310 to 325°C for KT880.

During the various steps of the temperature cycle, the glass transition, melting and crystallization of PEEK crystals can be monitored. For every ramp, the glass transition is measured at 150°C (points A in Figure 51). The first heating ramp allows characterizing the pellets as received. The polymer is then melted at 380°C to erase the thermal history before fast cooling at 20°C.min^{-1} down to the chosen isothermal temperature. The sample is then maintained at isotherm temperature until crystallization is complete before being cooled down to room temperature at 10°C.min^{-1}. The second heating ramp enables characterizing the isothermally crystallized (IC) sample. The shapes of the melting peaks of initial pellets (point B) and IC sample (point C) are different as the melting peak of IC is double, with a melting peak at a temperature slightly above the crystallization temperature, distinct from the main melting peak.

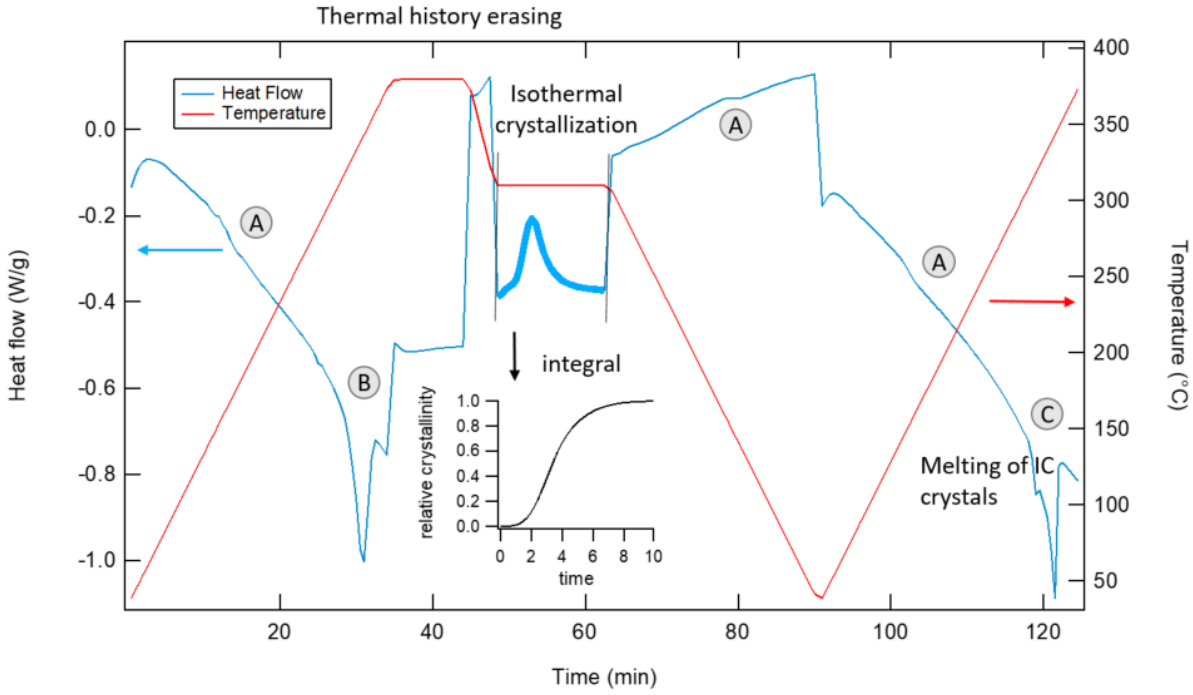


Figure 51. Temperature cycle used to study isothermal crystallization at T_{iso} = 310°C and corresponding heat flow obtained by DSC. A: glass transition, B: melting of initial pellet and C: melting of the isothermally crystallized sample.

c. Physical ageing

Physical ageing of PEEK samples was carried out with the temperature cycle depicted in Figure 52. Both pellets and compression-molded tensile specimens were aged. In an oven at ambient atmosphere

Cette thèse est accessible à l'adresse : https://theses.insa-lyon.fr/publication/2023ISAL0006/these.pdf
© [H. Willeman], [2023], INSA Lyon, tous droits réservés

and at a temperature of 135°C (T_g – 15°C), the samples were annealed from 1 to 1000h before characterization by DSC. The first heating ramp enables characterizing the aged sample. The polymer is then melted to erase the thermal history associated with process and ageing steps, then recrystallized in standard conditions (same cooling rate as before). The second heating ramp enables characterizing the unaged (rejuvenated) sample for comparison and quantification of the ageing.

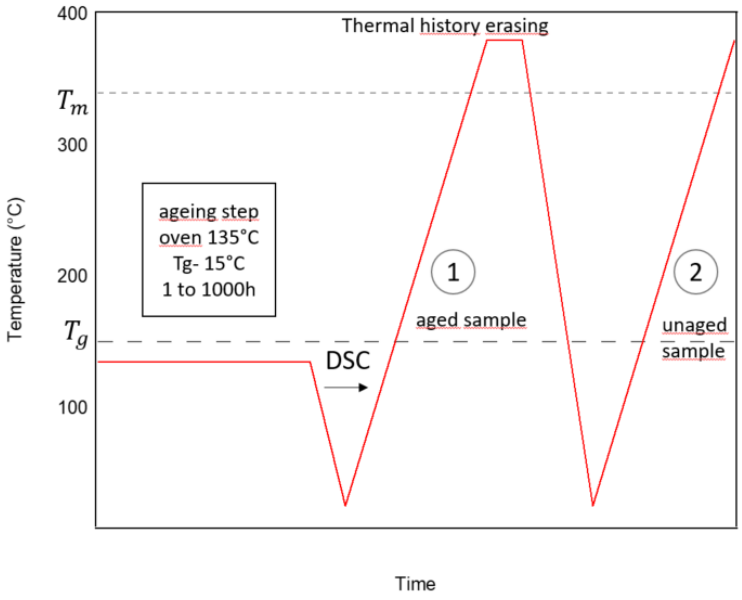


Figure 52. Temperature cycle used to study ageing

V. X-ray Scattering

1. Small Angle X-ray Scattering (SAXS)

Small Angle X-ray Scattering (SAXS) is used to characterize the crystalline morphology at the scale of crystalline lamellar stackings in semi-crystalline polymers. The periodicity (so-called long period) of crystalline lamella stackings can be measured, as well as the possible anisotropy (orientation) of the morphology. With some hypotheses, the thickness of crystalline lamellae may be estimated. (see below) The scattered intensity is collected on a 2D detector. The scattering vector $\vec{q}$ is defined by $\vec{q} = \vec{k} - \overrightarrow{k_0}$ (Figure 53) where $\overrightarrow{k_0}$ and $\vec{k}$ are the wave vectors of the incident and scattered beams respectively. The norm of the vector $\vec{q}$, q can be expressed as a function of the scattering angle 2θ.

$$q = \frac{4\pi sin\theta}{\lambda} \qquad (20)$$

In the small angle limit, $\vec{q}$ is within the plane of the detector. The accessible range of scattering vectors q (or equivalently of scattering angles 2θ) is determined by the distance D between the sample and the detector. $q_{max}$is given by $\tan 2\theta_{max} \approx d/D$ (d: radius of the detector) while q_{min} is given by the radius of the beam stop, $q_{min} \approx \frac{d\ beamstop}{D}$.

The values of q_{max} and q_{min} are given in the section 4. of this chapter depending on the SAXS set-up.

The resolution of SAXS acquisition is $\Delta q = 0{,}0038\ Å^{-1}$ so $\frac{\Delta q}{q} = 0.1\%$.

Cette thèse est accessible à l'adresse : https://theses.insa-lyon.fr/publication/2023ISAL0006/these.pdf
© [H. Willeman], [2023], INSA Lyon, tous droits réservés

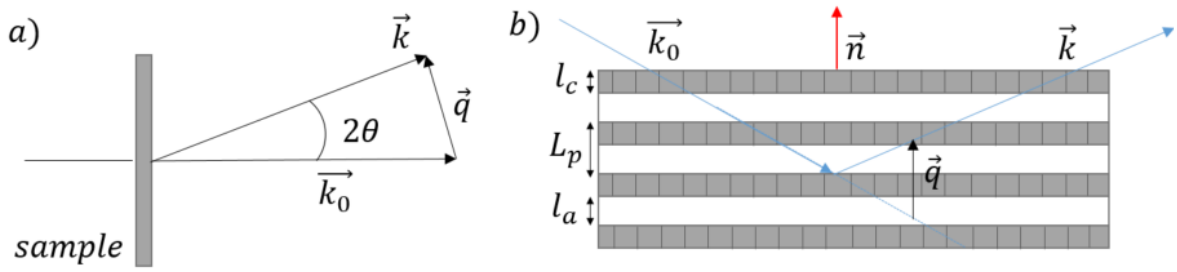


Figure 53. SAXS conditions applied to a) the whole sample and b) at the scale of lamellae stacks

We consider the transmission geometry, as schematized in Figure 54.The intensity (i.e. the number of photons) collected per second within the solid angle $d\Omega$ is noted:

$$dI = VTi_0 \left(\frac{d\sigma}{d\Omega}\right) d\Omega \qquad (21)$$

Where T is the transmission of the sample, i_o is the flux of the incident beam (in W/m^2 or number of photons/s/m^2). Ti_0 is the average flux within the sample. V is the scattering volume V=eS, with e the thickness and S the section of the incident beam. $I_0 = Si_0$ is the total intensity of the incident beam. Equation (21) can be rewritten:

$$\frac{dI(q)}{I_0 Te} = \left(\frac{d\sigma}{d\Omega}\right) d\Omega \qquad (22)$$

$\frac{d\sigma}{d\Omega}$ is the differential cross section per unit volume. It has the dimension of length^{-1} (usually expressed in cm^{-1} or mm^{-1})

The transmission T of the sample is expressed as:

$$T = exp(-\mu e) \qquad (23)$$

Where μ is the linear absorption coefficient, usually expressed in cm^{-1}.

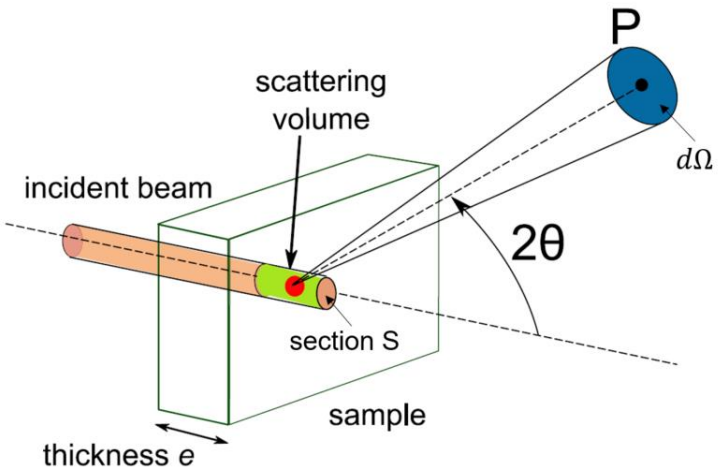


Figure 54. Schematic of collected intensity for a considered volume of the sample

Cette thèse est accessible à l'adresse : https://theses.insa-lyon.fr/publication/2023ISAL0006/these.pdf
© [H. Willeman], [2023], INSA Lyon, tous droits réservés

Estimation of crystalline lamellar thickness

In general, the lateral dimensions of lamellar stacks may be supposed to be large with respect to the long period L_p. In this case, lamellae stacks scatter along the normal $\vec{n}$ to the lamellae. Regular stacking gives rise to an interference with maximum $q = \frac{2\pi}{L_p}$ where $L_p$is the stacking long period.

The crystalline lamellar thickness L_c can be estimated with the following relation, considering that the material is fully composed of lamellar stacks:

$$L_c = L_p \cdot \frac{\rho}{\rho_c} \cdot \chi_c \quad (24)$$

With L_p, the long period as determined previously with SAXS; ρ, the density of the material ρ_c = 1.4 g.cm^{-3}, the density of the crystalline phase χ_c, the crystallinity index determined by DSC

The density of the material can be calculated as follows:

$$\frac{1}{\rho} = \frac{\chi_c}{\rho_c} + \frac{1-\chi_c}{\rho_a} \quad (25)$$

With ρ_a=1.26 g.cm^{-3}, the density of the amorphous phase of PEEK

Analysis of SAXS patterns

Under tensile strain, the samples become anisotropic. The scattered intensity i(q) is modulated as a function of the azimuthal angle ψ. It follows that the 2D SAXS pattern is modulated as a function of the azimuthal angle ψ. The intensity i(q) must thus be measured for each angle ψ in order to enable an analysis of the azimuthal distribution. In this case, the 2D pattern files were divided into 72 sectors of 5° ([0,5°], [5,10°],…,[355,360°]) and the intensity was averaged in each sector. In order to preserve the symmetry of the sectors around the tensile (HORI, 0°) and perpendicular (VERTI, 90°) directions, the sectors were regrouped two by two, leading to 36 sectors of 10° centered on 0,10,…350° ([355,5°], [5,15°] etc…). Considering the central symmetry of the pattern, all possible orientations can then be covered with only 18 azimuthal sectors of 10° centered on 0, 10,… 90,… 170° as represented on Figure 55.

Cette thèse est accessible à l'adresse : https://theses.insa-lyon.fr/publication/2023ISAL0006/these.pdf
© [H. Willeman], [2023], INSA Lyon, tous droits réservés

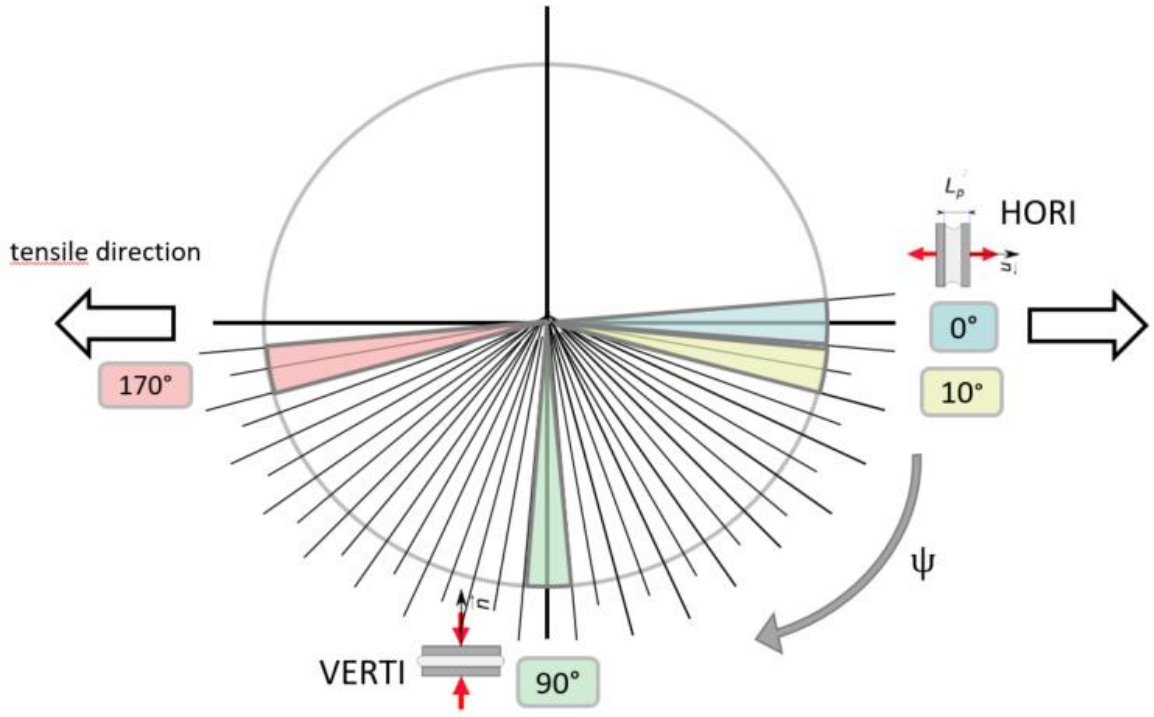


Figure 55. 2D SAXS pattern azimuthal distribution analysis. Ψ is the azimuthal angle with respect to tensile direction. The horizontal (HORI) direction corresponds to the tensile direction

Correction of SAXS spectra

In the case of an isotropic material, scattering objects (for example, stacks of amorphous/crystalline lamellae) are oriented randomly, isotropically in all directions. Then, in the reciprocal space, the intensity is distributed uniformly on a sphere of radius q. The surface of this sphere is $4\pi q^2$and the measured intensity must then be multiplied by $4\pi q^2$. It depends only on the norm q of the vector $\vec{q}$ and not on the orientation of $\vec{q}$. This q^2 multiplication is sometimes improperly denoted Lorentz correction. Both raw and corrected spectra are presented in Figure 56.

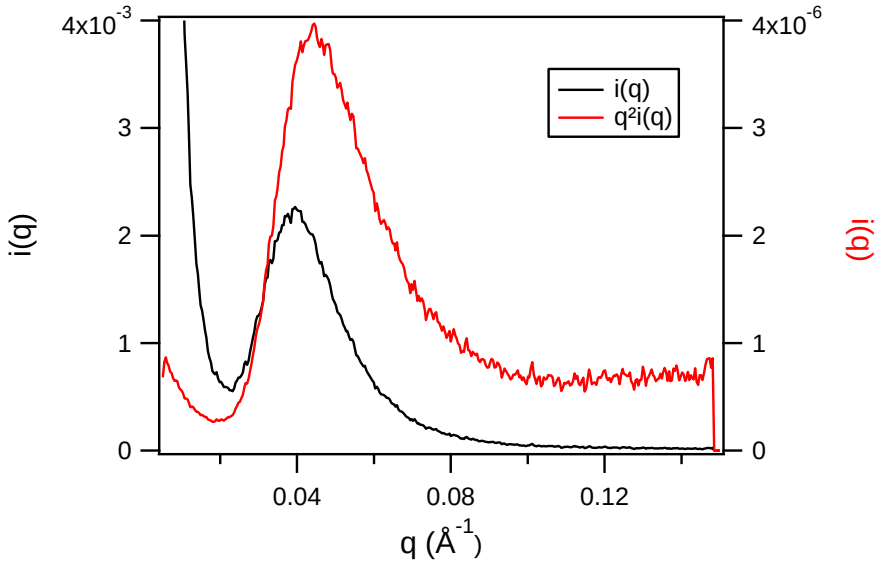


Figure 56. Raw and corrected intensities as a function of the scattering vector q in the HORI direction of the SAXS pattern

Cette thèse est accessible à l'adresse : https://theses.insa-lyon.fr/publication/2023ISAL0006/these.pdf
© [H. Willeman], [2023], INSA Lyon, tous droits réservés

Determination of local strain: evolution of long period L_p

Considering an isotropic material, the random distribution of the stacks in the material results in a uniform ring in the SAXS pattern, as depicted in Figure 57 .

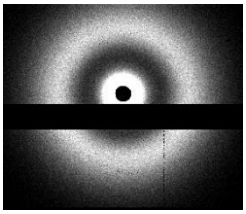


Figure 57. SAXS pattern of isotropic PEEK specimen

In order to extract quantitative information on the variation of the long period as a function of the macroscopic strain and of the azimuthal angle, as well as on the variation of the intensity as a function of the azimuthal angle for a given strain value, we need to fit the SAXS correlation peak. Thus, the Lorentz-corrected intensity is plotted as a function of the scattering vector q, as shown in Figure 58 (corrected data) and the peak is fitted with an empirical function of the form:

$$f(q) = y_0 + A\, exp\left(-\left(\frac{q}{q_1}\right)^{a_1} - \left(\frac{q}{q_2}\right)^{a_2}\right) \tag{26}$$

The exponent parameters a_1 and a_2 account for the possible asymmetry of the peak. The parameter y_0 was set to zero. The maximum of the peak is then obtained for the value q_{peak} of the scattering vector, given by (note that a_1 and a_2 are of opposite signs):

$$q_{peak} = \left[\left(-\frac{a_1}{a_2}\right)\left(\frac{{x_1}^{a_1}}{{x_2}^{a_2}}\right)\right]^{\frac{1}{a_1 - a_2}} \tag{27}$$

And the amplitude at the maximum of the peak is given by:

$$I_{max} = A\, exp\left(-\left(\frac{q_{peak}}{x_1}\right)^{a_1} - \left(\frac{q_{peak}}{x_2}\right)^{a_2}\right) \tag{28}$$

Note that the function f(q) (equation (26)) is heuristic. It is not related to a model for the scattering and fit parameters q_1, q_2, a_1, a_2 do not have specific physical meaning.

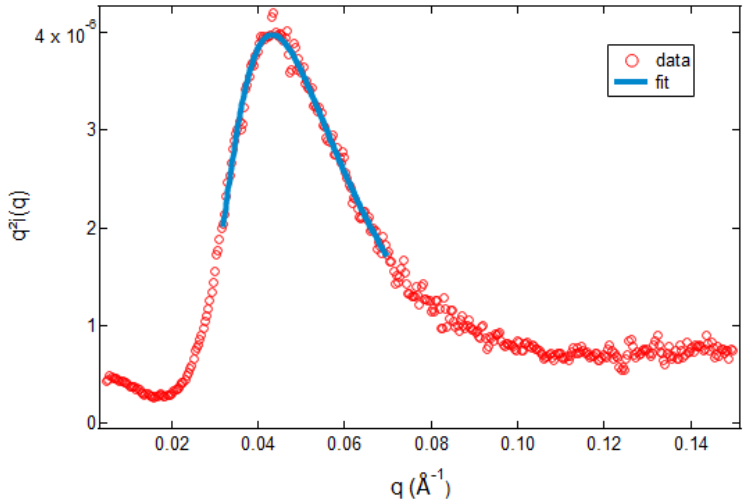


Figure 58. Fit of experimental data using function (9)

Cette thèse est accessible à l'adresse : https://theses.insa-lyon.fr/publication/2023ISAL0006/these.pdf
© [H. Willeman], [2023], INSA Lyon, tous droits réservés

The local tensile strain ε_{micro} at the scale of lamellae stacks is measured via the strain induced shift of the correlation peak. The resolution of SAXS acquisition is $\Delta q = 0{,}0038\ \text{Å}^{-1}$ so $\frac{\Delta q}{q} = 0.1\%$.

$$\varepsilon_{micro} = \frac{\Delta q_{peak}}{q_{peak,0}} = \frac{\Delta L_p}{L_{p,0}} \tag{29}$$

Thus, the resolution on the measure of strain at the scale of lamellae stacks is of the order of $\frac{\Delta L_p}{L_p} = 0.1\%$.

In Figure 59 is represented the shift of the maximum of the correlation peak towards lower q values along stretching in the HORI direction. This is coherent as scattering in the HORI direction arises from lamellae stacks in tension. Their long period is increasing thus the value of the scattering vector q_{peak} decreases. The evolution of the amplitude of the peak with deformation will be discussed in the following chapters.

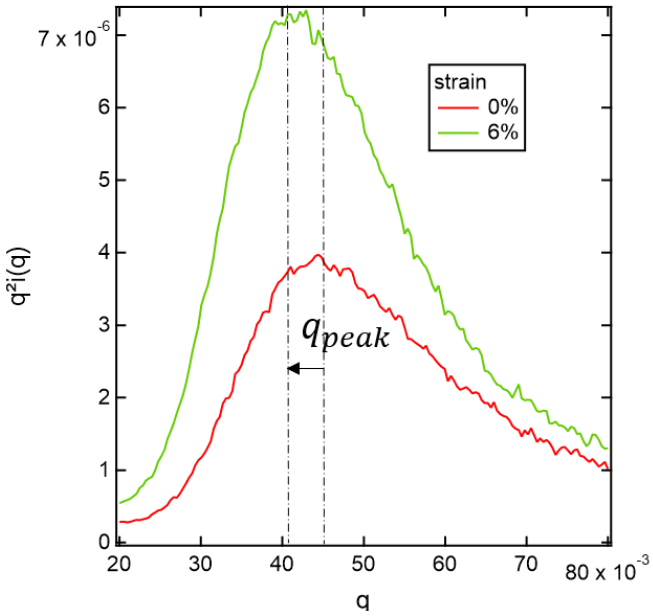


Figure 59. SAXS intensity as a function of the scattering vector q in the HORI direction for the initial sample and at a macroscopic strain ε=6% illustrating the strain induced shift of the correlation peak

Using this analysis, the local strain can be monitored with the evolution of the long period as a function of macroscopic strain and azimuthal angle as depicted in Figure 60. The local strain at ψ = 0° (HORI direction) increases with deformation as lamellae stacks undergo tensile stress whereas the local strain for ψ = 90° decreases towards negative values as lamellae stacks undergo compressive strain due to Poisson effect.

Cette thèse est accessible à l'adresse : https://theses.insa-lyon.fr/publication/2023ISAL0006/these.pdf
© [H. Willeman], [2023], INSA Lyon, tous droits réservés

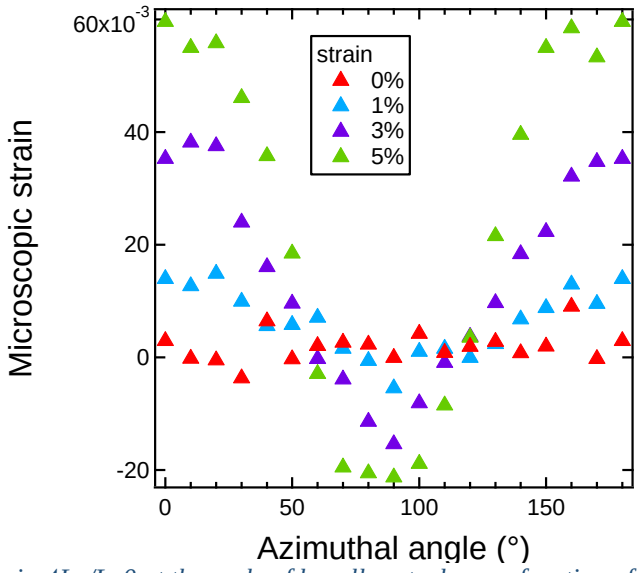


Figure 60. Local strain ΔLp/Lp0 at the scale of lamellae stacks as a function of the azimuthal angle ψ for ε=0,1,3 and 5%

Central scattering

The scattered intensity contains two distinct contributions as the raw data curve shows in Figure 61. First, there is the correlation peak at about 0.04 A^{-1} originating from the periodicity of the lamellae stacks. In addition, a quite large central scattering at low q values is present. Central scattering is associated to large scale heterogeneities in the material. The typical size of the heterogeneities is of the order of $2\pi/q$ where q is the scattering vector. In Figure 61, central scattering arises for q between 5.10^{-3} and 2.10^{-2} $Å^{-1}$ which correspond to entities of about 30 to 120 nm (the upper detected size being limited by q_{min}. These heterogeneities may have various origins: a contrast between semi crystalline zones and an amorphous "matrix" or a contrast between the material and cavities generated during the process or the stretching.

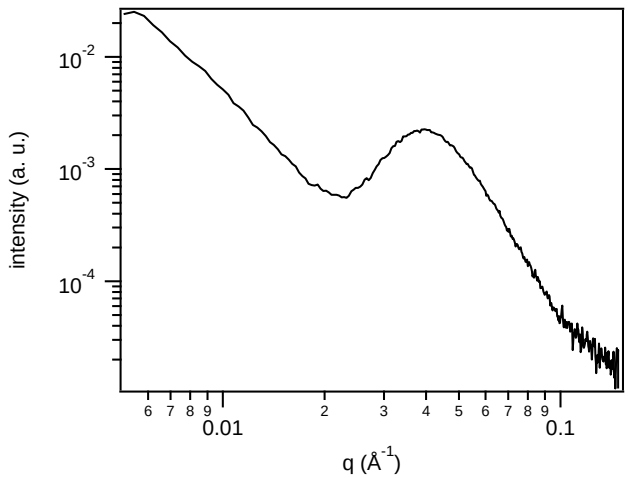


Figure 61. Raw intensity of the initial sample SAXS pattern in the HORI direction as a function of the scattering vector q in log-log scale.

2. Wide Angle X-ray Scattering (WAXS)

Wide Angle X-ray Scattering (WAXS) gives information at the scale of the crystalline unit cell. It allows identifying structural and crystalline phases, measuring crystalline parameters, crystalline index, and in some cases the crystallite size. When a material is stretched, information on the distribution of orientation of crystal lattice planes may be obtained.

Cette thèse est accessible à l'adresse : https://theses.insa-lyon.fr/publication/2023ISAL0006/these.pdf
© [H. Willeman], [2023], INSA Lyon, tous droits réservés

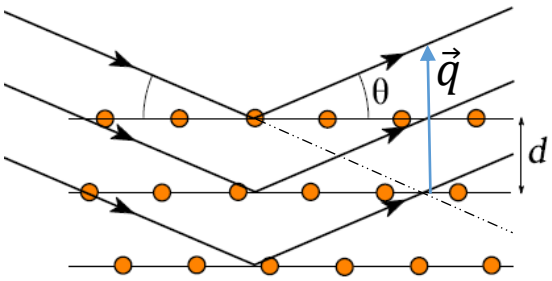


Figure 62. Schematic representation of X-ray diffraction from crystal planes

The diffraction spectrum is analyzed according to the Bragg's law, which makes it possible to obtain the spectra of the crystal lattice:

$$2d\ sin\theta = n\lambda \tag{30}$$

Where n is an integer, λ is the wavelength of incident wave (X-ray radiation), d is the spacing between the planes containing the atoms and θ the angle between the incident beam and the scattering planes (reflexion angle). This is the Bragg's law, which is the basic relation in X-ray scattering. The angle between the incident beam and the diffracted beam is 2θ. Thus, for a given family of periodic crystal planes, only the directions defined by the angle θ given by Bragg's law give scattering. This ensemble of directions is called the reciprocal space of the given family of planes.

The scattering vector $\vec{q}$ is defined as $\vec{q} = \vec{k} - \overrightarrow{k_0}$, where $\vec{k}$ and $\overrightarrow{k_0}$ are the wave vectors of the incident and diffracted beams respectively. The ensemble of all possible scattering vectors is called the Ewald's sphere as represented on Figure 63. Scattering is thus constrained by two conditions on q (or 2θ): q (or 2θ) should obey Bragg's law and q should be on the Ewald sphere.

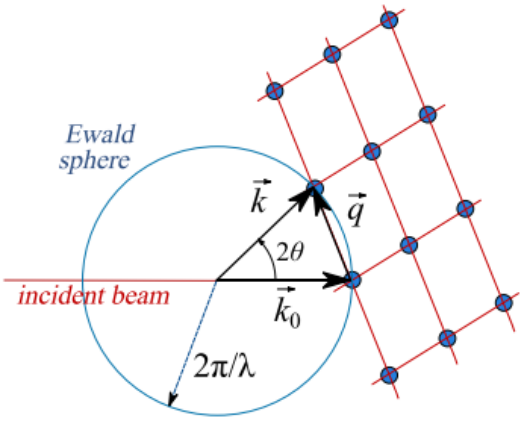


Figure 63. Ewald sphere with $\vec{q} = \vec{k} - \overrightarrow{k_0}$

For an orthorhombic lattice, it is possible to index the spots of WAXS with the corresponding planes using the following formula:

$$q_{h,k,l}^2 \frac{2\pi^2}{d^2} = \frac{h^2}{a^2} + \frac{k^2}{b^2} + \frac{l^2}{c^2} \tag{31}$$

The crystal thickness can be determined with WAXS analysis using the Scherrer's formula. [109] The crystallite size in the direction of $\vec{q}$ is linked to the width of the diffraction peak with the following

Cette thèse est accessible à l'adresse : https://theses.insa-lyon.fr/publication/2023ISAL0006/these.pdf
© [H. Willeman], [2023], INSA Lyon, tous droits réservés

formula where K is a constant approximately equal to 0.89, λ is the wavelength of the X-ray beam, H is the width at half-heightof the diffraction peak and θ the diffraction angle.

$$d = \frac{K\lambda}{Hcos\theta} \tag{32}$$

WAXS pattern presented in Figure 64 can be decomposed in two contributions: a broad amorphous halo and crystalline peaks. By deconvoluting the spectra and integrating the amorphous halo and the crystalline peaks, the crystalline ratio can in principle be retrieved.

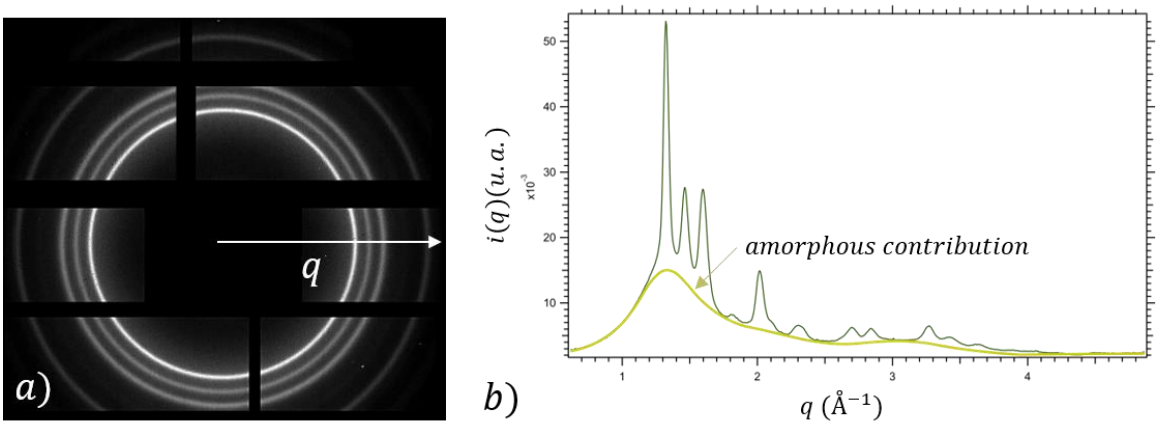


Figure 64. a) WAXS pattern and b) corresponding intensity in the HORI direction as a function of the scattering vector q

Determination of local strain: evolution of the distance between crystal planes

In the same way as for SAXS experiments, in order to extract quantitative information on the variation of the distance between crystal planes as a function of the macroscopic strain and of the azimuthal angle, as well as on the variation of the intensity as a function of the azimuthal angle for a given strain value, we need to fit each WAXS diffraction peaks. Thus, the intensity is plotted as a function of the scattering vector q, as shown in Figure 65 and the peaks are fitted with a Gaussian function:

$$f(q) = y0 + A\ exp\left(-\frac{(q-q0)^2}{w}\right) \tag{33}$$

The local tensile strain $\varepsilon_{micro}^{(hkl)}$ at the scale of crystal planes is measured via the strain-induced shift of the positions of the diffraction peaks.

$$\varepsilon_{micro}^{(hkl)} = \frac{\Delta q^{(hkl)}}{q_0{}^{(hkl)}} = -\frac{\Delta d^{(hkl)}}{d_0^{(hkl)}} \tag{34}$$

The resolution of WAXS acquisition is $\Delta q = 0.0042$ Å^{-1} so $\frac{\Delta q}{q} = 0.1\%$. Thus, the resolution on the measurement of strain at the scale of crystals is of the order of $\frac{\Delta d}{d} = 0.1\%$.

Cette thèse est accessible à l'adresse : https://theses.insa-lyon.fr/publication/2023ISAL0006/these.pdf
© [H. Willeman], [2023], INSA Lyon, tous droits réservés

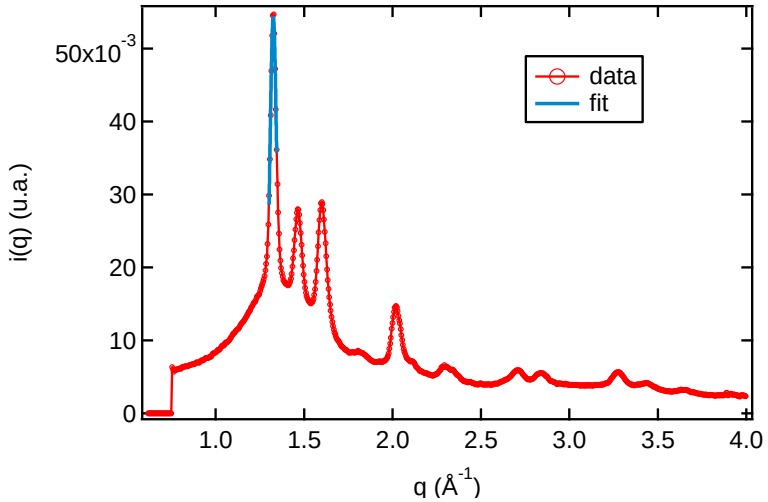


Figure 65. WAXS pattern intensity in the HORI direction and fit (110) diffraction peak with equation (33)

This analysis can be used for every diffraction peak of the WAXS pattern for the whole azimuthal distribution. As an example, the local strain at the scale of crystal planes as a function of azimuthal angle is plotted in Figure 66 for (110) and (200) crystal planes for different values of the macroscopic strain. The results from this analysis gives information on the local strain depending on the orientation of the crystals with tensile direction or the ratio between longitudinal and transverse strain.

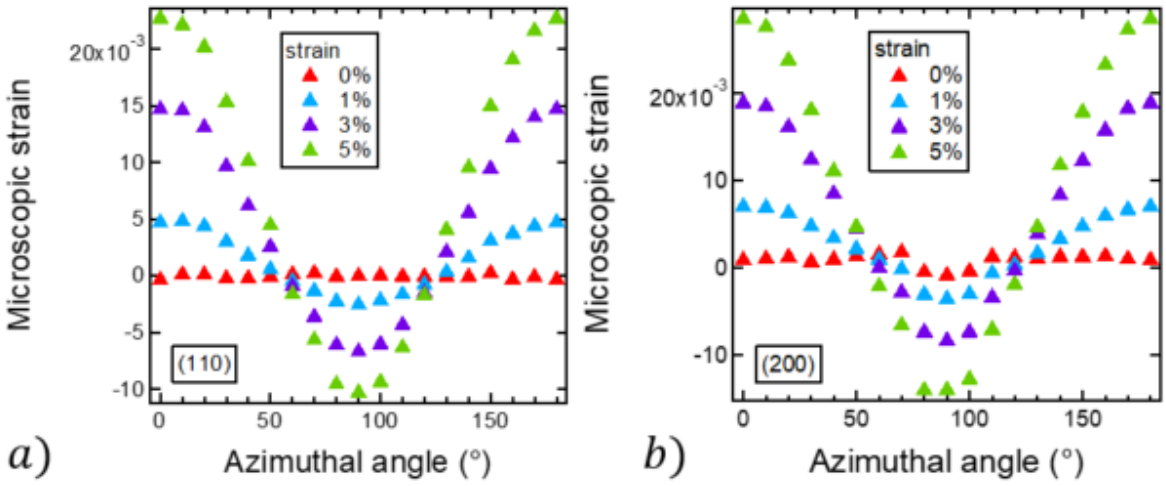


Figure 66. Local strain Δd/d0 at the scale of crystal planes as a function of the azimuthal angle ψ for ε=0,1,3 and 5% for a) (100) planes and b) (200) planes

3. Case of anisotropic system

Let us consider a system made of an ensemble of identical uniaxial scattering objects, for example, stacks of amorphous/crystalline lamellae, which are defined by the orientation of their normal vector $\vec{n}$. The number dN(Ω) of objects oriented within a solid angle $d\Omega$ around a given direction Ω is $\mathrm{dN}(\Omega) = D(\vec{n})\mathrm{d}\Omega$. This is the definition of the distribution of orientation $\mathrm{D}(\vec{n})$.

The corresponding distribution of intensity in the reciprocal space is:

$$i(\vec{q}) \approx i_0(q)\frac{D(\vec{n})}{4\pi q^2} \qquad (35)$$

Cette thèse est accessible à l'adresse : https://theses.insa-lyon.fr/publication/2023ISAL0006/these.pdf
© [H. Willeman], [2023], INSA Lyon, tous droits réservés

in which the vector $\vec{q}$ is in the same direction as $\vec{n}$ since objects (lamellar stacks) scatter in the direction of their normal $\vec{n}$ (this is imposed anyway by their assumed uniaxial symmetry). There is of course a proportionality coefficient (not indicated here) related to the contrast and the overall sensitivity of the experimental setup. $4\pi q^2$ represents the surface area of the sphere of radius q. It is very important to realize that the separation in one factor D($\vec{n}$) depending only on the orientation $\vec{n}$ and one factor $i_0(q)$ depending only on q holds only if all objects are identical (but with different orientations). It is no longer valid if, for instance, the long periods of the lamellar stacks vary as a function of their orientation, which will actually be the case in stretched samples. On the other hand, this separation is strictly valid for crystal planes in WAXS.

4. In situ SAXS/WAXS tensile tests

In situ SAXS/WAXS tensile tests were performed using a home-made MATEIS remote-control (denoted X-JICO), temperature regulated tensile apparatus specifically dedicated to synchrotron measurements as represented in Figure 67. The stretching stage is equipped with a temperature-controlled chamber, from 0 to 200°C.

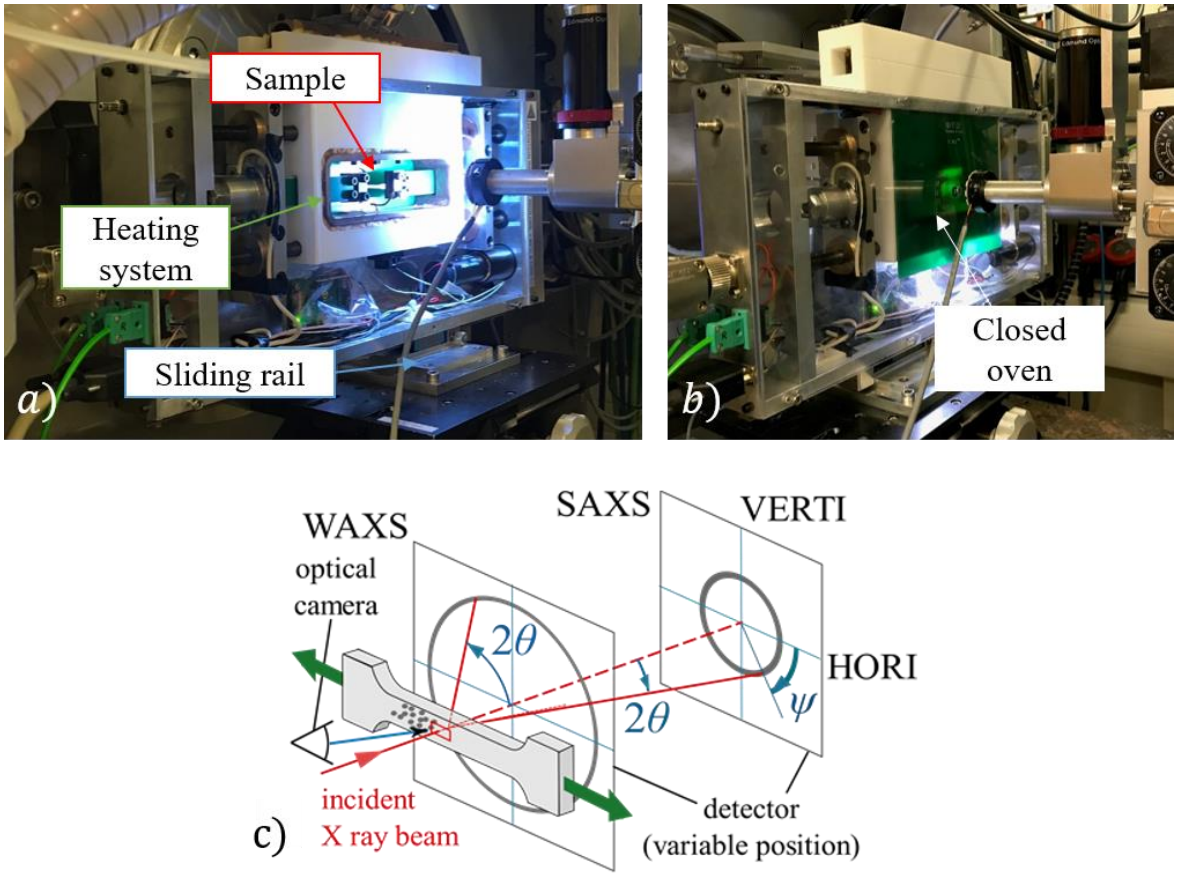


Figure 67. X-JICO tensile device installed on a Synchrotron beamline for the configurations at a)room temperature and b) 170°C; c) Schematic in situ SWAXS tensile tests experiments principle

Synchrotron radiation is necessary as in-situ tensile tests at a constant drawing rate with simultaneous SAXS acquisition require a short acquisition time. Simultaneous SAXS and WAXS tests were performed at Synchrotron ESRF in Grenoble, France on the BM02 beamline and at Synchrotron SOLEIL in Paris, France on the SWING beamline. The chosen X-ray wavelength was λ = 0.103 nm corresponding to 12 keV energy.

Cette thèse est accessible à l'adresse : https://theses.insa-lyon.fr/publication/2023ISAL0006/these.pdf
© [H. Willeman], [2023], INSA Lyon, tous droits réservés

The strain (machine displacement) and engineering stress (load cell 2 kN) are measured in real time. This device enables symmetrical stretching in order to keep the same region of the sample in front of the X-ray beam. Dumbbell specimens as schematized on Figure 68 with a gauge length 20 mm and width 2 mm were cut out from the hot-molded sheets. Each tensile tests was carried out twice, only a representative curve will be shown in the following results.

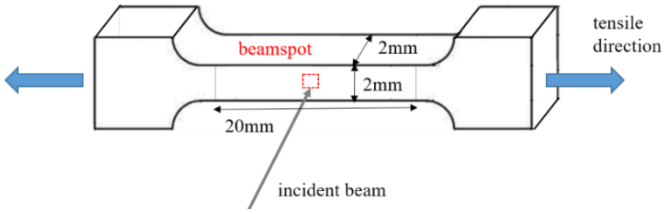


Figure 68. Test sample dimension

SOLEIL Synchrotron experiments

For SOLEIL experiments, the distance between the sample and the SAXS detector was set to 2.003m which corresponds to a range of scattering vector from 0.005 to 0.33Å^{-1}. For WAXS experiments, only one detector of 10x10cm was used, which limited the acquisition of WAXS to the top right quarter of the pattern. WAXS detector was placed 10.9cm from the sample. The accessed range of scattering vector is from 1.52 to 3.16 Å^{-1}.

The X-JICO device imposes a constant nominal deformation with a constant displacement rate $\dot{\varepsilon}$, the macroscopic nominal strain of the sample follows the simple equation: $\varepsilon(t) = \dot{\varepsilon} \cdot t$.Tensile tests were carried out at room temperature for various strain rates $\dot{\varepsilon}$ = 10^{-2}, 10^{-3} and 10^{-4} s^{-1}. For strain rates of 10^{-2} s^{-1} and 10^{-3} s^{-1}, the exposure time was set to 1s with a delay of 0.5s between each exposure. Thus, SAXS and WAXS patterns are acquired every 1.5s. Thus, a pattern is acquired every $\Delta\varepsilon$ = 0.015 and $\Delta\varepsilon$ = 0.0015 respectively. For a nominal strain rate of 10^{-4} s^{-1}, the exposure time was also set to 1s but with a delay time of 9s. A pattern is acquired every 10s, thus every $\Delta\varepsilon$ = 0.001.

The deformation of the sample was obtained by measuring the displacement of dots on the sample using image analysis of the picture taken of the sample simultaneously with the acquisition of SAXS and WAXS patterns.

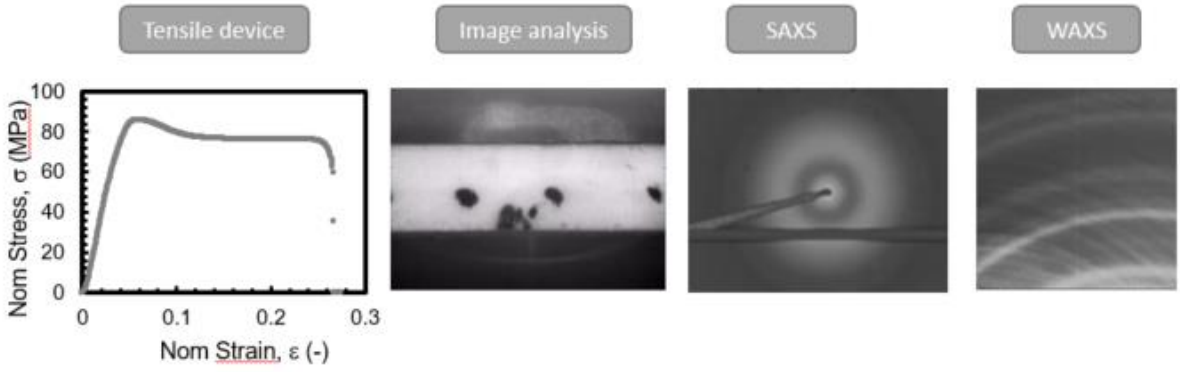


Figure 69. Outputs of in situ SWAXS tensile experiments for SOLEIL experiments

Cette thèse est accessible à l'adresse : https://theses.insa-lyon.fr/publication/2023ISAL0006/these.pdf
© [H. Willeman], [2023], INSA Lyon, tous droits réservés

ESRF Synchrotron experiments

For ESRF experiments, the distance between the sample and the SAXS detector was 1.51 m, so that the corresponding range of observation (scattering vector q) spans from 0.005 to 0.15 $Å^{-1}$. The WAXS detector distance from the sample was 0.59m to access a range of scattering vector q between 0.75 and 4.4 $Å^{-1}$ which corresponds to scattering angles between 7 and 42°. Besides, a remote control, stereo correlation system was installed in order to follow the deformation process throughout acquisition. In this way the beam could be precisely adjusted in the middle of the sample and the local macroscopic strain at beam location could be measured in real time by measuring the strain field on the surface. A speckled pattern was made on the surface of the sample with black paint. Digital image correlation was carried out using the Vic-2D software.

Tensile tests were carried out with a nominal strain rate $\dot{\varepsilon} = 10^{-3}\ s^{-1}$ for two tests temperatures: 23°C and 170°C, below and above glass transition temperature. The exposure time was 1s with a delay time of 1s necessary to download the patterns. Thus, SAXS and WAXS patterns are acquired every 2s. The strain increment was then of $\Delta\varepsilon = 0.002$. An image of the sample for stereo correlation was taken every 2s too. It is important to note that DIC analysis was led only for tensile tests at room temperature as the use of the enclosed oven for high temperature tensile tests obstructs the display of the specimen. Above Tg, less localization phenomena are involved in the deformation process as the amorphous phase is in the rubbery state. The macroscopic strain will thus be supposed to be equal to the imposed (nominal) macroscopic strain defined by the displacement rate of the tensile device.

The four different outputs of the experiments which are displayed on Figure 70 correspond to different scales of observation. Stress strain curves obtained via the tensile device correspond to the global macroscopic behavior. Digital image correlation from video follow up along stretching gives access to the macroscopic local deformation of the sample at beam position. SAXS experiments give the deformation at the scale of lamellae stacks and WAXS experiments allow to measure the strain at the scale of the crystalline lattice.

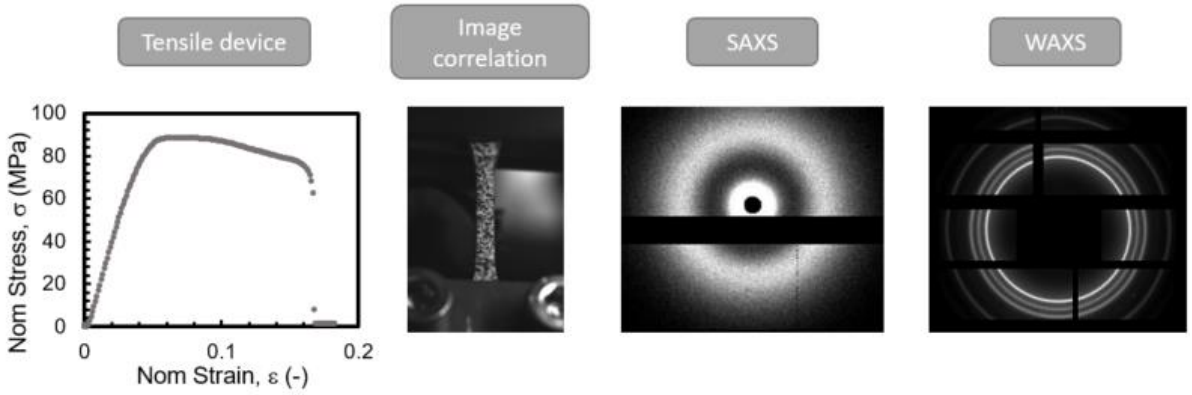


Figure 70. Outputs of in situ SWAXS tensile experiments for ESRF experiments

All experimental conditions for in situ tensile tests SAXS/WAXS are summarized in the following Table 2 and Table 3. $\Delta\varepsilon$ acquisition is the variation in ε during one acquisition. $\Delta\varepsilon$ is the difference in ε between successive acquisitions.

Cette thèse est accessible à l'adresse : https://theses.insa-lyon.fr/publication/2023ISAL0006/these.pdf
© [H. Willeman], [2023], INSA Lyon, tous droits réservés

Temperature (°C)	Nominal strain rate (s^{-1})	Exposure time (s)	Delay time (s)	Δε acquisition	Δε
23	10^{-2}	1	0.5	0.01	0.015
	10^{-3}	1	0.5	0.001	0.0015
	10^{-4}	1	9	0.0001	0.001

Table 2. Experimental conditions of in situ SAXS/WAXS tensile tests used at Synchrotron SOLEIL

Temperature (°C)	Nominal strain rate (s^{-1})	Exposure time (s)	Delay time (s)	Δε acquisition	Δε
23 170	10^{-3}	1	1	0.001	0.002

Table 3. Experimental conditions of in situ SAXS/WAXS tensile tests used at Synchrotron ESRF

Cette thèse est accessible à l'adresse : https://theses.insa-lyon.fr/publication/2023ISAL0006/these.pdf
© [H. Willeman], [2023], INSA Lyon, tous droits réservés

Chapter III. General, thermal and mechanical properties of PEEK

I. Crystallization 69
1. Memory effects 69
2. Crystallization kinetics 73
II. Compression molding 79
1. Crystallinity 79
2. Spherulite morphology 79
3. Thermal stability 80
III. Mechanical properties under tensile stretching 82
1. DMA 82
2. Tensile tests 83
3. Strain localization 86
IV. Physical ageing 88
1. DSC 88
2. DMA 89
3. Tensile tests 90
V. Conclusion 91

Cette thèse est accessible à l'adresse : https://theses.insa-lyon.fr/publication/2023ISAL0006/these.pdf
© [H. Willeman], [2023], INSA Lyon, tous droits réservés

In this chapter, the general properties of PEEK are investigated. First, the crystallization behavior of PEEK is evaluated. Then, the processing of PEEK samples by compression molding is described. In the following part, the macroscopic mechanical properties of these samples are discussed. Lastly, the results of the physical ageing study in PEEK are presented.

I. Crystallization

In order to understand the relationships between the process conditions and the structure of the studied PEEK grades, the crystallization and melting processes must be characterized in details. The influence of the molten state parameters and cooling rates on crystallization kinetics will be presented. The crystalline properties of compression molded samples later used for tensile tests experiments will be determined.

1. Memory effects

The influence of crystallization parameters such as the molten state temperature and cooling rates have been studied by DSC using a self-nucleation and annealing method as described in the work of Fillon et al. [110]

The erasing of the thermal history was thus firstly studied in order to determine the molten state temperature which would erase all crystalline memory. Using this temperature, the final structure of the material would be independent of whatever thermal treatments the material has known before processing.

The "standard" melting peak of PEEK pellets (grade KT820) recorded at a heating rate of 10°C.min^{-1} is shown in Figure 71. The melting curve is representative of the original state of the material obtained when it was pelletized.

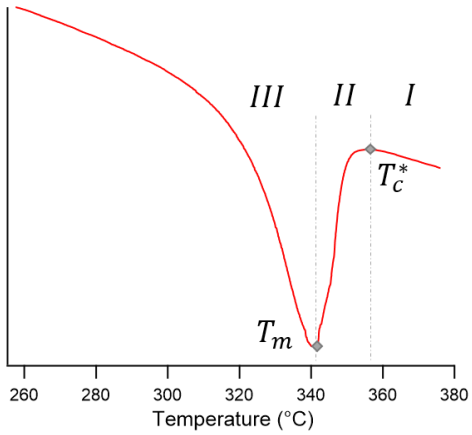


Figure 71. Standard melting peak of KT820 PEEK pellets obtained by heating at 10°C/min

The melting peak in Figure 71 shows that melting should be complete above T_c^* ≈355°C (region I), corresponding to the upper limit of the melting endotherm. Conversely, just below T_c^*, melting should be only partial (region II).

Using DSC, the polymer pellets were melted at several temperatures T_s from 350°C up to 400°C for 10 minutes. The temperature cycle used in DSC is shown in Figure 72. Cooling the polymer at 10°C/min, the shift of the crystallization during the cooling step was measured as a function of T_s. In this case of non-isothermal crystallization upon cooling from the molten state, memory effects appear when crystallization is shifted to higher temperature.

Cette thèse est accessible à l'adresse : https://theses.insa-lyon.fr/publication/2023ISAL0006/these.pdf
© [H. Willeman], [2023], INSA Lyon, tous droits réservés

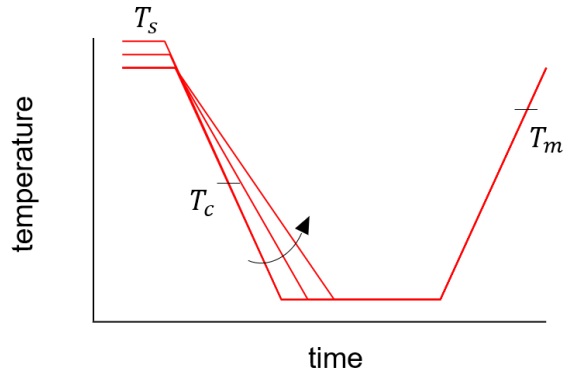


Figure 72. Temperature cycle used in DSC to study memory effects of PEEK using several melting temperatures T_s and several cooling rates

Figure 73.a,c shows crystallization peaks for molten state temperatures T_s from 350 to 400°C for KT820 and KT880 PEEK grades respectively. The maxima of the peaks are reported in Figure 73.b,d as a function of T_s.

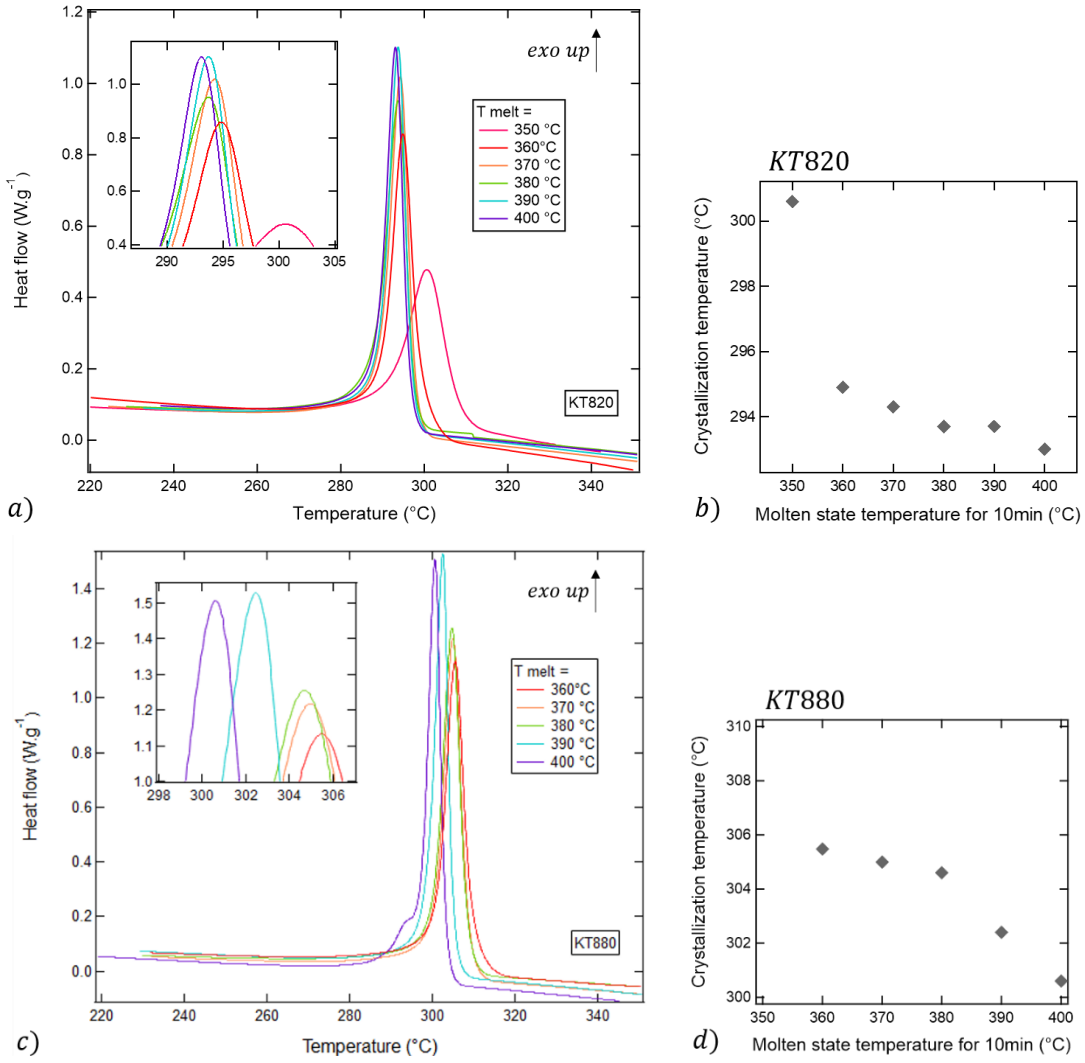


Figure 73. Crystallization peaks from thermograms of for different molten state temperature from 350 to 400° then cooled at 10°C.min^{-1} a) KT820 c) KT880 and temperature of the maximum of the crystallization peak b) KT820 and d) KT880

Cette thèse est accessible à l'adresse : https://theses.insa-lyon.fr/publication/2023ISAL0006/these.pdf
© [H. Willeman], [2023], INSA Lyon, tous droits réservés

It is observed that the crystallization temperature actually depends on the molten state temperature. There is a brutal change from 350 to 360°C. Indeed, below 355°C, which corresponds to the upper limit of the melting peak in Figure 71, all crystals may not be fully melted and may act as nucleating agents for the crystallization during the cooling step. Nucleation is thus accelerated and crystallization is effectively shifted towards higher temperature in non-isothermal crystallization. In addition, a very small fraction of crystals may perhaps survive up to T_m^0 (see the Gibbs-Thomson equation) which has been estimated to be around 385°C. [85] For molten state temperatures higher than 360°C, the crystallization temperature nearly stabilizes around 294°C. From these results, we conclude that the erasing of the thermal history is successful once the crystallization peak is stabilized, i.e. from and above 380°C. Note that a further slight decrease of the crystallization temperature after melting at high temperatures (400°C and above) may be due to some degree of degradation.

Influence of the cooling rate

The influence of the cooling rate on crystallization was then studied. For a heat-cool-heat cycle in DSC (Figure 72), using 380°C as the molten state temperature T_s, the cooling rate was varied from 0.3 up to 30 °C.min^{-1}. The crystallization temperature was then recorded during the cooling step.

The crystallization exotherms are presented in Figure 74.a and associated crystallization temperatures are plotted in Figure 74.b as a function of the cooling rate. We observe that T_c strongly depends on the cooling rate. The faster is the cooling rate, the lower is the crystallization temperature. Indeed, when cooled rapidly, faster cooling rates are effectively probed, which correspond to large super-cooling values, hence to lower crystallization temperatures. Moreover, the shape of the crystallization peaks varies significantly with the cooling rate. The faster the cooling rate is, the wider is the crystallization peak. In Figure 74.c is represented the heat flow divided by the cooling rate as a function of temperature. The corresponding crystallization enthalpy, obtained by integrating between 360 and 330°C, is plotted in Figure 74.d as a function of the cooling rate. ΔH is stable which indicates that the polymer nearly reaches its maximum crystallinity in the whole range of cooling rates indicated.

Different crystallization temperatures, associated to different thermal histories, should a priori correspond to difference in the crystalline morphology, namely e.g. different thicknesses of crystalline lamellae. This in turn should correspond to different melting temperatures. The melting temperature associated to the crystallization for several cooling rates is presented on Figure 75. The heating rate is 10°C.min^{-1} for all experiments. The thermograms show that the melting temperature increases as the cooling rate decreases. Moreover, we can see a transition from a double melting peak for cooling rates below 10°C.min^{-1} to a single melting peak for cooling rates above 10°C.min^{-1}.

The presence of a double melting peak has been documented in various polymers and crystallization conditions. [110], [111] It can be interpreted as follows. For the lower cooling rates (0.3 and 0.5°C.min^{-1}), the crystallization temperature is around 315°C. When referred to Figure 73.b, this would correspond to an effective molten state temperature below 350°C, i.e. within region II of the thermogram shown in Figure 71. In this region, annealing may occur and the double melting peak would correspond to annealed crystals. However, both situations are quite different when cooling at a very slow rate, time is left for nuclei to grow and form crystal lamellae with comparatively large long period. A secondary crystallization step may follow, as reflected by the wide exotherm on the left hand (low temperature) side of the main crystallization peak. Secondary crystalline lamellae may be responsible for the secondary (low temperature) melting peak. The secondary crystalline lamellae may be less prefect (i. e. thinner) as the cooling rate increases, which may explain that the secondary melting peak shifts towards lower temperature as the cooling rate increases. (see Figure 75.a)

Cette thèse est accessible à l'adresse : https://theses.insa-lyon.fr/publication/2023ISAL0006/these.pdf
© [H. Willeman], [2023], INSA Lyon, tous droits réservés

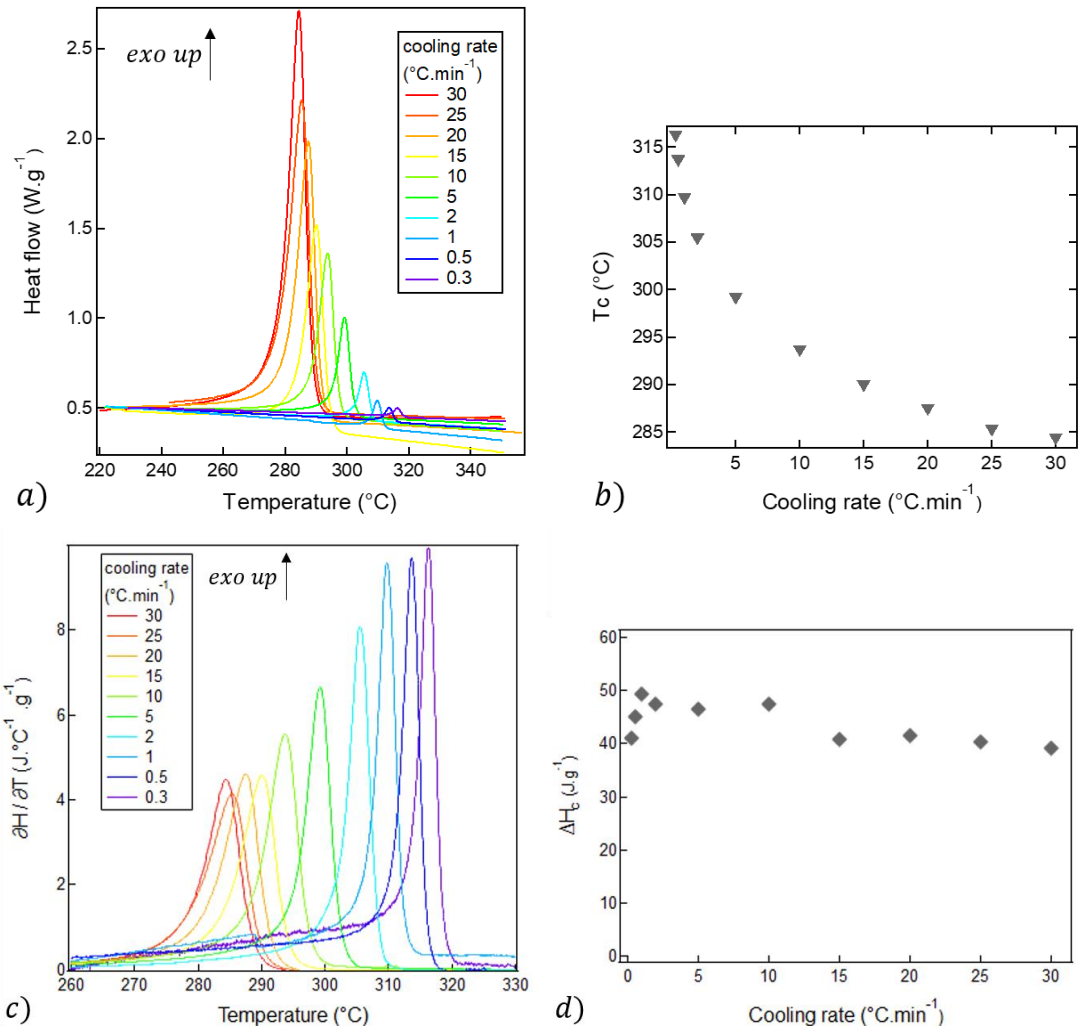


Figure 74. a) Crystallization exotherms of KT820 for different cooling rates from 0.3 to 30°C.min^{-1} b) temperature of the maximum of the crystallization peak c) heat flow divided by the cooling rate for cooling rates from 0.3 to 30°C.min^{-1} and d) ΔH_c enthalpy of crystallization as a function of the cooling rate

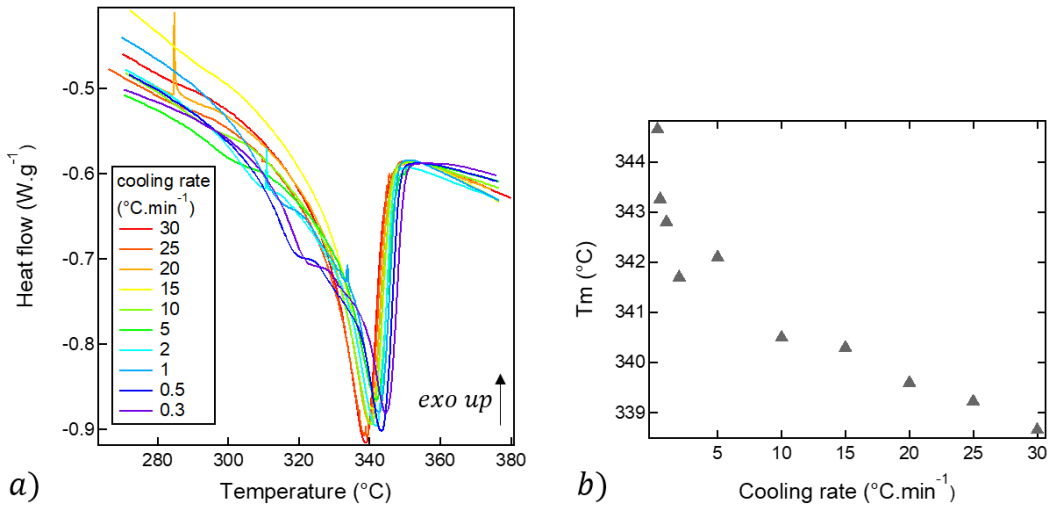


Figure 75. a) Melting endotherms of KT820 for samples crystallized at different cooling rates from 0.3 to 30°C.min^{-1} then heated at 10°C.min^{-1} b) temperature of the maximum of the melting peak

Cette thèse est accessible à l'adresse : https://theses.insa-lyon.fr/publication/2023ISAL0006/these.pdf
© [H. Willeman], [2023], INSA Lyon, tous droits réservés

When plotting the melting temperature as a function of the corresponding crystallization temperature as represented in Figure 76, the thermodynamic melting point can be estimated at the intersection of the $T_m = T_c$ (full line) and $T_m = f(T_c)$ (dashed line) curves. For these experiments on PEEK KT820, the estimated T_m^∞ would be about 350°C. However, as stated previously, 350°C is located in the zone II of the thermogram (Figure 71) where the melting can only be partial.

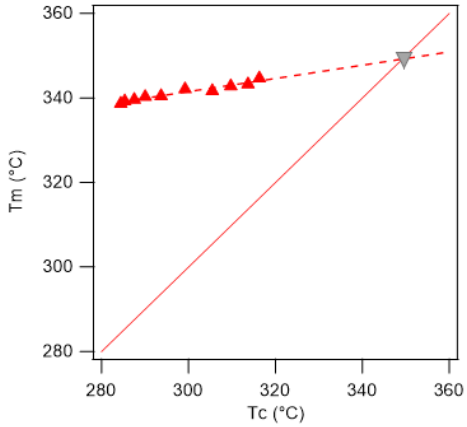


Figure 76. Observed melting point T_m as a function of crystallization temperature T_c (°C)

2. Crystallization kinetics

a. Isothermal crystallization

Isothermal crystallization of both grades of PEEK have been studied by DSC. The isotherm temperature range was set between 308 and 322°C. The samples were first molten at 380°C for 10 minutes then cooled from the melt at 20°C.min^{-1} to the specific temperature chosen for the isotherm. The evolution of the crystallinity is then measured as a function of time. The crystallization exotherm during the isotherm is shown is Figure 77 as well as the determination of the value t_0 corresponding to the beginning of crystallization.

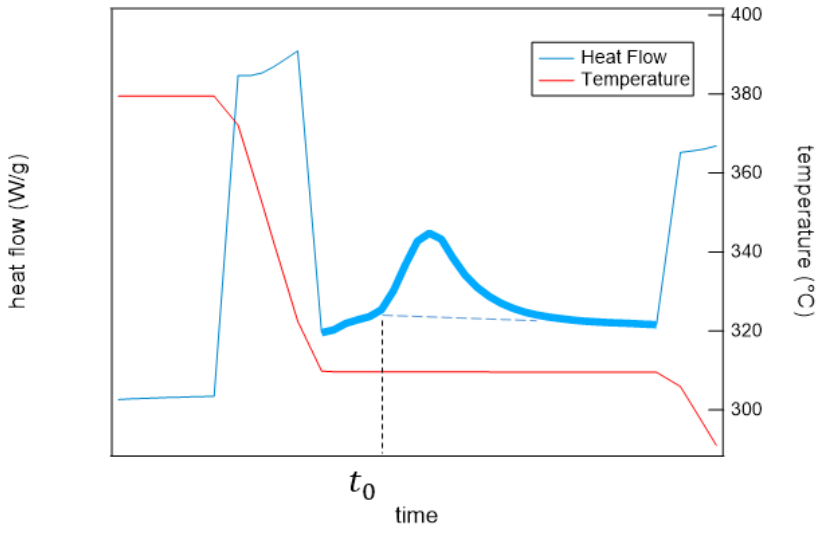


Figure 77. Heat flow measured by DSC during isothermal crystallization at 308°C. T_0 is the point where the integration of the peak starts.

Cette thèse est accessible à l'adresse : https://theses.insa-lyon.fr/publication/2023ISAL0006/these.pdf
© [H. Willeman], [2023], INSA Lyon, tous droits réservés

The relative crystallinity, reported in Figure 78 for KT820, is calculated by integrating the enthalpy of the crystallization peak with time.

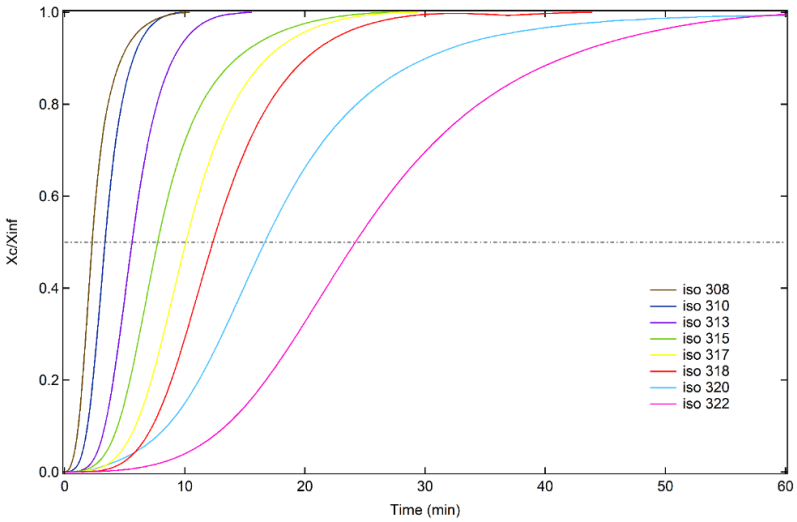


Figure 78. Relative crystallinity index as a function of time for KT820 PEEK at different crystallization temperatures

From these curves, the crystallization half-time can be obtained for each temperature of isothermal crystallization. The time for half-crystallization increases as the crystallization temperature increases, according to the classical nucleation theory which states that the nucleation rate increases as the undercooling increases. (see Chap I)

Isothermal crystallization was investigated for both grades KT820 and KT880 of PEEK. For every crystallization temperature, KT880 exhibits a shorter crystallization time as a shorter chain length allows more mobility in the polymer. Both grades of PEEK are compared in the following Figure 79 for an isothermal crystallization at 322°C. On this example, KT880 crystallizes around five times faster than KT820.

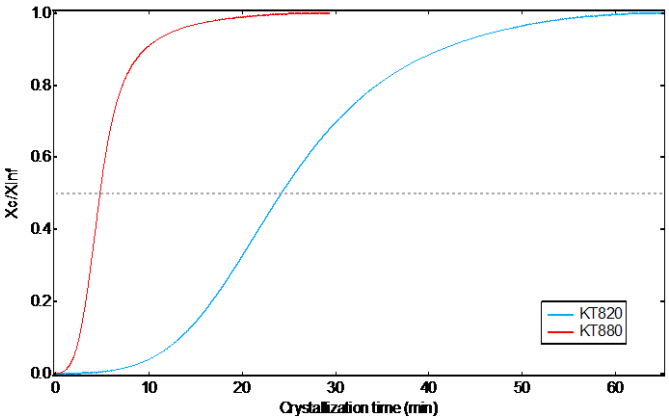


Figure 79. Relative crystallinity for isothermal crystallization at 322°C for both grades of PEEK

The relative crystallinity indices are presented in Figure 80 in the form $\log(-\ln(1-X_c/X_{cinf})$ vs log(time). The Avrami's theory discussed in the literature review was applied to these experimental values of the crystallization time and results are presented in Figure 80. The Avrami's exponent gives information on the type of nucleation and growth.

Cette thèse est accessible à l'adresse : https://theses.insa-lyon.fr/publication/2023ISAL0006/these.pdf
© [H. Willeman], [2023], INSA Lyon, tous droits réservés

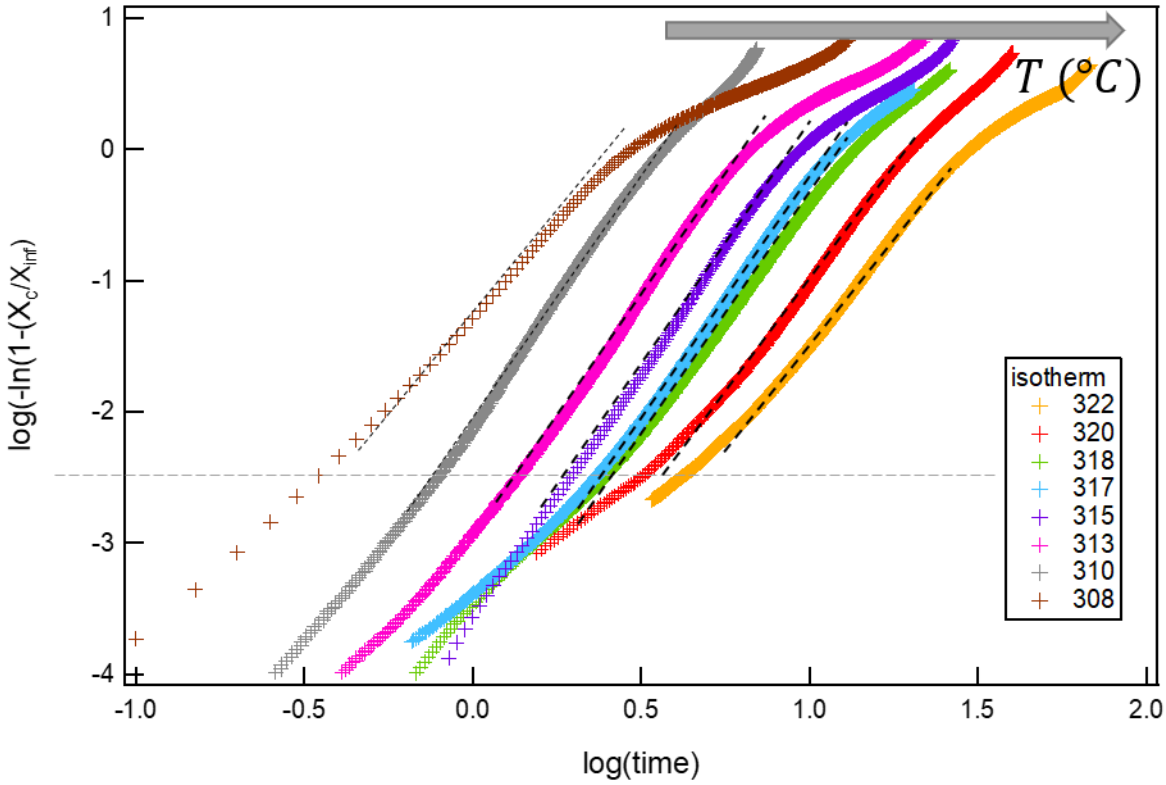


Figure 80. Avrami plot for isothermal crystallization of PEEK KT820 from 308 to 322°C. The dashed horizontal line indicates the lower limit for the Avrami fit.

From the Avrami plot, two successive steps of crystallization are present. The curves cannot be fitted by one single Avrami process. This was already observed by Cruz-Pinto et al. [112] This corresponds to a secondary crystallization process. The nature of this process is not fully clear. It may correspond either to new lamellae formed within already present lamellar stacks, or to newly formed lamellar stacks.

Isotherm T (°C)	308	310	313	315	317	318	320	322
n Avrami's exponent	2.41	3.43	3.48	3.79	3.02	2.88	319	3.12

The isothermal crystallization of PEEK KT820 is described by an Avrami exponent varying around the value of 3 which corresponds to a crystallization process composed of athermal nucleation accompanied by three-dimensional growth. This indicates that the crystallization kinetics may be primarily driven by heterogeneous nucleation (on impurities etc…) On the other hand, in some cases, the exponent is larger than 3, which indicates that a significant contribution of homogeneous (sporadic, thermally activated) nucleation may also be present. However, the choice of the starting point of the crystallization step (t_0) ,here chosen as described in Figure 77, influences a lot the value of the Avrami's coefficient, as shown for example by Jonas and Legras. [8]

Further in situ optical microscopy experiments have been led complementary to this study to get more information on the crystallization processes in our samples. Isothermal crystallization of PEEK was investigated by optical microscopy combined with a hot stage. Figure 81 shows a representative example of an observation of isothermal crystallization of KT880 from the melt at 308°C. The appearance of nuclei and the growth of spherulites can be observed. The pictures show that most spherulites are nucleated at the beginning of the experiment. Only few appears later on in a sporadic way. This is coherent with the previously determined Avrami exponents, which indicate that athermal nucleation is predominant.

Cette thèse est accessible à l'adresse : https://theses.insa-lyon.fr/publication/2023ISAL0006/these.pdf
© [H. Willeman], [2023], INSA Lyon, tous droits réservés

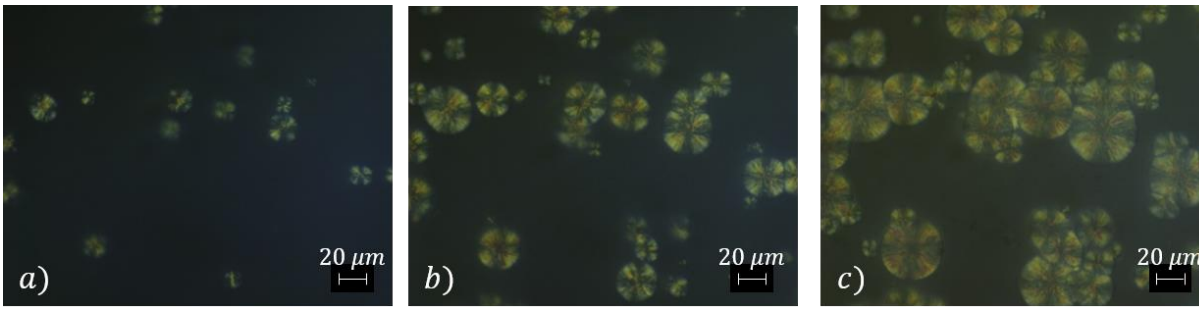


Figure 81. Optical microscopy of isothermal crystallization of PEEK KT880 at 308°C for crystallization times of : a) 88s, b) 247s and c) 383s

The growth of spherulites can be followed along time. Using ImageJ to process micrographs, the diameter of each spherulites is measured as a function of time as reported in Figure 82a. The experiments are repeated for several isotherm temperatures. The results for growth rates are presented in Figure 82b.

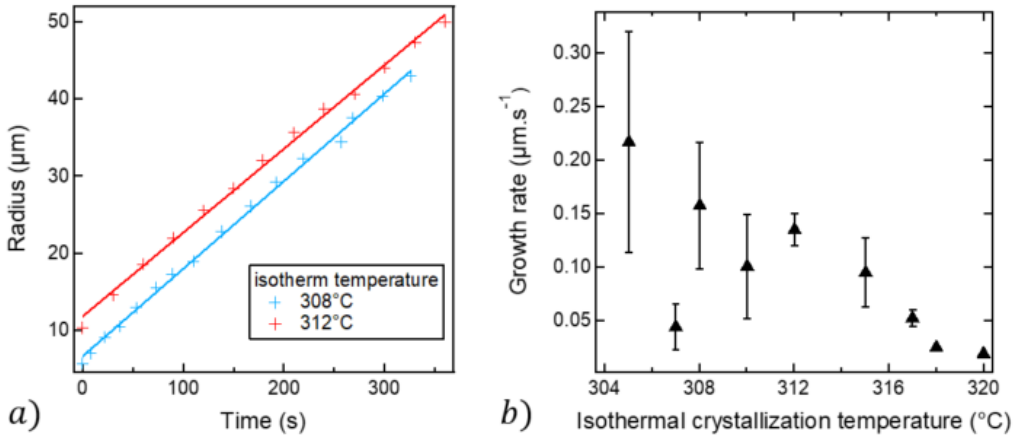


Figure 82. Spherulite growth rate as a function of crystallization temperature for KT880

b. Cold-crystallization

To study the cold-crystallization kinetics close to T_g, we elaborated amorphous samples by quenching molten polymer into ice water to reach fast enough cooling rates. The temperature cycle used for these experiments is presented in Figure 83.

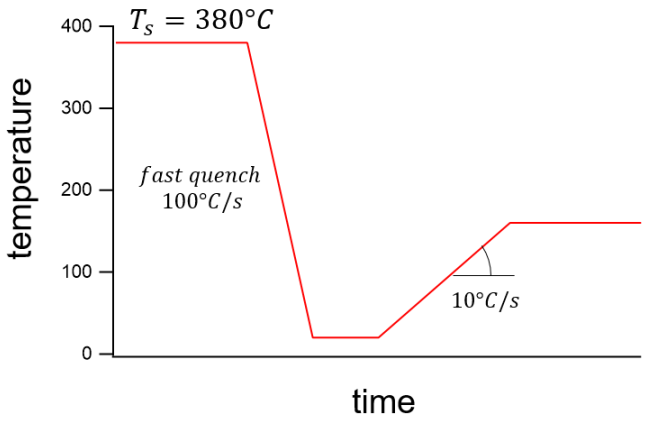


Figure 83. Temperature cycle used to study cold-crystallization of PEEK

Cette thèse est accessible à l'adresse : https://theses.insa-lyon.fr/publication/2023ISAL0006/these.pdf
© [H. Willeman], [2023], INSA Lyon, tous droits réservés

Amorphous samples were obtained by quenching melted pellets at 380°C into ice water which enables to have cooling rates of order of 100°C.s^{-1}. Amorphization process was confirmed by WAXS. WAXS spectra of quenched and virgin pellets are displayed in Figure 84. The pattern obtained in the amorphous sample was renormalized to superpose the amorphous contribution on both spectra.

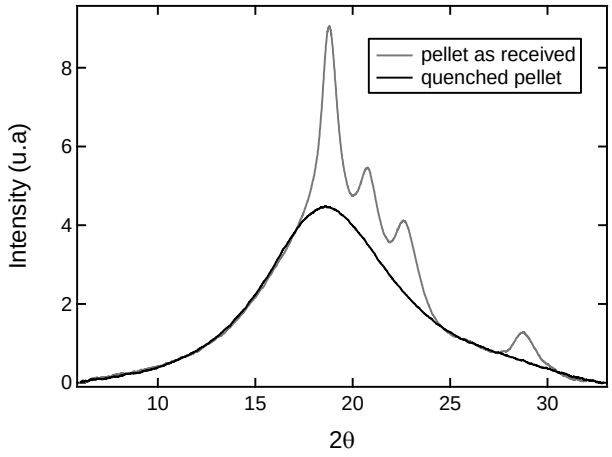


Figure 84. WAXS patterns of quenched and virgin pellets. Diffraction patterns were obtained at the Henri Longchambon diffraction center of university of Lyon

The crystallization exotherm during the isotherm is shown in Figure 85.

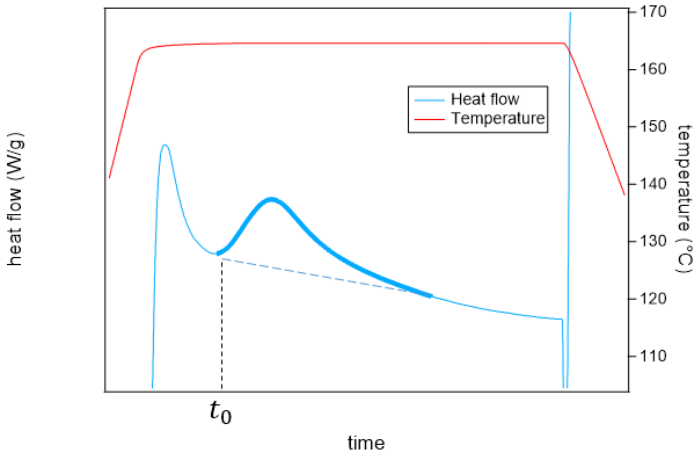


Figure 85. Heat flow measured by DSC during annealing at 165°C. t_0 is the point chosen as the starting point of the integration of the crystallization peak.

c. TTT diagram

The half time crystallization values as a function of crystallization temperature are reported and compared with values found in the literature in Figure 86. [80], [97], [98] The graph is U-shaped with T_g and T_m as limits. For a crystallization time typically below 10s, it is impossible to measure the crystallization peak using the standard DSC cooling ramp. The values found in the literature in Tardif et al. [80], corresponding to the region close to the minimum of the curve, with extremely short crystallization time, were obtained using flash DSC with cooling rates up to 5000 K.s^{-1}. The measurements on KT820 and KT880 are coherent with values from the literature.

Cette thèse est accessible à l'adresse : https://theses.insa-lyon.fr/publication/2023ISAL0006/these.pdf
© [H. Willeman], [2023], INSA Lyon, tous droits réservés

On the right-hand part of the curve, the half time of crystallization rises as the crystallization temperature increases and gets closer to the melting temperature. As mentioned in the previous part, for a given crystallization temperature, the crystallization half-time is about 5 times slower for KT820 than for KT880. On the other hand, at a fixed time scale, there is about 10°C difference between the crystallization temperature of each grade. (as shown also when comparing Figure 73.b and Figure 73.d)

On the other side of the graph, the trend is reversed as the half-time of crystallization rises when the crystallization temperature decreases and gets closer to the glass transition temperature. Polymer chains near the glass transition have less mobility to organize into a crystalline network. In this case too, for a given crystallization temperature, the half-time of crystallization for KT820 is lower than for KT880. However, in this case, the ratio is approximately 2.5.

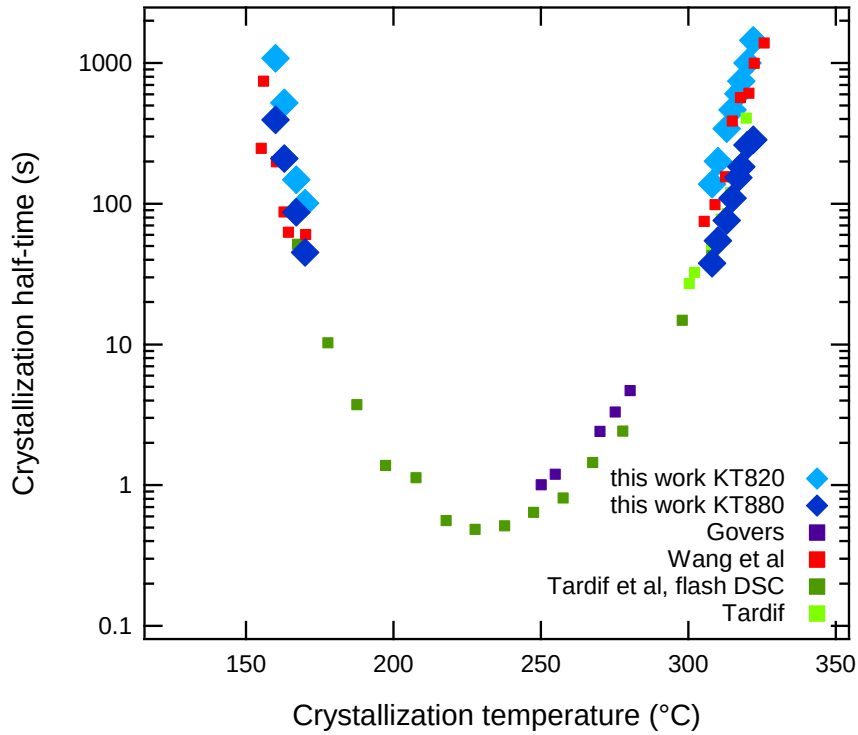


Figure 86. crystallization half-time as a function of the crystallization temperature of PEEK

As the studied grades have relatively similar molecular weight (see Chap II), differences in mobility may not be sufficient to explain the quite large difference in crystallization time on the high temperature side of the curve. The presence of some nucleating agent may play a role also.

Cette thèse est accessible à l'adresse : https://theses.insa-lyon.fr/publication/2023ISAL0006/these.pdf
© [H. Willeman], [2023], INSA Lyon, tous droits réservés

II. Compression molding

The crystalline structures of compression molded samples were studied by DSC, WAXS and optical microscopy to investigate the structural differences between PEEK grades and the influence of the process conditions. For both grades, three different molten state temperatures were used: 380,400 and 420°C. (see the temperature and pressure cycles described in Chapter II)

1. Crystallinity

The crystallinity ratio was measured by DSC and WAXS for each thermal treatment for both grades of PEEK and compiled in Table 4. The molten state temperature does not seem to affect the crystallinity ratio of our polymers. The difference in crystallinity comes from the grade of PEEK, KT880 specimens showing globally higher crystallinity than KT820.

Table 4. Crystallinity ratio for hot molded PEEK

	KT820			KT880		
Molten state T (°C)	380	400	420	380	400	420
DSC Xc (%)	30	33	32	34	36	36

At the microscopic scale, the initial structure of the compression-molded samples may be characterized by the initial SAXS and WAXS patterns. The initial parameters of the crystal unit cell obtained by WAXS are reported in Table 5. The distances between planes are identical for all samples within the pattern resolution ($\pm$0.01 Å). At the scale of lamellae stacks, there is a small but significant decrease of the long period as the molten state temperature during process is increased. This decrease is consistent with the slight decrease of the crystallization temperature shown in Figure 73 and also with the decrease of the melting temperatures, as thinner lamellae have a lower crystallization and melting temperatures.

Table 5. Initial long period of the lamellar stacks and distances between crystal planes for hot molded PEEK

Sample		SAXS L_p (Å)	WAXS d(Å)		
			$d_{(110)}$(Å)	$d_{(113)}$(Å)	$d_{(200)}$(Å)
KT820	380	146.18	4.73	4.28	3.92
	400	145	4.72	4.28	3.91
	420	142.55	4.74	4.29	3.93
KT880	380	145.14	4.74	4.29	3.93
	400	143.83	4.75	4.30	3.93
	420	142.36	4.74	4.29	3.93

2. Spherulite morphology

The temperature cycle used for compression molding was mimicked in in-situ crystallization experiments in the optical microscope equipped with a hot stage to investigate the influence of the molten state temperature on the final structure. The sizes of spherulites were measured at the end of the temperature cycle and results are reported in Figure 87. KT880 presents much larger spherulites than

Cette thèse est accessible à l'adresse : https://theses.insa-lyon.fr/publication/2023ISAL0006/these.pdf
© [H. Willeman], [2023], INSA Lyon, tous droits réservés

KT820 and seems more sensitive to the molten state temperature. The presence of a nucleating agent in KT820 can then be discussed.

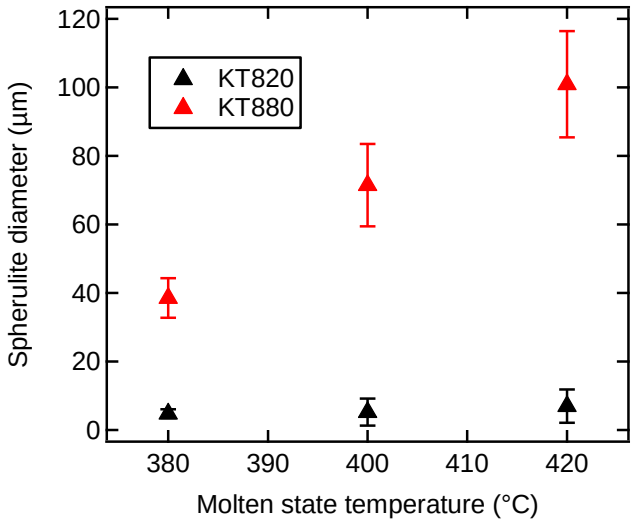


Figure 87. Spherulite size as a function of molten state temperature. Morphologies obtained in non-isothermal conditions at a cooling rate of 20°C/min

The influence of the molten state temperature has then been analyzed for compression molded samples. Cross-polarized optical microscopy was used to determine the final microstructure of the polymer. Morphologies obtained for compression-molded KT820 samples are presented in Figure 88. In contrast to previous results from in situ hot stage crystallization microscopy, little or no difference is observed in the size or distribution of spherulites when varying process conditions. The temperature cycle is perhaps not well-controlled in the press or some elements in the process are acting as nucleating agents.

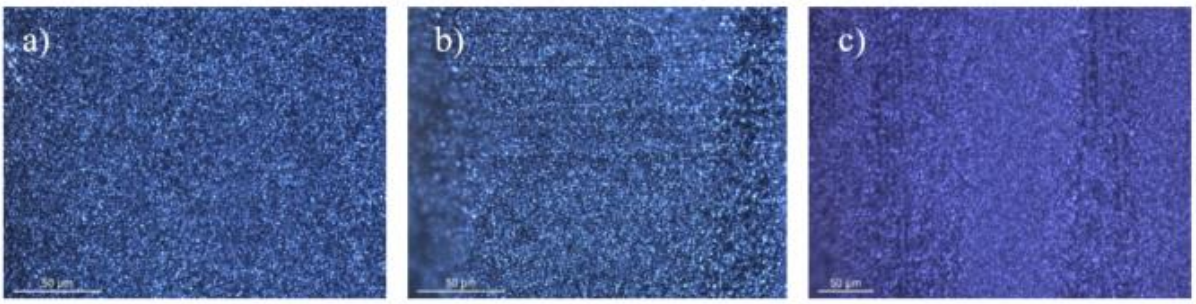


Figure 88. Morphology of PEEK samples with different melting temperatures a) 380°C b) 400°C c) 420°C

3. Thermal stability

The thermal stability of PEEK was studied by TGA. First, a ramp of 10°C.min^{-1} was applied from 20 to 1000°C. The associated weight loss is shown in Figure 89.a. The weight loss during this temperature ramp decomposes in two steps. First, PEEK reaches 1% weight loss at 525°C and undergo a 32% weight loss from 550 to 580°C. Then, from 600 to 800°C, the whole sample mass is lost. This proves the excellent thermal stability of PEEK up to about 500°C.

Cette thèse est accessible à l'adresse : https://theses.insa-lyon.fr/publication/2023ISAL0006/these.pdf
© [H. Willeman], [2023], INSA Lyon, tous droits réservés

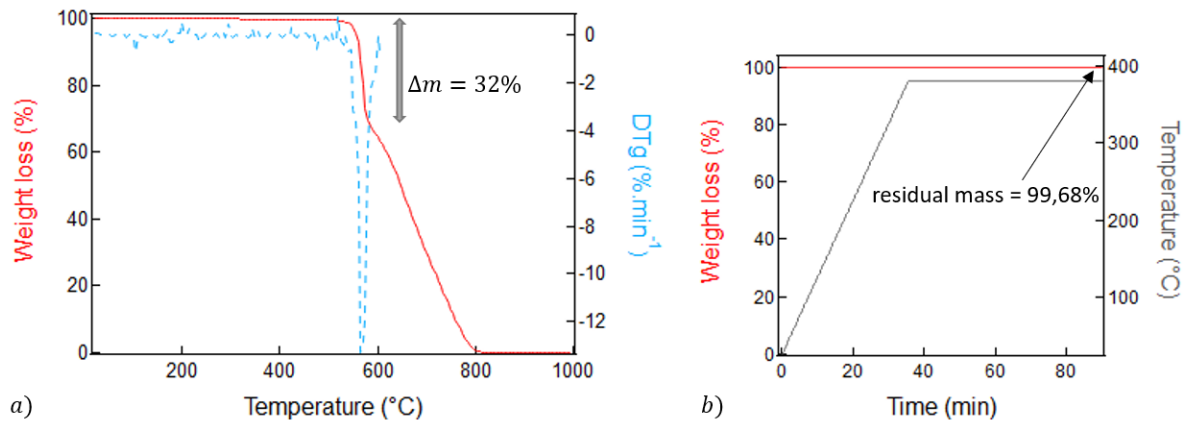


Figure 89. ATG thermograms for a) a ramp from 20 to 1000°C at 10°C/min and b) a ramp from 20 to 380°C at 10°C/min then an isotherm of 10min at 380°C

The weight loss for a 1 hour isotherm at 380°C is displayed in Figure 89.b. No significant weight loss is observed after 1 hour. This would confirm that no significant degradation of the polymer happens during DSC studies or compression-molding. However, some degree of branching may occur when the polymer is maintained at high temperature (above 400°C) for long durations (30 minutes and more). This was observed by Jonas and Legras by rheology. ([8] see Chapter I)

IR spectra of as received pellets and hot molded KT820 are presented in Figure 90 . The spectra are very similar. Only ν C-H bands at 2850-2919 cm^{-1} are slightly less intense and ν C-O-C ether band base is slightly broader after compression molding. This confirms that no detectable degradation of the material occurred during compression molding step.

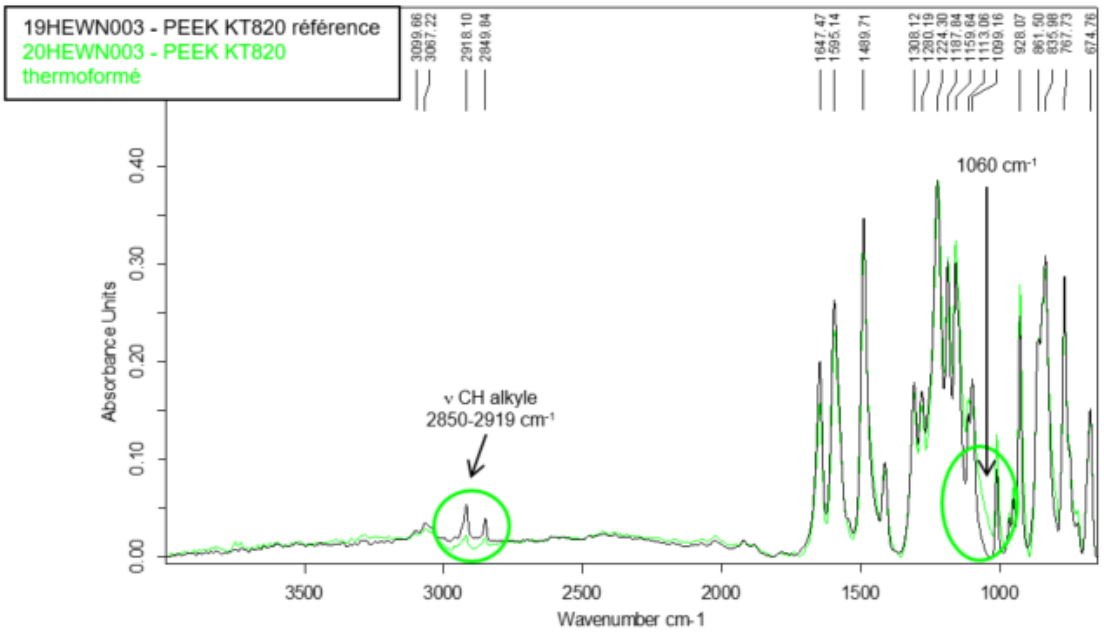


Figure 90. IR spectrum of reference pellets of PEEK KT820 (black) and hot molded KT820 (green)

Cette thèse est accessible à l'adresse : https://theses.insa-lyon.fr/publication/2023ISAL0006/these.pdf
© [H. Willeman], [2023], INSA Lyon, tous droits réservés

III. Mechanical properties under tensile stretching

Experiments to determine the macroscopic mechanical properties of PEEK under tensile stretching and the influence of process and testing parameters were carried out.

1. DMA

Temperature sweep measurements were performed at frequencies of 0.1, 1, 3 and 10 Hz. For each frequency, the temperature associated to each relaxation was determined as the maximum of the relaxation peak observed in the loss modulus E". The temperature dependences of the storage modulus E', the loss modulus E" and the damping factor tan δ, as determined at 1 Hz, are shown in Figure 91. The large temperature gap between the α and β relaxations may explain the toughness of the amorphous phase, as the β relaxation fives some degree of mobility below T_g.

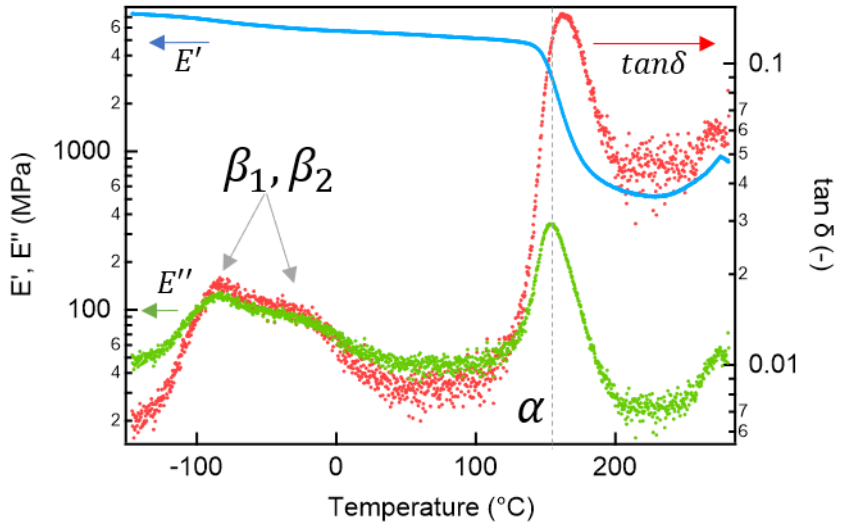


Figure 91. DMA curve of PEEK KT820 for f = 1 Hz

From the DMA curves obtained at several frequencies, a frequency/temperature relaxation map of the β_1, $\beta_2$and α relaxations processes can be established as plotted in Figure 92.

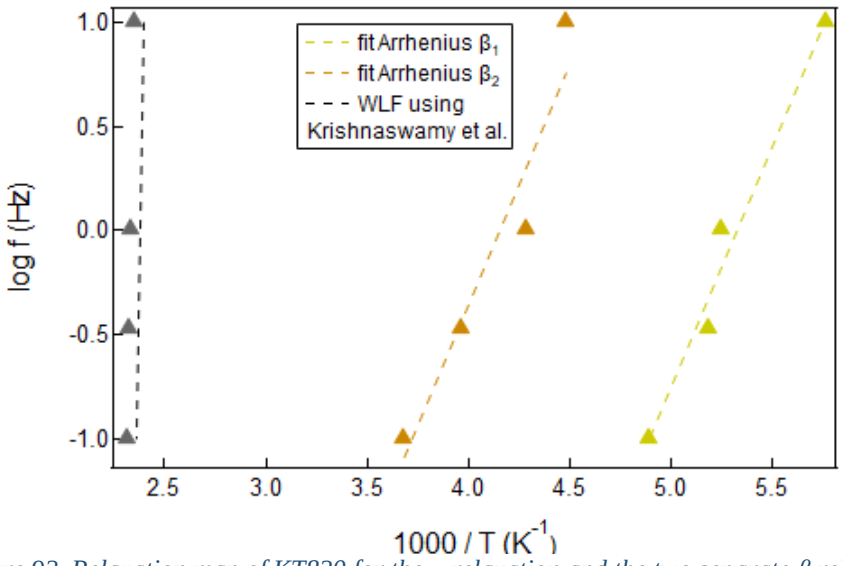


Figure 92. Relaxation map of KT820 for the α relaxation and the two separate β relaxations

Cette thèse est accessible à l'adresse : https://theses.insa-lyon.fr/publication/2023ISAL0006/these.pdf
© [H. Willeman], [2023], INSA Lyon, tous droits réservés

The β_1 and β_2 relaxation processes are fitted using the Arrhenius law. The corresponding energy of activation are reported in the following table.

Relaxation	β_1	β_2
Ea (kJ.mol^{-1})	103	79

In the literature, values of the energy of activation corresponding to the sub-glass β relaxations are reported between 80 for an amorphous sample and 177 kJ.mol^{-1} for a semi-crystalline, annealed sample. [50] The main α-relaxation should follow the Williams-Landel-Ferry (WLF) law defined as follows:

$$log(a_T) = \frac{-C_1(T - T_{ref})}{C_2 + (T - T_{ref})} \quad (36)$$

More data points would be needed to fit data from Figure 92 with the WLF law. C1 and C2 values can be found in the literature from the study of Krishnaswamy and Kalika (C1 = 25.4 and C2 = 90.2 for T_{ref}=147°C). [50] The WLF law corresponding to these values is plotted in Figure 92.

2. Tensile tests

a. Influence of the PEEK grade (molecular weight)

The mechanical properties of both grades of PEEK considered in this study were compared for similar processing and testing conditions. The corresponding stress-strain curves are presented in Figure 93.

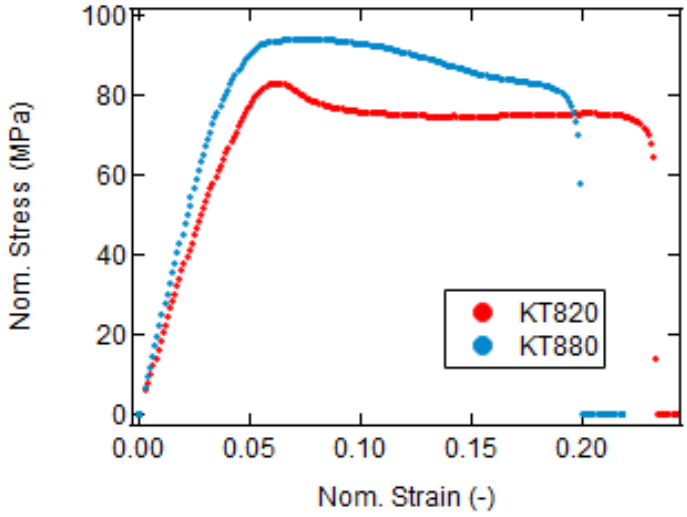


Figure 93. Stress strain curves for KT820 and KT880 grades of PEEK at room temperature for $\dot{\varepsilon}$ = 10^{-3} s^{-1}

Several observations can be made from these curves. First, the slope in the elastic regime is higher for the KT880 grade which means the Young's modulus is higher for this grade. This was expected as crystallinity ratio is generally higher for KT880 polymer (see Table 4). The strain softening phenomenon is however more pronounced for KT820.

Material	Young's modulus (GPa)
KT820	1.75
KT880	2.15

Cette thèse est accessible à l'adresse : https://theses.insa-lyon.fr/publication/2023ISAL0006/these.pdf
© [H. Willeman], [2023], INSA Lyon, tous droits réservés

b. Influence of processing conditions

The influence of processing conditions, especially the molten state temperature during hot molding, was studied and characterized by DSC and microscopy as described in the previous part.

As the final morphology and crystallinity ratio are quite similar when varying the melt temperature, the mechanical properties are not expected to be significantly different. The stress-strain curves for both grades are presented in Figure 94. In each case, the yield stress increases with the molten state temperature of the compression molding step but the Young's modulus does not evolve significantly. For KT820 grade, the strain softening seems to decrease as the melt temperature increases. It could be related to the slight increase in crystallinity where crystals constrain the deformation of the amorphous phase.

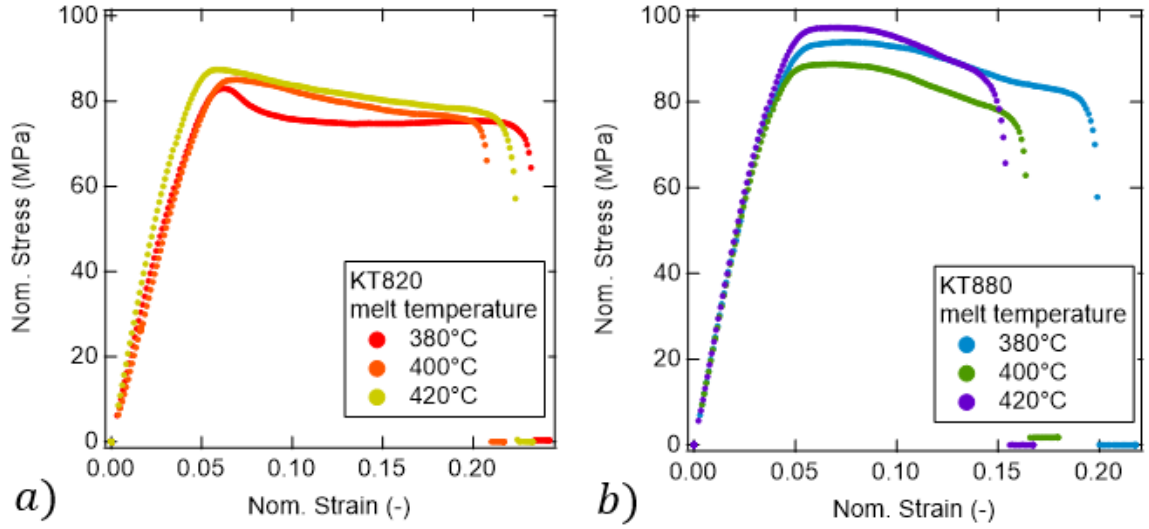


Figure 94. Stress-strain curves for several temperatures of the melt during hot molding process for a) KT820 and b) KT880

c. Influence of temperature

In order to investigate the influence of temperature on the mechanical properties, experiments below and above the glass transition temperature (150°C) were carried out. Regarding macroscopic tensile tests, the mechanical coupling of the amorphous and crystalline phases is expected to be significantly different depending on the rubbery or glassy state of the amorphous component. This should thus impact the macroscopic properties.

Representative results of tensile tests below and above T_g have been summarized in Figure 95. The "bump" on the curve of tensile tests at 170°C at about 60% strain corresponds to a change in strain rate from 10^{-3} s^{-1} to 5.10^{-3} s^{-1}. As expected, the Young's modulus and the yield stress are significantly lower at 170°C but the elongation at break goes up to 200% as the mobility of the amorphous phase increases with temperature. The behavior of the material beyond the yield point at 170°C will be discussed in more details in chapter V.

Cette thèse est accessible à l'adresse : https://theses.insa-lyon.fr/publication/2023ISAL0006/these.pdf
© [H. Willeman], [2023], INSA Lyon, tous droits réservés

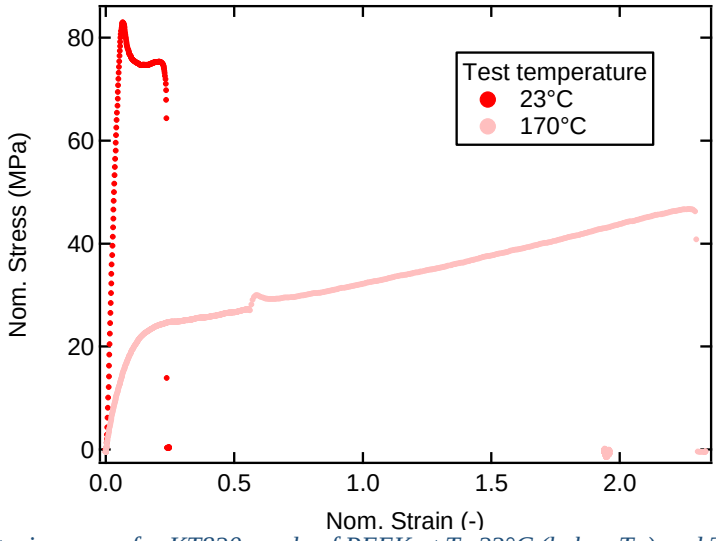


Figure 95. Stress strain curves for KT820 grade of PEEK at T=23°C (below Tg) and T=170°C (above Tg) for $\dot{\varepsilon}$ = 10-3 s-1

d. Influence of strain rate

The strain rate used for tensile tests was varied from 10^{-4} to 10^{-2} s^{-1}. The representative stress-strain curves for KT820 are displayed in Figure 96. A typical evolution of the mechanical behavior is induced by the variation of the strain rate, that is, the yield stress increases as the strain rate increases.

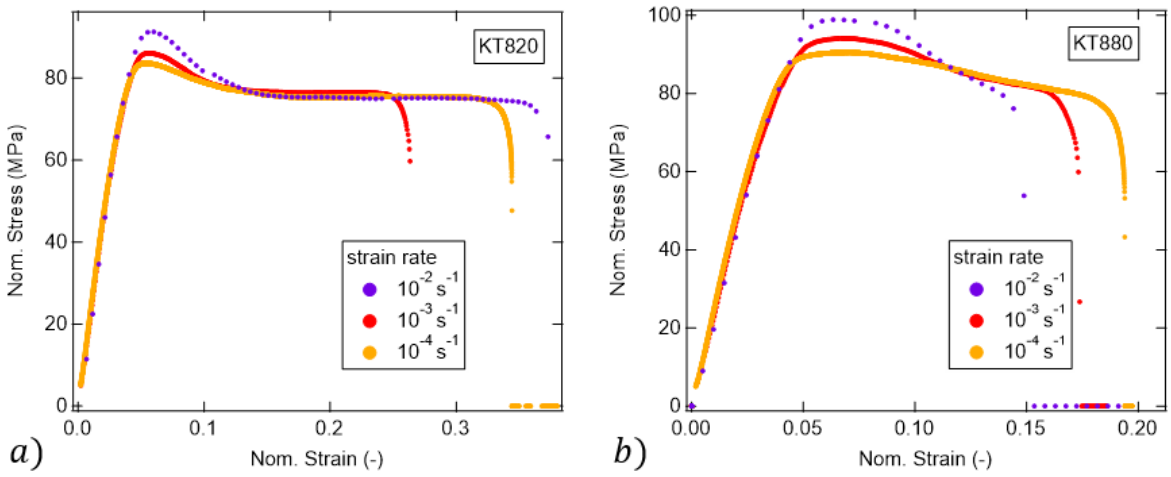


Figure 96.Stress strain curves for KT820 grade of PEEK at T=23° for $\dot{\varepsilon}$ =10-2,10-3and 10-4 s-1 obtained with tensile device X-JICO during Synchrotron in situ experiments for a) KT820 and b) KT880

The relationship between yield stress and strain rate can compared with the study of Pastukhov et al. [58] The strain rate dependence of the yield stress shows a linear relation with the logarithm of the strain rate for both PEEK grades as shown in Figure 97.

Cette thèse est accessible à l'adresse : https://theses.insa-lyon.fr/publication/2023ISAL0006/these.pdf
© [H. Willeman], [2023], INSA Lyon, tous droits réservés

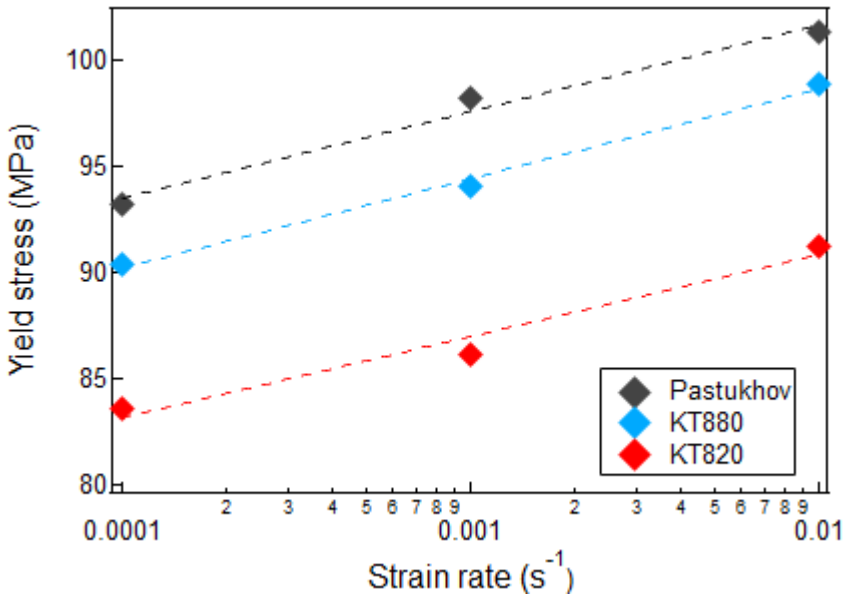


Figure 97. Strain rate dependence of the yield stress. Results from Pastukhov et al values are shown comparison. [58]

3. Strain localization

Using Digital Image Correlation (DIC) technique, the strain field in the whole specimen can be monitored.

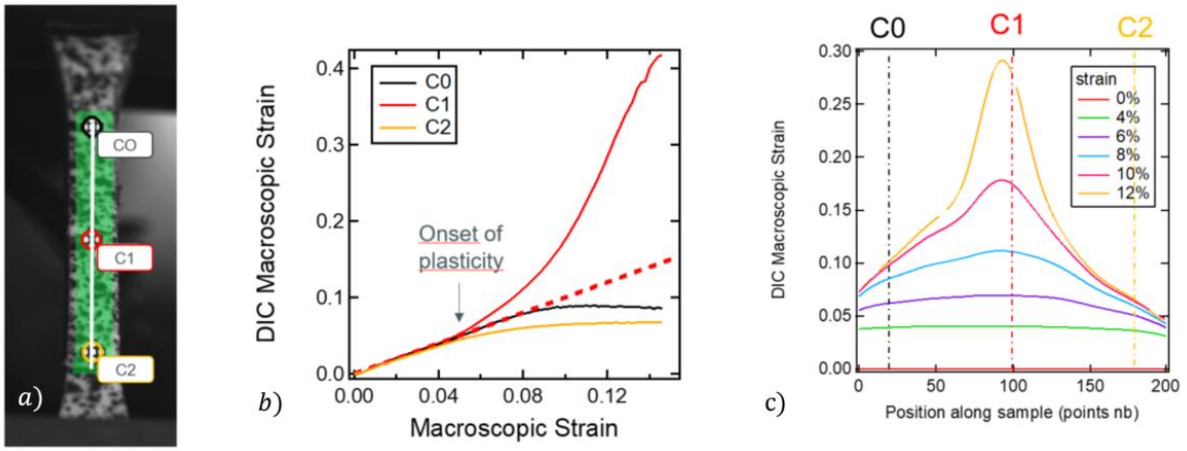


Figure 98. DIC study a) speckled samples and zone of interest b) local strain in three spots C0 C1 C2 with macroscopic strain c) strain along sample for several state of deformation. C0 C1 C2 are placed along the line as reference

With a rich set of data, the local strain can be presented in various ways as showed in Figure 98 for a tensile test on KT820 at room temperature with $\dot{\varepsilon} = 10^{-3}\,s^{-1}$.

Punctual measures of the strain made on three distinct spots noted C0 C1 and C2, represented on Figure 98.a, are displayed on Figure 98.b. In the elastic regime, the deformation is homogeneous within these three spots and equals to the global macroscopic strain. Near yield, the onset of plasticity is marked with a strong localization phenomenon in the C1 zone whereas the tensile strain stabilizes in the other zones. When considering the cross-head displacement as the macroscopic strain, the deformation is expected to be 12%, whereas the strain within C1 zone is almost four times higher.

Cette thèse est accessible à l'adresse : https://theses.insa-lyon.fr/publication/2023ISAL0006/these.pdf
© [H. Willeman], [2023], INSA Lyon, tous droits réservés

Localization within the C1 zone can also be accessed when measuring the strain along the length of the sample, represented by the white line on Figure 98.a. The results are exposed in Figure 98.c. The homogeneity of deformation in the elastic regime, at least until 4%, is confirmed. Then, the maximum strain localization can precisely be defined within the sample, with maximum of deformation happening near C1 spot.

In principle, DIC measurements allow accessing the strain field in different directions. The longitudinal and transverse strains might then be compared and the Poisson's ratio can be retrieved. In Figure 99 is plotted the strain at the beamspot in both directions as a function of the cross-head displacement. However, the precision of the DIC measurements is not high enough to measure precisely the Poisson coefficient ν in the elastic regime.

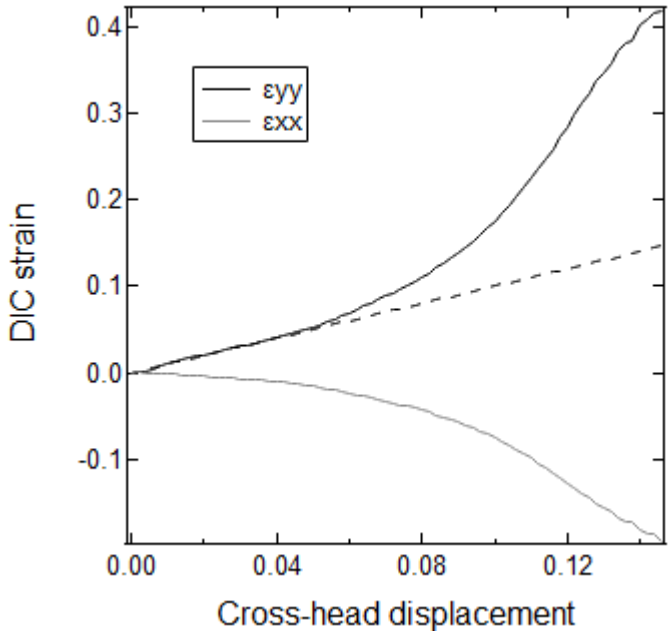


Figure 99. DIC strain measurements at the beamspot in the longitudinal (ε_{yy}) and in the transverse (ε_{xx}) directions as a function of the cross-head displacement

Monitoring the strain localization within the samples will be of key importance for in situ tensile tests SAXS/WAXS experiments as the objective is to compare the macroscopic and the microscopic strain. It is thus necessary to know the real state of deformation of the sample along tensile stretching at the beam position, where SAXS and WAXS data will be acquired.

Cette thèse est accessible à l'adresse : https://theses.insa-lyon.fr/publication/2023ISAL0006/these.pdf
© [H. Willeman], [2023], INSA Lyon, tous droits réservés

IV. Physical ageing

As introduced in Chap I, PEEK is sensitive to physical ageing. Physical ageing is possible due to the presence of a beta relaxation at low temperatures. Thus, some degree of local molecular mobility is possible below T_g. Physical ageing was studied on both grades of PEEK, for amorphous and semi crystalline forms by DSC. The influence of the ageing process on the mechanical properties of the polymer was investigated by DMA and tensile tests.

1. DSC

The thermograms obtained for amorphous samples aged at 135°C for different ageing times for both grades are presented in Figure 100.

On these thermograms, we first observe an endothermic peak around 150°C, corresponding to the glass transition, and an exothermic peak near 180°C corresponding to the cold crystallization. We also notice an endothermic undershoot peak near the glass transition, corresponding to the enthalpy lost by the sample during the ageing step. The values of the overshoot area are reported in Figure 101. This overshoot increases with the ageing time, which confirms that samples have aged. The ageing process does not seem to be complete after 1000 hours as the overshoot area has not stabilized yet.

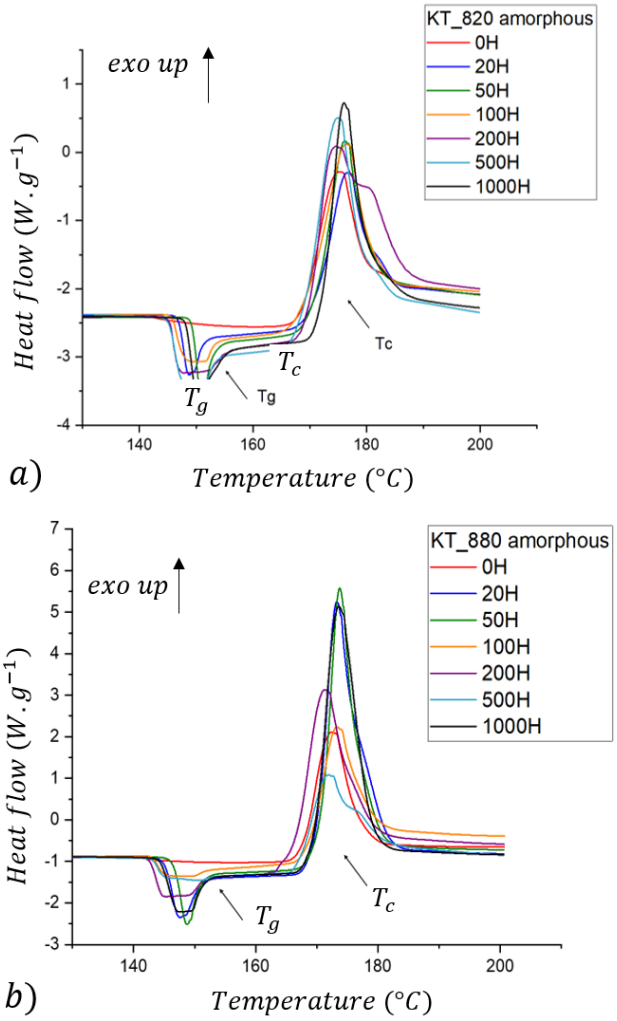


Figure 100. DSC thermograms for amorphous samples aged at 135°C

Cette thèse est accessible à l'adresse : https://theses.insa-lyon.fr/publication/2023ISAL0006/these.pdf
© [H. Willeman], [2023], INSA Lyon, tous droits réservés

The evolution of T_g and the cold crystallization temperature as a function of T_g can also be analyzed. These observations can be explained by the fact that during physical ageing, the amorphous phase gets more rigid and will need more energy to get mobility, and thus going higher in temperature so that they can undergo the glass transition and crystallize. For ageing times between 100 hours and 1000 hours, T_g does not seem to increase anymore. As the overshoot area seems to keep increasing for these ageing times, we can infer that the ageing process is not finished. The fact that T_g doesn't seem to increase anymore could be explained by the following hypothesis: the T_g value is measured on the TA analysis software, and might be influenced by the width of the overshoot peak: for the samples aged between 50 hours and 1000 hours, the peak is getting wider and therefore could make the T_g measurements less accurate.

As regards T_g, the onset of the C_p jump shifts towards higher temperature by about 5°C. The cold crystallization temperature also tends to increase by a few degrees.

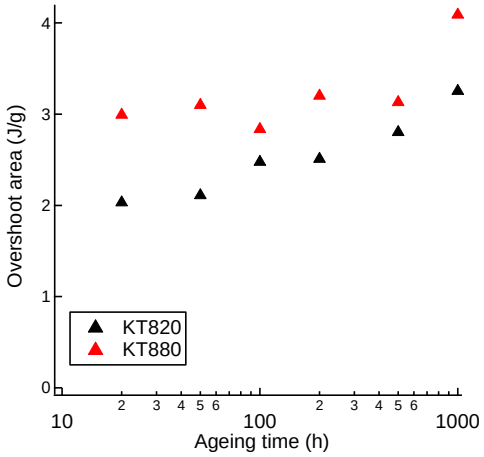


Figure 101. Evolution of the overshoot area for aged amorphous samples

2. DMA

Aged DMA samples were studied in order to observe the impact of physical ageing on the alpha relaxation, which corresponds to the same relaxation process as the glass transition measured in DSC.

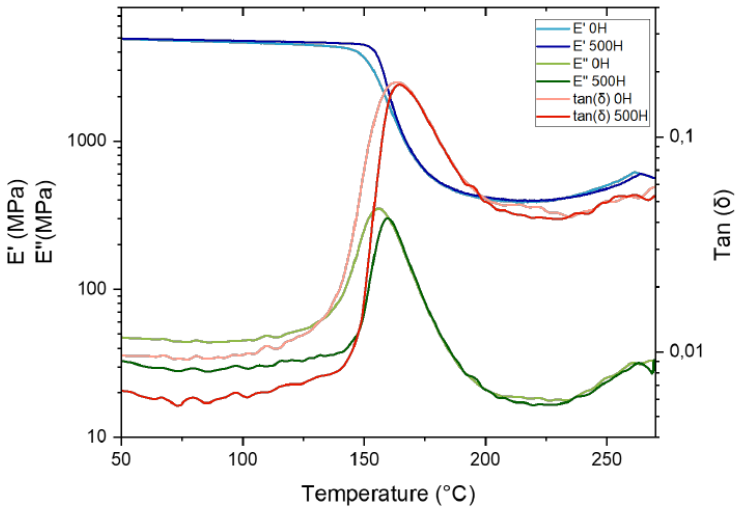


Figure 102. DMA thermograms obtained for initial and aged 500H samples

Cette thèse est accessible à l'adresse : https://theses.insa-lyon.fr/publication/2023ISAL0006/these.pdf
© [H. Willeman], [2023], INSA Lyon, tous droits réservés

A shift of T_α towards higher temperatures is observed (Figure 102), which was measured from the maximum of the E" curve. As T_α corresponds to the same mechanism as T_g (though measured at a different time scale), this phenomenon can be explained once again by the hypothesis of the rigidification of the amorphous phase. By analogy with the analysis of DSC curves, T_g may also be characterized by the temperature at the onset of mobility, which is the point at which the modulus E' starts to decrease. This point is shifted to higher temperature upon ageing (and the decrease also becomes more abrupt). Once the system is above T_g, it has recovered its mobility and can reach equilibrium. The curves of the aged and unaged samples are then perfectly superposed. The E" peak, corresponding to the chains mobility, seems to be narrower for the aged samples. While physical ageing occurs, the distribution of the relaxation times is modified, which directly impacts the width of the E" peak.

3. Tensile tests

The stress-strain curves of aged semi-crystalline PEEK samples are displayed in Figure 103 for several ageing times. Figure 104 indicates the evolution of mechanical characteristics as the Young's modulus, the yield stress and the elongation at break as a function of ageing time. The Young's modulus increases for aged samples, as well as the yield stress, which once again confirms the hypothesis of the rigidification of aged materials. However, the elongation at break decreases considerably, even after only 20 hours of ageing, which implies that the material becomes less ductile quite rapidly. Moreover, it seems that the plastic instability (stress overshoot) increases with the ageing time, which would mean that this phenomenon is driven by the state of rigidity of the amorphous phase modified here with the ageing process.

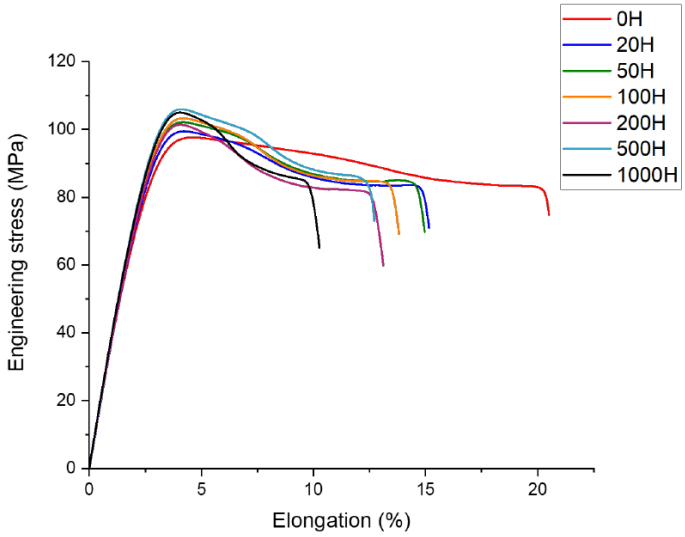


Figure 103. Overlay of stress-train curves obtained for different ageing times

Cette thèse est accessible à l'adresse : https://theses.insa-lyon.fr/publication/2023ISAL0006/these.pdf
© [H. Willeman], [2023], INSA Lyon, tous droits réservés

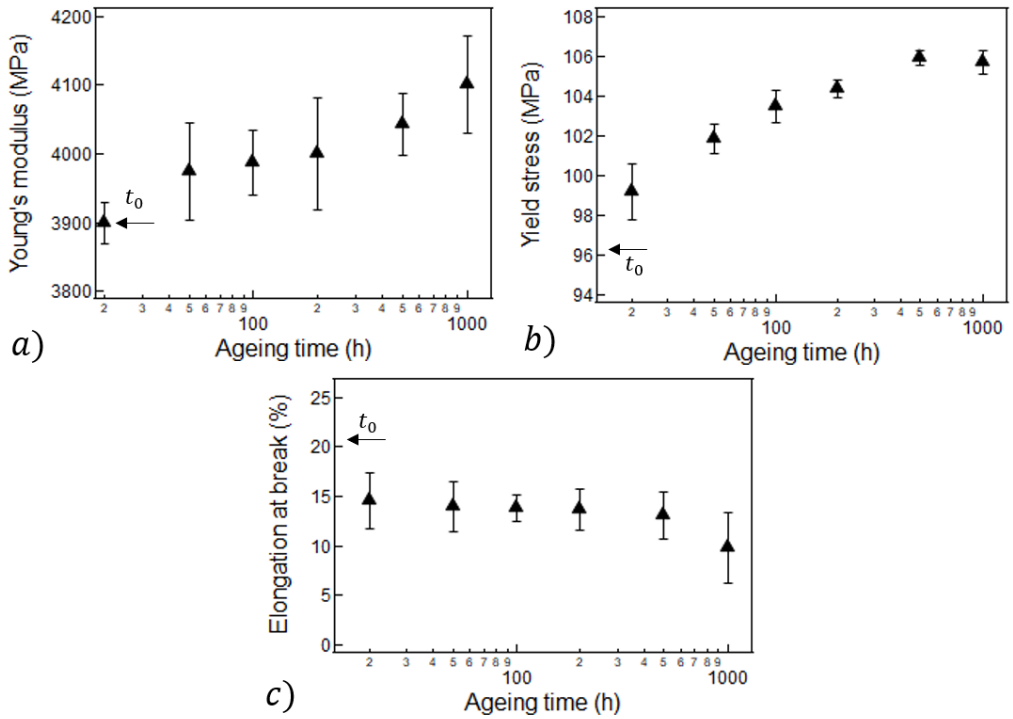


Figure 104. Impact of physical ageing at 135°C on Young's modulus, yield stress and elongation at break

4. A tentative model for the effect of ageing on the thermo-mechanical response of PEEK

We may assume that T_g occurs in the material when the free volume reaches a given value (assuming that the mobility, or more precisely the predominant relaxation time, is related to the free volume in the material). The enthalpy may be related to the density, that is to the free volume, as well. The variation of the enthalpy as a function of temperature has a slope simply given by the heat capacity. The same value of the enthalpy may thus be recovered after ageing just by changing the temperature, as illustrated in Figure 105.

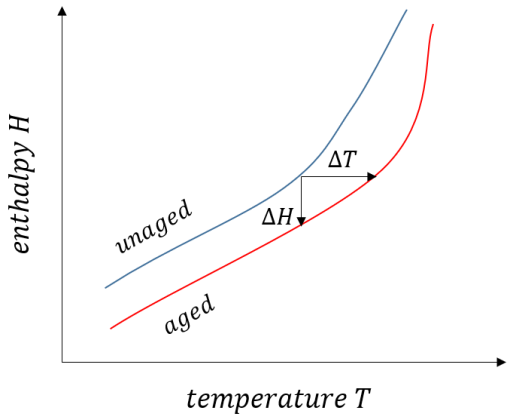


Figure 105. Schematic of the

In the solid (glassy) state, the heat capacity is given by [107] (see equation (17)):

$$C_{p,s} = 0.0891 + 0.003412T\ (J.g^{-1}.K^{-1})$$

Which gives, in the vicinity of T_g (T_g = 150°C = 383 K):

$$C_p(T_g) = 1.53\ J.g^{-1}.K^{-1}$$

Cette thèse est accessible à l'adresse : https://theses.insa-lyon.fr/publication/2023ISAL0006/these.pdf
© [H. Willeman], [2023], INSA Lyon, tous droits réservés

The enthalpy gained by the material during ageing is given by the area of the endothermic undershoot, as shown in Figure 101, which amounts to 2 to 4 J. g^{-1}. This enthalpy change ΔH would thus correspond to a shift in the glass transition temperature ΔT_g given by:

$$\Delta T_g = \frac{\Delta H}{C_p(T_g)} \cong 1.3 \; to \; 2.6°C$$

Which is indeed coherent with the observed order of magnitude of the shift of the T_g onset observed in DSC as well as in DMA.

For the cold crystallization, we may assume that it initiates when the polymer reaches a given degree of mobility, that is at a given distance from T_g, which would explain that cold-crystallization is shifted towards high temperature by about the same amount as T_g.

As regards DMA results, the steeper decrease of the modulus E' (or steeper increase in E", Figure 102) are also qualitatively coherent with the steeper increase of the enthalpy curve towards the equilibrium curve above T_g (this steeper increase actually corresponds to the undershoot peak observed in DSC).

V. Conclusion

In this chapter, the crystallization of PEEK was firstly investigated by DSC. The influence of memory effects and cooling rates was studied. Then, isothermal crystallization was investigated for both grades and Avrami's theory was used to study the type of crystallization, nucleation and 3D growth. In situ microscopy allowed determining the sizes of spherulites depending on the crystallization conditions. In non-isothermal conditions, in identical process conditions, KT880 crystallizes about 10°C higher than KT820. At a given temperature, (on the high temperature side), it crystallizes about five times faster than KT820. Differences in molecular mobility, induced by differences in molecular weight, do not seem to be sufficient to explain such a large difference in behavior between the two grades, as they do not have largely different molecular weights. The differences in crystallization kinetics might therefore be related to the presence of nucleating agents.

The process used for the elaboration of PEEK tensile specimens was then described. Compression molding was chosen as this process leads to more isotropic morphologies. Different molten state temperatures were used. The influence of processing and test conditions on the mechanical properties was then reviewed. The modification of the molten state temperature, the test temperature and the strain rate modify the global behavior of the material.

In the last part, physical ageing was characterized in both KT820 and KT880 PEEK grades quenched into a fully amorphous state and aged at 135°C for various durations. Significant ageing is observed n the form of an undershoot in the heat capacity jump measured by DSC. The gain in enthalpy is qualitatively coherent with the shift if the onset of T_g towards higher temperature. At a given temperature, this corresponds to the rigidification of the amorphous phase. Concomitantly, the cold-crystallization temperature is shifted towards high temperature by an amount of the same order as for T_g. The mechanical properties of semi-crystalline sample are significantly affected by ageing. The Young's modulus and the yield stress increase with ageing, which confirms the rigidification of the material. The increase of strain softening (stress overshoot) with the ageing time also highlights that the plastic instability is mostly driven by the rigidity of the amorphous phase as only the amorphous phase evolves during physical ageing.

Cette thèse est accessible à l'adresse : https://theses.insa-lyon.fr/publication/2023ISAL0006/these.pdf
© [H. Willeman], [2023], INSA Lyon, tous droits réservés

Chapter IV. Study of the microscopic strain: elastic regime

I. Introduction 94
II. Elastic strain regime at the scale of lamellar stacks 97
1. SAXS protocol 97
2. Local strain at the scale of HORI lamellar stacks 99
3. Local strain as a function of orientation 102
4. Orientation distribution of lamellar stacks 108
III. Elastic strain regime at the scale of crystal unit cell, by WAXS 113
1. WAXS protocol 113
2. Local strain at the scale of crystal planes 114
3. Local strain as a function of orientation 116
4. Orientation distribution of crystal planes 119
IV. Discussions: deformation mechanisms in the elastic pre-yield regime 121
1. SAXS experiments 121
2. Models 124
3. Conclusion 126
V. Conclusion 127

Cette thèse est accessible à l'adresse : https://theses.insa-lyon.fr/publication/2023ISAL0006/these.pdf
© [H. Willeman], [2023], INSA Lyon, tous droits réservés

I. Introduction

The In-situ characterization of the mechanical behavior of PEEK was performed in "real time" by combining tensile tests with Small and Wide-Angle X-ray Scattering (SAXS and WAXS) in order to fully describe the microscopic deformation mechanisms behavior and to relate them with the macroscopic behavior described in the previous chapter. Digital image correlation used during tensile tests enables determining the macroscopic state of deformation at the beam position. Results concerning the elastic strain domain are reported in this chapter. The plastic strain domain (beyond the yield) will be discussed in chapter V. The in-situ tensile study is performed in the aim of understanding the microscopic deformation mechanisms leading to plasticity in PEEK. However, X-ray techniques do not allow following the evolution of the morphology at all scales: lamellar stacks and crystalline planes can be analyzed (corresponding to scales of Å to 100 nm typically), while larger scales (1 to 100µm, spherulite structure) are not investigated in this way.

As for macroscopic tensile tests performed in the lab, in-situ experiments were carried out at two temperatures to vary the state (glassy or rubbery) of the amorphous phase. Ideally, tests above T_g should be led at a temperature of about 200°C corresponding to a minimum of the loss factor of the α relaxation, so that the amorphous phase would be the less mechanically dissipative as possible, or, equivalently, the mechanical response would be the less dependent on the drawing rate (see Figure 91). However, the maximum temperature reached in the oven of the tensile device was 170°C. Thus 170°C was the temperature used for tensile tests above T_g. At this temperature, the loss factor $tan\delta$ is of order 0,1. For tests below T_g, in which the amorphous phase is in the glassy state, tests were carried out at room temperature (23°C) wich roughly corresponds to the region in which $tan\delta$ is minimum, in between the β and α relaxations. At 23°C, the loss factor $tan\delta \approx 0.01$. (see Figure 91)

In order to properly identify the different parts of the material and the corresponding scattering, in relation to the tensile strain direction, the following notation have been adopted.

Crystalline unit cells are defined by three distinct, orthogonal directions corresponding to the unit cell vectors ($\vec{a}, \vec{b}, \vec{c}$) (see chap I). Vector $\vec{c}$ along the chain direction is normal to the plane of the crystalline lamellae and is thus parallel to the unit vector $\vec{n}$ normal to the plane of the lamella.

For PEEK, $\vec{b}$ has been identified as the preferential direction of growth [15] as stated in chapter I. Within the spherulites, lamellae grow radially, thus $\vec{b}$ should predominantly be oriented in the radial direction. (see Figure 106). In spherulites, the equator and polar regions are defined with respect to the tensile direction. In Figure 106, the tensile direction is horizontal. Lamellae in equator can be in so-called 'in-plane' or 'on-edge' orientations. The direction of the incident beam then gives a second reference direction, perpendicular to the tensile direction. In Figure 106, it is perpendicular to the plane of the figure, so that the plane of the detector is in the plane of the figure.

Cette thèse est accessible à l'adresse : https://theses.insa-lyon.fr/publication/2023ISAL0006/these.pdf
© [H. Willeman], [2023], INSA Lyon, tous droits réservés

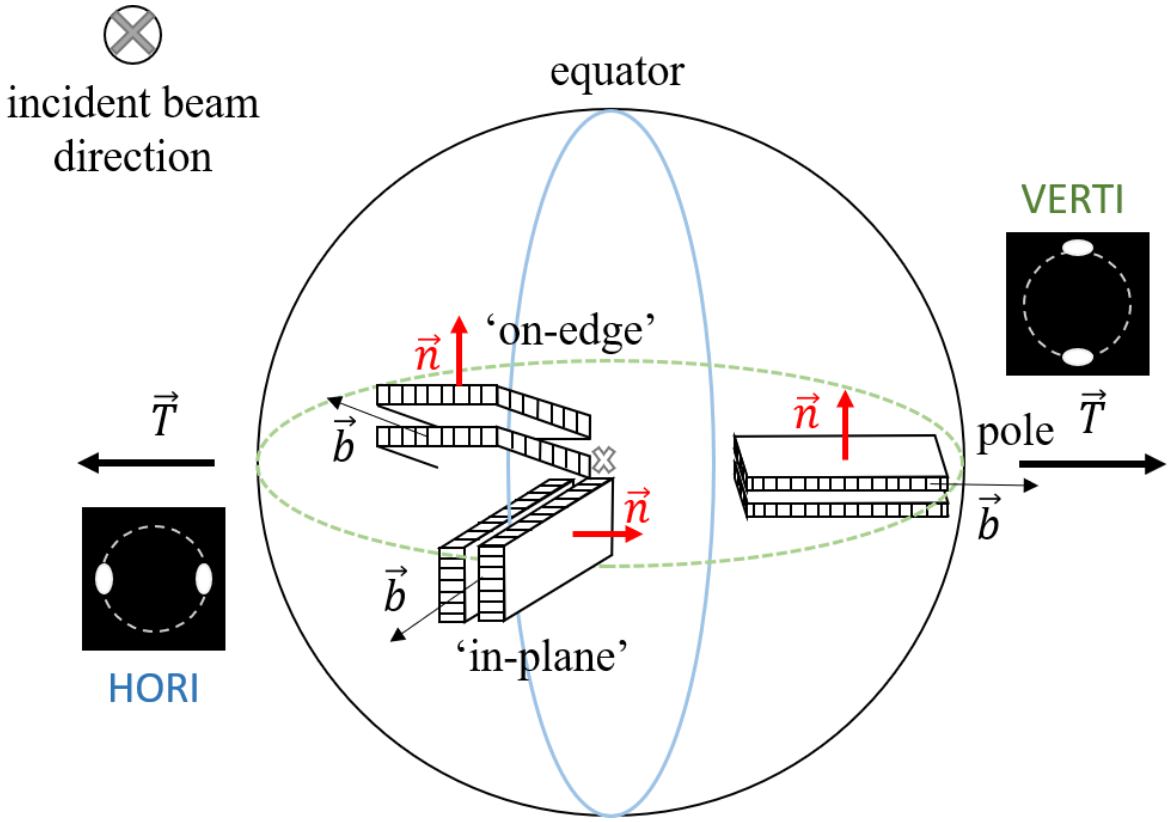


Figure 106. Lamellae distribution in a spherulite and corresponding 2D SAXS patterns. The incident beam direction is perpendicular to the figure so that the detector plane is the plane of the figure. $\vec{T}$ denotes the tensile direction

In SAXS, lamellar stacks scatter along the direction of their normal. HORI lamellae, which have horizontal normal $\vec{n}$, only scatter horizontally as represented in Figure 107. These lamellae are necessarily located in the equator of spherulites ('in-plane' lamellae). *The deformation of these lamellae can thus be considered as a probe of the tensile deformation in the equator of the spherulites*. VERTI lamellar stacks (lamellae which scatter in the VERTI direction of the SAXS pattern) have vertical normal $\vec{n}$, and can be located either in the equator ('on-edge' lamellae) or in the polar region.

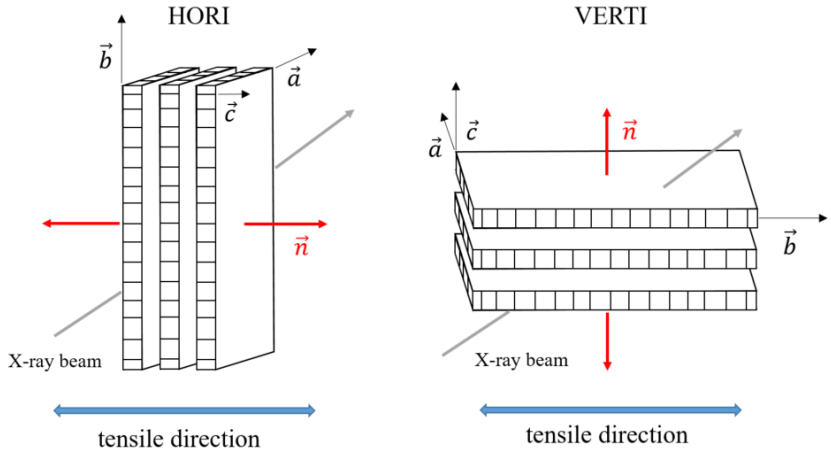


Figure 107. Representation of HORI and VERTI lamellar stacks

Cette thèse est accessible à l'adresse : https://theses.insa-lyon.fr/publication/2023ISAL0006/these.pdf
© [H. Willeman], [2023], INSA Lyon, tous droits réservés

In this chapter, the focus is made on the elastic (pre-yield) strain domain of the stress-strain curves. The pre-yield domain is presented in Figure 108 for both test temperatures. For tensile tests at room temperature, the yield point occurs:

- for KT820 at a stress σ_y=85±2 MPa and strain ε_y=6±0.2%
- for KT880, at a stress σ_y=92±5 MPa and strain ε_y=5.6±0.1%

For experiments at 170°C:

- the yield stress is σ_y=23±1 MPa and ε_y=18±1% for KT820.
- the yield stress is σ_y=32±2 MPa and ε_y=19±1% for KT880.

For the rest of this chapter, only KT820 experiments will be presented as no significant qualitative differences in their tensile behavior have been observed between the two grades.

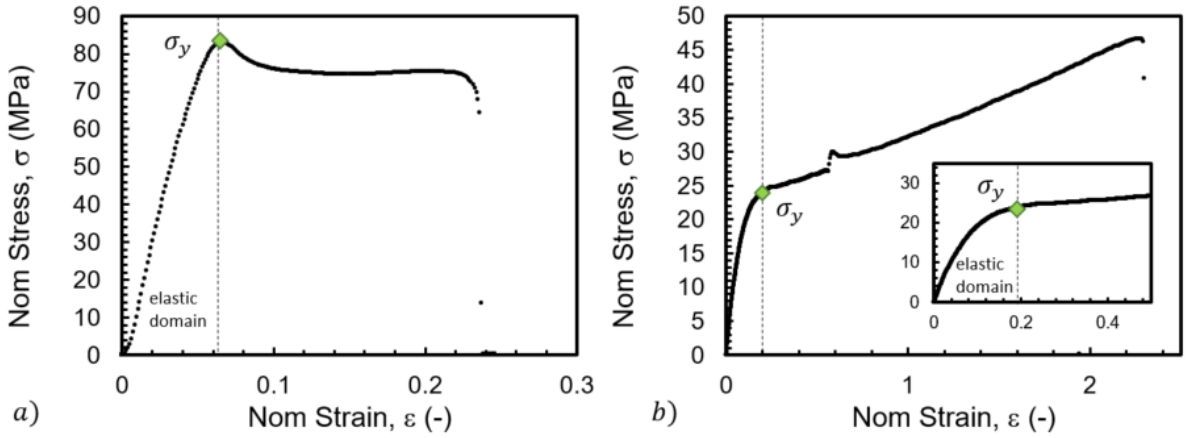


Figure 108. Strain-stress curves of in situ tensile tests of KT820 at a constant nominal strain rate $\dot{\varepsilon}=10^{-3}\ s^{-1}$ a) at room temperature and b) at T=170°C. In b), The bump on the curve near 60% strain corresponds to a change in draw rate from $\dot{\varepsilon}=10^{-3}\ s^{-1}$ to $\dot{\varepsilon}=5.10^{-3}\ s^{-1}$.

To investigate the yielding process and the reversibility of deformation in the elastic regime, more complex loading was applied to the specimens (Figure 109):

- The first step consists in tensile loading up to 300N (blue point in Figure 109, 70MPa for a section of 4.3mm²), in the pre-yield regime, then unloading back to 0N which enables verifying the reversibility of the deformation in the elastic domain,
- The second tensile loading is applied up to post yield $\varepsilon = 8.3\pm1\%$ (depending on the test) before unloading back to 0N which allows observing residual deformation in the plastic regime,
- The final step is the tensile loading up to failure.

The stress-strain curve corresponding to these experiments is presented in Figure 109.

Cette thèse est accessible à l'adresse : https://theses.insa-lyon.fr/publication/2023ISAL0006/these.pdf
© [H. Willeman], [2023], INSA Lyon, tous droits réservés

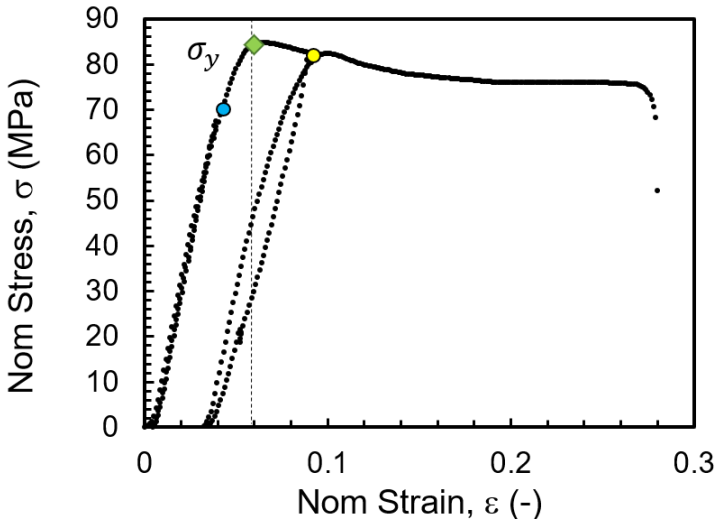


Figure 109. Stress-strain curve of complex tensile loading experiments used to study yielding process and reversibility of strain and residual deformation. A first loading-unloading cycle is performed up to the blue point (below the yield point represented by the green diamond), then a second one to the yellow point then the sample is stretched up to failure

In the first part of this chapter, the deformation mechanisms are first studied at the scale of lamellar stacks via the analysis of SAXS. Two aspects of deformation are discussed, which give access to a description of the local structure under stretching: the variation of the long period of the lamellar stacks, and the distribution of lamella orientations. In the second part, the deformation mechanisms are studied at the scale of the crystalline unit cell by WAXS. The deformation of the unit cell under stress and the distribution of orientation of crystalline lattice planes are discussed. Finally, some hypotheses on deformation mechanisms unifying both SAXS and WAXS results are presented.

II. Elastic strain regime at the scale of lamellar stacks

1. SAXS protocol

Uniaxial tensile tests are performed as described in chapter II at a constant nominal strain rate $\dot{\varepsilon} = 10^{-3}$ s^{-1} for T = 23°C and T = 170°C. During tensile tests, a 2D SAXS pattern is recorded every 0.2% of deformation with a deformation increment 0.1% during each acquisition. SAXS patterns are collected and analyzed as described in chapter II. Each lamella stack scatters along its normal $\vec{n}$. As the material is isotropic in its initial state, scattering is isotropic and the pattern has the shape of a perfectly circular ring. The maximum of intensity as a function of the scattering vector q allows determining the long period.

The reference direction of the problem is the tensile direction (denoted TD in the rest of the manuscript, as in Figure 106). The overall macroscopic deformation is presumed to be uniaxial around this direction. The orientation of a lamellae stack is completely described by the orientation of its normal $\vec{n}$ which is described by the azimuthal angle ψ only, due to the overall cylindrical (uniaxial) symmetry of the deformed sample, as schematized in Figure 110.

Cette thèse est accessible à l'adresse : https://theses.insa-lyon.fr/publication/2023ISAL0006/these.pdf
© [H. Willeman], [2023], INSA Lyon, tous droits réservés

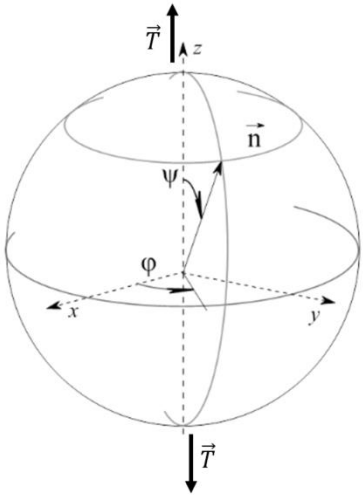


Figure 110. Schematic description of lamellae orientation with normal $\vec{n}$ [113] Here, the tensile direction is vertical.

The horizontal direction on 2D SAXS patterns is parallel to the tensile direction (TD) as schematized in Figure 111.b. As already specified, scattering in the horizontal direction corresponds to the lamellae with the normal parallel to the tensile direction, which according to the previous notation, belong to the family of "in-plane" equatorial lamellae. Scattering in vertical direction corresponds to lamellae with $\vec{n}$ vertical (see Figure 111).

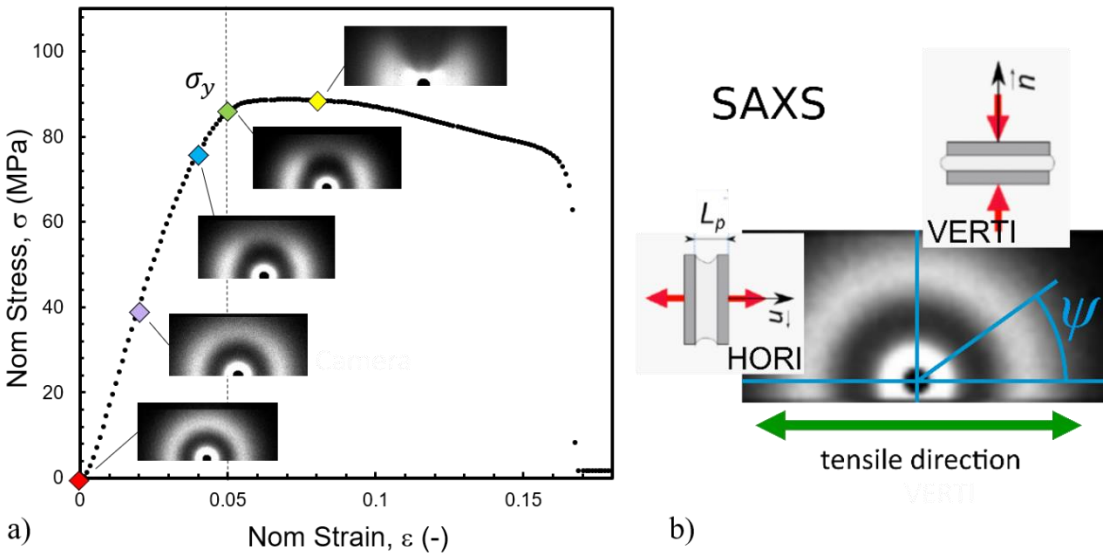


Figure 111.a) Evolution of SAXS patterns with the macroscopic (nominal) strain during tensile test at room temperature b) Analysis of SAXS pattern, definition of azimuthal angle ψ, scattering directions and the corresponding orientation of lamellar stacks. In b) the tensile or compressive strain in each family of lamellar stacks is indicated by the red arrows.

During tensile tests, the scattering ring becomes an ellipse with a shorter horizontal axis (HORI,along TD) and a longer vertical axis (VERTI, perpendicular to TD). This means that, during tensile tests, the long period contracts for lamellar stacks with vertical $\vec{n}$ and it expands for lamellae with $\vec{n}$ along TD, as depicted in Figure 112. Also, the intensity becomes modulated along the azimuthal angle ψ, with progressively more intensity in the HORI direction.

Cette thèse est accessible à l'adresse : https://theses.insa-lyon.fr/publication/2023ISAL0006/these.pdf
© [H. Willeman], [2023], INSA Lyon, tous droits réservés

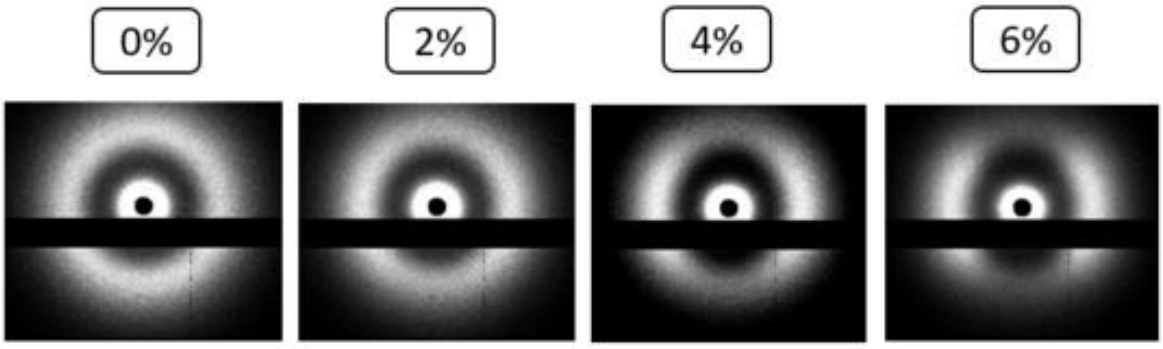


Figure 112. Evolution of SAXS patterns in the pre-yield regime up to ε=6%

As described in Chapter II, the local strain in lamellar stacks can be measured via the strain-induced shift of the SAXS correlation peak. The evolution of the position of q_{max} related to the evolution of the long period allows measuring the local strain at the scale of the lamellar stacks, defined by:

$$\varepsilon_{micro(lamellar\ stacks)} = \frac{\Delta L_p}{L_p} \qquad (37)$$

2. Local strain in HORI lamellar stacks

The measurement of the strain ($\varepsilon_{local} = \frac{\Delta L_p}{L_p}$) within horizontal lamellar stacks is particularly interesting as these stacks are only submitted to tensile stress and specifically probe the equator of spherulites (see Figure 106). The microscopic strain within these lamellar stacks can then be compared to the macroscopic strain. The behavior of these lamellar stacks will thus be firstly presented before analyzing the strain as a function of orientation (i.e. of the azimuthal angle ψ).

First, on the SAXS patterns displayed in Figure 112, the position of the peak maximum in the horizontal direction gradually shifts to lover q values. This is hardly visible on the patterns themselves but this is clearly illustrated in Figure 113. This indeed corresponds to an increase of the long period of the corresponding lamellar stacks which are submitted to tensile stress only.

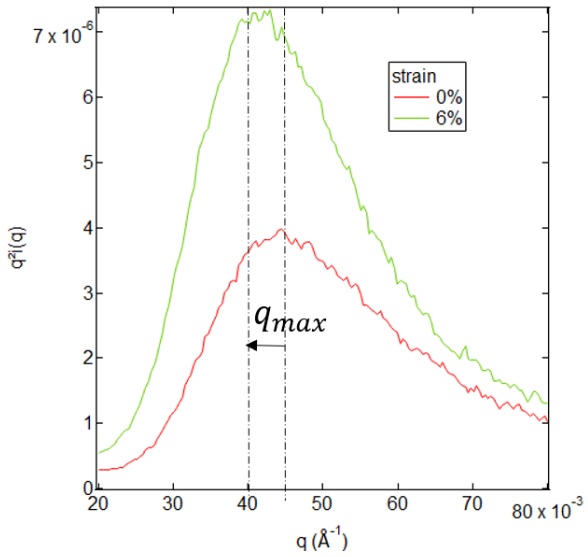


Figure 113. Intensity of SAXS pattern in the HORI direction for strain ε=0 and 6%, qmax shifts towards low q values with deformation

Cette thèse est accessible à l'adresse : https://theses.insa-lyon.fr/publication/2023ISAL0006/these.pdf
© [H. Willeman], [2023], INSA Lyon, tous droits réservés

The measured local strain in HORI lamellar stacks is plotted as a function of the nominal macroscopic strain (defined from the cross-head displacement) in Figure 114 for both test temperatures, both below and above T_g. As mentioned in Chapter II, the actual local macroscopic strain at the beam position was measured using DIC only for tests at room temperature. In Figure 114.a, in the elastic regime up to 5%, the local macroscopic strain (full black curve) measured by DIC is equal to the macroscopic strain i.e. the cross-head displacement (dotted line). When stretched at 170°C, the amorphous phase is in the rubbery state and the Young's modulus of the material is much lower than at room temperature. The sample is less prone to deformation localization phenomena. Thus, the local macroscopic strain at 170°C was supposed to be equal to the nominal strain (defined from the cross-head displacement).

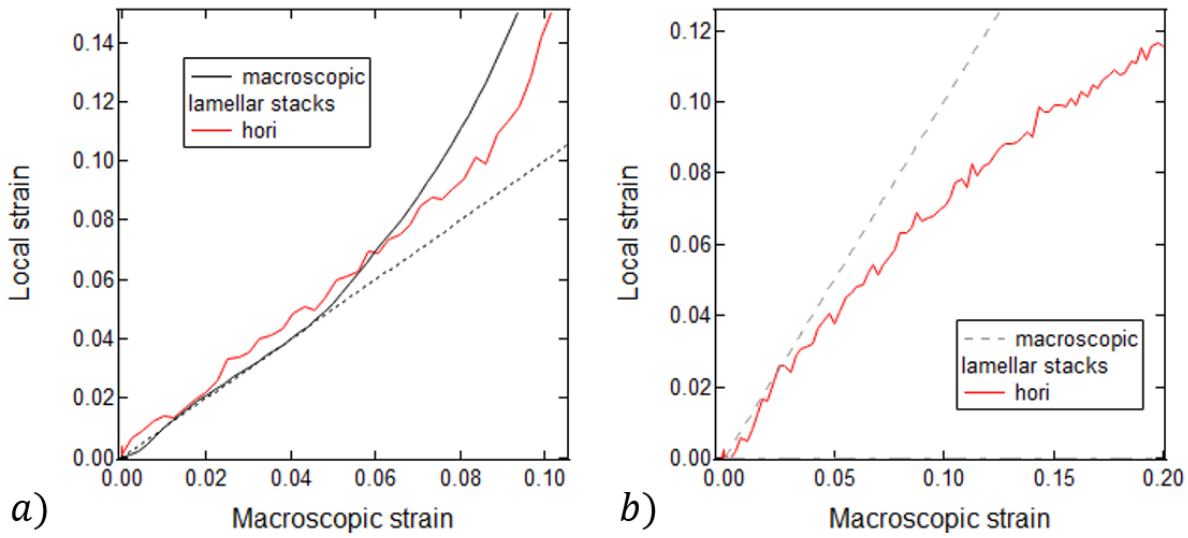


Figure 114. Local strain at the microscopic scale (HORI lamellar stacks) and corresponding local macroscopic strain measured by DIC (full black curve) as a function of the nominal macroscopic strain for tensile tests at a) 23°C and b) 170°C

At room temperature (Figure 114.a), up to about 6% which corresponds to the end of the elastic regime, the deformation at the scale of lamellar stacks is nearly equal to the macroscopic strain. From 6% the localization of the macroscopic deformation in the studied zone starts (black curve). A change of slope is also observed for the local strain in HORI lamellar stacks (red curve), which means that these lamellae, located in the equator of the spherulite, take part in the macroscopic localization process.

Conversely, above T_g, in Figure 114.b, the local microscopic strain in HORI lamellar stacks is lower that the macroscopic strain in nearly the whole elastic regime.

Reversibility of strain in the pre-yield regime

The reversibility of the macroscopic and microscopic strains in the elastic has been investigated during tensile tests with complex loading described in the introduction of this chapter. The measurements of the microscopic strain with the time and the nominal strain in the first loading-unloading cycle in the pre-yield regime are plotted in Figure 115 (room temperature) and Figure 116 (170°C) alongside the corresponding stress strain curves.

At room temperature, during the first tensile loading step up to 300N, the local macroscopic and microscopic strains (HORI stacks) are equal to the imposed macroscopic strain, as stated in the previous part. The following unloading step back to zero force is performed at the same rate $\dot{\varepsilon} = -10^{-3}\ s^{-1}$. Once back at zero force, the sample is back to the initial state, no residual deformation is observed. Below T_g,

Cette thèse est accessible à l'adresse : https://theses.insa-lyon.fr/publication/2023ISAL0006/these.pdf
© [H. Willeman], [2023], INSA Lyon, tous droits réservés

when stretched up to 300N corresponding in this case to 70 MPa ($\approx 0.85\sigma_y$), the strain in HORI lamellar stacks as well as the macroscopic strain are reversible.

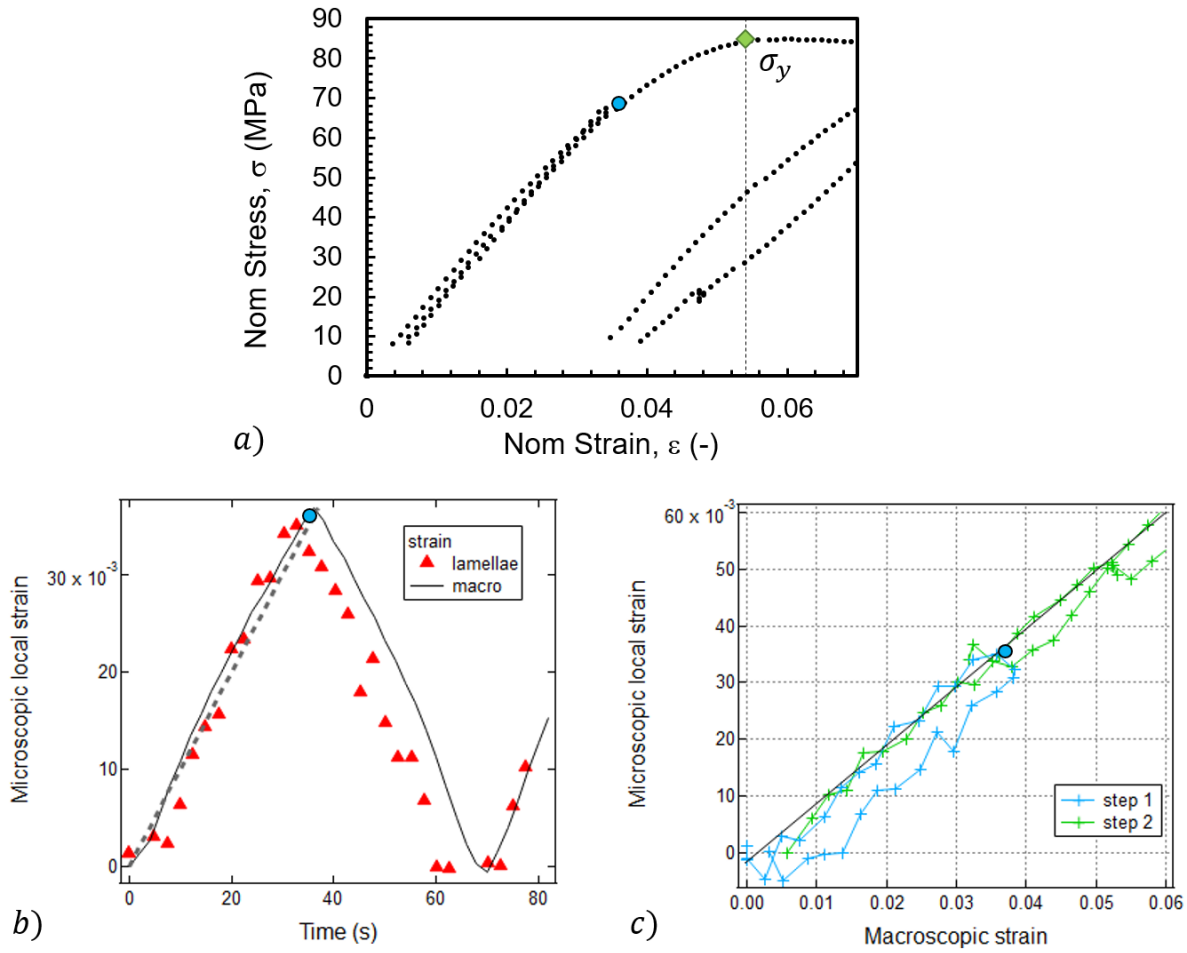


Figure 115. a) Stress-strain curve for the first loading in the preyield regime, up to the blue point and back to zero force, b) corresponding measure of the local macroscopic strain and local microscopic strain, in horizontal lamellar stacks obtained by SAXS. The dashed line represents the cross-head displacement as a function of time and c) local microscopic strain as a function of the nominal strain

At 170°C, as stated in the previous part, the deformation of lamellar stacks in the HORI direction is slightly lower than the macroscopic nominal strain. At the macroscopic scale, it seems that the deformation is not fully reversible, a residual deformation of 2% is observed in the first cycle back at force zero (Figure 116.a). However, the reversibility of the deformation in the elastic regime at the scale of lamellar stacks is observed for experiments at 170°C where the polymer is stretched up to 90N and then unloaded back to zero force, as represented in Figure 116.b.

Cette thèse est accessible à l'adresse : https://theses.insa-lyon.fr/publication/2023ISAL0006/these.pdf
© [H. Willeman], [2023], INSA Lyon, tous droits réservés

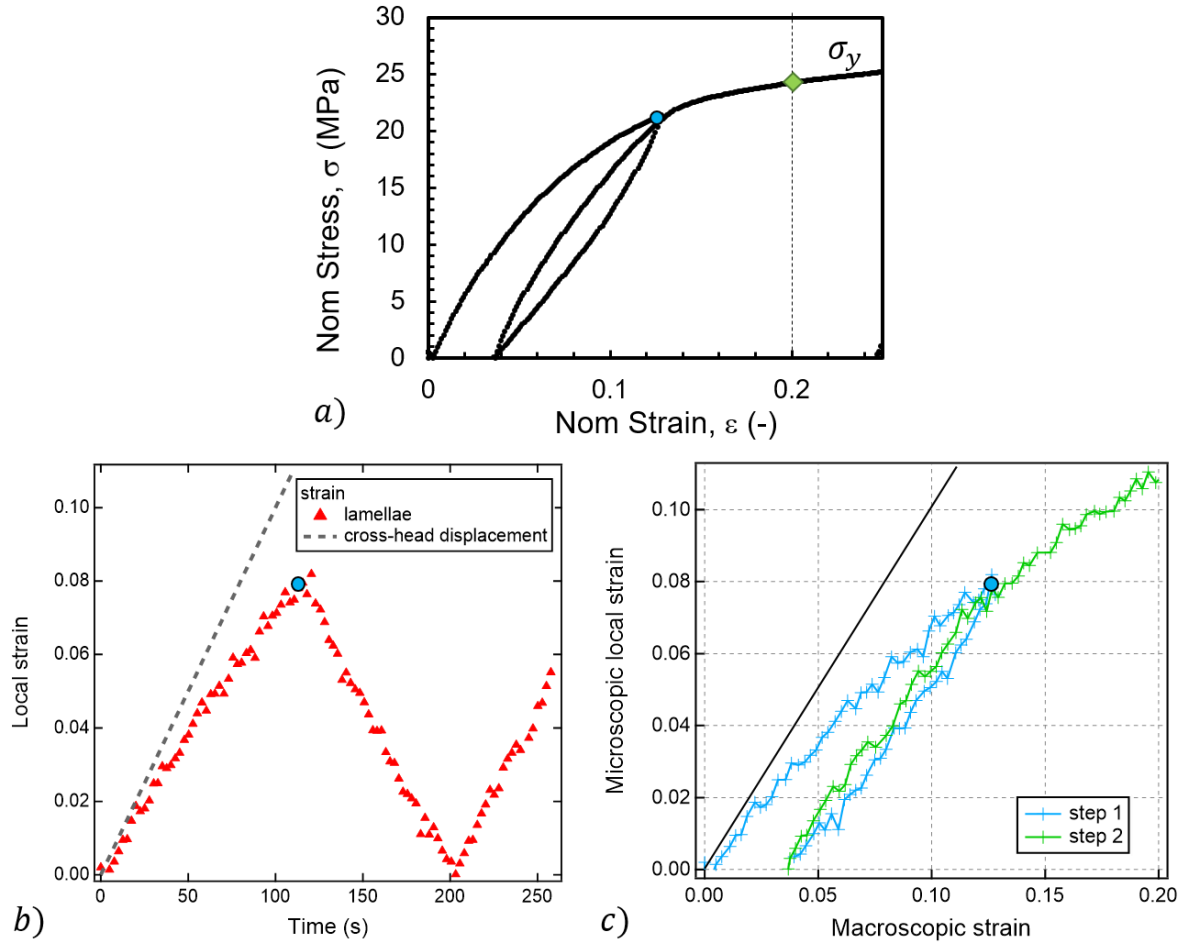


Figure 116. a) Stress-strain curve for the first cycle of complex tensile loading in the pre-yield regime at 170°C, up to the blue point and back to force 0, b) corresponding measurement of local microscopic horizontal lamellar stacks strain obtained by SAXS, dashed line representing the cross-head displacement and c) local microscopic strain as a function of the cross-head displacement

3. Local strain as a function of orientation

As noted before, the SAXS patterns gradually evolve from a circular, isotropic pattern into an ellipse with long axis in the VERTI direction. In the previous section, the local strain was only analyzed for HORI lamellae (ψ = 0°) corresponding to stacks with their normal along the tensile direction. The long period L_p has been measured for all azimuthal angles of the 2D SAXS patterns, for various macroscopic strain values ε in the pre-yield regime. The analysis has been described in details in chapter II. The following Figure 117 shows the results of the global analysis of SAXS patterns. The microscopic strain $\frac{\Delta L_p}{L_p}$ is plotted as a function of the scattering vector q and of the azimuthal angle ψ.

Cette thèse est accessible à l'adresse : https://theses.insa-lyon.fr/publication/2023ISAL0006/these.pdf
© [H. Willeman], [2023], INSA Lyon, tous droits réservés

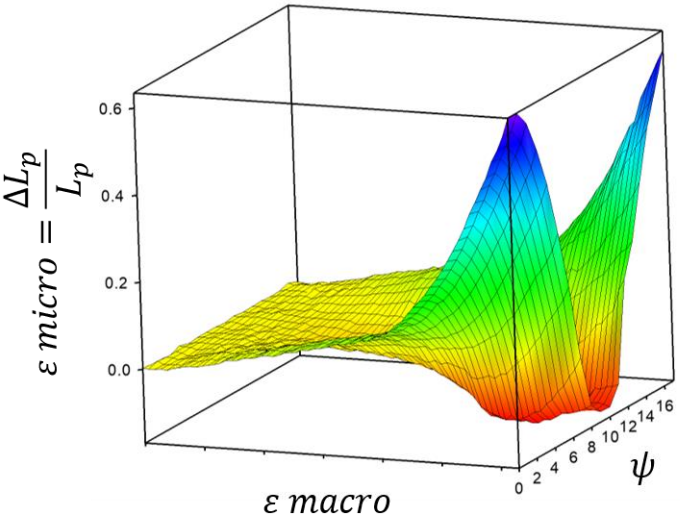


Figure 117. 3D representation of the local microscopic strain $\varepsilon_{micro} = \frac{\Delta L_p}{L_p}$ as a function of the macroscopic (nominal) strain and of the azimuth sector at room temperature

a. Tensile tests at T = 23°C, $T < T_g$

Let us now generalize the previous analysis for the full distribution of lamella orientation as a function of azimuthal angle ψ. The values of the microscopic deformation ε_{micro} are presented in Figure 118 as a function of the azimuth sector for ε_{macro}=1,3 and 5%. The isotropy of the initial sample is verified in the initial state as $\Delta L_p/L_p$ is nearly constant within experimental uncertainties.

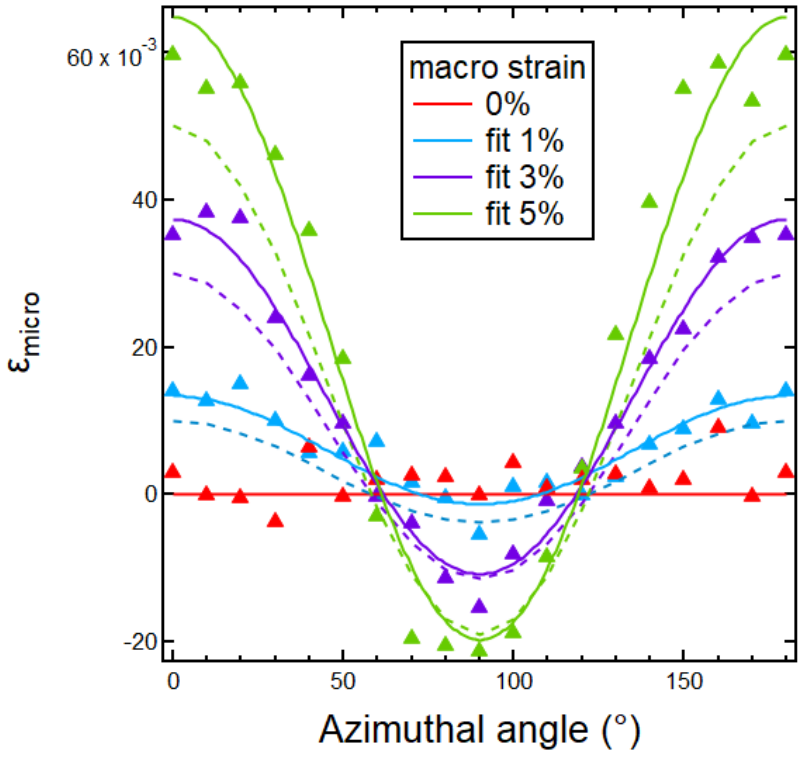


Figure 118. The local strain at the scale of lamellar stacks $\varepsilon_{micro} = \Delta Lp/Lp$ as a function of the azimuth angle ψ for different values of the macroscopic strain for tensile test at room temperature. Symbols are experimental points, curves are fits using eq (50) and dashed lines are the expected behavior for $\nu\ micro = \nu\ macro = 0.38$. Experimental points at $\psi = 0$ and $\psi = 180°$ correspond to the same data points, due to the symmetry of the pattern.

Cette thèse est accessible à l'adresse : https://theses.insa-lyon.fr/publication/2023ISAL0006/these.pdf
© [H. Willeman], [2023], INSA Lyon, tous droits réservés

To analyze these curves, let us consider what would be the predicted behavior of a homogeneous material. In a homogeneous isotropic material uniaxially stretched with the tensile direction in the direction of axis Oz, the deviatoric stress tensor is:

$$\bar{\bar{\sigma}} = \begin{bmatrix} 0 & 0 & 0 \\ 0 & 0 & 0 \\ 0 & 0 & \sigma_{zz} \end{bmatrix} \quad (38)$$

If the material is uniformly deformed, the deformation tensor u_{ij}(i,j = x,y,z) is related to the stress tensor σ_{ij} by the general constitutive law of elasticity: [114]

$$u_{ij} = \frac{1}{E}\left[(1+\nu)\sigma_{ij} - \nu\sigma_{kk}\delta_{ij}\right] \quad (39)$$

where E is the Young's modulus and ν the Poisson's ratio of the material. Implicit summation over repeated indices (Einstein's convention) has been used in equation (39). This gives here:

$$\begin{cases} u_{xx} = u_{yy} = -\dfrac{\nu}{E}\sigma_{zz} \\ u_{zz} = \dfrac{\sigma_{zz}}{E}\sigma_{zz} \end{cases} \quad (40)$$

Considering a small vector $\overrightarrow{dr}$ in the material of length dl with an azimuthal angle ψ with respect to the tensile direction (axis Oz), its components are:

$$\begin{cases} dx = dl\ sin\psi\ cos\varphi \\ dy = dl\ sin\psi\ cos\varphi \\ dz = dl\ cos\varphi \end{cases} \quad (41)$$

$\overrightarrow{dr}$ will be distorted into $\overrightarrow{dr'}$ of components dx'_i and length dl' (see Figure 119).

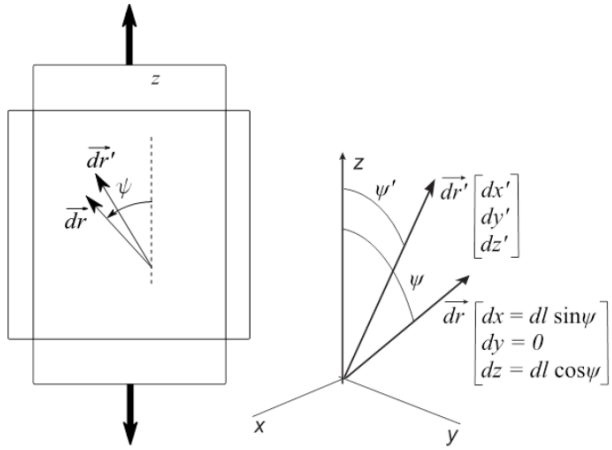


Figure 119. Vector (the normal to a lamellae stack) before and after affine uniaxial deformation

dl' is given by the general relation: [114]

$$dl'^2 = dl^2 + 2u_{ij}dx_i dx_j \quad (42)$$

Substituting equations (40) and (41) into equation (42), it gives:

$$dl'^2 = dl^2\left[1 - \nu\frac{2\sigma zz}{E}sin^2\psi + 2\frac{\sigma zz}{E}cos^2\psi\right] \quad (43)$$

Cette thèse est accessible à l'adresse : https://theses.insa-lyon.fr/publication/2023ISAL0006/these.pdf
© [H. Willeman], [2023], INSA Lyon, tous droits réservés

Which may be rewritten (writing $\sigma = \sigma_{zz}$):

$$dl'^2 = dl^2 \left[1 + \frac{2}{3}\frac{\sigma}{E}(1 - 2\nu) + \frac{4}{3}\frac{\sigma}{E}(1 + \nu)\left(\frac{3cos^2\psi - 1}{2}\right)\right] \quad (44)$$

And for small distortions:

$$dl' = dl \left[1 + \frac{1}{3}\frac{\sigma}{E}(1 - 2\nu) + \frac{2}{3}\frac{\sigma}{E}(1 + \nu)P_2(cos\,\psi)\right] \quad (45)$$

where $P_2(\cos\psi)$ is the second order Legendre polynomial:

$$P_2(cos\,\psi) = \frac{3cos^2\psi - 1}{2} \quad (46)$$

Thus, in a uniaxially stretched homogeneous material, by identifying the relative variation $\Delta L_p/L_p$ to the relative length variation $(dl' - dl)/dl$, the microscopic strain i.e. the variation of the long period of lamellar stacks should then be expressed as a function of the azimuth angle ψ with the following equation (47):

$$\frac{\Delta L_p}{L_p^0} = \frac{\varepsilon}{3}\left[(1 - 2\nu) + 2(1 + \nu)P_2(cos\psi)\right] \quad (47)$$

Where $\varepsilon = \frac{\sigma}{E}$ is the tensile homogeneous strain. For an incompressible material (ν = 0.5), the following relation is recovered as expected:

$$\frac{\Delta L_p}{L_p} = \varepsilon P_2(cos\,\psi) \quad (48)$$

The quantity $\Delta L_p/L_p$, as well as the fit of the experimental data with equation (47) are plotted as a function of the azimuth angle ψ in Figure 118.

Experimental data are relatively well fitted with eq. (47) in the pre-yield regime. The outputs of the fitting process are the local strain ε_{micro} at the scale of lamellar stacks and an apparent Poisson's coefficient, ν_{micro}. One should be careful with the interpretation of the apparent microscopic Poisson's coefficient. More precisely, ν_{micro} corresponds to the ratio of the tensile strain in lamellar stacks in contraction (which scatter in the VERTI direction) and in those in tension (which scatter in the HORI direction). ε_{micro} measured in the HORI and VERTI azimuth directions ($\psi = 0$ and $\psi = 90°$) are shown in Figure 120.a as a function of the macroscopic strain in the pre-yield regime. The ratio $\nu_{micro} = \varepsilon_{micro\,(0°)}/\varepsilon_{micro\,(90°)}$ is shown in Figure 120.b. Examining Figure 113, one may estimate that the position of the peak is determined with a uncertainty of $\pm\delta \approx 10^{-3}$ Å^{-1}. This corresponds to a relative uncertainty in the determination of the local strain.

$$\frac{\Delta q_{max}}{q_{max}} = \frac{\Delta L_p}{L_p} \cong \pm\frac{\delta}{q_{max}} \approx \frac{10^{-3}}{4.10^2} \approx 2.5\%$$

It follows that below about 2.5%, the determination of ν_{micro} should not be considered reliable. This value is indicated by the dashed vertical line in Figure 120.b. The ratio of microscopic strains in VERTI (compressive strain) and HORI (tensile strain) directions thus seems to be of order 0.3.

Cette thèse est accessible à l'adresse : https://theses.insa-lyon.fr/publication/2023ISAL0006/these.pdf
© [H. Willeman], [2023], INSA Lyon, tous droits réservés

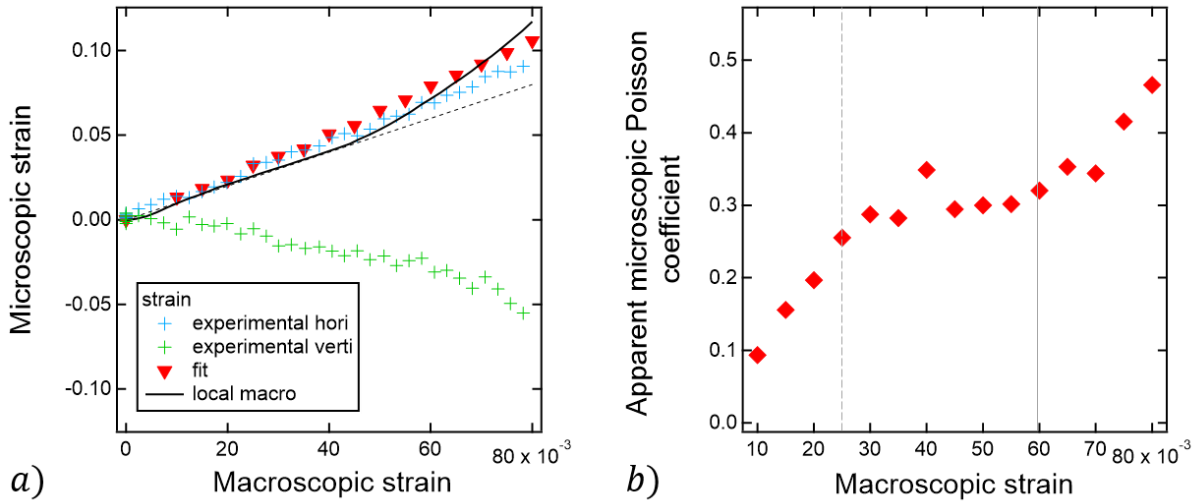


Figure 120. a) Microscopic strains in HORI and VERTI directions and b) Evolution of ν_{micro} with macroscopic strain. The change of slope at ε≈6% (vertical line) marks the onset of plasticity. Value below 2.5% (dashed vertical line) are not reliable.

As previously mentioned, the microscopic strain in the HORI azimuth direction is nearly equal to the macroscopic strain. Since lamellar stacks which scatter in the HORI direction are necessarily located within the equator of spherulites, this indicates that the equator of spherulites deform equally as the average spherulite. The overall strain within spherulites, as probed by lamellar stacks which scatter in the VERTI direction, is equal to the macroscopic strain. The onset of plasticity can be observed on both outputs of the fit. Along with macroscopic strain localization, the microscopic strain follows the same slope and concentrates in the HORI direction too. The marked change of slope in the microscopic Poisson's coefficient at about ε_{macro}=6% is another indicator of a change in the material behavior, from homogenous elastic regime to plastic deformation.

b. Tensile tests at T = 170°C, $T > T_g$

The strain at the scale of lamellar stacks as a function of orientation in the elastic regime has also been investigated for tensile tests at a temperature above T_g and analyzed using equation (47) which describes the expected behavior of a homogeneous material. The results and the fitting process of the microscopic strain ε_{micro} as a function of azimuthal angle for deformation up to yield at ε_{macro}=20% are plotted in Figure 121.

Cette thèse est accessible à l'adresse : https://theses.insa-lyon.fr/publication/2023ISAL0006/these.pdf
© [H. Willeman], [2023], INSA Lyon, tous droits réservés

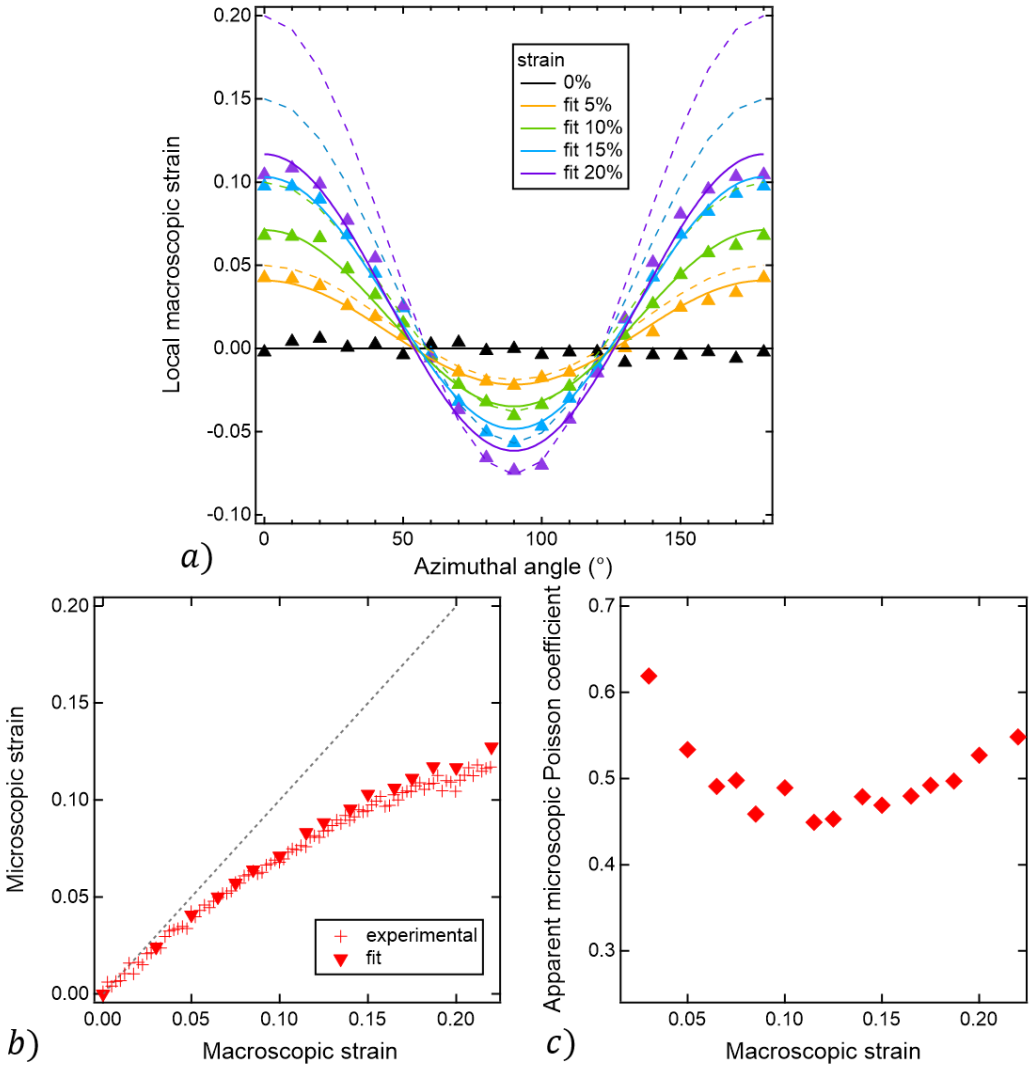


Figure 121.a) The local strain at the scale of lamellar stacks ε_{micro} =ΔLp/Lp as a function of the azimuth angle ψ for different values of the macroscopic strain during a tensile test at 170°C. Symbols are experimental points, curves are fits using eq.(47) and dashed lines are the expected behavior for $\nu micro = \nu macro = 0.38$. Experimental points at $\psi = 0$ and $\psi = 180°$ correspond to the same data points, due to the symmetry of the pattern. Evolution of the fitting outputs with macroscopic strain are described b) microscopic strain ε_{micro} and c) apparent microscopic Poisson coefficient ν_{micro}

Experimental data are well fitted with eq. (47) in the pre-yield regime. ε_{micro} and ν_{micro} measured in the HORI azimuth direction ($\psi = 0$) are shown in Figure 121.b) and c) as a function of the macroscopic strain in the pre-yield regime. The strain at the scale of the lamellar stacks, $\varepsilon_{micro,}$ is lower than the macroscopic strain. This may be explained by the difference between the shear modulus of the amorphous phase and the average modulus of the material above T_g. Above T_g, the amorphous phase is in the rubbery state and its shear modulus must be considerably lower than below T_g. Shearing lamellar stacks (which does not affect the long period) shall be easier than applying a tensile strain and a significant part of the macroscopic deformation shall be accommodated by local shear. This point will be discussed in more details in section IV of this chapter.

ν_{micro} is in the range between 0.45 and 0.5 in the pre-yield regime. Compared to PEEK's behavior for temperature below T_g, the lamellar stacks deformation seems to be closer to one of an isotropic incompressible material. However, it is hard to conclude on the compressibility of the material as we would need a geometrical model describing the lamellae disposition within the material.

Cette thèse est accessible à l'adresse : https://theses.insa-lyon.fr/publication/2023ISAL0006/these.pdf
© [H. Willeman], [2023], INSA Lyon, tous droits réservés

4. Orientation distribution of lamellar stacks

In the previous section, we have characterized the microscopic tensile deformation in the samples using the variation of the long period as a function of orientation along stretching. In addition, as a result of sample deformation, the distribution of orientation of lamellae (supposed to be initially in a nearly isotropic state) becomes anisotropic. Experimentally, the manifestation of this evolution is characterized by the intensity of the patterns becoming anisotropic. 3D representation of the evolution of SAXS patterns as a function of the azimuthal sector are presented in Figure 122.

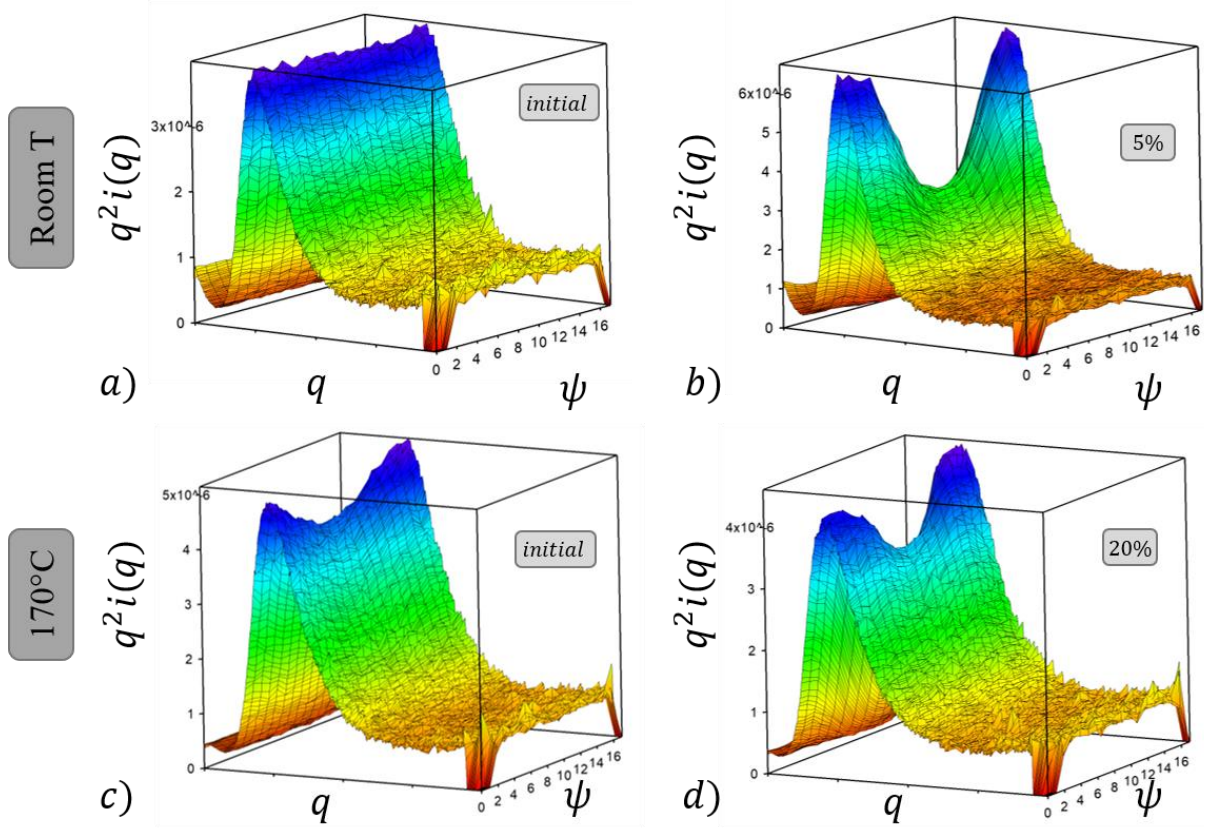


Figure 122. Azimuthal distributions of the corrected amplitude q²i(q) of SAXS patterns in the elastic regime at room temperature a) in the initial state and b) ε=5%. And at 170°C c) in the initial state and d) ε=20%

The anisotropy of the distribution of orientation of lamellae can then be studied quantitatively to fully characterize the local deformation in the stretched samples. In complement to Figure 121Figure 122, the evolutions of the amplitude of SAXS patterns with the deformation in the HORI and VERTI directions are presented in Figure 123.

Cette thèse est accessible à l'adresse : https://theses.insa-lyon.fr/publication/2023ISAL0006/these.pdf
© [H. Willeman], [2023], INSA Lyon, tous droits réservés

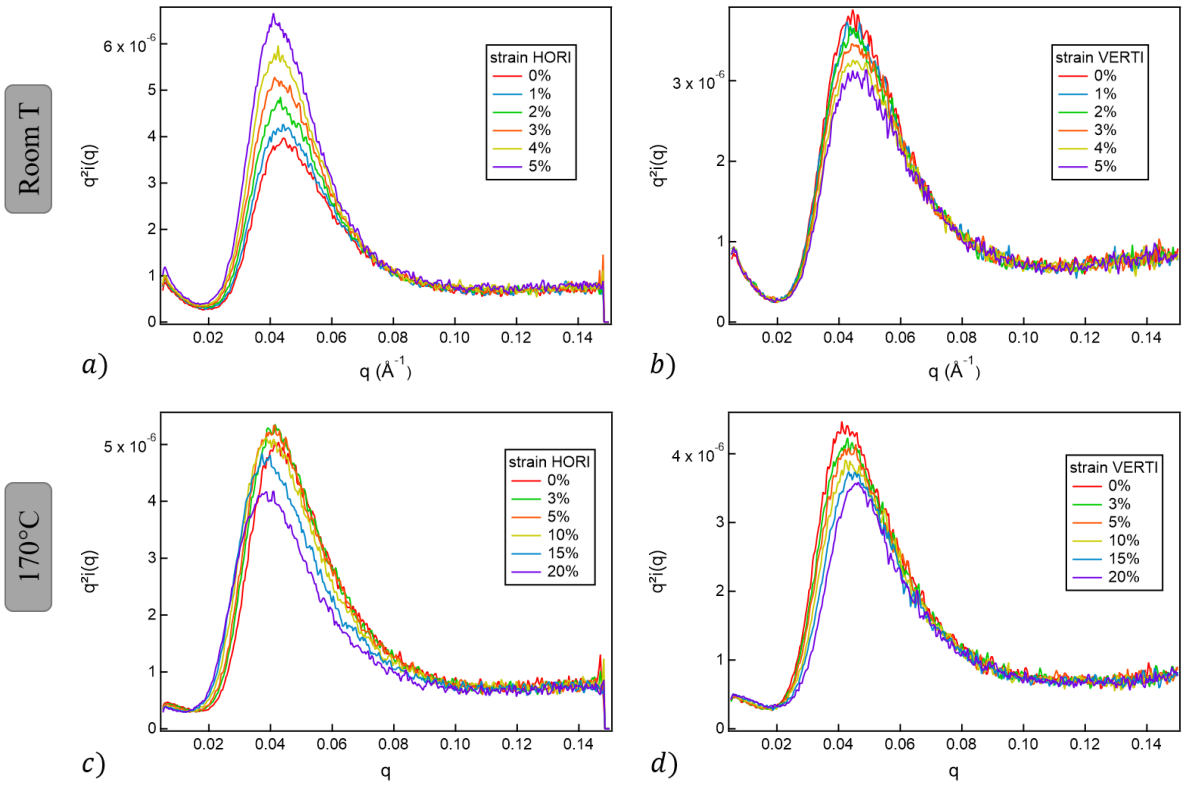


Figure 123. Evolution of SAXS spectra with deformation at room T (a,b) and 170°C (c,d) in the HORI and VERTI direction

In SAXS experiments, scattering occurs in the direction of the normal to lamella surfaces. An enhancement of the ring intensity is generally observed in the horizontal directions (parallel to the tensile direction). This means that, in the stretched state, there is an excess of lamellar stacks with their normals oriented in the horizontal region, that is, parallel to the stretching direction (i.e. lamellae with their larger surface perpendicular to the stretching direction, or horizontal lamellae), and conversely a relative deficit of lamellae with their normals perpendicular to the stretching direction, meaning vertical lamellae.

This tendency is illustrated on Figure 123.a and b for tests at room temperature with the relative amplitude increasing in the HORI direction and decreasing in the VERTI direction.

The evolution of the amplitude of the SAXS correlation peak as a function of azimuthal angle ψ and for different values of the local strain for experiments below and above T_g is summarized in Figure 124.

Cette thèse est accessible à l'adresse : https://theses.insa-lyon.fr/publication/2023ISAL0006/these.pdf
© [H. Willeman], [2023], INSA Lyon, tous droits réservés

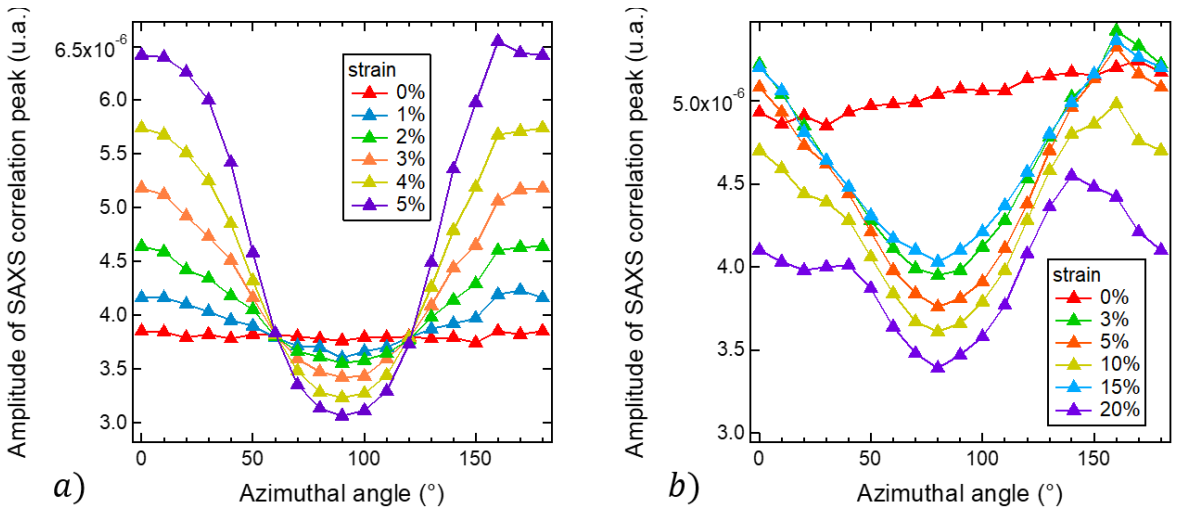


Figure 124. Amplitude of SAXS correlation peak as a function of azimuthal angle in the elastic regime various strains for tensile tests at a) 23°C and b) 170°C

At room temperature, in the initial, isotropic state, the amplitude of the SAXS correlation peak is nearly constant (within experimental uncertainties) with the azimuthal angle ψ. Then, with stretching, the intensity of the pattern modulates with ψ around the initial value of intensity. A large relative increase is noted in the direction corresponding to HORI lamellar stacks. Close to yield at ε = 5%, the amplitude has nearly doubled for these lamellar stacks.

Above T_g, the evolution of the amplitude exhibits a different behavior. First, the overall average intensity decreases. Instead of an important increase of intensity due to HORI lamellar stacks, we can observe a small decrease of intensity due to VERTI lamellar stacks. Also, near yield at 20%, peak of intensity appears at 45% which would suggests shearing or buckling of lamellae.

Reversibility of the orientation distribution

The reversibility of the evolution of amplitude of the SAXS correlation peak in the elastic (pre-yield) regime has been investigated during tensile tests with cyclic loading described in the introduction of this chapter.

For tensile tests at room temperature, the evolution of the amplitude of SAXS patterns in both horizontal and vertical directions as a function of the (macroscopic) strain during the first loading-unloading cycle in the pre-yield regime is plotted in Figure 125 alongside the corresponding stress strain curve. The slope of the curve is the same (reversed) in the unloading and loading steps. When the applied force and deformation of the sample are back to zero, the amplitudes of the SAXS peak comes back to their initial values in both directions.

For tensile tests at 170°C, above glass transition temperature, the evolution of the amplitudes of SAXS patterns in the HORI and VERTI directions are represented in Figure 126. The behavior of the HORI and VERTI lamellar stacks is this time different. An inflexion in the evolution of the amplitude of lamellae scattering in the HORI direction can be observed during the first loading step of the cycle (Figure 126.a). The unloading step corresponds more to a linear evolution but the ampitude reaches a lower value than in its initial state.

As for lamellae which scatter in the VERTI direction, in the same way as when stretched at room temperature, the amplitude of the peak evolves linearly with deformation and almost comes back to its initial value when the sample is unloaded back to force zero (macroscopic residual deformation is also observed on Figure 126.b).

Cette thèse est accessible à l'adresse : https://theses.insa-lyon.fr/publication/2023ISAL0006/these.pdf
© [H. Willeman], [2023], INSA Lyon, tous droits réservés

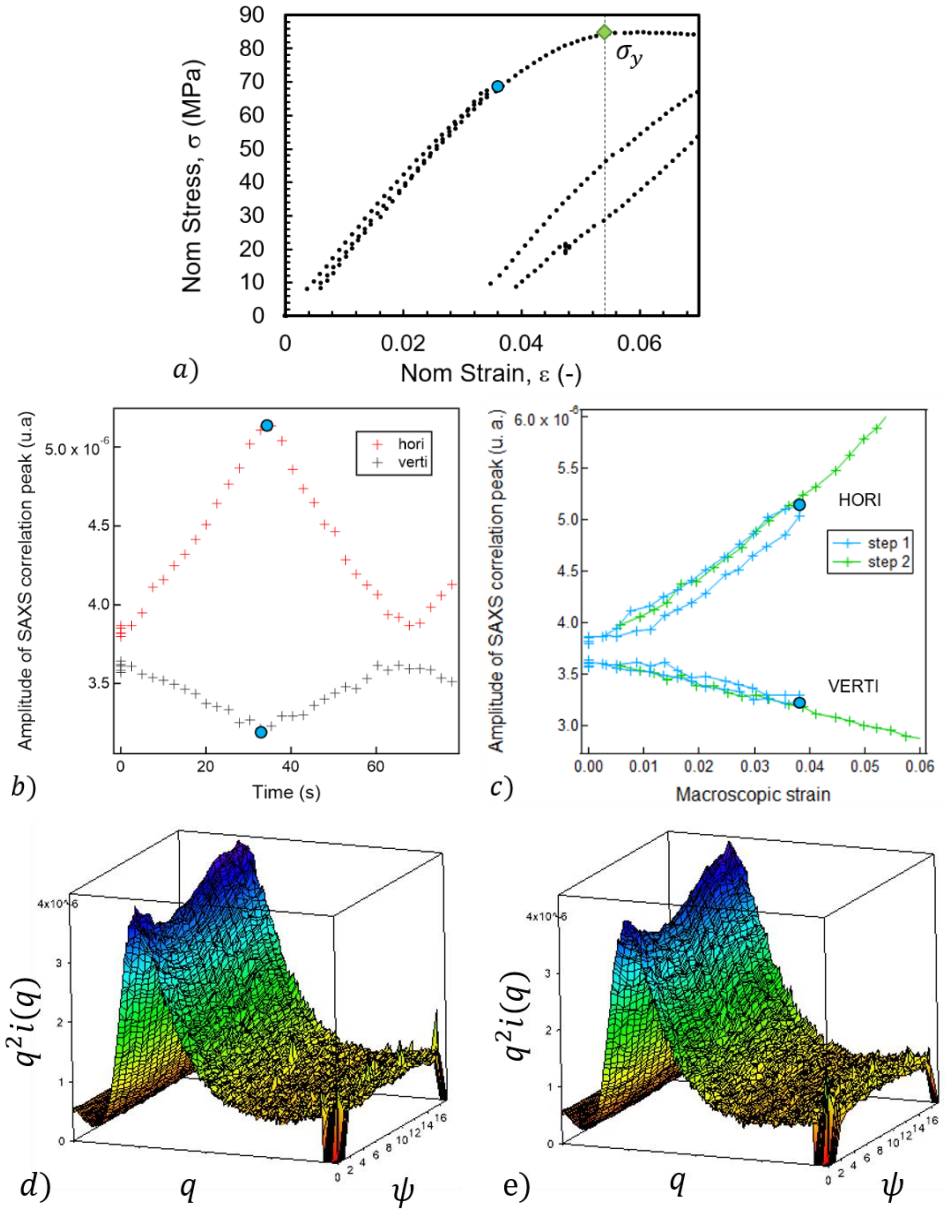


Figure 125. a) Stress-strain curve for the first cycle of complex tensile loading in the pre-yield regime at room temperature, up to the blue point and back to zero force, b) corresponding evolution of the amplitude of the correlation peak in the horizontal (HORI) and vertical (VERTI) directions as a function of time, c) amplitude as a function of macroscopic (nominal) strain; and azimuthal distribution of the corrected amplitude $q^2 i(q)$ in d) the initial state and e) after the first loading and back to zero force

Cette thèse est accessible à l'adresse : https://theses.insa-lyon.fr/publication/2023ISAL0006/these.pdf
© [H. Willeman], [2023], INSA Lyon, tous droits réservés

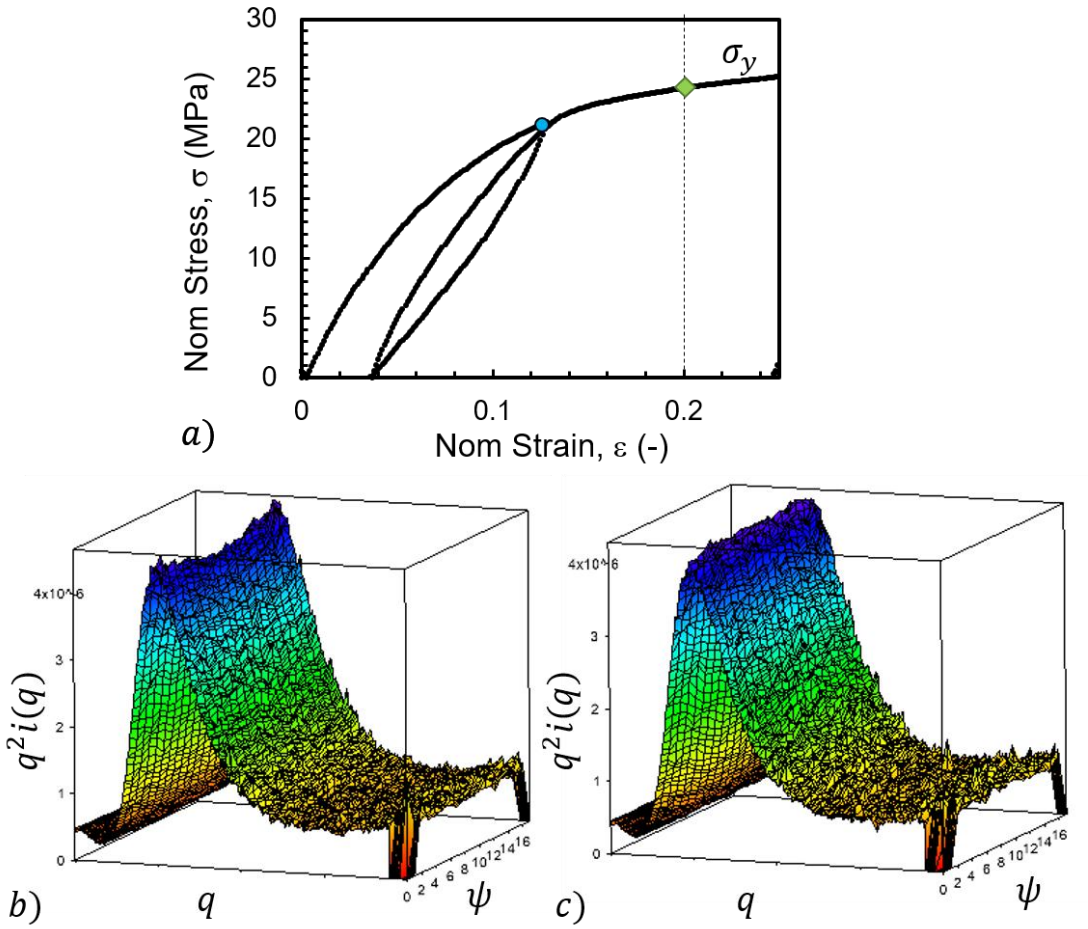


Figure 126. a) Stress-strain curve for the first cycle of complex tensile loading in the pre-yield regime at 170°C, up to the blue point and back to zero force; and azimuthal distribution of the corrected amplitude $q^2i(q)$ in b) the initial state and c) after the first loading and back to zero force

At both temperatures, the evolution of the orientation distribution of lamellae is reversible in the pre-yield regime.

a. Discussion

However, it is hazardous to conclude on lamellar stack orientation in a quantitative way using the evolution of the amplitude of the correlation peak. Indeed, the amplitude measured in a given direction would be directly related to the relative number of lamellar stacks in this direction if lamellar stacks would stay unchanged during the tensile tests. However, the intensity of the peak is also related to the contrast factor between the crystalline and the amorphous phases as well as to the form and structure factors of lamellar stacks. As the long period changes depending on the orientation, both the contrast factor and the structure factor of lamellar stacks may be affected. This point will be discussed in section III below.

Cette thèse est accessible à l'adresse : https://theses.insa-lyon.fr/publication/2023ISAL0006/these.pdf
© [H. Willeman], [2023], INSA Lyon, tous droits réservés

III. Elastic strain regime at the scale of crystal unit cell, by WAXS

Wide-angle X-ray scattering (WAXS) arises from the crystallographic arrangement of the chains in the crystalline phase. It allows identifying the nature of the crystalline phases and gives access to crystal lattice spacing and orientation. Anisotropic 2D WAXS patterns were analyzed following a procedure similar to the one used for SAXS patterns to get a precise measurement of the positions of the diffraction peaks.

1. WAXS protocol

During tensile tests, as for SAXS patterns, a 2D WAXS pattern is recorded every 0.2% of deformation. WAXS patterns are collected and analyzed as described in chapter II. WAXS patterns are presented in Figure 127.a at different steps of the tensile test. As discussed in Chapter II, WAXS patterns are composed of sharp rings of intensity to the diffraction bycrystal planes. The study of the deformation of the samples at the scale of crystal planes will focus on the behavior of the three main crystal plane families (110), (113) and (200) corresponding to the three main diffraction peaks noted on Figure 127.b.

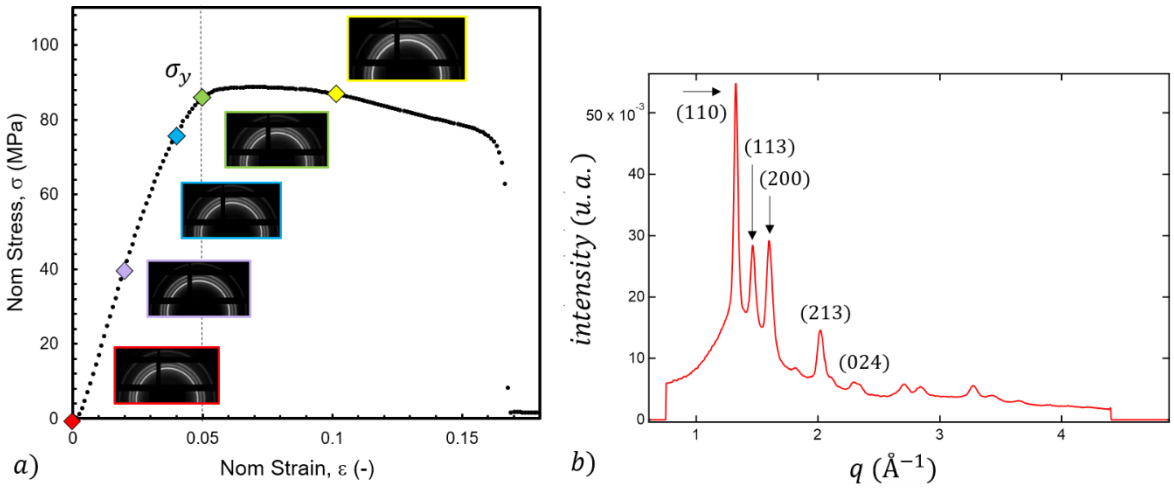


Figure 127. a) Evolution of WAXS patterns with macroscopic strain during tensile test of KT880 at room temperature b) Indexation of diffraction peaks on integrated WAXS pattern for $\psi = 0°$

Each crystal plane scatters along its normal $\vec{n}$. As the material is isotropic in its initial state, the scattering is initially isotropic and the pattern has the shape of perfectly circular rings corresponding to crystal plane families. The position of each diffraction peak is related to the distance between corresponding planes according to the Bragg's law (see Chapter II)

Schematic representations of these crystal planes in the crystalline lattice and within crystal lamellae, based on the results of Lovinger, with lamellae growth direction along b axis are presented in Figure 128. [15]

Cette thèse est accessible à l'adresse : https://theses.insa-lyon.fr/publication/2023ISAL0006/these.pdf
© [H. Willeman], [2023], INSA Lyon, tous droits réservés

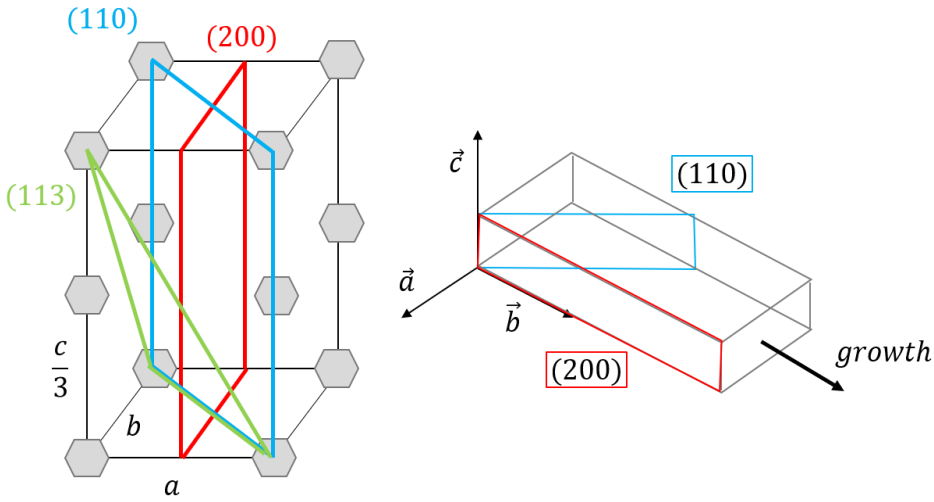


Figure 128. Schematic representation of (110), (113) and (200) crystal planes (cf fig 7 chap1)

The diffraction peaks will be analyzed as a function of the azimuthal angle. Figure 129 shows a 3D representation of the initial pattern.

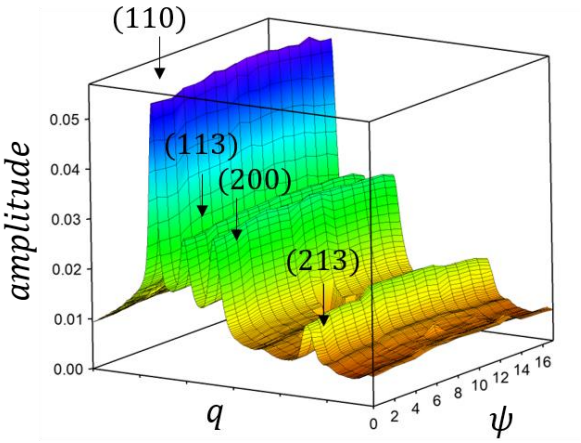


Figure 129. 3D representation of initial WAXS pattern as a function of the scattering vector q and the azimuthal angle ψ and indexation of diffraction peaks

2. Local strain at the scale of crystal planes

The deformation measured in a given plane family (h,k,l) is defined as:

$$\frac{\Delta d_{h,k,l}}{d_{h,k,l}} = -\frac{\Delta q_{h,k,l}}{q_{h,k,l}} \quad (49)$$

Where $q_{h,k,l}$ is the position of the peak and $\Delta q_{h,k,l}$ the variation of the position of the peak with respect to the initial isotropic value.

The deformations of the three main plane families along stretching at room temperature and at 170°C are shown in Figure 130 (for planes scattering to the two directions HORI and VERTI). In the pre-yield regime at room temperature, the strains of all crystal plane family nearly have the same slope. This result is trivial as crystals are anisotropic and moduli in different directions of the crystals may be likely different. At 170°C, some oscillations in the strain plateau can be observed. They are most likely due to instabilities in the tensile device. Nevertheless, the amplitudes of these oscillations are small and may not be significant at this step.

Cette thèse est accessible à l'adresse : https://theses.insa-lyon.fr/publication/2023ISAL0006/these.pdf
© [H. Willeman], [2023], INSA Lyon, tous droits réservés

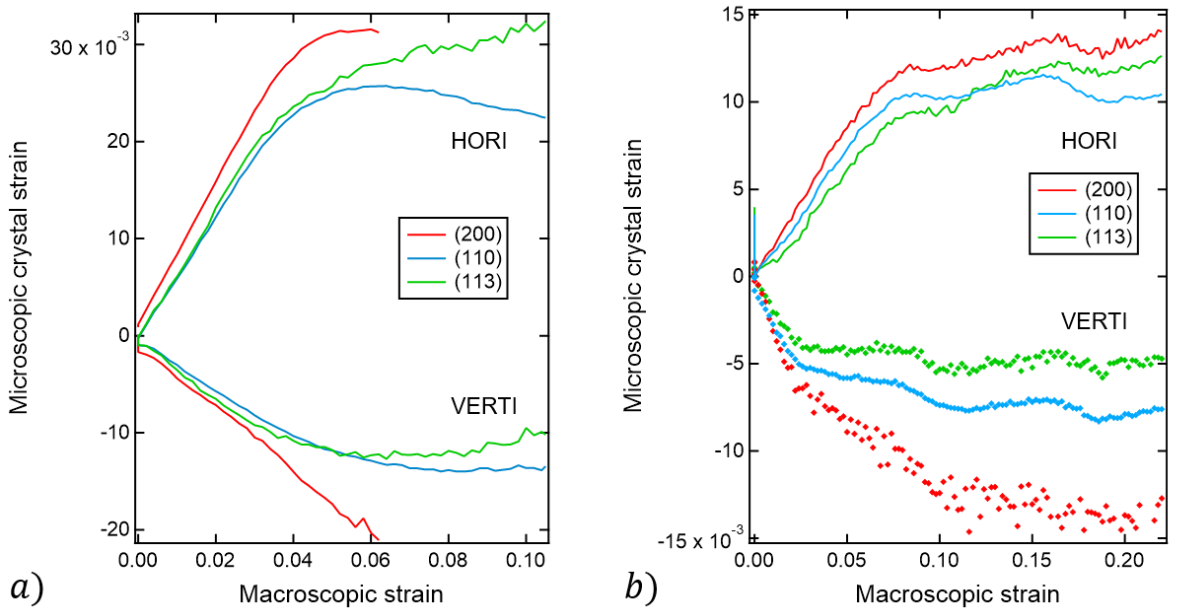


Figure 130. Evolution of crystal strain as a function of macroscopic strain for (110), (113) and (200) planes families at a) room temperature and b) 170°C. For each plane family, the strain is measured in the HORI and VERTI directions, i.e. for crystal planes submitted to pure tensile or pure compressive strain, that is when the corresponding planes are perpendicular or parallel to the tensile direction, respectively.

Measurements of the microscopic strain for the (110) plane family is reported in Figure 131 and compared to the macroscopic strain for tensile tests at temperatures below and above T_g. From the beginning of the tensile test, the strain within crystals is much lower than the macroscopic strain (about two times lower at 4% at room temperature and 10 times lower at 10% for tests at 170°C).

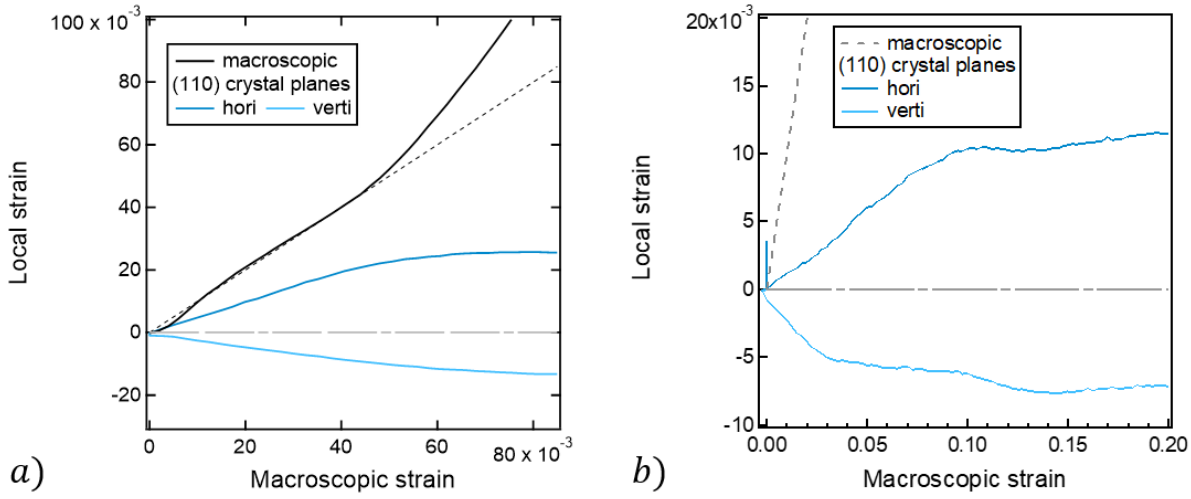


Figure 131. Local microscopic strain in the pre-yield regime at the scale of crystal planes (110) in the HORI and VERTI directions compared to macroscopic strain as a function of cross-head displacement a) room temperature, where the macroscopic strain is measured by DIC (full line) and b) 170°C, where macroscopic strain is considered to be equal to the cross-head displacement (dashed line)

Beyond some macroscopic strain value, the deformation within crystal planes stabilizes. This is true for the three families of planes under consideration (Figure 130), even though the macroscopic strain concomitantly increases in the investigated region of the sample. For tensile tests at room temperature,

Cette thèse est accessible à l'adresse : https://theses.insa-lyon.fr/publication/2023ISAL0006/these.pdf
© [H. Willeman], [2023], INSA Lyon, tous droits réservés

this critical strain value roughly corresponds to the onset of plasticity. However, for tensile tests at 170°C (above T_g), this stabilization of crystal strain occurs at about 10% for the HORI direction (crystal planes in tensile strain), that is, well before the macroscopic yield point (20%).

From this point, two hypotheses that will be explored in the next chapter are possible:

- Beyond the yield point, the amorphous phase supports the whole deformation,
- Beyond the yield poit, crystals only undergo shear along crystal planes.

At T = 170°C, the ratio of the strains in crystal planes perpendicular and parallel to the tensile direction (which are submitted to tensile and compressive stress respectively) would correspond to an apparent Poisson's coefficient much larger than 0.5 (perhaps even larger than one as it is visible in Figure 131.b). For a homogeneous isotropic material, this is forbidden by the laws of elasticity and thermodynamics. Therefore, this demonstrates that the response of the material, at the scale of crystal unit cell, must not be described as a homogeneous deformation. Or, equivalently, that crystals with different orientations are not submitted to the same level of stress. This point is further discussed in the next section.

3. Local strain as a function of orientation

At the scale of lamellar stacks as observed by SAXS, the deformation was found to be nearly homogeneous, in the sense that a variation of the form $P_2(\cos\psi)$ was observed as a function of the azimuth angle ψ (as detailed in Section 1, see equation (47)).

The microscopic strain at the scale of crystal lattice planes for the first diffraction peak related to (110) crystal planes is represented as a function of the azimuthal angle in Figure 132. Homogeneous deformation of crystal unit cells would correspond to the following equation (50), similar to equation (47):

$$\frac{\Delta d}{d^0} = \frac{\varepsilon}{3}\left[(1-2\nu) + 2(1+\nu)P_2(cos\psi)\right] \qquad (50)$$

Cette thèse est accessible à l'adresse : https://theses.insa-lyon.fr/publication/2023ISAL0006/these.pdf
© [H. Willeman], [2023], INSA Lyon, tous droits réservés

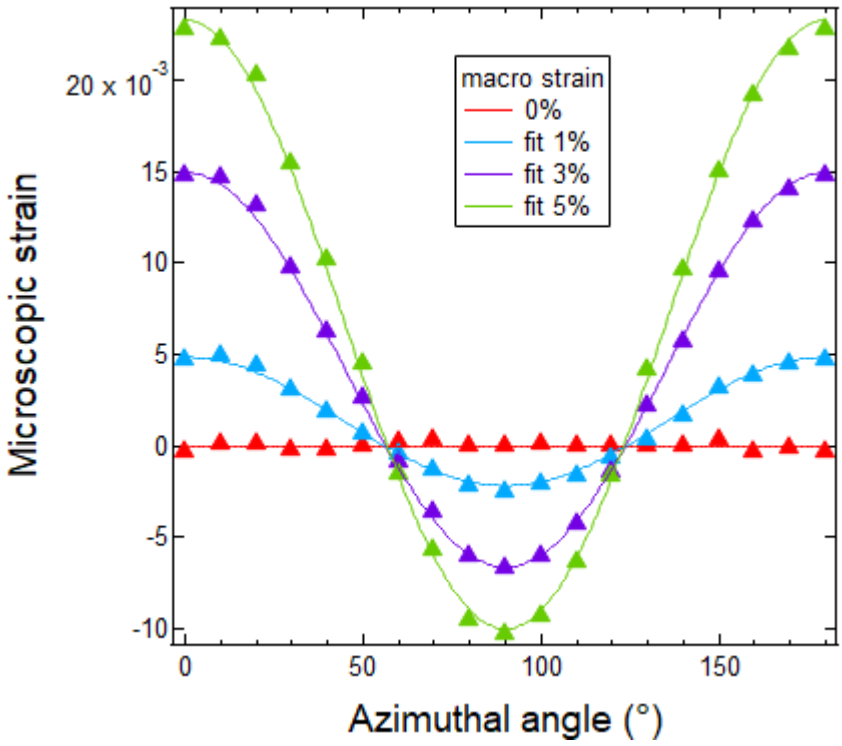


Figure 132. The local strain at the scale of (110) crystal planes Δd/d as a function of the azimuth angle ψ for different values of the macroscopic strain for tensile test at room temperature. Symbols are experimental points, curves are fits using eq 1

Experimental data are well fitted with equation (50), as shown in Figure 132. No significant deviation from equation (50) is observed. This means that the deformation is homogeneous in the elastic regime at the scale of crystal planes. The outputs of the fits are the values of the microscopic strain ε and the effective microscopic Poisson's coefficient ν. The outputs of the fit are plotted in Figure 133.

Below about 2.5% strain, the high apparent ν values should probably be considered as an artifact of the measurements. Above about 2.5% strain, ν stabilizes up the the yield point (at about 6% strain). This stabilized value should be considered as the actual value of the effective microscopic Poisson's coefficient.

It is important to specify that the apparent Poisson coefficient given by the fitting process is the ratio of deformation between crystal planes scattering in the HORI and VERTI directions. These crystal planes belong to different lamellar stacks and thus may be located in different zones of a spherulite. The final value of this coefficient is thus more related to the global behavior of the material at the scale of a spherulite rather than to one crystal which may present anisotropy with different moduli in parallel and perpendicular directions.

The microscopic strain at the scale of the crystalline lattice is considerably smaller than the macroscopic strain as crystals are more rigid than the amorphous phase. In the small strain domain, uncertainty on the measurements of the strain induce a large uncertainty of the values of the apparent microscopic Poisson's coefficient. For (110) crystal planes family presented in Figure 133, the apparent microscopic Poisson's coefficient seems to stabilize at a value close to 0.44. Error bars are estimated from the resolution in the local strain measurement. This graph shows that the estimate of ν_{micro} is not reliable below about 2% strain.

Cette thèse est accessible à l'adresse : https://theses.insa-lyon.fr/publication/2023ISAL0006/these.pdf
© [H. Willeman], [2023], INSA Lyon, tous droits réservés

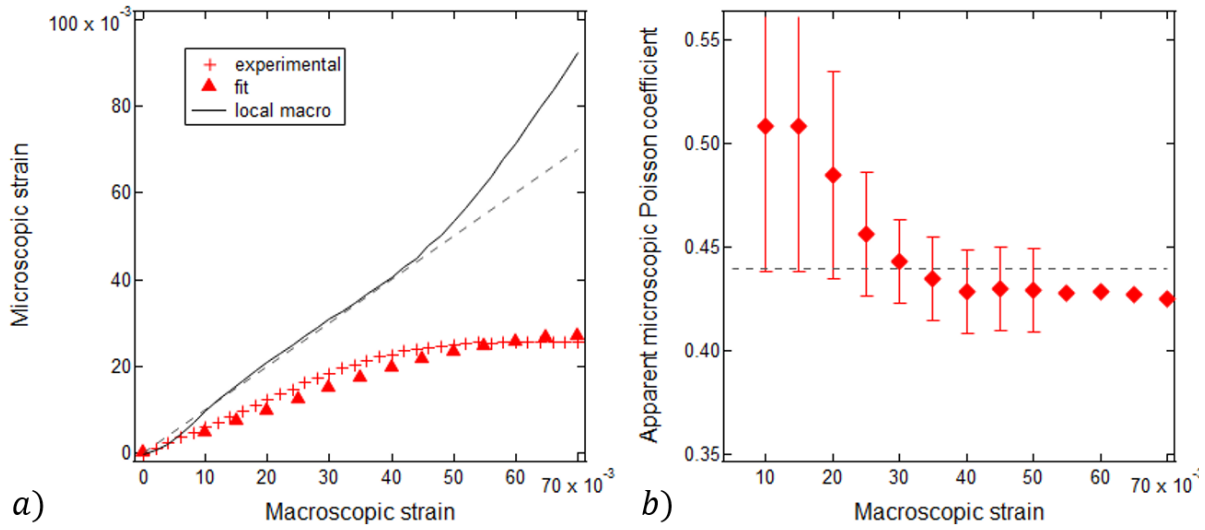


Figure 133. Evolution of fitting outputs: microscopic strain for (110) crystal planes in the HORI direction and Poisson's coefficient ν with macroscopic strain at room temperature.

This procedure can be repeated for each diffraction peak in order to compare the behavior of each family of planes. The microscopic deformations are of similar order for the three families of crystal planes studied. However, the values of the apparent microscopic Poisson's coefficient are slightly different but all within the range of about 0.44-0.50. (Figure 134.b) At yield, the ratio of (110) and (220) planes scattering in HORI and VERTI directions seems to stabilize whereas this ratio increases dramatically for (200) planes. This represents the fact that strain in the VERTI direction stabilizes whereas the strain in the HORI direction increases comparatively largely.

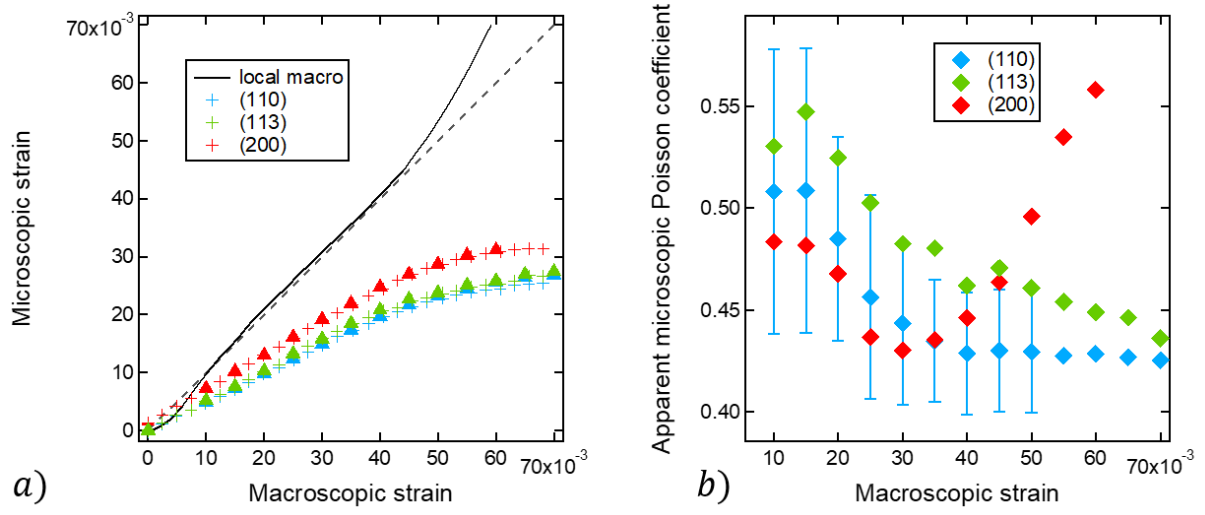


Figure 134. Fitting outputs for the three main plane family (110), (113) and (200) in the HORI direction: a) microscopic strain and b) apparent Poisson coefficient at room temperature

The whole strain field at the scale of crystal planes in the elastic regime has also be investigated for tests at temperature above T_g using equation (50) describing the expected behavior of a homogeneous material. The results of the fitting of the strain as a function of azimuthal angle for deformation up to 20% is plotted on Figure 135.

Cette thèse est accessible à l'adresse : https://theses.insa-lyon.fr/publication/2023ISAL0006/these.pdf
© [H. Willeman], [2023], INSA Lyon, tous droits réservés

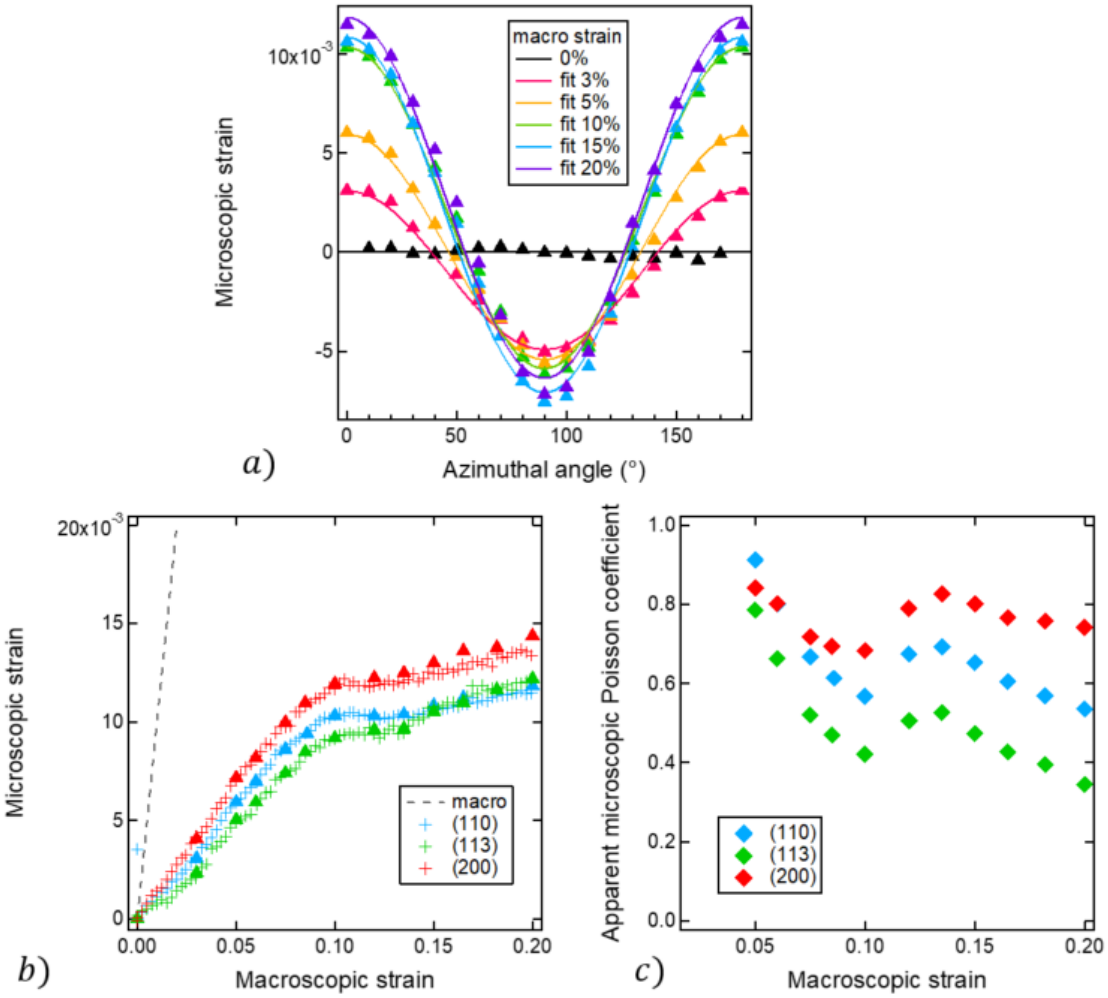


Figure 135. a) The local strain at the scale of (110) crystal planes Δd/d as a function of the azimuth angle ψ for different values of the macroscopic strain. Symbols are experimental points, curves are fits using eq 1 b) Microscopic strain in the HORI direction for (110) (113) and (200) crystal planes compared to macroscopic strain and c) corresponding apparent microscopic Poisson's coefficient. Tests at 170°C.

At 170°C, the stabilization of the strain observed from ε=10% in the HORI direction (Figure 131.b) is also observed in every direction (Figure 135.a). This observation is also valid for (113) and (200) planes too. At 170°C, the apparent microscopic Poisson's coefficient exhibits here similar types of behavior for all crystal planes. The values of this coefficient are about 0.4, 0.6 and 0.7 respectively for (113), (110) and (220) crystal planes. As explained before, such values would be unphysical in a homogeneous material. However, these values reflect the anisotropy of the crystal, which may have largely different moduli in different directions.

4. Orientation distribution of crystal planes

The reorientation processes at the scale of crystal planes have also been investigated by analyzing the distribution of the amplitudes of diffraction peaks as a function of the azimuth angle under strain, as shown in Figure 136.

No significant changes in amplitude and distribution are observed in the pre-yield regime.

Cette thèse est accessible à l'adresse : https://theses.insa-lyon.fr/publication/2023ISAL0006/these.pdf
© [H. Willeman], [2023], INSA Lyon, tous droits réservés

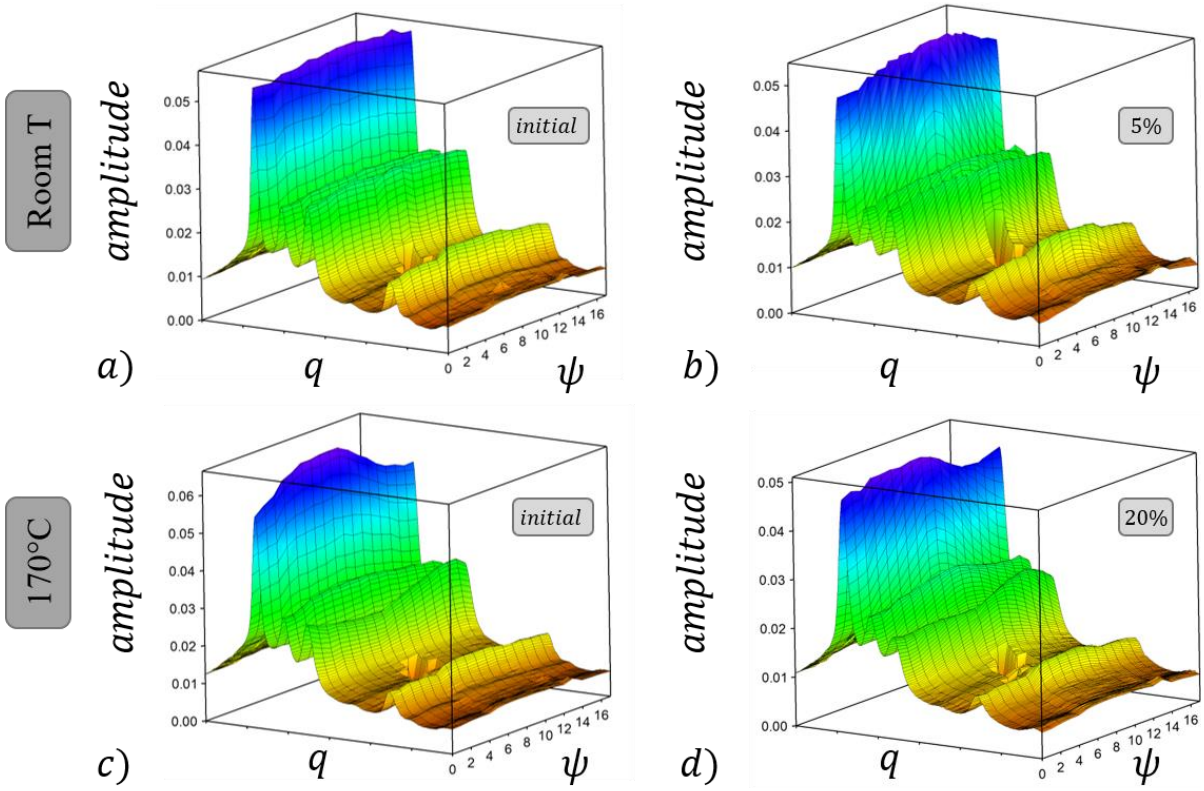


Figure 136. Azimuthal distribution of amplitude of WAXS patterns in the elastic regime at room temperature for a) in the initial state and b) ε =5%. And at 170°C for c) in the initial state and d) ε =20%

At room temperature, it seems that the intensity decreases in the HORI direction and stays stable in the VERTI direction. This is coherent with the observation made on lamellar stacks. It seems there is less lamellar stacks in the VERTI direction which contains crystal planes scattering in the HORI direction. Above T_g, the amplitude globally decreases with stretching with a maximum at 90° in the VERTI direction.

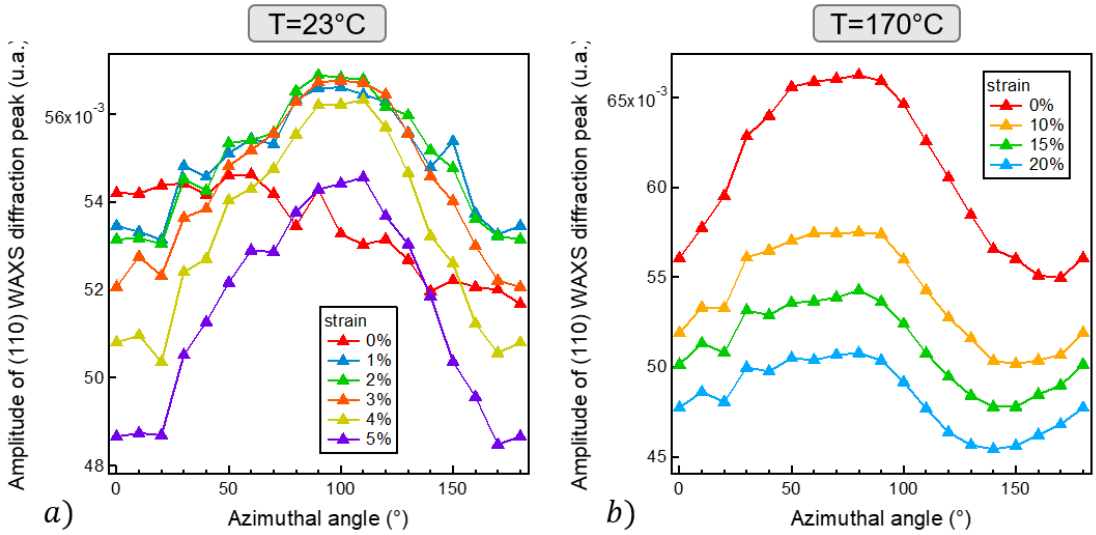


Figure 137. Amplitude of (110) diffraction peak as a function of azimuthal angle in the elastic regime for various strains for tensile tests at a) 23°C and b) 170°C

Cette thèse est accessible à l'adresse : https://theses.insa-lyon.fr/publication/2023ISAL0006/these.pdf
© [H. Willeman], [2023], INSA Lyon, tous droits réservés

IV. Discussions: deformation mechanisms in the elastic pre-yield regime

The final part of this chapter has the objective to correlate SAXS and WAXS observations described above and to propose mechanical models. Furthermore, both in SAXS and WAXS, changes in lamellar spacing and orientation or changes in crystalline lattice planes are detected as a function of lamella or crystal orientation. Here we discuss the connection to the spherulitic morphology.

First, it is important to remind that observations made in SAXS or WAXS do not represent the entire populations of lamellae or crystalline planes but only those which are in Bragg's conditions for scattering. However, since the tensile experiment has uniaxial symmetry, it allows to deduce the global distributions from scattering patterns.

1. SAXS experiments

a. Local strain within lamellar stacks

Let us propose a hypothesis that may explain the behavior of our material described in this part. If we model a vertical lamellar stack by stacking of thin disks alternatively of crystalline and amorphous phases as represented on Figure 138. Above T_g, the modulus of the amorphous phase in the rubbery state is much smaller than that of the crystalline phase (2 to 3 orders of magnitude lower). A disk of amorphous phase behaves as an elastomer disk glued on two rigid substrates (the adjacent crystalline lamellae), submitted to tensile stress. As this elastomer disk cannot fully contract in the horizontal plane because it is attached to the crystalline lamellae, the tensile normal force is amplified by a mechanical mechanism similar to lubrication effect [115], [116]. This results in an amplified effective Young's modulus.

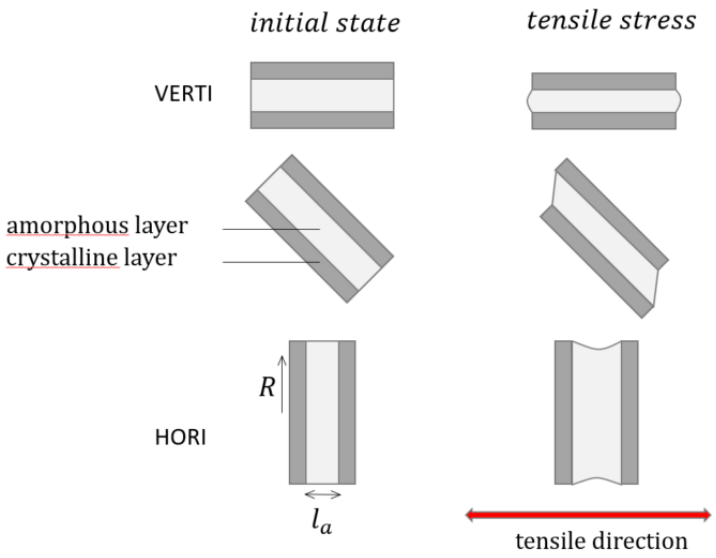


Figure 138. Schematics of a lamellar stack: stacking of thin disks alternatively of crystalline and amorphous phases submitted to tensile stress

Various regimes are described by various expressions, depending on the aspect ratio R/l_a of the stretched amorphous layer (where La is the thickness of the amorphous layer and R the lateral dimension of lamellae), for instance: [117]

Cette thèse est accessible à l'adresse : https://theses.insa-lyon.fr/publication/2023ISAL0006/these.pdf
© [H. Willeman], [2023], INSA Lyon, tous droits réservés

$$E_{eff} \cong E\left[1+\frac{1}{2}\left(\frac{R}{l_a}\right)^2\right] \quad (51)$$

where E is the Young's modulus of the elastomer disk (i.e. of the amorphous phase). If R/l_a becomes even larger, the effective modulus becomes $Eeff{\sim}E/(1-2\nu)$, which is comparable to the bulk modulus. The same effect (amplification of the effective Young's modulus) is present for vertical lamellae, which are submitted to compressive strain.

Above T_g, the shear modulus of the amorphous phase is much lower than the average modulus of the material. Lamellar stacks which are at an angle with respect to the tensile direction can thus be sheared easily. Above Tg, the effective modulus for horizontal (and vertical) lamellae is amplified, and therefore the strain in horizontal and vertical lamellae is decreased, while this lower strain is compensated by large shear strain in inclined lamellar stacks. This shear strain, however, is not detected in SAXS experiments.

b. Lamellar stacks orientation

Let us first discuss the variation of the contrast factor as a function of orientation along tensile strain. Although this phenomenon is hard to quantify, the following order of magnitude can be estimated. The following data shall be used: density of the (undeformed) alpha crystal phase $\rho_c = 1.4\ g.cm^{-3}$ [9]; amorphous phase density $\rho_a = 1.26\ g.cm^{-3}$ [10]. The molar mass of the monomer is 288 g and the electron number per monomer is 150. Altogether this gives an initial contrast factor

$$b^2 = r_e^2 * \Delta\rho^2 = 1.512 \times 10^{20} cm^{-4} \quad (52)$$

where $r_e^2 = 7.9 \times 10^{-26}\ cm^2$ is the electronic cross section.

In the case of stretching above glass transition temperature, the amorphous phase is in the incompressible rubber state with a Poisson's coefficient $\nu \approx 0.5$. The average density does not evolve, assuming that no cavitation occurs in tension in the elastic regime. However, the density of the crystal phase may change with local strain.

For HORI lamellar stacks under tensile strain, the local density in both phases does not evolve significantly because the strain in the crystal lamella is negligible as the crystal tensile modulus is way higher than the amorphous phase modulus. It may be considered that only the amorphous deforms.

VERTI lamellar stacks are submitted to tensile strain/stress in the plane of the lamellae.

In general, for polymer crystals the tensile modulus in the direction of chains (in the direction of the normal to the lamellae) is much larger than the modulus in other direction. [118]–[120]It results that contraction of the crystal lamellae thickness will be extremely small, if not negligible. This would correspond to a very small (nearly 0) coefficient for the crystalline lamella in this configuration.

For VERTI lamellar stacks undergoing compressive strain, for $\varepsilon_{macro} \cong 0.1$, the measured local strain in crystals is $\varepsilon_{local} \cong -0.006$ (see Figure 135.a). The relative variation of volume and density for a crystalline lamella can be calculated as follows:

$$\frac{\Delta\rho}{\rho} = -\frac{\Delta V}{V} \cong \varepsilon_{local} * (1-2\nu) \quad (53)$$

In this configuration with a Poisson's coefficient ν nearly equal to zero, the relative variation of volume is negligible.

In the case of tensile loading under glass transition temperature, local mechanical properties of amorphous and crystal phases are more similar as the amorphous phase is rigid. It can then be expected

Cette thèse est accessible à l'adresse : https://theses.insa-lyon.fr/publication/2023ISAL0006/these.pdf
© [H. Willeman], [2023], INSA Lyon, tous droits réservés

that the variation of the contrast as a function of orientation would be even smaller than above T_g and hence considered to be negligible.

This discussion on contrast factor lead us to conclude that with assumption on the Poisson's coefficient and moduli of each phase, the variation of the contrast as a function of orientation should be smaller than the observed effect.

Then, the variation of form and structure factors due to local strain has to be reviewed. As a very general rule, the overall scattered intensity for a collection of identical lamella stacks (excluding the central scattering) can be written as the product of a structure factor related to the (one dimensional) periodic stacking of long period L (note that the structure factor includes line broadening due to finite size or finite correlation length) and a form factor, related to the motif inside one long period (one amorphous and one crystal lamella), i.e. to the relative thickness of amorphous and crystalline lamellae and the sharpness of interfaces. Assuming perfectly sharp, plane interfaces, the form factor would be of the form of equation (54):

$$F(q) \approx h^2 \left(\frac{sin(qh/2)}{qh/2}\right)^2 \qquad (54)$$

With h the thickness of crystal lamellae.

As represented on Figure 139, the amplitude of the SAXS correlation peak is scaled by an intensity factor estimated by taking $q = q_{max} = 2\pi/L$ in equation (54). The intensity modulation as a function of the azimuthal angle related to the modulation $\Delta L(\theta)$of the long period L and modulation $\Delta h(\theta)$ of the crystal thickness is expressed is the equation below:

$$\frac{\Delta I_F(\theta)}{I_F} \approx \frac{1}{I_F}\frac{dI_F}{dL}\Delta L(\theta) \approx -2\left(x\frac{cosx}{sinx} - 1\right)\frac{\Delta L(\theta)}{L} + 2\frac{cosx}{sinx}\frac{\Delta h(\theta)}{h} \qquad (55)$$

With $x = \pi h/L$

The representative case of average crystallinity of 35% which is close to our sample crystallinity is represented on Figure 139 with $h \approx L/3$. If we consider $\Delta h/h \approx 0.5\,\Delta L/L$, we get $\Delta I_F/I_F \approx \Delta L/L$. This means that for a strain of 10%, the intensity would change by about as the orientation changes.

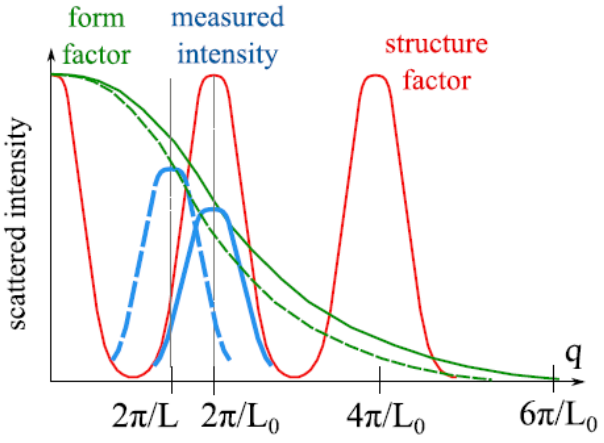


Figure 139. The scattered intensity as a function of q is the product of the structure factor (red curve) and the form factor (green curve)

Cette thèse est accessible à l'adresse : https://theses.insa-lyon.fr/publication/2023ISAL0006/these.pdf
© [H. Willeman], [2023], INSA Lyon, tous droits réservés

2. Models

a. Chain network (CN) model

In the studied PEEK samples, the crystallinity index is roughly between 30 and 40%. At low crystallinity index, a semi crystalline polymer may be described as a dispersion of crystalline entities or inclusions (lamellar stacks) embedded within a matrix of amorphous phase.

In the "chain network" model, the molecular chains between lamellae, acting as tie molecules, play the predominant role and transmit the stress. When submitted to a tensile load, chains are elongated. Crystalline parts of the chains (which are perpendicular to lamella surfaces) tend to orient along the tensile direction and thus exert a torque on crystalline lamellae, which tend to orient the normal to lamella surfaces parallel to tensile direction. In this process, lamellae follow the motion of chains and tend to orient towards the equator. In the initial (undeformed) state, the material is supposed to be isotropic, both in terms of lamellar spacing and orientational distribution of crystalline lamellae.

In order to orient towards horizontal orientation, initially inclined lamellar stacks have to undergo both rotation and shear (shear cannot be detected in our scattering experiments, however).

This process is schematized in Figure 140: during tensile load, a chain is stretched and this leads to the tilting of lamellar stacks as well as a slight shear.

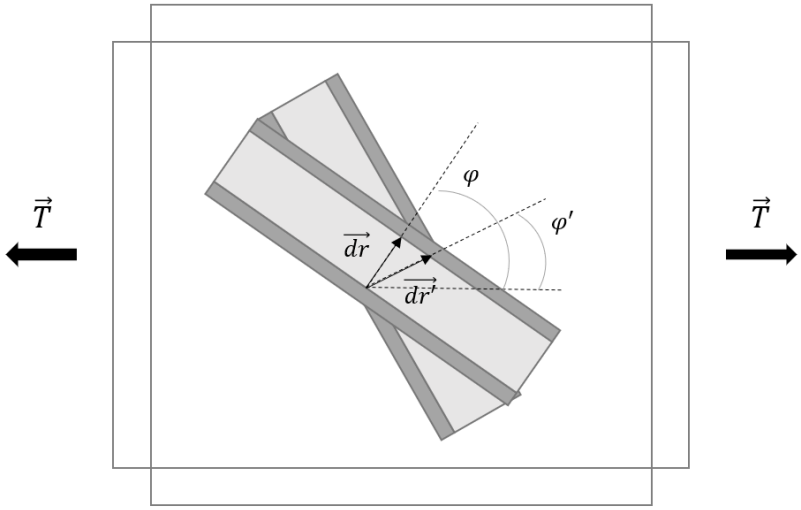


Figure 140. Local deformation of a lamella stacks with its normal vector at angle ψ from the tensile direction $\vec{T}$ in the so-called chain-network model

The consequences of the "Chain network" (CN) model on SAXS and WAXS patterns are:

- In SAXS, as the lamellae rotate to the equator, this means that more normals to lamella surfaces scatter in the horizontal direction, resulting in an enhancement of intensity in HORI direction. This effect is illustrated in Figure 140 .

- In WAXS, main diffraction peaks come from lattice planes which are perpendicular to lamella surfaces and contain chain axis. Since lamella surfaces tend to orient perpendicular to the tensile direction, diffracting planes tend to orient parallel to the tensile direction, that is, they tend to scatter horizontally.

Cette thèse est accessible à l'adresse : https://theses.insa-lyon.fr/publication/2023ISAL0006/these.pdf
© [H. Willeman], [2023], INSA Lyon, tous droits réservés

b. Rigid lamella (RL) model

A quite different deformation mechanism may possibly occur. Consider a lamella or a crystallite made of a lamellar stack with large aspect ratio, embedded within a homogeneously deformed material. Under tensile strain, the crystallite will tend to orient with the larger dimension parallel to the tensile direction, as depicted in Figure 141. In this situation, the stress is not transmitted to crystallites by stretched individual chains, but by the amorphous phase as a whole, acting as a homogeneous elastic (or viscoelastic) matrix. This mode of deformation is denoted here "Rigid lamella" model (RL).

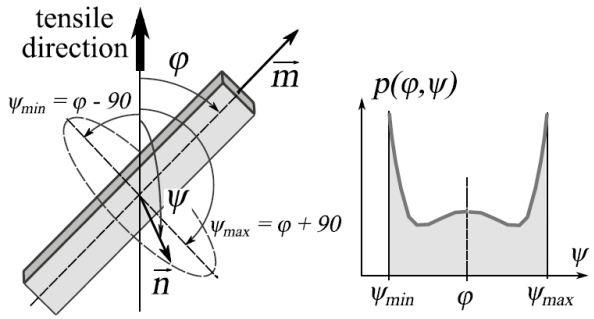


Figure 141. Schematics of the orientation distribution $p(\psi,\varphi)$ of the normal vectors $\vec{n}$ for an ensemble of lamellae which are at an angle φ with respect to the tensile direction

In the case of a crystalline network, the crystallinity index is supposed to be high. In our case, the higher crystallinity index concerns KT880 samples. Microscopic observations under polarized lights have revealed the presence of spherulites. That is why we have already adapted the model for the case of spherulite. So at undeformed state, lamellae are homogeneously and randomly distributed. When the stretching starts, as lamellae are thick and numerous, their motion is stronger than the ones of amorphous chains. That is why lamellae follow a fluid motion: lamellae tend to orient parallel to the tensile direction. This means that more lamellae orient in polar way. As the tensile is uniaxial but homogeneous, equatorial lamellae are considered to remain oriented at equator but their long period L_p increases as lamellar stacks are getting away from each other. This is represented in Figure 142.

The consequences of the "Rigid lamella" model (RL) on SAXS and WAXS patterns are:

- In SAXS, as the crystallites (lamellar stacks) tend to rotate parallel to the tensile direction, this means that more normals to lamella surfaces scatter in horizontal direction, resulting in an enhancement of intensity in horizontal direction. This effect is illustrated in Figure 141.

- In WAXS, since crystallites (lamellae) tend to orient vertically, chain axis tends to orient horizontally.

Both modes of deformation are represented in Figure 142 at the scales of the lamellar stack and the spherulite.

Cette thèse est accessible à l'adresse : https://theses.insa-lyon.fr/publication/2023ISAL0006/these.pdf
© [H. Willeman], [2023], INSA Lyon, tous droits réservés

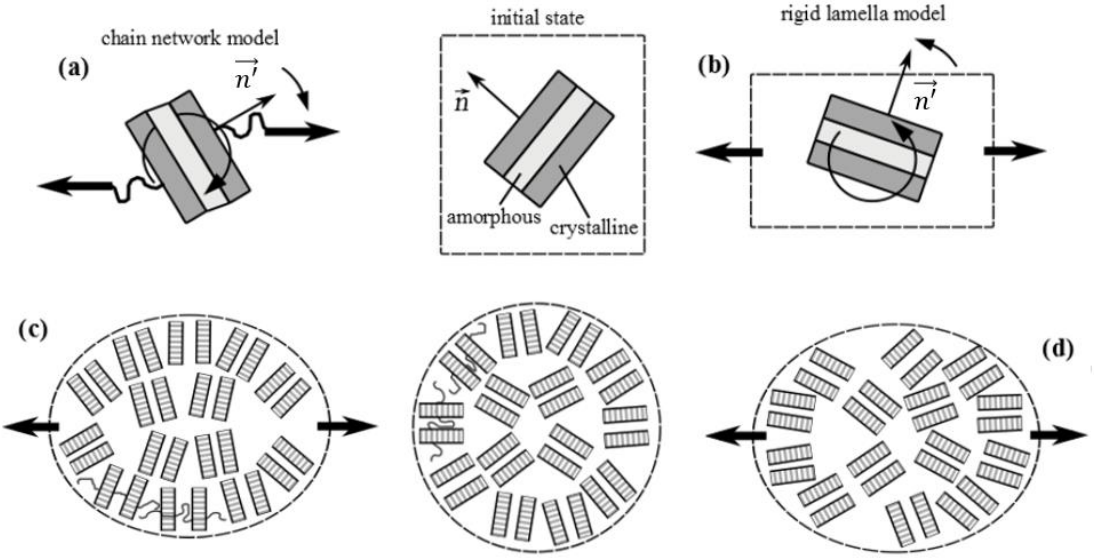


Figure 142. a): Schematics of two distinct modes of deformation: (a) and c) (left): below Tg; b) and d) (right): above Tg. a) and b) show a single lamella stack, c) and d) show a set of lamella stacks within a spherulite.

3. Conclusion

Analyzing the evolution of the SAXS and WAXS pattern during tensile tests, the 'chain network' model is the best candidate to describe deformation of PEEK in the pre-yield regime.

Local tensile deformations in lamellar stacks could be described by an affine transformation of the vectors normal to lamellar planes, which corresponds to a homogeneous description of the local deformation process. This is a further indication of the overall high degree of homogeneity of the local deformation in the material.

Cette thèse est accessible à l'adresse : https://theses.insa-lyon.fr/publication/2023ISAL0006/these.pdf
© [H. Willeman], [2023], INSA Lyon, tous droits réservés

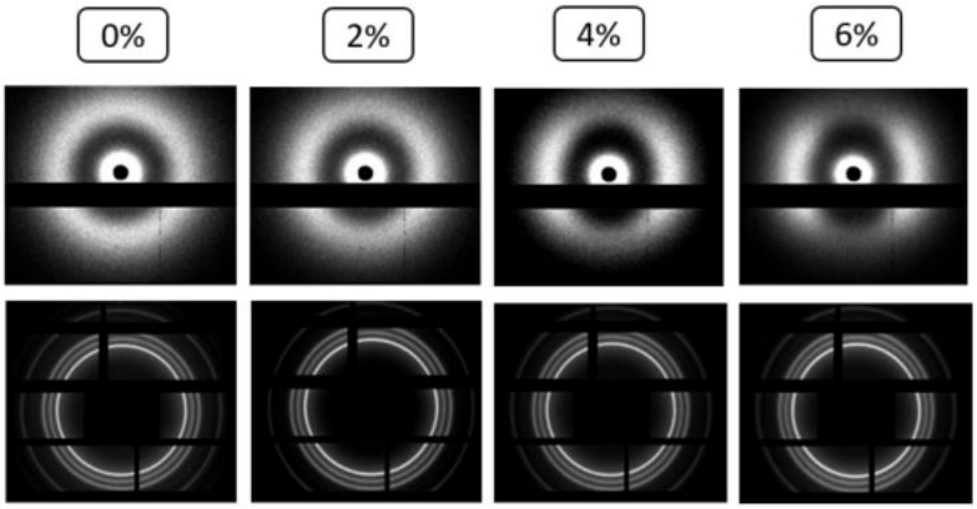


Figure 143. Evolution of SAXS and WAXS patterns in the elastic regime during tensile stretching at room temperature. Intensity concentrates in the HORI direction for SAXS patterns, lamellae orients with their normal perpendicular to the tensile direction.

V. Conclusion

Firstly, the study of the local microscopic strain by SAXS has shown that polar lamellae contract and equatorial lamellae stretch. Furthermore, the ratio between the local and the macroscopic strains depends on the test temperature. At room temperature, far below from T_g, strain at the scale of lamellar stacks is equal to the macroscopic strain. Above glass transition temperature, where the amorphous phase is in the rubbery state, the microscopic strain within lamellar stacks is rapidly lower than macroscopic deformation. For both test temperatures, the reversibility of deformation has been highlighted in the pre-yield regime. In addition, by analyzing the azimuthal distribution of the local strain, it was also found that the deformation of the lamellae system was relatively homogeneous with small but significant deviations however through the material for all samples.

Concerning the crystal strain, the WAXS study has revealed that crystallites are more rigid than the amorphous phase as strain within crystals is always smaller than strain within lamellar stacks and thus smaller than macroscopic strain. A stabilization of tensile strain can be observed for both temperatures but it occurs before yield for tests at 170°C. Hypotheses have been proposed to explain this phenomenon: either the amorphous phase absorbs all the deformation, either only shear may exist within crystals. The degree of homogeneity of the local strain/stress state was also deduced from the azimuthal distribution of the crystal strain. At room temperature, deformation within crystals may be considered homogeneous whereas results of this study for experiments at 170°C demonstrates a non-homogenous deformation of crystals.

For the study of deformation mechanisms scenarios, two models have been developed: the Chain Network (CN) and the Rigid Lamella (RL) models. In the CN model, the orientation mechanisms are ruled by the amorphous chains which transmit the stress between adjacent lamellae. In the RL model, the lamellae govern their own mechanisms of orientation, possibly due to their high aspect ratio. By compiling the SAXS and WAXS data, for both test temperatures, the Chain Network model applies to deformation within PEEK samples.

Cette thèse est accessible à l'adresse : https://theses.insa-lyon.fr/publication/2023ISAL0006/these.pdf
© [H. Willeman], [2023], INSA Lyon, tous droits réservés

Chapter V. Microscopic strain study: plastic regime

I. Introduction 129
II. Deformation in the plastic regime 129
1. Tensile tests at room temperature, $T < T_g$ 129
2. Tensile tests at 170°C, $T > T_g$ 132
III. Deformation at the scale of crystal planes in the plastic regime 133
1. Local strain at the scale of crystal planes, WAXS 133
2. Orientation distributions at room temperature and at T=170°C 136
IV. Deformation at the scale of lamellae stacks in the plastic regime 141
1. Local strain at the scale of lamellar stacks, SAXS 141
2. Orientation distribution 144
V. Central scattering: damage mechanisms 147
1. Tensile tests at T=23°C, $T < T_g$ 147
VI. Proposed mechanisms of deformation in PEEK 153
1. Below glass transition temperature 153
2. Above glass transition temperature 154
Conclusion 157

Cette thèse est accessible à l'adresse : https://theses.insa-lyon.fr/publication/2023ISAL0006/these.pdf
© [H. Willeman], [2023], INSA Lyon, tous droits réservés

I. Introduction

In the previous chapter, the microscopic deformation of PEEK along stretching was investigated essentially in the pre-yield regime, trying to elucidate the deformation processes leading to plasticity of the polymer. In this chapter, we extend the same approach with the same combination of SAXS and WAXS experiments to higher deformation, in the plastic strain domain up to final failure of the material.

The same convention for the description of the orientation of lamellae as adopted in chapter IV will be used. In all figures and schematics, the tensile direction (TD) is horizontal. The azimuthal angle ψ in 2D WAXS and SAXS patterns is referred to the tensile direction (TD): vertical scattering (perpendicular direction) corresponds to ψ = 90°, horizontal scattering (along tensile direction) to ψ = 0°.

Let us now focus on the plastic strain domain below and above the glass transition. As mentioned in chapter IV, the onset of the plastic deformation is a complex process during which a transition from a lamellar (spherulitic) morphology into a fibrillar structure is incipient. In the first part of this chapter, the deformation of the samples is described at a macroscopic scale. Then the second part of the chapter is focused on the impact of deformation on the orientation of crystalline lattice, investigated by WAXS. The third part is focused on deformation processes at large scales, investigated by SAXS: fibrillation and cavitation phenomena are described. Lastly, the global PEEK behavior under tensile stretching in the plastic regime will be tentatively described.

II. Deformation in the plastic regime

1. Tensile tests at room temperature, T < T_g

A representative nominal stress-strain curves for a tensile test performed on KT880 at room temperature (the amorphous phase is in the glassy state) is presented in Figure 144. (see also Figure 94 in which the stress-strain curves for all samples are shown)

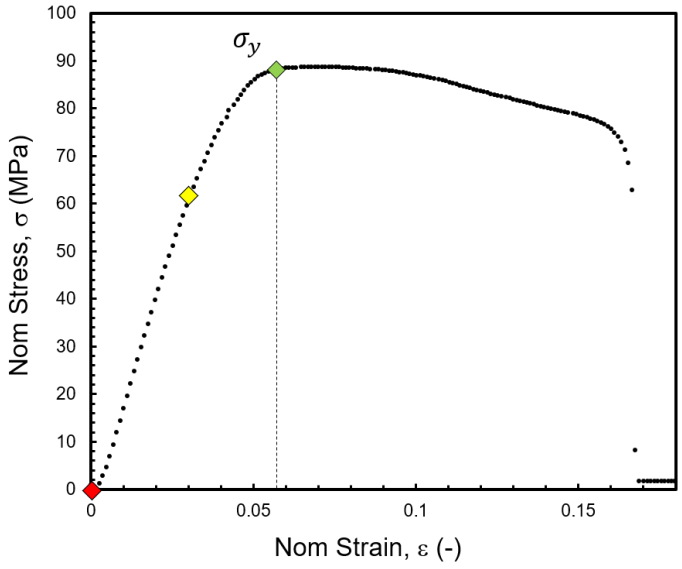


Figure 144. Nominal stress-strain curves for tensile test of KT880 at T=23°C at $\dot{\varepsilon}$ =10-3 s-1

Cette thèse est accessible à l'adresse : https://theses.insa-lyon.fr/publication/2023ISAL0006/these.pdf
© [H. Willeman], [2023], INSA Lyon, tous droits réservés

In the previous chapter, we focused on deformation up to yield (ε=5%). In this part, tensile stretching from yield up to failure will be described. The SAXS patterns near failure of the sample indicate a fibrillar structure of the material.

For tensile tests at room temperature, the video follow-up of the sample during stretching and DIC (Digital Image Correlation) allow measuring the real macroscopic strain in the zone studied by X-ray scattering, at beam location. Several scenarios of observation may happen, depending on whether the beam is localized within or outside the necking zone, in which the deformation is localized. The macroscopic strain at the beamstop measured with DIC in the case of localization of the deformation at the beamstop is reported in Figure 145 as a function of the imposed cross-head displacement of the tensile device.

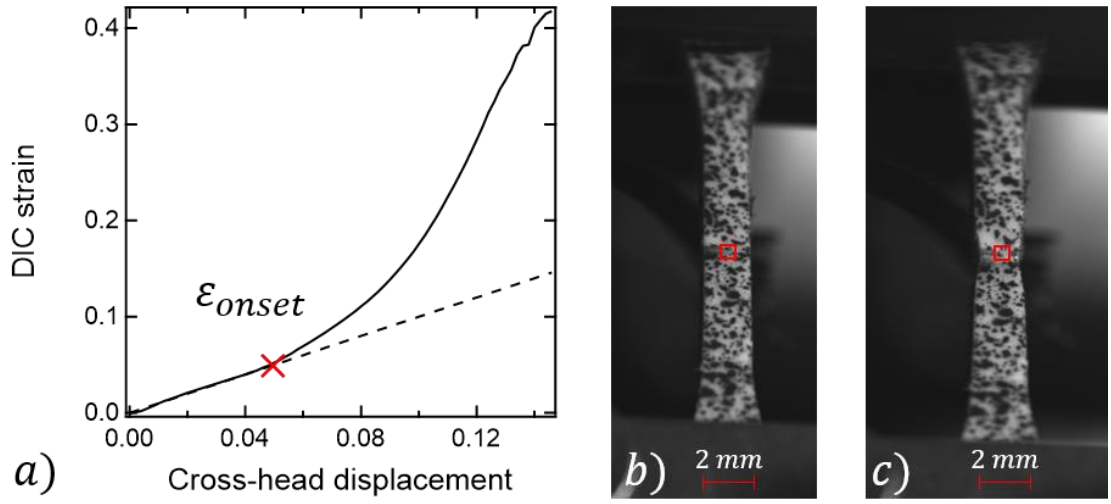


Figure 145. a) Macroscopic strain measured with DIC at the beamstop as a function of cross-head displacement for tensile tests at T=23°C and $\dot{\varepsilon} = 10^{-3}s^{-1}$ and pictures of the samples b) in the initial state and c) for a cross-head displacement of 12%. This figure illustrates the case in which the beam is localized in the necking zone.

With DIC measurements, the localization of macroscopic strain in the sample at the beamstop is highlighted from ε =5%. Indeed, the curve in Figure 145.a allows defining the onset of localization quite precisely. The pictures of the sample in Figure 145.b and c show the state of deformation of the sample at the initial state and for a cross-head displacement of 12%. The actual deformation within the stretched zone of the sample at the beamstop is close to 30%. (Figure 145.a)

Conversely, the macroscopic strain at the beamstop measured with when the deformation is localized outside the zone studied by SWAXS is reported in Figure 146 as a function of the imposed cross-head displacement of the tensile device.

The strain at the beamstop starts to deviate from the expected behavior early on in the elastic regime (see yellow dot in Figure 146.a). This deviation would occur around 2.5% which roughly corresponds to the onset of non-linearity in the mechanical response (see Figure 144). However, the material remains nearly elastic up to about 5%. Then, from the yield point, the strain nearly stabilizes in the studied zone at it localizes further in the sample. This confirms that the strain varies much slower than the macroscopic elongation, and much faster in the necking zone. Further extension of the sample then involves essentially the relative growth of the necking zone as compared to the unstretched zone.

Following the real strain seen by the sample at the beamstop by digital image correlation is thus necessary as the local strain values for the two presented cases may be very different. The real strain for

Cette thèse est accessible à l'adresse : https://theses.insa-lyon.fr/publication/2023ISAL0006/these.pdf
© [H. Willeman], [2023], INSA Lyon, tous droits réservés

the same cross-head displacement of 12% is 30% at the beamspot in the first case whereas it is 6.5% in the second one. In order to compare with X-ray scattering results, the knowledge of the real state of deformation of the sample at the studied zone is of key importance.

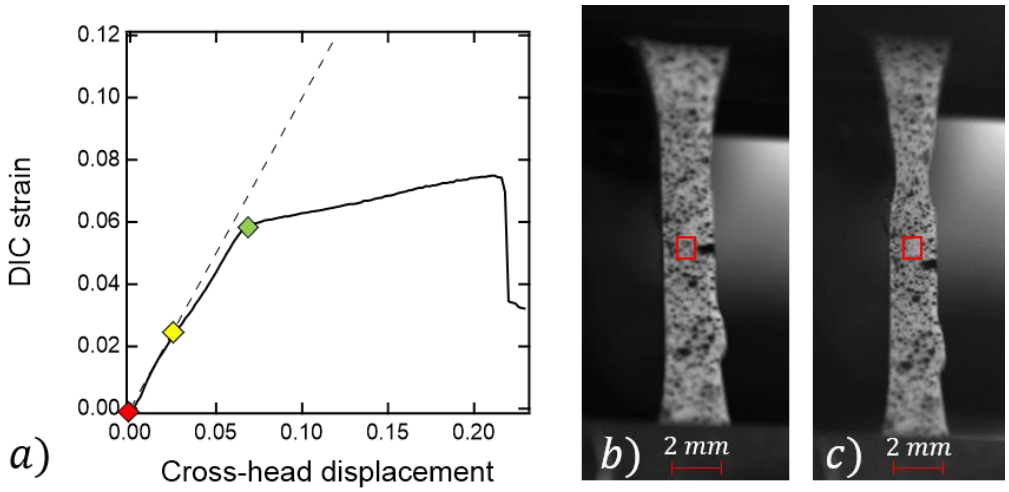


Figure 146. a) Macroscopic strain measured with DIC at the beamstop as a function of cross-head displacement for tensile tests at T=23°C and $\dot{\varepsilon} = 10^{-3}s^{-1}$ and pictures of the samples b) in the initial state and c) for a cross-head displacement of 15%. The sudden drop in the curve corresponds to final failure of the sample. This figure illustrates the case in which the beam is localized outside the necking zone.

Residual deformation during loading-unloading tensile tests

The residual deformation in the plastic regime was studied via loading-unloading tensile tests presented in the previous chapter (see Figure 115). The second cycle of these experiments consists in stretching the polymer beyond yield before unloading back to zero force. A full loading-unloading experiment is displayed in Figure 147.

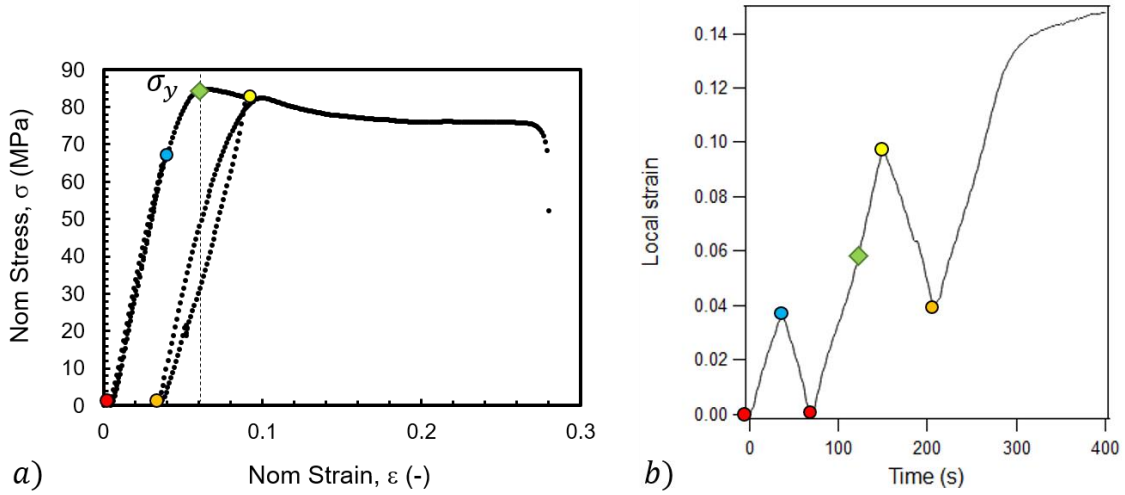


Figure 147. a) Stress-strain curve of a loading-unloading tensile experiment b) evolution of local macroscopic strain measure by DIC with time

The first cycle of this experiment has been described in the previous chapter. At the beginning of the second loading-unloading step, the material has been stretched below yield stress and has come back to its initial state after unloading to zero force. Then, the material is stretched past the yield point. The slope observed is the same as in the first tensile step. When unloading back to force zero, a macroscopic residual strain of 4% is observed. The last tensile cycle up to failure which starts from this residual stress exhibits then the same slope and shape as the first and second cycles.

Cette thèse est accessible à l'adresse : https://theses.insa-lyon.fr/publication/2023ISAL0006/these.pdf
© [H. Willeman], [2023], INSA Lyon, tous droits réservés

2. Tensile tests at 170°C, T > T_g

A representative nominal stress-strain curve for a tensile test performed on KT820 at 170°C (the amorphous phase is in the rubbery state) is presented in Figure 148.

For tensile tests at 170°C, no access for video follow-up of the sample deformation was possible because of the presence of Kapton windows to seal the oven. The localization of deformation in real time was thus not studied. However, results are reproducible for all tests at every scale. This would indicate that no significant localization of deformation occurs in the samples for tensile tests at temperature above T_g.

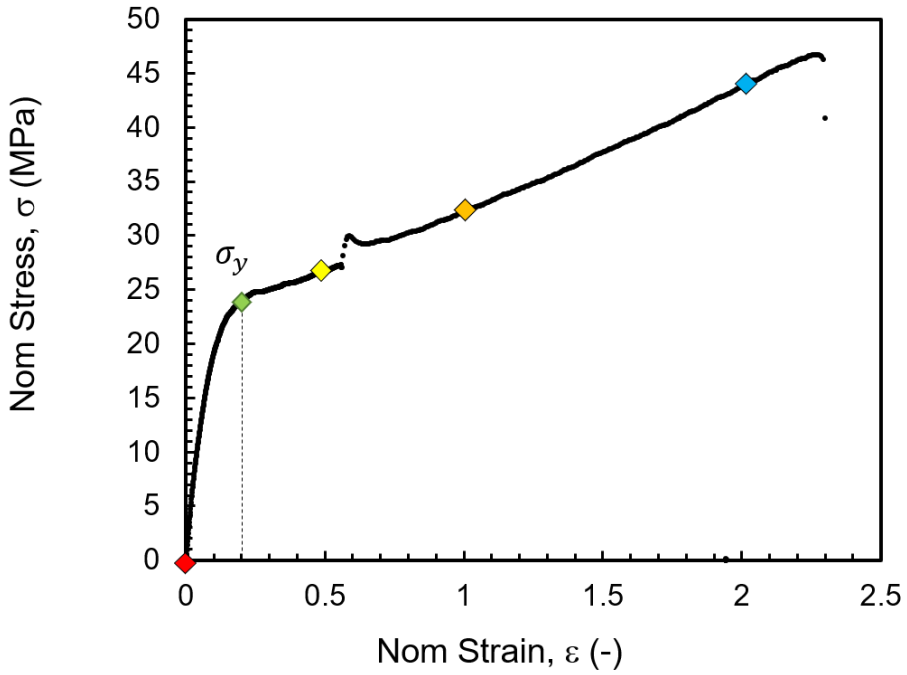


Figure 148. Nominal stress-strain curves for tensile test of KT820 at T=170°C at $\dot{\varepsilon}$ =10-3 s-1

At about 50% strain, the strain rate was increased from 10^{-3} s^{-1} to 5. 10^{-3} s^{-1}. A stress overshoot corresponds to this increase followed by a relaxation of the stress (see Figure 148).

Besides, the temperature T=170°C is quite close to T_g. It is even located within the tanδ peak associated to T_g (see DMA curve in Figure 91). As a consequence, it may be expected that the mechanical response depends on the strain rate. Effectively, it is observed in Figure 148 that the slope measured in the upper part of the curves (between orange and blue diamond, $\dot{\varepsilon}$ =5.10^{-3} s^{-1}) is larger than in the lower part (between green and yellow diamond, $\dot{\varepsilon}$ =10^{-3} s^{-1}). Nevertheless, the material is not fully plasticized, as the stress goes on increasing beyond the yield point. This would further strengthen that no necking occurs at this temperature and the macroscopic deformation is homogeneous.

The slope $\frac{\partial \sigma}{\partial \varepsilon}$ (corresponding to an effective modulus in this post-yield regime) is of the order of 10 MPa. As said before, this slope should depend on the strain rate (as T=170°C is close to T_g). However, this value is compatible with the modulus corresponding to chain extension. We may thus speculate that the response of the material in this pseudo-plastic regime is driven by the elastic response (extension) of chain portions connecting crystallites.

Cette thèse est accessible à l'adresse : https://theses.insa-lyon.fr/publication/2023ISAL0006/these.pdf
© [H. Willeman], [2023], INSA Lyon, tous droits réservés

III. Deformation at the scale of crystal planes in the plastic regime

In this part, the deformation of the crystalline lattice of PEEK during tensile stretching in the plastic regime up to failure will be reviewed. The influence of temperature on deformation processes like orientation of crystallites will be analyzed.

1. Local strain at the scale of crystal planes, WAXS

a. Tensile tests at room temperature, $T < T_g$

WAXS patterns corresponding to the deformation of crystal planes in the plastic regime for tensile tests at room temperature are displayed in Figure 149.a. The measured local strain in HORI and VERTI lamellae stacks through the whole tensile test is plotted as a function of the machine macroscopic strain in Figure 149.b. The macroscopic behavior of the following tensile test is described in Figure 145.

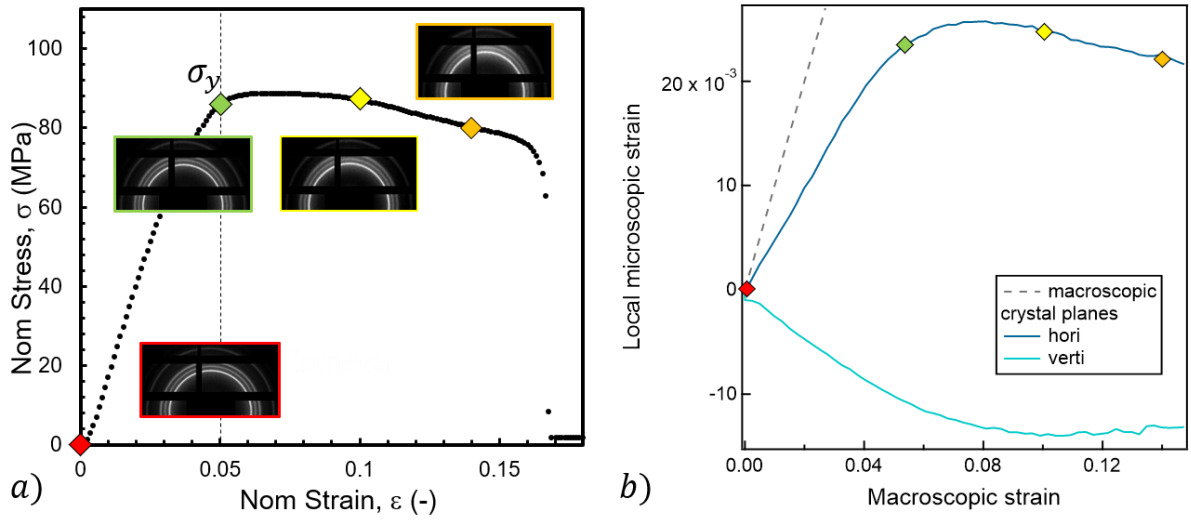


Figure 149. a) Evolution of WAXS patterns with stretching along stress-strain curve for room temperature tensile tests and b) local microscopic strain at the scale of (110) crystal planes in the HORI and VERTI direction

From the yield point (green diamond on the stress-strain curve), the tensile strain both in the HORI and VERTI directions starts to stabilize then decreases slightly but consistently. This would mean that beyond yield, either the amorphous phase absorbs all the deformation, or, crystal shear (which would not affect the distance between planes) is a part of the deformation process.

Figure 150 illustrates the evolution of the WAS pattern along the tensile test. The shape of the diffraction peaks does not seem to evolve significantly with deformation up to near final failure of the sample and this consideration is valid in every direction. However, a slight increase of the width of the diffraction peaks is observed. In Figure 151 is represented the evolution of the width of the (110) peak obtained during the fitting of the maximum of the peak process. As expected, no evolution of the width is observed during the elastic regime. However, the width of the peak is indeed increasing with strain. This would mean that the size of the crystallites decreases with deformation. At this point we did not attempt to estimate the evolution of the transverse crystal size using the Scherrer equation, as the fitting of the peak was not precise enough yet.

Cette thèse est accessible à l'adresse : https://theses.insa-lyon.fr/publication/2023ISAL0006/these.pdf
© [H. Willeman], [2023], INSA Lyon, tous droits réservés

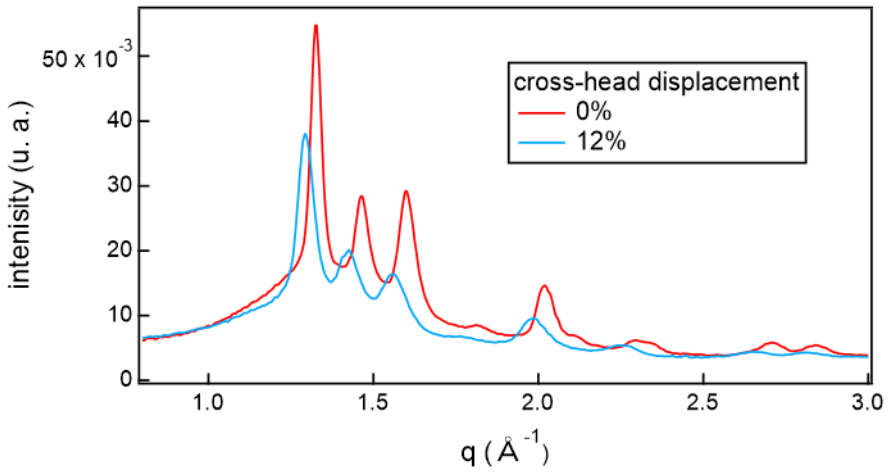


Figure 150. WAXS diffraction patterns in the HORI direction for samples in the initial state and for ε=12% (room temperature). The width of the diffraction peaks does not evolve significantly with stretching.

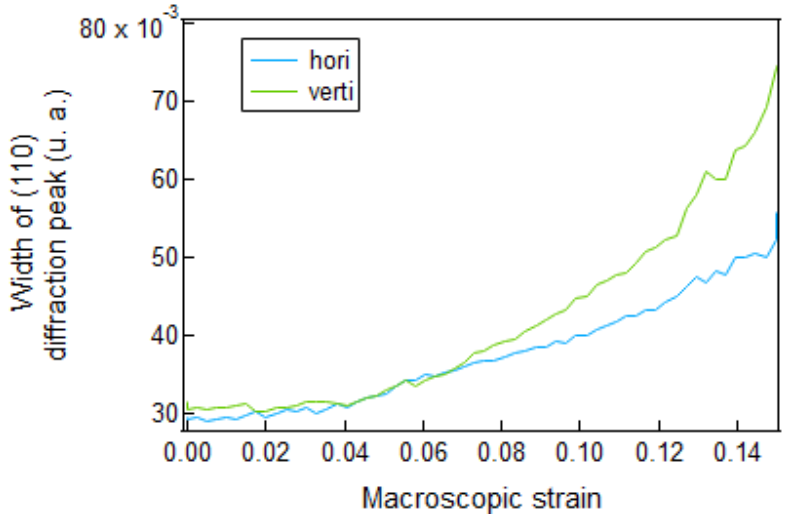


Figure 151. Evolution of the width of (110) diffraction peak with the macroscopic strain

Residual deformation during loading-unloading tensile tests

The evolution of the local macroscopic strain (measured by DIC) and the microscopic strain at the scale of crystal planes, both in the HORI and VERTI direction are plotted as a function of time in Figure 152. Plasticity is firstly and mostly observed in the HORI direction at the scale of crystal planes in the second tensile step. Then, when unloading the sample back to zero force, a residual deformation of 4% can be observed at the macroscopic scale. This information can also be retrieved from the stress-strain curve. However, no residual deformation is present at the scale of (110) crystal planes.

Cette thèse est accessible à l'adresse : https://theses.insa-lyon.fr/publication/2023ISAL0006/these.pdf
© [H. Willeman], [2023], INSA Lyon, tous droits réservés

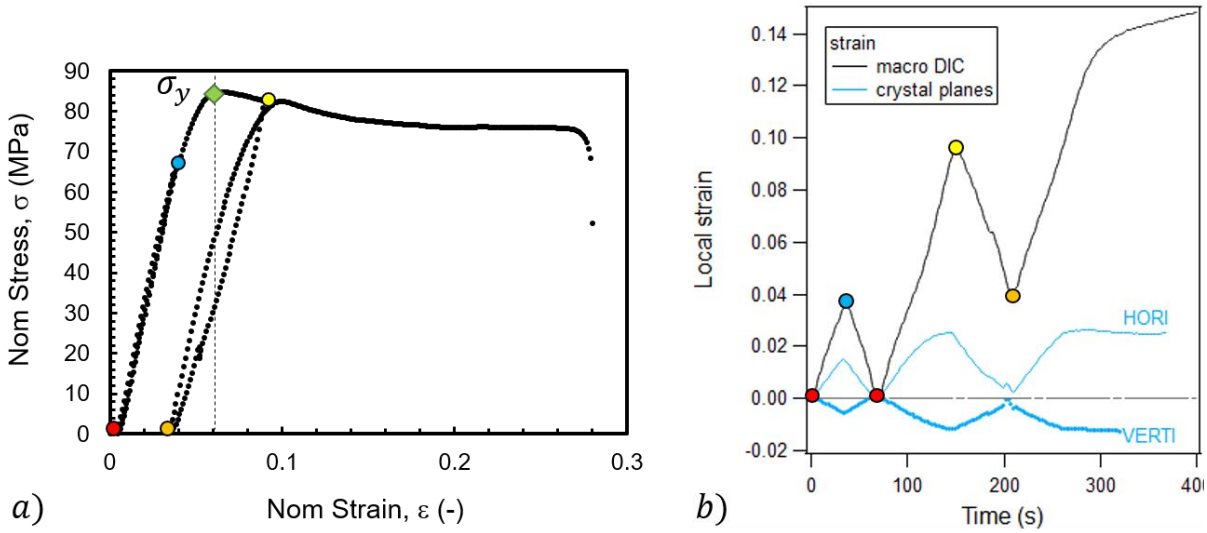


Figure 152. a) Stress-strain curve of a loading-unloading tensile experiment b) evolution of local macroscopic strain measured by DIC and of microscopic strain of (110) crystal planes with time

b. Tensile tests at T=170°C, T > T_g

WAXS patterns corresponding to deformation of crystal planes in the plastic regime for stretching above glass transition at 170°C are displayed in Figure 153.a. The measured local strain in HORI and VERTI lamellae stacks through the whole tensile test is plotted as a function of the machine macroscopic strain in Figure 153.b. The macroscopic behavior of this tensile test is described in Figure 148.

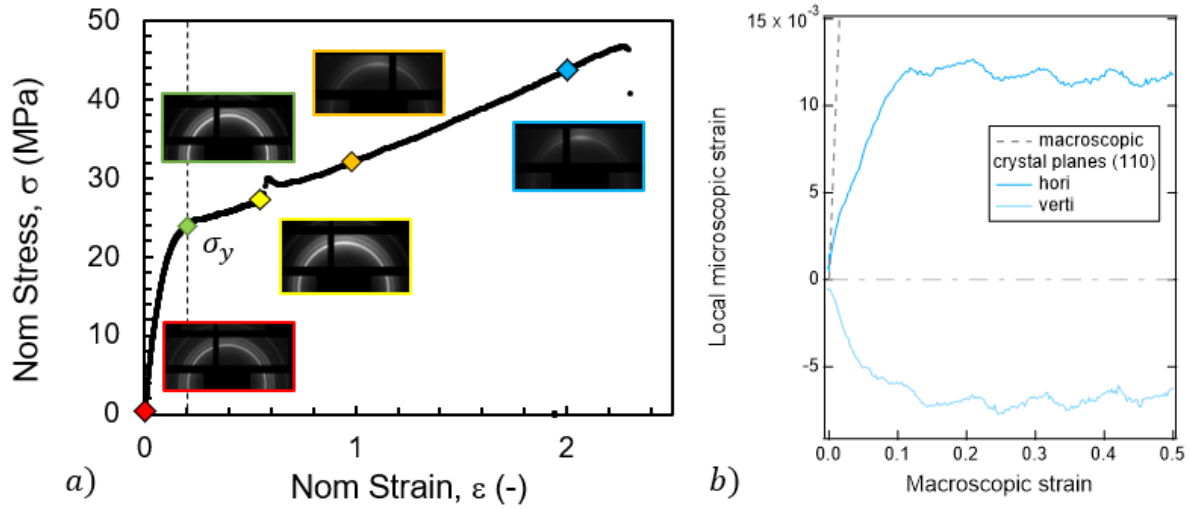


Figure 153. a) Evolution of WAXS patterns with stretching along stress-strain curve for tensile tests at 170°C and b) local microscopic strain at the scale of crystal planes in the HORI and VERTI direction

From the beginning of stretching, the microscopic strain within (110) planes is much lower (in order of magnitude, it is 10 times lower) than the macroscopic strain. This behavior is expected as the amorphous phase (in the rubbery state) is less rigid than crystallites and will sustain most of the deformation. This is consistent with the hypothesis that the behavior is driven by chain extension as mentioned before. The oscillation observed in the strain plateau are likely to originate only from the displacement of the tensile device.

Cette thèse est accessible à l'adresse : https://theses.insa-lyon.fr/publication/2023ISAL0006/these.pdf
© [H. Willeman], [2023], INSA Lyon, tous droits réservés

2. Orientation distributions at room temperature and at T=170°C

The different possible configurations of crystallites and crystalline planes are represented in Figure 154. The corresponding scattering is schematized (see also Figure 128). This allows identifying from which crystallites the scattering is arising from.

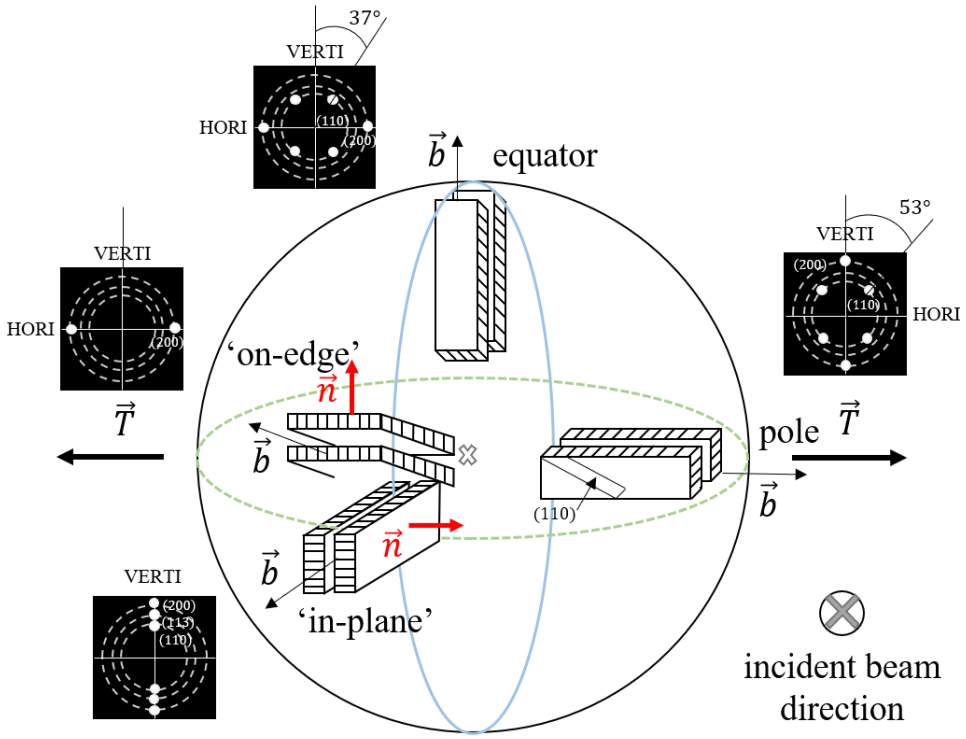


Figure 154. Lamellae distribution in a spherulite and corresponding 2D WAXS patterns. The incident beam direction is perpendicular to the figure.

The angles of diffraction of (110) planes for different lamellae configurations are calculated using the crystalline lattice parameters as represented in Figure 155.

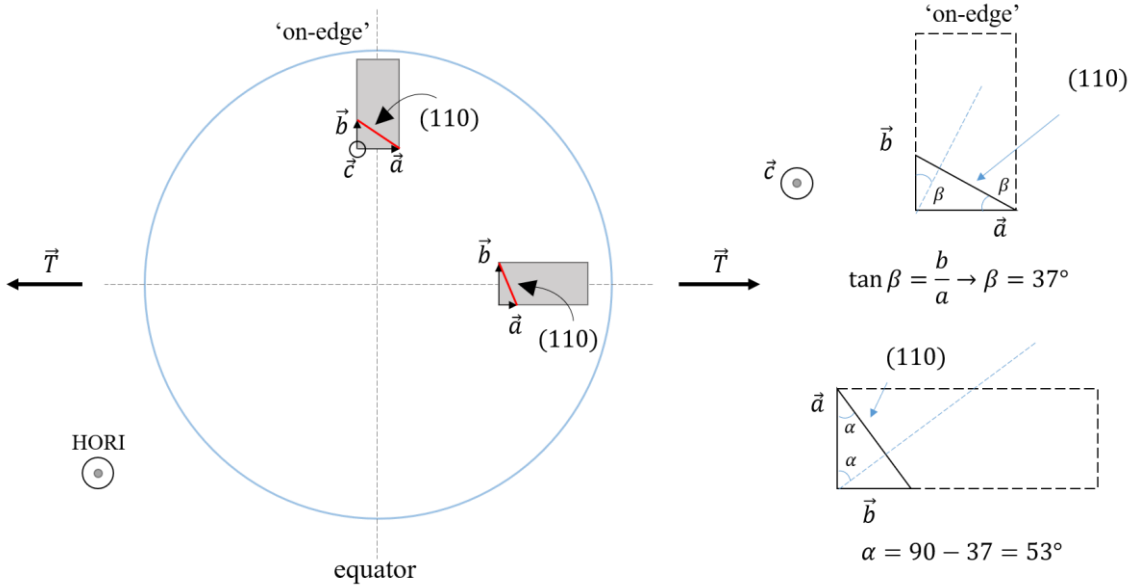


Figure 155. Schematics of 'on-edge' and 'in-plane' lamellae and the corresponding WAXS diffraction angle of (110) planes

Cette thèse est accessible à l'adresse : https://theses.insa-lyon.fr/publication/2023ISAL0006/these.pdf
© [H. Willeman], [2023], INSA Lyon, tous droits réservés

For better representation of the global behavior of the crystal planes, for each test temperature, 3D representation of WAXS patterns are presented below along deformation.

In Figure 156, a tensile test at room temperature with localization of deformation at the beamstop is described. For all crystal planes, the intensity is initially nearly isotropic. As deformation increases, the intensity globally decreases. From the yield point, an anisotropic distribution of intensity appears first for the (113) and (200) planes. The intensity concentrates in the VERTI direction. The (10) plane family has a slightly different behavior. It stays very little oriented up to well into the plastic regime. Only at very high extension (ε_{macro}=0.4) it shows significant orientation. The presence of a double maximum of intensity around the VERTI direction indicates that the material is not yet fully oriented in a fibrillar type of morphology. Near failure for a strain of 40%, for (200) planes, diffraction in the HORI direction has disappeared. This diffraction is due to lamellae 'on edge' in the equator. Thus, these lamellae disappear at high elongation. If we consider a rotation model of the lamellae, 'on-edge' lamellae (or lamellae located in the equator and in intermediate position between 'on-edge' and 'in-plane) position rotate towards the 'in-plane' position. All the diffraction of (200) crystal planes is thus in the VERTI direction.

The same representation is used on Figure 157 for tensile test at 170°C. The global scenario of orientation if similar to the room temperature stretching one detailed previously. However, the orientation of crystal planes in the VERTI direction is more pronounced that for tensile tests at room temperature. At higher temperature, the material has more mobility to orient their chain with deformation before failure.

The main observation is that no significant orientation is detected at the onset of the plastic (or pseudo-plastic) regime. This may be expected as the corresponding strain is small in any case (about 5% at room T, about 20% at T=170°C). Significant orientation starts to be detected quite far into the post-yield regime.

Cette thèse est accessible à l'adresse : https://theses.insa-lyon.fr/publication/2023ISAL0006/these.pdf
© [H. Willeman], [2023], INSA Lyon, tous droits réservés

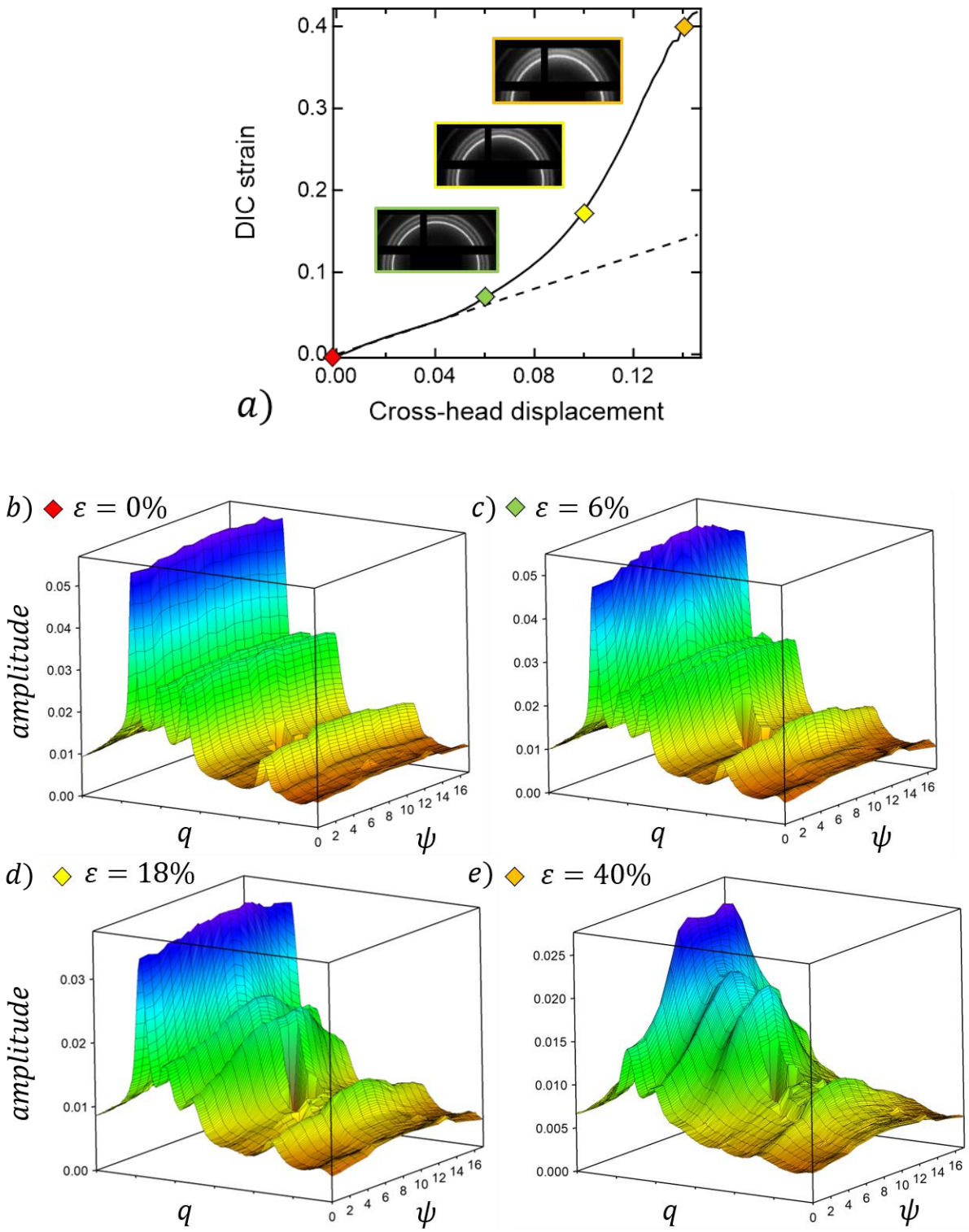


Figure 156. a) Macroscopic strain measured by DIC for tensile tests at room temperature and corresponding 3D representation WAXS patterns as a function of q and ψ (here the azimuthal sector, each sector being 10° wide) for reel strain of b) 0% c) 6% d) 18% and e) 40%. The azimuthal angle ψ = 90° corresponds to plans perpendicular to tensile direction, i.e. with chains along the tensile direction. The indicated strain values are those measured by DIC at the beamstop location.

Cette thèse est accessible à l'adresse : https://theses.insa-lyon.fr/publication/2023ISAL0006/these.pdf
© [H. Willeman], [2023], INSA Lyon, tous droits réservés

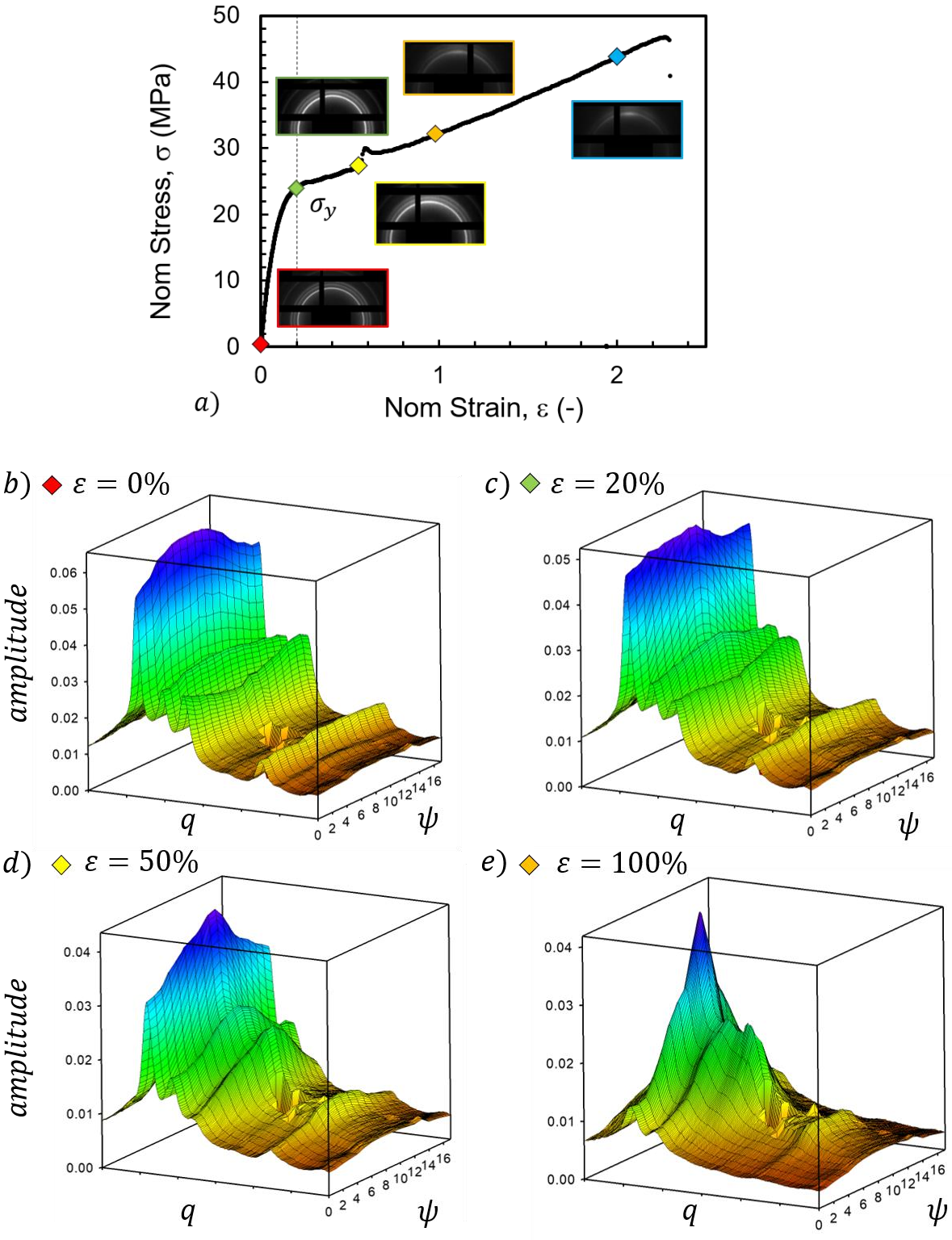


Figure 157. a) Macroscopic strain measured by DIC for tensile tests at 170°C and corresponding 3D representation WAXS patterns as a function of q and ψ for reel strain of b) 0% c) 20% d) 50% and e) 100%

Cette thèse est accessible à l'adresse : https://theses.insa-lyon.fr/publication/2023ISAL0006/these.pdf
© [H. Willeman], [2023], INSA Lyon, tous droits réservés

To describe more quantitatively the evolution of the amplitude of the peak, the intensities of (110) planes of WAXS patterns as a function of the azimuthal angle ψ are plotted in Figure 158, for the two different temperatures studied. At both temperatures, the behavior is qualitatively the same. The crystal planes tend to orient with their normals in the vertical direction, that is, chains tend to orient along the tensile direction.

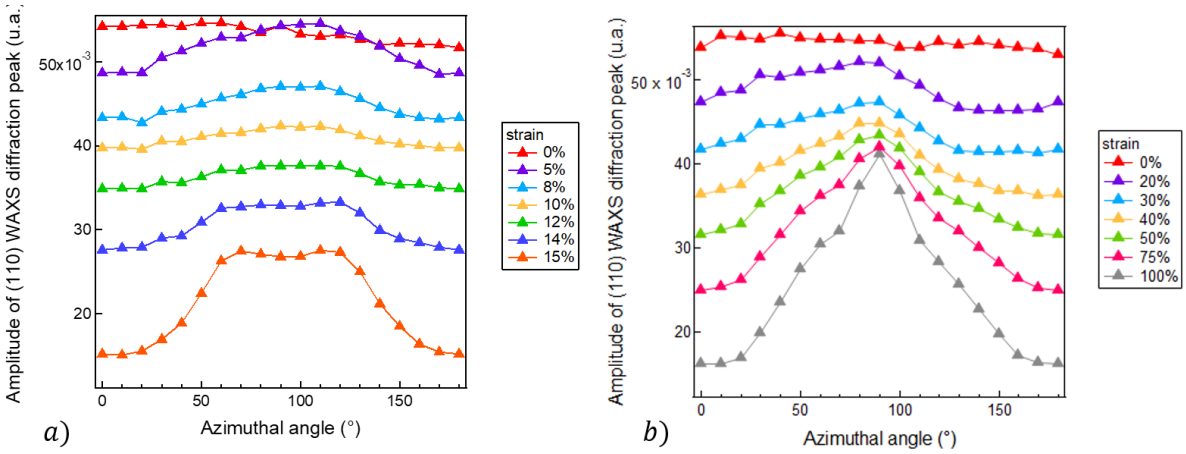


Figure 158. Amplitude of (110) WAXS diffraction peak as a function of azimuthal angle in the elastic regime various strains for tensile tests at a) 23°C and b) 170°C

At 170°C, the (110) plane family shows a much more marked orientation than at room temperature.

Cette thèse est accessible à l'adresse : https://theses.insa-lyon.fr/publication/2023ISAL0006/these.pdf
© [H. Willeman], [2023], INSA Lyon, tous droits réservés

IV. Deformation at the scale of lamellae stacks in the plastic regime

This part of this chapter will focus on plasticity and deformation processes taking place in the stretched sample at the scale of lamellar stacks. The distribution of orientation of lamellae shall be studied throughout the whole plastic regime to fully characterize the local deformation in the stretched samples.

1. Local strain at the scale of lamellar stacks, SAXS

a. Tensile tests at room temperature, $T < T_g$

SAXS patterns corresponding to deformation of lamellar stacks in the plastic regime at room temperature are displayed in Figure 159.a. The measured local strains in HORI and VERTI lamellar stacks along tensile tests up to failure are plotted as a function of the machine macroscopic strain in Figure 159.b.

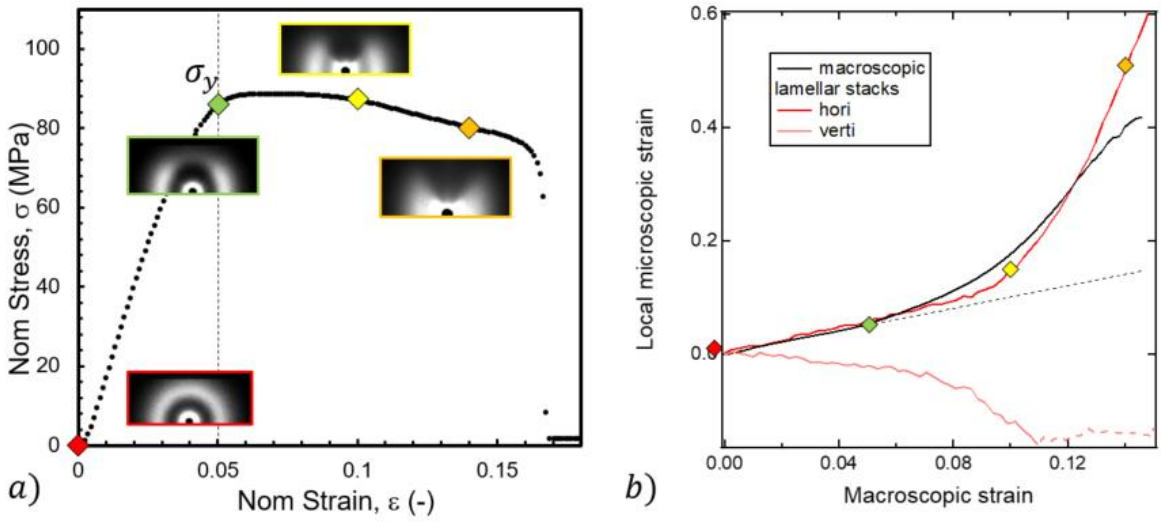


Figure 159. a) Evolution of SAXS patterns with stretching along stress-strain curve for room temperature tensile tests and b) local microscopic strain at the scale of lamellae stacks in the HORI and VERTI direction compared with the macroscopic strain measured by DIC, the dashed line represents the nominal macroscopic strain.

As previously stated, the local tensile strain in HORI lamellar stacks is equal to the macroscopic strain in the elastic regime. Starting at the yield point (represented by the green diamond in Figure 159), localization of strain at the beam position occurs. The macroscopic strain starts to deviate from the expected behavior from ε=6%. From this point, the slopes of the microscopic strains within HORI and VERTI lamellar stacks change quite abruptly. The strain within HORI dramatically increases. For VERTI lamellae, the compressive strain increases as well, but from about ε=11%, the correlation peak becomes too broad to fit it as it overlaps with central scattering.

Residual deformation during loading-unloading tensile tests

The full loading-unloading experiment is displayed in Figure 160. The evolution of the local macroscopic strain (measured by DIC) and the microscopic strains at the scales of lamellar stacks and crystal planes, both in the HORI and VERTI directions are displayed as a function of time. The microscopic strain within lamellar stacks is also represented as a function of the cross-head displacement.

Cette thèse est accessible à l'adresse : https://theses.insa-lyon.fr/publication/2023ISAL0006/these.pdf
© [H. Willeman], [2023], INSA Lyon, tous droits réservés

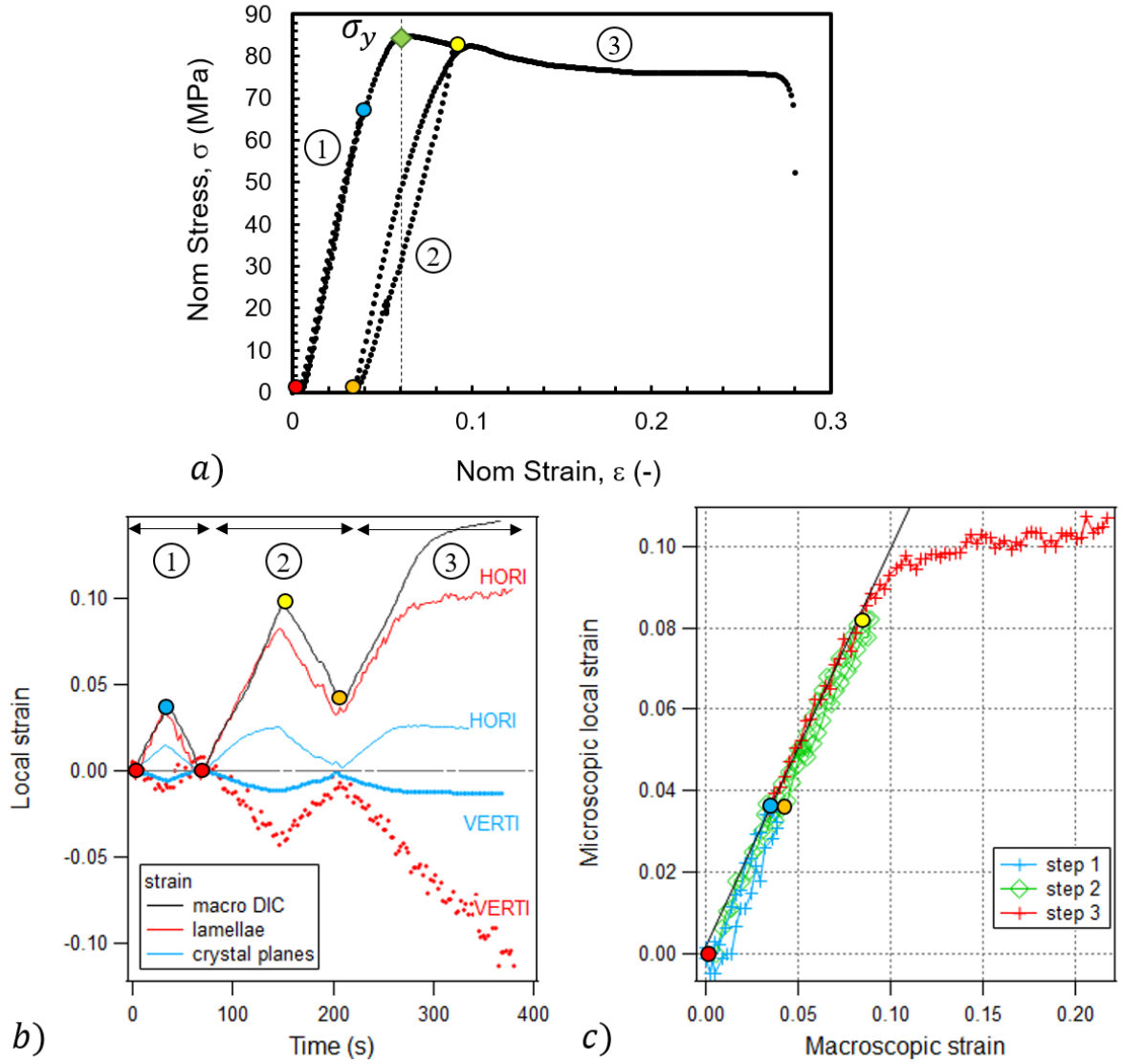


Figure 160. a) Stress-strain curve for a tensile test with loading-unloading cycles b) macroscopic and microscopic strains at the scale of lamellae stacks and crystal planes as a function of time c) evolution of the microscopic tensile strain (HORI direction) within lamellae as a function of the macroscopic strain (cross-head displacement). Full black curve represents y=x

As in the first step, the microscopic strain within lamellar stacks is equal to the macroscopic strain and follows the same slope. As seen before, plasticity is firstly observed at the scale of crystal planes. When unloading back the sample to zero force, a residual deformation of 4% can be observed at the macroscopic scale. At the lamellar stacks scale, a residual deformation of 4% is also observed but only in the HORI direction. However, no residual deformation is present at the scale of (110) crystal planes. *This would mean that the plastic deformation close to yield initiates in the amorphous phase of lamellae scattering in the HORI direction, with their normal aligned with the tensile direction.*

b. Tensile tests at T=170°C, T > T_g

The measured local strains in HORI and VERTI lamellar stacks are plotted as a function of the machine macroscopic strain for tensile tests at 170°C in Figure 161. The first parts of the curves were described in the previous chapter. In the elastic regime, the microscopic strain at the scale of lamellae stacks is globally smaller than the macroscopic strain. Up to the yield strain (ε=20%), no large qualitative change is observed in the SAXS patterns, the intensity is distributed in all directions, with some anisotropy however, reflecting some tendency to orient (Figure 122). For a nominal strain of 50% (yellow dot),

Cette thèse est accessible à l'adresse : https://theses.insa-lyon.fr/publication/2023ISAL0006/these.pdf
© [H. Willeman], [2023], INSA Lyon, tous droits réservés

intensity starts to concentrate in the HORI direction. Then, the strain rate was increased to 5.10^{-3} s^{-1} until failure occurs at about 230%. Close to failure, only central scattering remains in SAXS patterns, no signal from the periodic lamellar stacking is detected anymore, in any direction. This indicates that the initial morphology of lamellar stacks has been completely transformed into a fibrillar material.

The observed apparent decrease of L_p as the deformation increases is an artefact created by the fitting procedure. In reality, q_{max} continually decreases in the HORI direction which means that L_p continually increases along the deformation. As presented in Figure 167, the central scattering completely overlaps the correlation peak starting from a macroscopic strain of the order 12%. It becomes then impossible to fit the correlation peak and to follow the evolution of q_{max}.

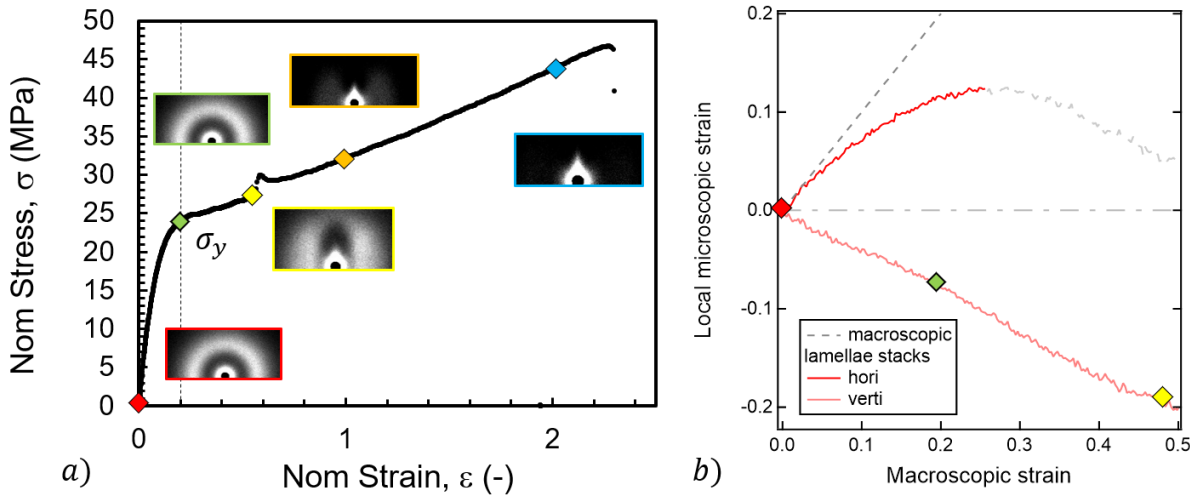


Figure 161. a) Evolution of SAXS patterns along the stress-strain curve for a tensile test at 170°C and b) local microscopic strain at the scale of lamellae stacks in the HORI and VERTI as a function of the macroscopic strain. The decrease of the HORI local strain (dashed curve) is a fitting artefact.

Comparison between the macroscopic and microscopic strains

In order to compare macroscopic and microscopic strain values along the localization zone, SAXS acquisition were led along the sample necking zone represented by the white line on the sample in Figure 162 for a fixed macroscopic elongation (cross-head displacement) of 20%. The tensile traction was paused in the plastic regime at ε=20%, the sample was let to relax (Fig 19a and b) up to the red point in Figure 162.b before SAXS acquisition started along the necking region. Nevertheless, some relaxation processes could still occur simultaneously during SAXS acquisition. During this experiment, the macroscopic strain was also calculated along the white with the DIC system described in chapter III and the measured strain is plotted in Figure 162.

Along the white line, the necking zone is divided into 200 points for DIC whereas only 12 points are acquired by SAXS in the same zone. However, the microscopic strain differs slightly from DIC macroscopic strain. One point measured by SAXS (yellow dot) represents an average strain that corresponds to 16 points calculated via DIC. All along the sample, the levels of deformation between microscopic and macroscopic are coherent, and phenomena like strain localization can be analyzed at both scales. However, the microscopic strain differs slightly from DIC macroscopic strain.

Cette thèse est accessible à l'adresse : https://theses.insa-lyon.fr/publication/2023ISAL0006/these.pdf
© [H. Willeman], [2023], INSA Lyon, tous droits réservés

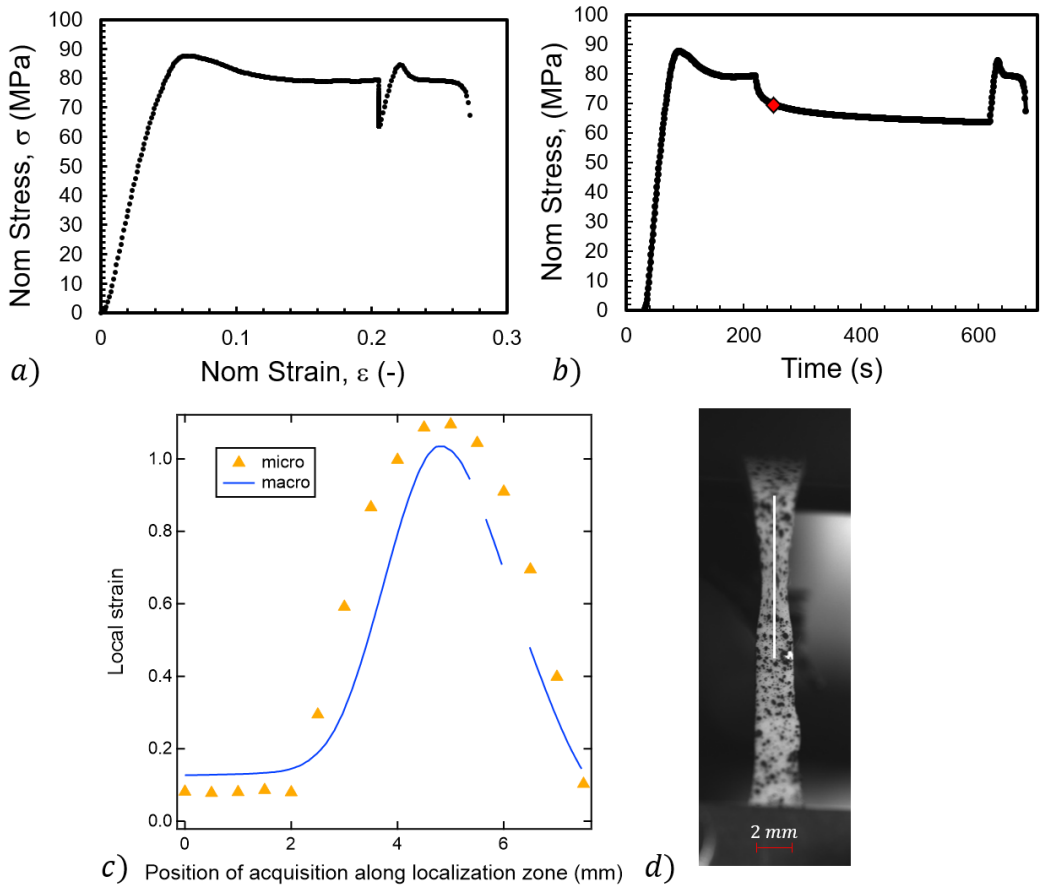


Figure 162. a) Stress-strain curve for a tensile test at room temperature. The cross-head displacement is paused for ε=20%, b) representation of the stress as a function of time, the sample is let to relax until the red diamond before SAXS acquisition during the stress plateau, c) macroscopic and microscopic strain acquired along sample through necking zone for ε=20% (represented by white line on sample) and d) picture of the sample

2. Orientation distribution

As for WAXS analysis, for a better representation of the global behavior of the lamellar stacks, 3D representation of SAXS patterns are presented below for different steps of elongation in Figure 163 for tensile tests at room temperature and in Figure 164 for experiments at T=170°C.

Cette thèse est accessible à l'adresse : https://theses.insa-lyon.fr/publication/2023ISAL0006/these.pdf
© [H. Willeman], [2023], INSA Lyon, tous droits réservés

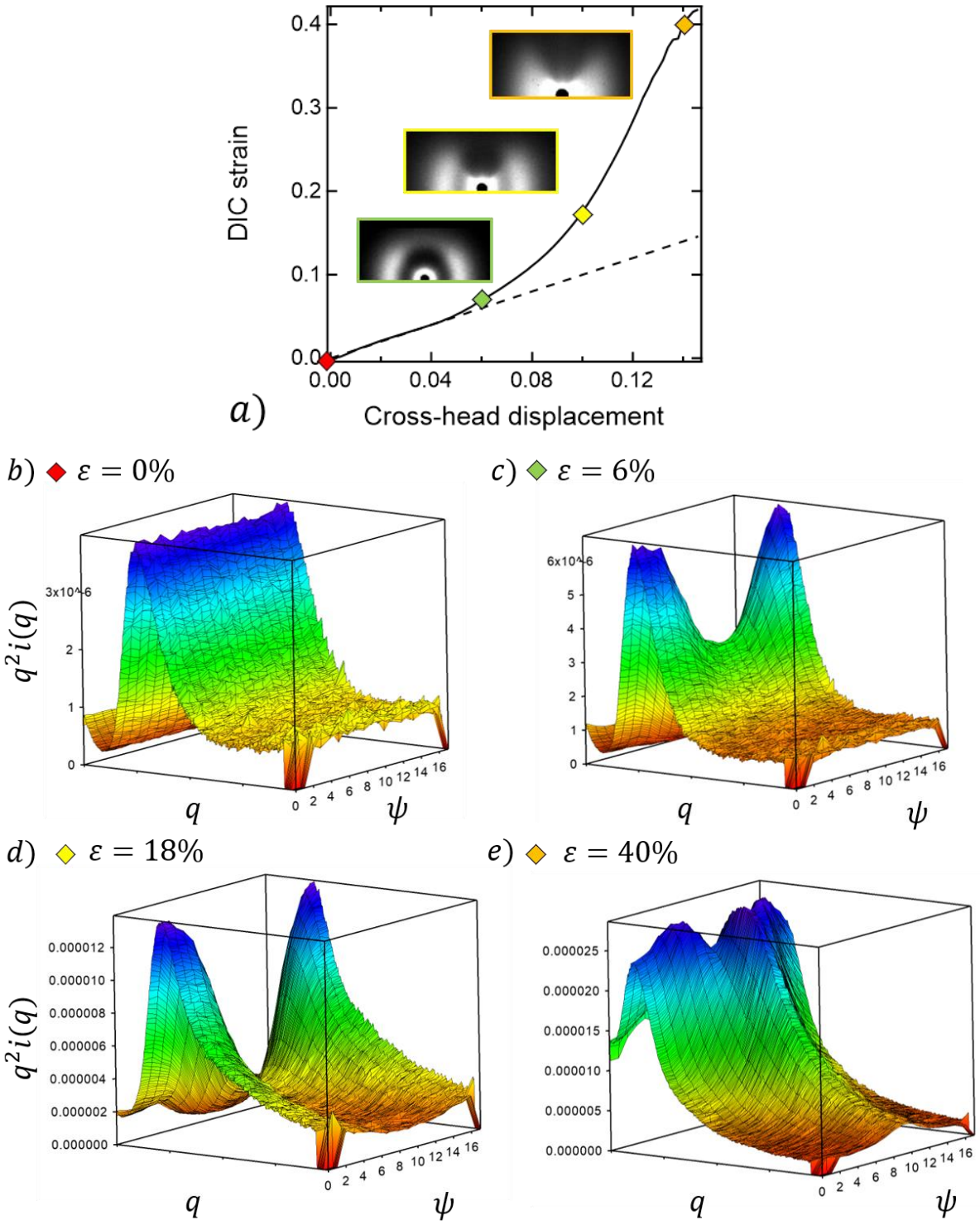


Figure 163. a) Macroscopic strain measured by DIC for a tensile test at room temperature and corresponding 3D representations of SAXS patterns as a function of q and azimuthal angle ψ for macroscopic strain values (measured by DIC) of b) 0% c) 6% d) 18% and e) 40%

Cette thèse est accessible à l'adresse : https://theses.insa-lyon.fr/publication/2023ISAL0006/these.pdf
© [H. Willeman], [2023], INSA Lyon, tous droits réservés

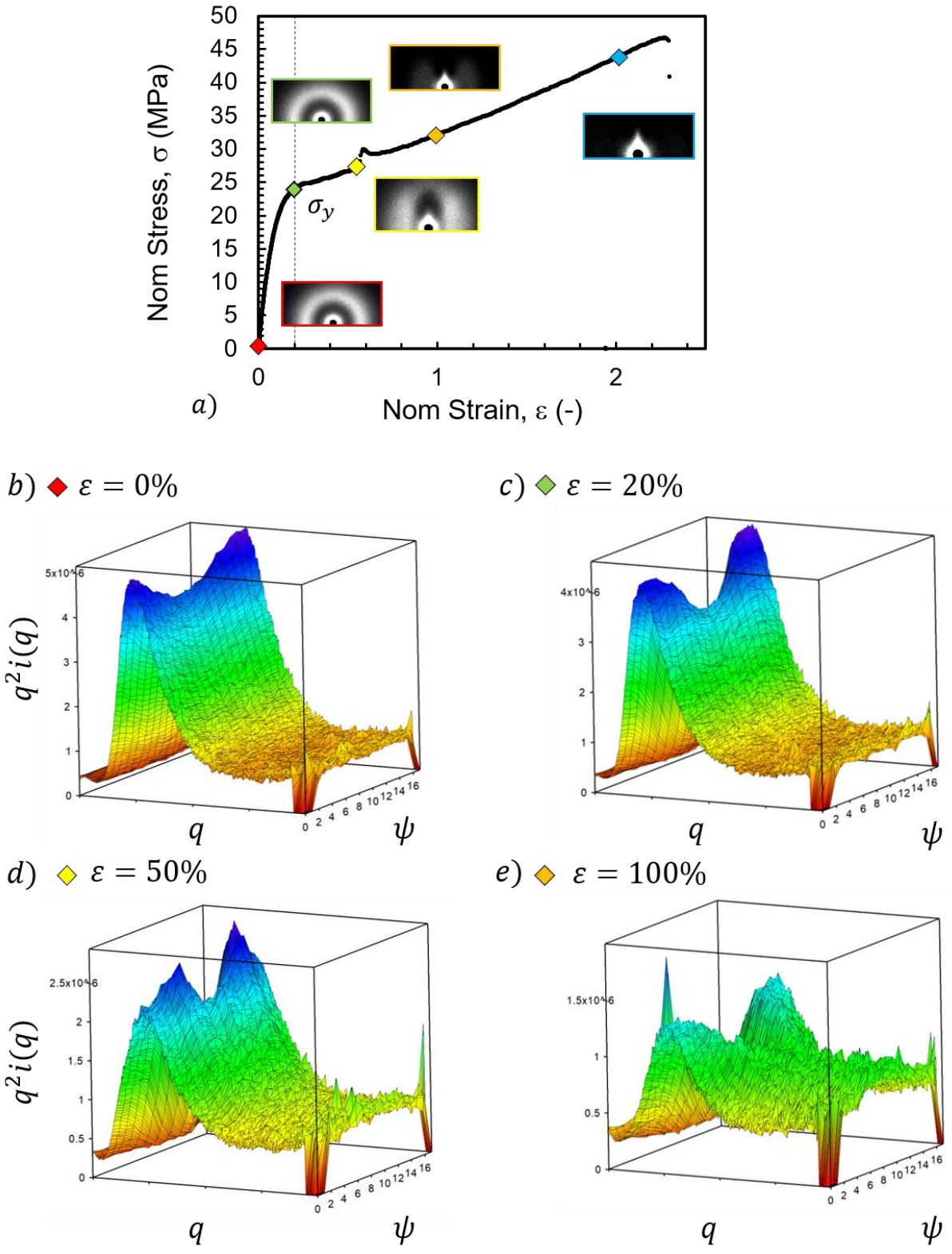


Figure 164. a) Nominal stress-strain curve for a tensile test at 170°C and corresponding 3D representation WAXS patterns as a function of q and ψ for macroscopic strain values of b) 0% c) 20% d) 50% and e) 100%

Cette thèse est accessible à l'adresse : https://theses.insa-lyon.fr/publication/2023ISAL0006/these.pdf
© [H. Willeman], [2023], INSA Lyon, tous droits réservés

Figure 165 quantitatively displays the evolution of the amplitude of the SAXS correlation peak as a function of azimuthal angle and local strain for experiments below and above T_g. For experiments below Tg, the evolution of the amplitude of the correlation peak follows the same trend as in the elastic regime. The relative amplitude increases a lot in the HORI direction whereas it decreases to nearly zero in the VERTI direction. The overall (average) starts to increase quite dramatically beyond ε=10%. This is due to the contribution of central scattering, which increases a lot at high elongation, reflecting damaging of the material. This will be discussed in the next section. Here, in general, we do not discuss the variations of the overall (average) amplitude as a function of the strain, we only discuss relative variations as a function of the azimuthal angle, for different strain values.

The evolution of the amplitude of the correlation peak for stretching at 170°C is quite different. The intensity globally decreases with elongation. A minimum of intensity is observed at 90° but maximum of intensities also appear at 45° and 145°, i.e. 90°±45°. This would suggest shearing or buckling of lamellae. At 170°C, crystalline lamellae are much more rigid as compared to the amorphous phase. Being much more elastic, the amorphous phase may accommodate large scale reorganization of lamellae such as buckling.

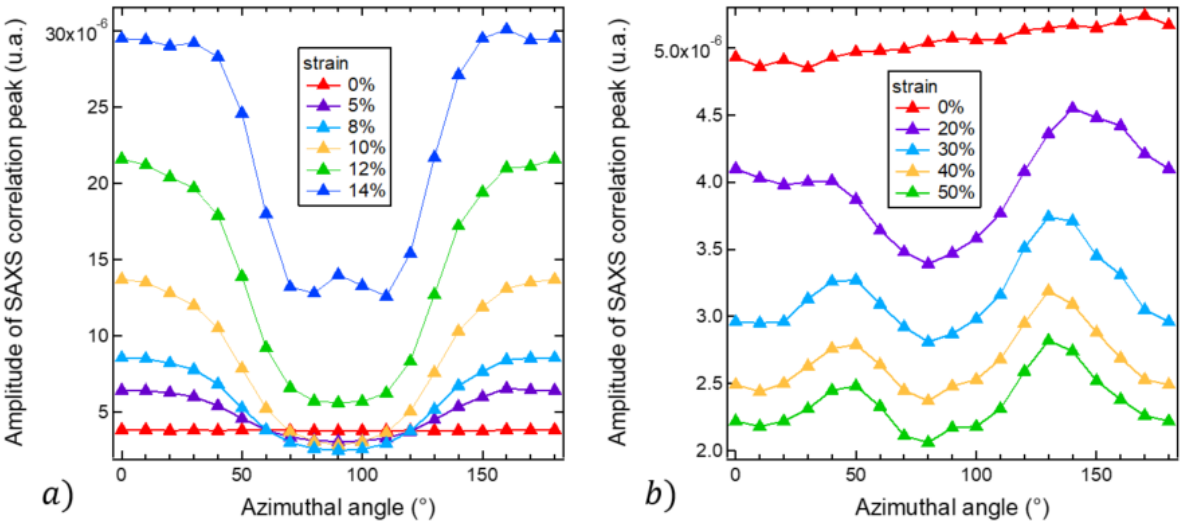


Figure 165. Amplitude of SAXS correlation peak as a function of azimuthal angle in the elastic regime various strains for tensile tests at a) 23°C and b) 170°C

V. Central scattering: damage mechanisms

Besides the correlation peak due to lamellar stacks, quite intense central scattering is observed in SAXS patterns. The central scattering gives information on the deformation and damage mechanisms of PEEK under tensile strain, often associated with cavitation.

1. Tensile tests at T=23°C, T < T_g

The evolution of central scattering on SAXS patterns as a function of the cross-head displacement of the tensile device for a tensile test at room temperature is shown in Figure 166 alongside the strain at the beamspot measured via digital image correlation (DIC). In the elastic regime, up to 6% strain, no significant change in central scattering is observed. From 6% where localization phenomena start within the sample, the central scattering profile changes and widens, especially around the HORI direction. The

Cette thèse est accessible à l'adresse : https://theses.insa-lyon.fr/publication/2023ISAL0006/these.pdf
© [H. Willeman], [2023], INSA Lyon, tous droits réservés

final central scattering pattern is a wide rectangular zone around the HORI direction with maxima of intensity at ±45°.

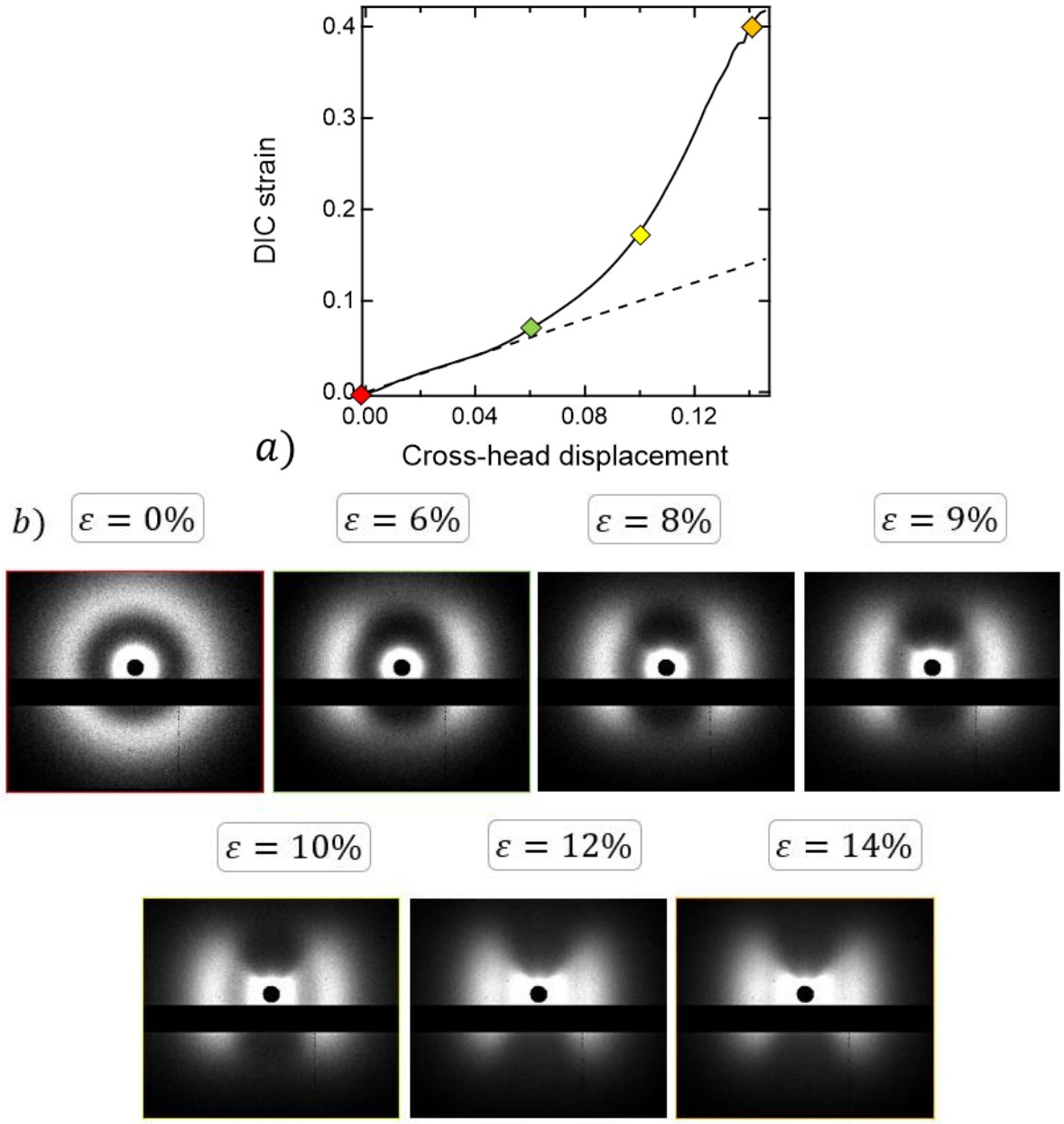


Figure 166. a) Macroscopic strain measured by DIC for tensile tests at room temperature and b) evolution of central scattering on corresponding SAXS patterns. The indicated strain values are nominal values.

The intensity of SAXS patterns is plotted as a function of the scattering vector q for several strain values in Figure 167. Figure 167.a represents the scattering in the HORI direction (lamellae in tension) and Figure 167.b the scattering in the VERTI direction (lamellae undergoing compressive strain).

As described before, the intensity of the correlation peak in the HORI direction increases while it decreases in the VERTI direction. As for the central scattering, a dramatic increase can be noted in between macroscopic strain values of 8% and 10%, which corresponds to local macroscopic strain values between 10% (see Figure 166.a) and 18%. Beyond ε=10%, the two contributions (central scattering and correlation peak of the lamellar stacking) start to overlap heavily. This is visible for both HORI and VERTI directions.

Cette thèse est accessible à l'adresse : https://theses.insa-lyon.fr/publication/2023ISAL0006/these.pdf
© [H. Willeman], [2023], INSA Lyon, tous droits réservés

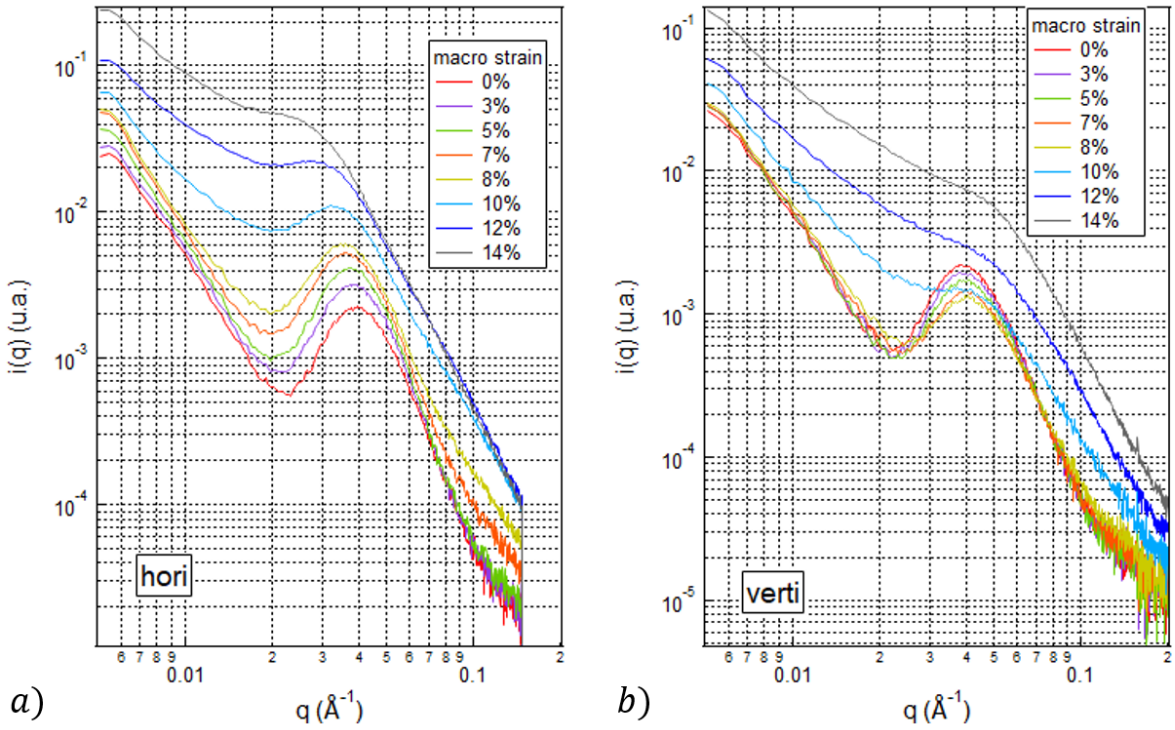


Figure 167. Raw intensity of SAXS patterns presented in Figure 166 for room temperature tensile tests including central scattering in b) HORI direction and c) VERTI direction

The azimuthal distribution of central scattering may also be observed more precisely directly on the SAXS patterns, as displayed in Figure 168 for a cross-head displacement of 14% corresponding to a deformation of the studied zone of about 30%. The shape of the central scattering does not look like a pattern corresponding to a population of cavities. Also, the contour plot on Figure 168.b also indicates maximum of intensity at ±45°. This central scattering profile could originate from singular lamellae randomly orientated and lamellar stacks that have been subjected to shear stress.

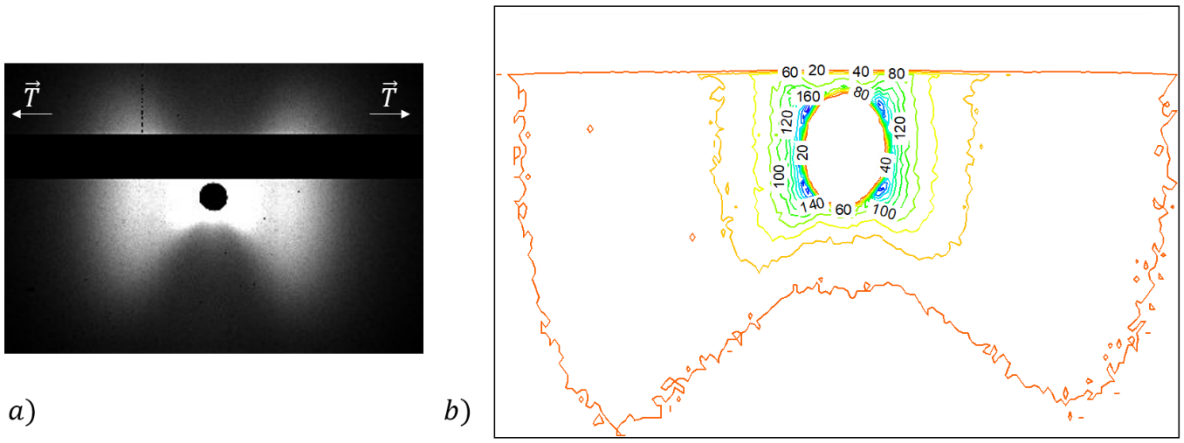


Figure 168.SAXS pattern for ε=14% at room temperature and b) corresponding contour plot

A very schematic, qualitative representation, may be as shown in Figure 169.

Cette thèse est accessible à l'adresse : https://theses.insa-lyon.fr/publication/2023ISAL0006/these.pdf
© [H. Willeman], [2023], INSA Lyon, tous droits réservés

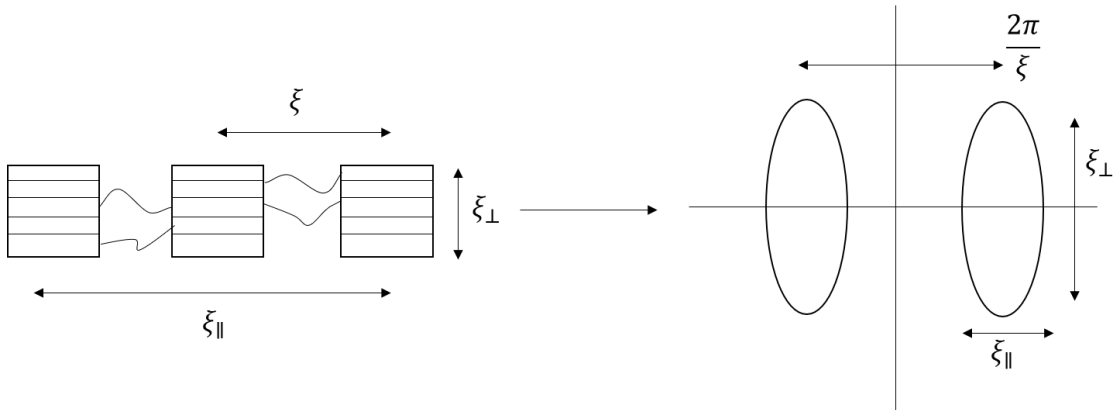


Figure 169. Schematic representation of crystalline lamellae organisation and corresponding SAXS pattern

2. Tensile tests at T=170°C, T > T_g

The evolution of central scattering on SAXS patterns as a function of the cross-head displacement of the tensile device for a tensile test at 170°C is presented in Figure 170.

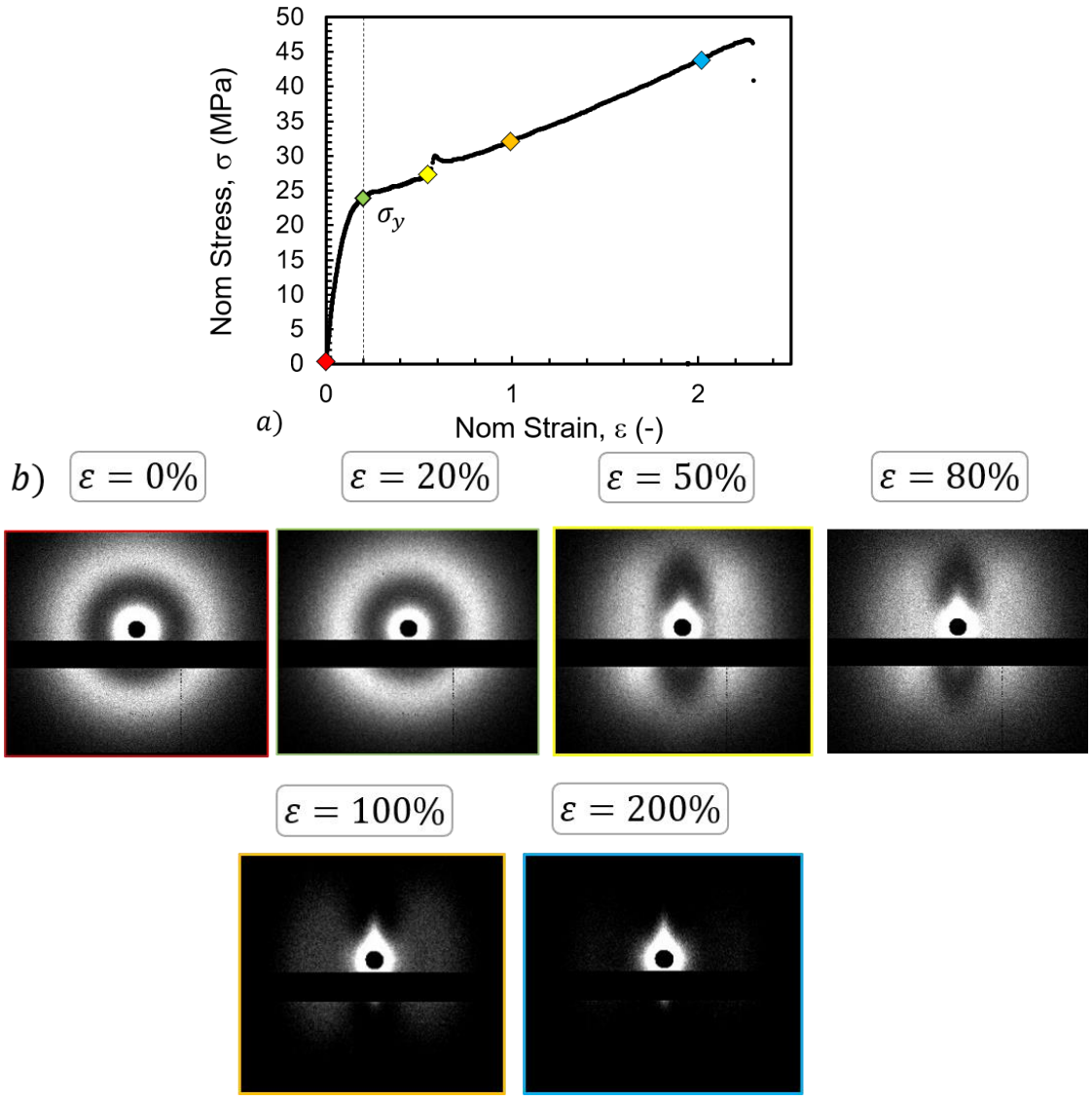


Figure 170. a) Stress-strain curve for a tensile test at 170°C and b) evolution of central scattering on corresponding SAXS patterns

Cette thèse est accessible à l'adresse : https://theses.insa-lyon.fr/publication/2023ISAL0006/these.pdf
© [H. Willeman], [2023], INSA Lyon, tous droits réservés

The quantitative representations of the intensity of the SAXS patterns in the HORI and VERTI directions for tensile tests at 170°C are plotted as a function of the scattering vector q for several strain values in Figure 171. For scattering in the HORI direction, only the shift of the maximum q_{max} of the correlation peak and the modulation of its intensity can be observed, no significant evolution of central scattering is evidenced. However, for central scattering in the vertical direction, an increase of intensity is observed starting from ε=80%. From ε=100%, the correlation peak has almost disappeared.

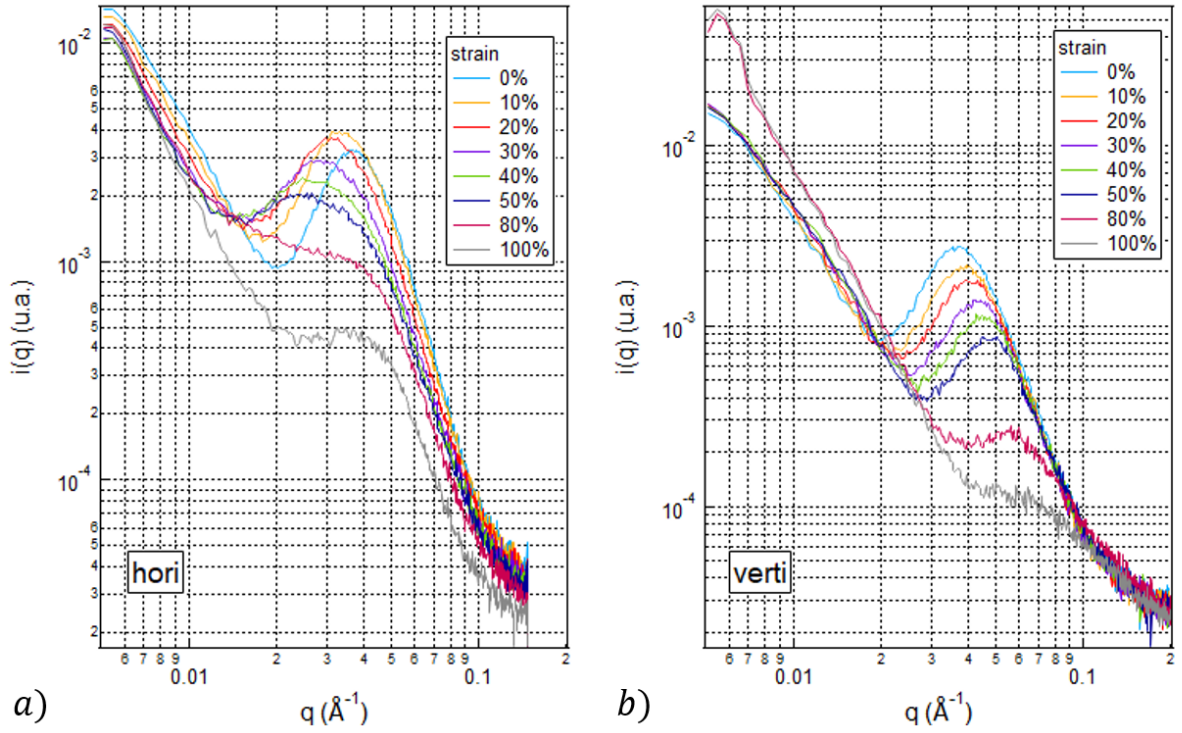


Figure 171. Raw intensity of SAXS patterns for tensile tests at 170°C including central scattering in a) HORI direction and b) VERTI direction

This demonstrates a significant difference in the material deformation behavior depending on the testing temperature. The increase of central scattering associated to cavitation or damage mechanisms appears only far in the plastic regime for stretching above T_g. The amorphous phase in the rubbery state is more capable of accommodating deformation without damage. In addition, the azimuthal distribution of central scattering is different depending on the temperature. The pattern detailed in Figure 172 for a deformation of 100% would correspond to the scattering of cavities elongated along to the tensile direction. Cavitation phenomenon is promoted at temperatures above T_g as more triaxial stress occurs.

A very schematic, qualitative representation of the lamellae and cavities arrangements and the corresponding pattern, may be as shown in Figure 173.

Cette thèse est accessible à l'adresse : https://theses.insa-lyon.fr/publication/2023ISAL0006/these.pdf
© [H. Willeman], [2023], INSA Lyon, tous droits réservés

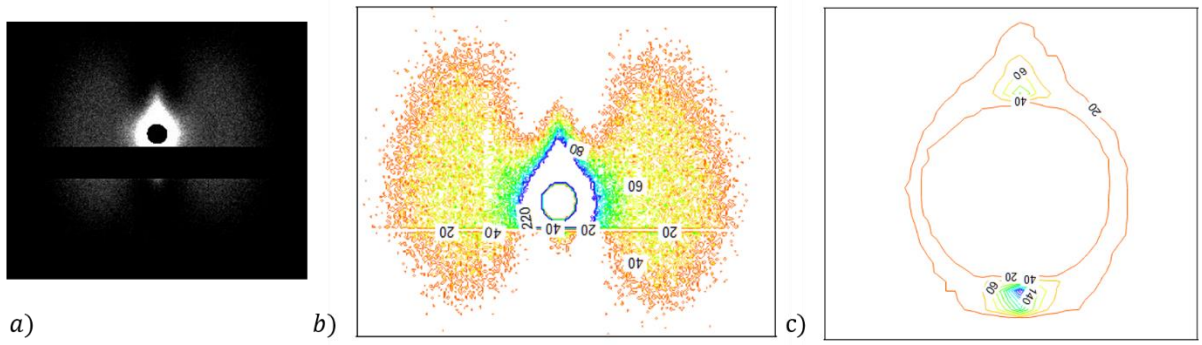


Figure 172. a) SAXS pattern for ε=100% at 170°C b) corresponding contour plot and c) zoom on the central scattering zone

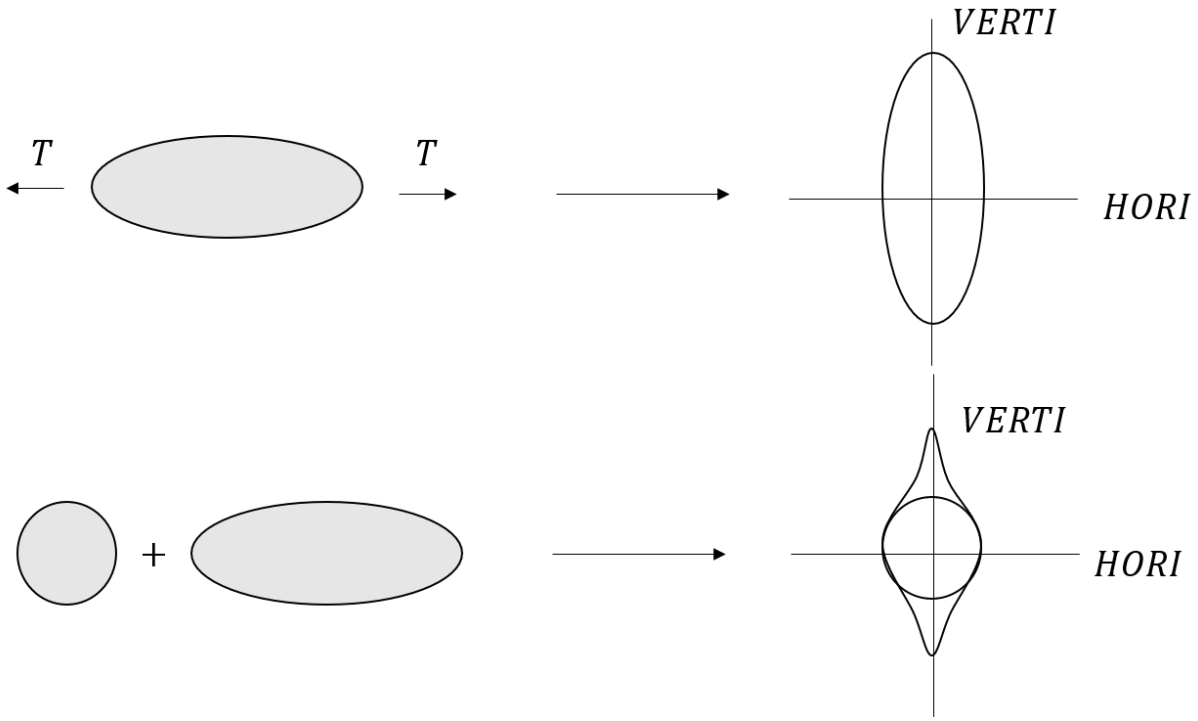


Figure 173. Schematic representation of crystalline lamellae and cavities organisation and corresponding SAXS pattern

Cette thèse est accessible à l'adresse : https://theses.insa-lyon.fr/publication/2023ISAL0006/these.pdf
© [H. Willeman], [2023], INSA Lyon, tous droits réservés

VI. Proposed mechanisms of deformation in PEEK

The objective of the final part of this chapter is to correlate SAXS and WAXS observations previously described and to propose mechanical scenarios for deformation processes all along stretching in the plastic regime.

1. Below glass transition temperature

In the pre-yield regime, that is, below about 6% strain, the strain at the scale of lamellar stacks is nearly equal to the macroscopic strain (which is homogeneous in the whole sample) and varies as a function of the azimuth angle like in a homogeneous material. The strain continues to vary according to equation (47) and to follow the macroscopic strain even above the yield point (which is at about 6%), up to about 20% strain, corresponding to about 11% nominal (calculated from the machine displacement) strain, as shown in Figure 174 below. At the same time, the orientation of lamellae follows the chain network model i.e., the distribution of orientation becomes anisotropic with more lamellae oriented with their normal parallel to the tensile direction. This orientation corresponds to chains oriented in the tensile direction. The orientation distribution evolves in a continuous, progressive way. All these observations indicate that the deformation remains mostly homogeneous at the scale of lamellar stacks up to the yield point and even a little beyond.

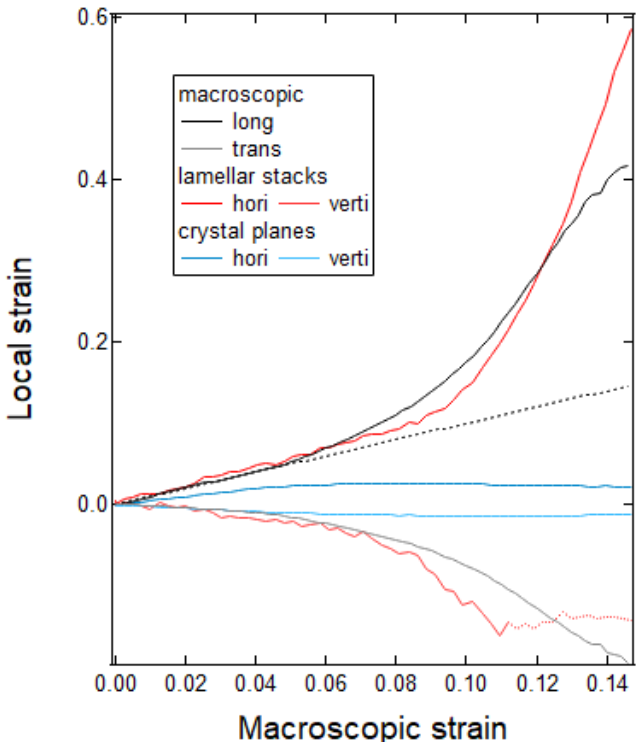


Figure 174. Microscopic strain at the scales of lamellar stacks and crystal planes as a function of the cross-head displacement compared with macroscopic strain in the longi (parallel to TD) and trans(perpendicular to TD) directions at the beam location measured by DIC for tensile test at room temperature

The behavior at the scale of crystal planes is quite different. In the pre-yield regime, crystal planes behave as in a homogeneous material as well (following equation (47)). The strain in crystal planes is lower than the macroscopic strain because the crystal is more rigid than the amorphous phase. The tensile strain within crystals stabilizes at the yield point, at about 6% strain. This is in sharp contrast with the behavior at the scale of lamellar stacks. This indicates that the stress is no longer transmitted to crystal planes. Either the amorphous phase sustains the whole deformation, or lamellae are submitted to

Cette thèse est accessible à l'adresse : https://theses.insa-lyon.fr/publication/2023ISAL0006/these.pdf
© [H. Willeman], [2023], INSA Lyon, tous droits réservés

shear along crystal planes (which should lead to some degree of fragmentation of the lamellae). Thus, heterogeneous modes of deformation occur at the scale of crystalline lamellae at and beyond the yield point.

At large strain values, some degree of periodicity is maintained in the tensile direction. The evolution of the central scattering also gives information on local damage in the material. The damages are mostly retrieved in a wide zone centered on the horizontal direction, with a maximum at 45°.

Compiling results from in-situ SAXS and WAXS experiments during a tensile test at room temperature, deformation processes of PEEK at room temperature can be described as in Figure 176.

2. Above glass transition temperature

In the pre-yield (elastic) regime, the microscopic strain within lamellar stacks is lower than the macroscopic strain as shown in Figure 175. Moreover, no significant orientation of these entities takes place in the sample. At this temperature, the amorphous phase is in the rubbery state and shall sustain most of the deformation. From the yield point, lamellar stacks start to reorganize. Following the chain network model, the chains are stretched in the tensile direction and pull the lamellae to orient their normal along the tensile direction. Ultimately the lamellar stack organization is completely lost.

The strain at the scale of crystal planes is considerably smaller than the macroscopic strain. This is expected as the contrast in modulus between the amorphous and crystal phases is expected to be even larger above Tg. The strain stabilizes above the yield point in the same way as below Tg.

Strong, qualitative changes of the central scattering occur quite far into the plastic regime, beyond the macroscopic yield point. In this case, the central scattering is quite narrow, centered on the vertical direction. Considering the ultimate stage of deformation that we have investigated in this work, the final fibrillar state strongly depends on the testing temperature, e.g on the state of the amorphous phase.

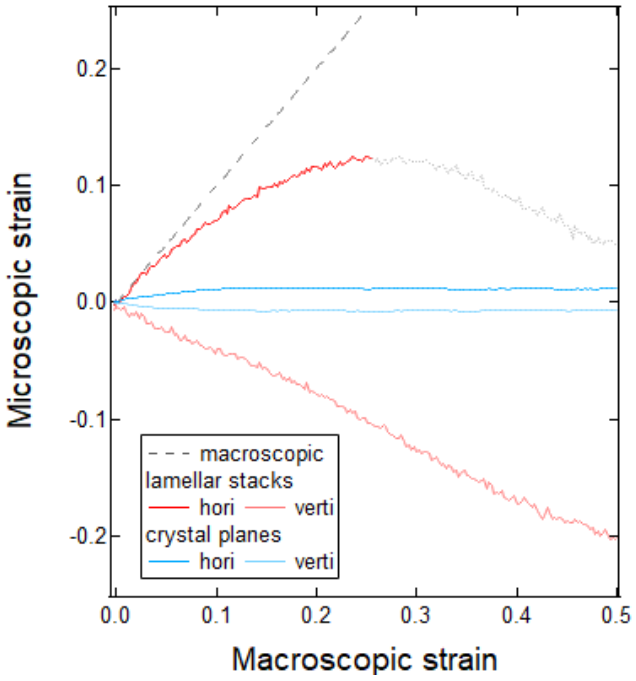


Figure 175. Microscopic strain at the scales of lamellar stacks and crystal planes as a function of the cross-head displacement compared with macroscopic strain for tensile test at 170°C

A proposed scenario of deformation of PEEK samples under tensile stretching at 170°C (above Tg) is schematized in Figure 177.

Cette thèse est accessible à l'adresse : https://theses.insa-lyon.fr/publication/2023ISAL0006/these.pdf
© [H. Willeman], [2023], INSA Lyon, tous droits réservés

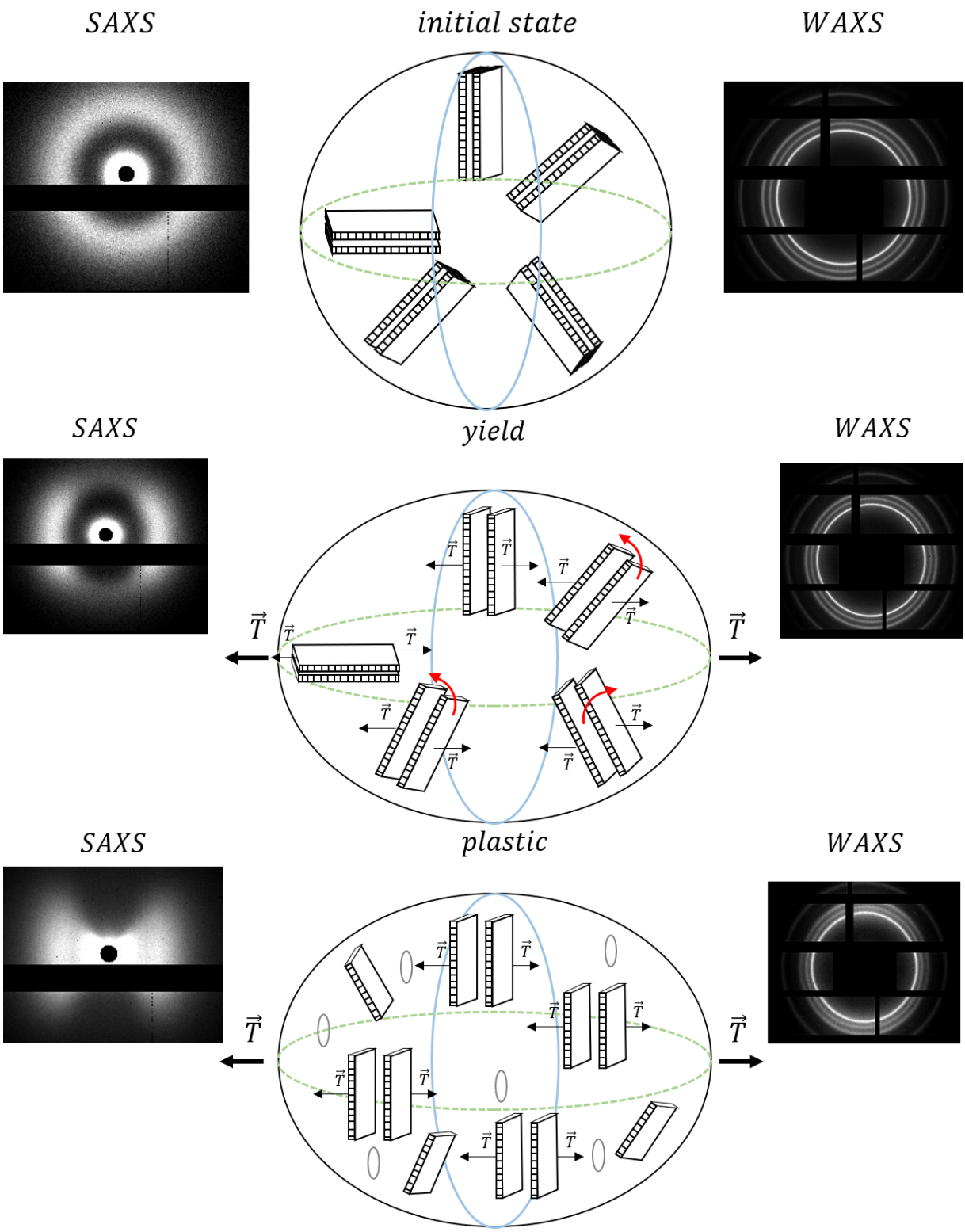


Figure 176. Deformation scenario of PEEK under tensile stretching at room temperature

Cette thèse est accessible à l'adresse : https://theses.insa-lyon.fr/publication/2023ISAL0006/these.pdf
© [H. Willeman], [2023], INSA Lyon, tous droits réservés

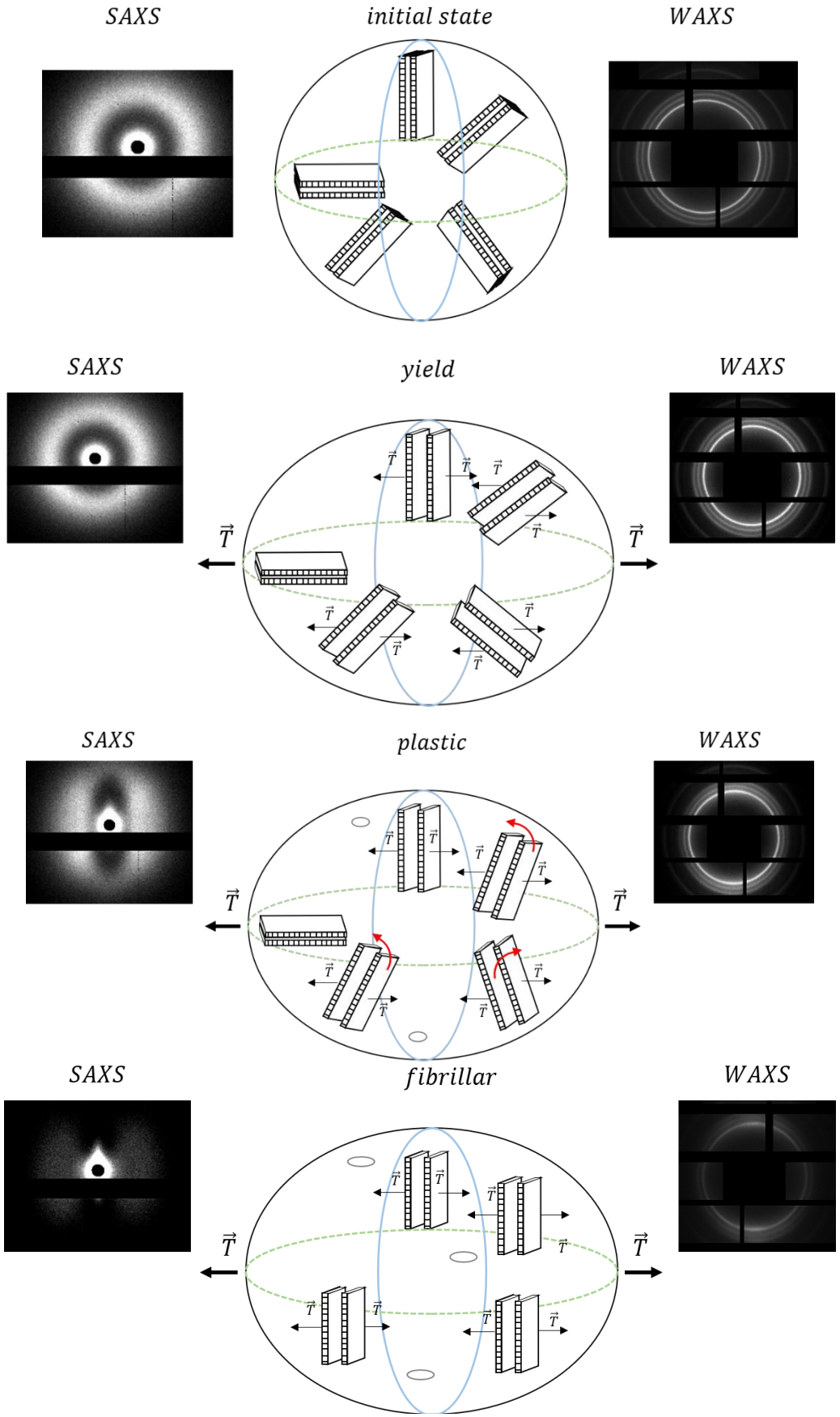


Figure 177. Deformation scenario of PEEK under tensile stretching at 170°C

Cette thèse est accessible à l'adresse : https://theses.insa-lyon.fr/publication/2023ISAL0006/these.pdf
© [H. Willeman], [2023], INSA Lyon, tous droits réservés

Conclusion

The main objective of this PhD thesis was to describe the mechanisms of deformation of the high performance polyetheretherketone (PEEK) polymer under uniaxial tensile stretching. In order to have a global view of the mechanisms, we followed an approach previously used with PA6 for a multi-scale investigation performed using in situ, real time tensile tests combined with X-ray scattering experiments below and above the glass transition temperature to modify the state of the amorphous phase (i.e. glassy or rubbery).

Two different commercial grades of PEEK with different molecular weights were studied (KT880, and KT820, short and long molecular weights respectively). The macroscopic properties of PEEK strongly depend on processing and crystallization conditions, as it is the case for most semi-crystalline polymers. The first part of this study focused on the influence of these conditions on the crystallization processes and the properties of the polymer. The temperature at which the thermal history of the material is fully erased was first investigated. For both PEEK grades, this temperature was found to be at about 380°C and was therefore used as the lower limit of the processing temperature range of PEEK. Isothermal crystallization of the polymer was characterized by DSC and optical microscopy to obtain information on the crystallization type of the polymer and TTS diagram for both grades were obtained. Tensile samples were then processed using compression molding in order to obtain morphologies as isotropic as possible. The molten state temperature was varied from 380 to 420°C. The crystallinity of the samples does not vary significantly, with perhaps a slight tendency to increase, as the molten state temperature increases. In identical crystallization conditions, KT880 has a slightly larger crystallinity index than KT820. The mechanical relaxation processes were studied by DMA. In DMA experiments, the presence of one and perhaps two combined β relaxation processes in a range of temperature (-80°C to -20°C) quite low with respect to the α relaxation (or equivalently the glass transition temperature T_g) was evidenced. The amplitude of this (or these) relaxation processes is relatively high. This may be the origin of a relatively high local mobility of the amorphous phase of PEEK in the surrounding of room temperature and up to T_g, which in turn may be responsible for the ductility and tenacity of the amorphous phase and of the whole semi-crystalline material. The minima of the tan δ curve on both sides of the main α relaxation of the amorphous phase would give the ideal test temperatures for tensile tests above and below T_g., as visco-elastic effects and dependence on the drawing rate in the pre-yield regime would be minimized at these temperatures. However, for practical reasons, the temperature 170°C was chosen for experiments above T_g, which is quite near to T_g (about 150°C) and partially overlaps the α relaxation peak.

The macroscopic mechanical properties of the tensile samples were studied by uniaxial tensile tests performed either below and above T_g. Below T_g, the yield point occurs for a stress of about 90 MPa and a deformation of 6% whereas at 170°C the yield point occurs at a deformation of about 20% for a stress of 25 MPa. As expected, KT880 exhibits a slightly stiffer behavior, higher Young's modulus and yield stress than KT820, related to the higher crystalline ratio of this grade. The localization of the deformation within the tensile specimens was followed by Digital Image Correlation (DIC) allowing to access the strain field in the samples.

The multiscale mechanical response of PEEK was then investigated by uniaxial tensile tests combined with in situ, real-time SAXS and WAXS measurements in the elastic and plastic strain domains below and above the glass transition temperature. By analyzing the azimuthal distribution of the local strain, it was found that in the elastic (pre-yield) strain regime, the material behaves like a homogeneous material

Cette thèse est accessible à l'adresse : https://theses.insa-lyon.fr/publication/2023ISAL0006/these.pdf
© [H. Willeman], [2023], INSA Lyon, tous droits réservés

down to the scale of lamellar stacks, with a local strain within lamellar stacks nearly equal to the macroscopic strain. This remains true at this scale even beyond the macroscopic yield point. T

Then, the strain in crystals was followed by WAXS at both temperatures. Above T_g, it was confirmed that the modulus of the amorphous phase drops down to a value much lower than the crystalline phase, as the crystal strain is much lower than below T_g, meaning that the amorphous phase is much more compliant than the crystals. The degree of homogeneity of the local strain/stress state was deduced from the azimuthal distribution of the crystal strain. Also, the reversibility of deformation in the elastic regime was studied using loading-unloading cycles. At both scales, in every direction, the deformation of PEEK in the elastic regime is reversible.

The evolution of the azimuthal distribution of the lamellae (SAXS) and the azimuthal distribution of the various crystalline planes (WAXS) shows that the mechanisms of deformation follow the Chain Network (CN) model, with chains of the amorphous phase having a tendency to orient parallel to the tensile direction (TD), i.e. the lamellae orienting normal to TD.

The mechanical investigation was then pursued in the plastic strain domain, i.e. beyond the yield point. The tendency of chains to orient along TD is magnified in the plastic strain regime until a high degree of orientation is reached. This type of behavior is commonly observed for semi-crystalline polymers.

Beyond the yield point, the deformation is completely sustained by the amorphous phase. The residual deformation in the plastic regime was also studied with loading-unloading cycles. After stretching the samples beyond the yield point, a macroscopic residual strain is observed after unloading back to force zero. However, no residual deformation is observed at the scale of crystal planes, which confirms that only the amorphous phase deforms beyond the yield point.

This behavior would deserve further SAXS and/or WAXS or other structural investigations on the mechanical behavior of amorphous samples to determine the behavior and tenacity of this phase itself.

Considering the ultimate stage of deformation that we have investigated in this work, the final fibrillar state seems to strongly depend on the testing temperature. The final stage is better oriented above the glass transition. Regarding the phenomenon of cavitation, it was found that, below Tg, cavitation occurs early in the plastic regime with a wide central scattering profile. The origin of this profile is uncertain, it could be scattering from single entities such as crystallites or small fragmented lamellar stacks randomly orientated. A maximum at 45° also indicates shearing of the lamellar stacks. For tensile tests above T_g, central scattering occurs far in the plastic regime with a profile indicating cavities along the tensile direction. It would be interesting to study more in details this phenomenon using ultra small-angle scattering (USAXS) in order to understand why the cavitation processes are different below and above Tg.

All these results tend to indicate that the amorphous phase plays a key role in the mechanical properties of PEEK. It has a high degree of toughness, possibly related to the local mobility enabled by the presence of the β transition. These characteristics would deserve further SAXS and/or WAXS or other structural investigations on the mechanical behavior of amorphous samples to determine the behavior and tenacity of this phase itself. Also, more extensive comparison with the behavior of other polyether or polyester aromatic polymers, such as PET or PEF, which have high stretching ability as well, is certainly an interesting perspective as well. It might be perhaps be interesting to investigate whether some degree of local π-π stacking is present in the amorphous phase, as it may also provide toughness to the amorphous phase. This might be investigated by molecular dynamics simulations.

Cette thèse est accessible à l'adresse : https://theses.insa-lyon.fr/publication/2023ISAL0006/these.pdf
© [H. Willeman], [2023], INSA Lyon, tous droits réservés

References

[1] J. B. Rose and P. Staniland, “75) Inventors: John B. Rose, Letchworth; Philip A.”

[2] K. L. White, L. Jin, N. Ferrer, M. Wong, T. Bremner, and H.-J. Sue, “Rheological and thermal behaviors of commercial poly(aryletherketone)s,” *Polymer Engineering & Science*, vol. 53, no. 3, pp. 651–661, 2013, doi: 10.1002/pen.23309.

[3] L. J. Fetters, D. J. Lohse, D. Richter, T. A. Witten, and A. Zirkel, “Connection between Polymer Molecular Weight, Density, Chain Dimensions, and Melt Viscoelastic Properties,” *Macromolecules*, vol. 27, no. 17, pp. 4639–4647, Aug. 1994, doi: 10.1021/ma00095a001.

[4] Parina Patel, T. R. Hull, R. W. McCabe, D. Flath, J. Grasmeder, and M. Percy, “Mechanism of thermal decomposition of poly(ether ether ketone) (PEEK) from a review of decomposition studies,” *Polymer Degradation and Stability*, vol. 95, no. 5, pp. 709–718, May 2010, doi: 10.1016/j.polymdegradstab.2010.01.024.

[5] J. N. Hay and D. J. Kemmish, “Thermal decomposition of poly(aryl ether ketones),” *Polymer*, vol. 28, no. 12, pp. 2047–2051, Nov. 1987, doi: 10.1016/0032-3861(87)90039-5.

[6] C. J. Tsai, L. H. Perng, and Y. C. Ling, “A study of thermal degradation of poly(aryl-ether-ether-ketone) using stepwise pyrolysis/gas chromatography/mass spectrometry,” *Rapid Communications in Mass Spectrometry*, vol. 11, no. 18, pp. 1987–1995, 1997, doi: 10.1002/(SICI)1097-0231(199712)11:18<1987::AID-RCM100>3.0.CO;2-Q.

[7] M. T. Bishop, F. E. Karasz, P. S. Russo, and K. H. Langley, “Solubility and properties of a poly(aryl ether ketone) in strong acids,” *Macromolecules*, vol. 18, no. 1, pp. 86–93, Jan. 1985, doi: 10.1021/ma00143a014.

[8] A. Jonas and R. Legras, “Thermal stability and crystallization of poly(aryl ether ether ketone),” *Polymer*, vol. 32, no. 15, pp. 2691–2706, Jan. 1991, doi: 10.1016/0032-3861(91)90095-Z.

[9] N. T. Wakelyn, “On the structure of PEEK,” *Polymer Communications*, vol. 25, pp. 306–308, 1984.

[10] D. J. Blundell and B. N. Osborn, “The morphology of poly(aryl-ether-ether-ketone),” *Polymer*, vol. 24, no. 8, pp. 953–958, Aug. 1983, doi: 10.1016/0032-3861(83)90144-1.

[11] N. T. Wakelyn, “Variation of unit cell parameters of poly(arylene ether ether ketone) film with annealing temperature,” *J. Polym. Sci. C Polym. Lett.*, vol. 25, no. 1, pp. 25–28, Jan. 1987, doi: 10.1002/pol.1987.140250105.

[12] J. N. Hay, J. I. Langford, and J. R. Lloyd, “Variation in unit cell parameters of aromatic polymers with crystallization temperature,” *Polymer*, vol. 30, no. 3, pp. 489–493, Mar. 1989, doi: 10.1016/0032-3861(89)90019-0.

[13] L. Jin, J. Ball, T. Bremner, and H.-J. Sue, “Crystallization behavior and morphological characterization of poly(ether ether ketone),” *Polymer*, vol. 55, no. 20, pp. 5255–5265, Sep. 2014, doi: 10.1016/j.polymer.2014.08.045.

[14] A. J. Lovinger and D. D. Davis, “Solution crystallization of poly(ether ether ketone),” *Macromolecules*, vol. 19, no. 7, pp. 1861–1867, Jul. 1986, doi: 10.1021/ma00161a014.

Cette thèse est accessible à l'adresse : https://theses.insa-lyon.fr/publication/2023ISAL0006/these.pdf
© [H. Willeman], [2023], INSA Lyon, tous droits réservés

[15] A. J. Lovinger and D. D. Davis, “Electron-microscopic investigation of the morphology of a melt-crystallized polyaryletherketone,” *Journal of Applied Physics*, vol. 58, no. 8, pp. 2843–2853, Oct. 1985, doi: 10.1063/1.335856.

[16] A. Jonas, R. Legras, and J.-P. Issi, “Differential scanning calorimetry and infra-red crystallinity determinations of poly(aryl ether ether ketone),” *Polymer*, vol. 32, no. 18, pp. 3364–3370, Jan. 1991, doi: 10.1016/0032-3861(91)90540-Y.

[17] P. Damman, Ch. Fougnies, J. F. Moulin, and M. Dosiere, “Crystallinity of Poly(aryl ether ether ketone) by Vibrational Spectroscopy,” *Macromolecules*, vol. 27, no. 6, pp. 1582–1587, Mar. 1994, doi: 10.1021/ma00084a046.

[18] P. J. Flory, “Conformations of macromolecules in condensed phases,” *Pure and Applied Chemistry*, vol. 56, no. 3, pp. 305–312, Jan. 1984, doi: 10.1351/pac198456030305.

[19] J. R. Collier and L. M. Neal, “Effect of melt history on polymer crystallization,” *Polym. Eng. Sci.*, vol. 9, no. 3, pp. 182–189, May 1969, doi: 10.1002/pen.760090306.

[20] J. Q. G. Maclaine and C. Booth, “Effect of molecular weight on spherulite growth rates of high molecular weight poly(ethylene oxide) fractions,” *Polymer*, vol. 16, no. 3, pp. 191–195, Mar. 1975, doi: 10.1016/0032-3861(75)90052-X.

[21] J. M. Schultz, “The influence of microstructure on the failure behaviour of PEEK,” p. 7.

[22] M. Zinet, “Modélisation de la cristallisation des polymères dans les procédés de plasturgie : quantification des effets thermiques et rhéologiques.”

[23] D. C. Bassett, R. H. Olley, and D. J. Blundell, “Permanganic etching of PEEK,” *Polymer*, vol. 27, no. 3, pp. 344–348, Mar. 1986, doi: 10.1016/0032-3861(86)90147-3.

[24] S. Kumar, D. P. Anderson, and W. W. Adams, “Crystallization and morphology of poly(aryl-ether-ether-ketone),” *Polymer*, vol. 27, no. 3, pp. 329–336, Mar. 1986, doi: 10.1016/0032-3861(86)90145-X.

[25] B. S. Hsiao, K. H. Gardner, R. R. Matheson, and B. A. Wood, “Structure, crystallization and morphology of poly (aryl ether ketone ketone),” *Polymer*, vol. 33, no. 12, pp. 2483–2495, Jan. 1992, doi: 10.1016/0032-3861(92)91128-O.

[26] Y. Wang, J. D. Beard, K. E. Evans, and O. Ghita, “Unusual crystalline morphology of Poly Aryl Ether Ketones (PAEKs),” *RSC Adv.*, vol. 6, no. 4, pp. 3198–3209, 2016, doi: 10.1039/C5RA17110E.

[27] P. B. Bowden and R. J. Young, “Deformation mechanisms in crystalline polymers,” *J Mater Sci*, vol. 9, no. 12, pp. 2034–2051, Dec. 1974, doi: 10.1007/BF00540553.

[28] G. Strobl, *The Physics of Polymers*. Berlin, Heidelberg: Springer, 2007. doi: 10.1007/978-3-540-68411-4.

[29] E. Mourglia-Seignobos, D. R. Long, L. Odoni, L. Vanel, P. Sotta, and C. Rochas, “Physical Mechanisms of Fatigue in Neat Polyamide 6,6,” *Macromolecules*, vol. 47, no. 12, pp. 3880–3894, Jun. 2014, doi: 10.1021/ma500256x.

[30] A. Galeski, A. S. Argon, and R. E. Cohen, “Changes in the morphology of bulk spherulitic nylon 6 due to plastic deformation,” *Macromolecules*, vol. 21, no. 9, pp. 2761–2770, Sep. 1988, doi: 10.1021/ma00187a021.

Cette thèse est accessible à l'adresse : https://theses.insa-lyon.fr/publication/2023ISAL0006/these.pdf
© [H. Willeman], [2023], INSA Lyon, tous droits réservés

[31] I. Narisawa and M. Ishikawa, “Crazing in semicrystalline thermoplastics,” p. 39.

[32] K. Friedrich, “Crazes and shear bands in semi-crystalline thermoplastics,” in *Crazing in Polymers*, vol. 52–53, H. H. Kausch, Ed. Berlin/Heidelberg: Springer-Verlag, 1983, pp. 225–274. doi: 10.1007/BFb0024059.

[33] H.-H. Kausch, R. Gensler, Ch. Grein, C. J. G. Plummer, and P. Scaramuzzino, “Crazing in semicrystalline thermoplastics,” *Journal of Macromolecular Science, Part B*, vol. 38, no. 5–6, pp. 803–815, Sep. 1999, doi: 10.1080/00222349908248140.

[34] C. J. G. Plummer and H.-H. Kausch, “Deformation of thin films of poly(ether ether ketone),” *Polymer*, vol. 34, no. 2, pp. 305–311, Jan. 1993, doi: 10.1016/0032-3861(93)90081-K.

[35] A. Peterlin, “Molecular model of drawing polyethylene and polypropylene,” *J Mater Sci*, vol. 6, no. 6, pp. 490–508, Jun. 1971, doi: 10.1007/BF00550305.

[36] J. M. Schultz, “Microstructural aspects of failure in semicrystalline polymers,” *Polymer Engineering & Science*, vol. 24, no. 10, pp. 770–785, 1984, doi: 10.1002/pen.760241007.

[37] M. F. Butler, A. M. Donald, W. Bras, G. R. Mant, G. E. Derbyshire, and A. J. Ryan, “A Real-Time Simultaneous Small- and Wide-Angle X-ray Scattering Study of In-Situ Deformation of Isotropic Polyethylene,” *Macromolecules*, vol. 28, no. 19, pp. 6383–6393, Sep. 1995, doi: 10.1021/ma00123a001.

[38] B. Xiong, O. Lame, J.-M. Chenal, C. Rochas, R. Seguela, and G. Vigier, “In-situ SAXS study of the mesoscale deformation of polyethylene in the pre-yield strain domain: Influence of microstructure and temperature,” *Polymer*, vol. 55, no. 5, pp. 1223–1227, Mar. 2014, doi: 10.1016/j.polymer.2014.02.004.

[39] H. Guo, R. G. Rinaldi, S. Tayakout, M. Broudin, and O. Lame, “Characterization of the spherulitic deformation in equatorial region and cavitation in HDPE materials submitted to mixed-mode oligo-cyclic tensile loading,” *Polymer Testing*, vol. 99, p. 107208, Jul. 2021, doi: 10.1016/j.polymertesting.2021.107208.

[40] K. Schneider, S. Trabelsi, N. E. Zafeiropoulos, R. Davies, C. Riekel, and M. Stamm, “The Study of Cavitation in HDPE Using Time Resolved Synchrotron X-ray Scattering During Tensile Deformation,” *Macromolecular Symposia*, vol. 236, no. 1, pp. 241–248, 2006, doi: 10.1002/masy.200690062.

[41] S. Humbert, O. Lame, and G. Vigier, “Analysis of the effects of local stress transmission on yielding properties of the polyethylenes,” *Int J Mater Form*, vol. 1, no. S1, pp. 611–614, Apr. 2008, doi: 10.1007/s12289-008-0330-7.

[42] S. Humbert, O. Lame, J.-M. Chenal, C. Rochas, and G. Vigier, “Small strain behavior of polyethylene: In situ SAXS measurements,” *Journal of Polymer Science Part B: Polymer Physics*, vol. 48, no. 13, pp. 1535–1542, 2010, doi: 10.1002/polb.22024.

[43] K. Schneider, “Investigation of structural changes in semi-crystalline polymers during deformation by synchrotron X-ray scattering,” *Journal of Polymer Science Part B: Polymer Physics*, vol. 48, no. 14, pp. 1574–1586, 2010, doi: 10.1002/polb.21971.

[44] K. Schneider, B. Chang, I. Kuehnert, and G. Heinrich, “Cavitation Behavior of Semi-Crystalline Polymers during Uniaxial Stretching Studied by Synchrotron Small-Angle X-Ray Scattering,” *Small Angle Scattering and Diffraction*, Jun. 2018, doi: 10.5772/intechopen.74224.

Cette thèse est accessible à l'adresse : https://theses.insa-lyon.fr/publication/2023ISAL0006/these.pdf
© [H. Willeman], [2023], INSA Lyon, tous droits réservés

[45] F. Paolucci, L. Govaert, and G. Peters, “In Situ WAXD and SAXS during Tensile Deformation Of Moulded and Sintered Polyamide 12,” *Polymers*, vol. 11, no. 6, p. 1001, Jun. 2019, doi: 10.3390/polym11061001.

[46] C. Millot, R. Séguéla, O. Lame, L.-A. Fillot, C. Rochas, and P. Sotta, “Tensile Deformation of Bulk Polyamide 6 in the Preyield Strain Range. Micro–Macro Strain Relationships via in Situ SAXS and WAXS,” *Macromolecules*, vol. 50, no. 4, pp. 1541–1553, Feb. 2017, doi: 10.1021/acs.macromol.6b02471.

[47] A. D’Amore, J. M. Kenny, L. Nicolais, and V. Tucci, “Dynamic-mechanical and dielectric characterization of PEEK crystallization,” *Polym. Eng. Sci.*, vol. 30, no. 5, pp. 314–320, Mar. 1990, doi: 10.1002/pen.760300509.

[48] E. Forestier, N. Guigo, C. Combeaud, N. Billon, and N. Sbirrazzuoli, “Conformational Change Analysis of Poly(ethylene 2,5-furandicarboxylate) and Poly(ethylene terephthalate) under Uniaxial Stretching,” *Macromolecules*, vol. 53, no. 19, pp. 8693–8703, Oct. 2020, doi: 10.1021/acs.macromol.0c00691.

[49] E. Forestier, C. Combeaud, N. Guigo, N. Sbirrazzuoli, and N. Billon, “Understanding of strain-induced crystallization developments scenarios for polyesters: Comparison of poly(ethylene furanoate), PEF, and poly(ethylene terephthalate), PET,” *Polymer*, vol. 203, p. 122755, Aug. 2020, doi: 10.1016/j.polymer.2020.122755.

[50] R. K. Krishnaswamy and D. S. Kalika, “Dynamic mechanical relaxation properties of poly(ether ether ketone),” *Polymer*, vol. 35, no. 6, pp. 1157–1165, Mar. 1994, doi: 10.1016/0032-3861(94)90006-X.

[51] T. Sasuga and M. Hagiwara, “Molecular motions of non-crystalline poly(aryl ether-ether-ketone) PEEK and influence of elecron beam irradiation,” *Polymer*, vol. 26, no. 4, pp. 501–505, Apr. 1985, doi: 10.1016/0032-3861(85)90148-X.

[52] M. Mourgues-Martin, A. Bernés, and C. Lacabanne, “Dielectric relaxation phenomena in PEEK,” *Thermochimica Acta*, vol. 226, pp. 7–14, Oct. 1993, doi: 10.1016/0040-6031(93)80201-K.

[53] H. W. Starkweather and P. Avakian, .“beta.-Relaxations in phenylene polymers,” *Macromolecules*, vol. 22, no. 10, Art. no. 10, Oct. 1989, doi: 10.1021/ma00200a042.

[54] J. Villoutreix and J.-D. Acetarin, “Polyétheréthercétone (PEEK),” p. 17, 1998.

[55] D. Barba, A. Arias, and D. Garcia-Gonzalez, “Temperature and strain rate dependences on hardening and softening behaviours in semi-crystalline polymers: Application to PEEK,” *International Journal of Solids and Structures*, vol. 182–183, pp. 205–217, Jan. 2020, doi: 10.1016/j.ijsolstr.2019.08.021.

[56] F. Chen, H. Ou, S. Gatea, and H. Long, “Hot tensile fracture characteristics and constitutive modelling of polyether-ether-ketone (PEEK),” *Polymer Testing*, vol. 63, pp. 168–179, Oct. 2017, doi: 10.1016/j.polymertesting.2017.07.032.

[57] N. D. Albérola, P. Mélé, and C. Bas, “Tensile mechanical properties of PEEK films over a wide range of strain rates. II,” *Journal of Applied Polymer Science*, vol. 64, no. 6, pp. 1053–1059, 1997, doi: 10.1002/(SICI)1097-4628(19970509)64:6<1053::AID-APP3>3.0.CO;2-K.

Cette thèse est accessible à l'adresse : https://theses.insa-lyon.fr/publication/2023ISAL0006/these.pdf
© [H. Willeman], [2023], INSA Lyon, tous droits réservés

[58] L. V. Pastukhov, M. J. W. Kanters, T. A. P. Engels, and L. E. Govaert, “Physical background of the endurance limit in poly(ether ether ketone),” *Journal of Polymer Science*, vol. 58, no. 5, pp. 716–736, Mar. 2020, doi: 10.1002/pol.20190091.

[59] R. A. Chivers and D. R. Moore, “The effect of molecular weight and crystallinity on the mechanical properties of injection moulded poly(aryl-ether-ether-ketone) resin,” *Polymer*, vol. 35, no. 1, pp. 110–116, Jan. 1994, doi: 10.1016/0032-3861(94)90057-4.

[60] M. Garcia-Leiner, M. T. F. Reitman, M. J. El-Hibri, and R. K. Roeder, “Structure-property relationships in commercial polyetheretherketone resins,” *Polymer Engineering & Science*, vol. 57, no. 9, pp. 955–964, 2017, doi: 10.1002/pen.24472.

[61] M. Yuan, J. A. Galloway, R. J. Hoffman, and S. Bhatt, “Influence of molecular weight on rheological, thermal, and mechanical properties of PEEK,” *Polymer Engineering & Science*, vol. 51, no. 1, pp. 94–102, 2011, doi: 10.1002/pen.21785.

[62] T. Colmer, S. R. Daniewicz, J. C. Newman, and R. Moser, “Measuring fatigue crack growth and closure in Polyether Ether Ketone (PEEK),” *International Journal of Fatigue*, vol. 95, pp. 243–251, Feb. 2017, doi: 10.1016/j.ijfatigue.2016.10.025.

[63] M. C. Sobieraj, J. E. Murphy, J. G. Brinkman, S. M. Kurtz, and C. M. Rimnac, “Notched fatigue behavior of PEEK,” *Biomaterials*, vol. 31, no. 35, pp. 9156–9162, Dec. 2010, doi: 10.1016/j.biomaterials.2010.08.032.

[64] A. Avanzini, G. Donzella, A. Mazzù, and C. Petrogalli, “Wear and rolling contact fatigue of PEEK and PEEK composites,” *Tribology International*, vol. 57, pp. 22–30, Jan. 2013, doi: 10.1016/j.triboint.2012.07.007.

[65] M. Buggy and G. Dillon, “Flexural fatigue of carbon fibre-reinforced PEEK laminates,” *Composites*, vol. 22, no. 3, pp. 191–198, May 1991, doi: 10.1016/0010-4361(91)90318-B.

[66] L. V. Pastukhov and L. E. Govaert, “Plasticity-controlled failure of fibre-reinforced thermoplastics,” *Composites Part B: Engineering*, vol. 209, p. 108635, Mar. 2021, doi: 10.1016/j.compositesb.2021.108635.

[67] R. Shrestha, J. Simsiriwong, and N. Shamsaei, “Mean strain effects on cyclic deformation and fatigue behavior of polyether ether ketone (PEEK),” *Polymer Testing*, vol. 55, pp. 69–77, Oct. 2016, doi: 10.1016/j.polymertesting.2016.08.002.

[68] A.-R. Martins, “Effect of intermolecular interactions on the viscoelastic behavior of polyamides,” *PhD Thesis*.

[69] D. J. Kemmish and J. N. Hay, “The effect of physical ageing on the properties of amorphous PEEK,” *Polymer*, vol. 26, no. 6, pp. 905–912, Jun. 1985, doi: 10.1016/0032-3861(85)90136-3.

[70] C. Carfagna, E. Amendola, A. D’Amore, and L. Nicolais, “Physical aging of amorphous poly(etheretherketone) (PEEK),” *Polymer Engineering & Science*, vol. 28, no. 18, pp. 1203–1206, 1988, doi: 10.1002/pen.760281811.

[71] A. D’Amore and A. Pompo, “The kinetics of volume relaxation amt related property changes duringphysical aging of poly(ether ether ketone) (PEEK),” p. 5, 1994.

Cette thèse est accessible à l'adresse : https://theses.insa-lyon.fr/publication/2023ISAL0006/these.pdf
© [H. Willeman], [2023], INSA Lyon, tous droits réservés

[72] A. D'Amore, A. Pompo, and L. Nicolais, "Viscoelastic effects in poly(ether ether ketone) (PEEK) and PEEK-based composites," *Composites Science and Technology*, vol. 41, no. 3, pp. 303–325, Jan. 1991, doi: 10.1016/0266-3538(91)90005-A.

[73] A. D'Amore, F. Cocchini, A. Pompo, A. Apicella, and L. Nicolais, "The effect of physical aging on long-term properties of of Poly-Ether-Ketone (PEEK) and PEEK-Based Composites," *Journal of Applied Polymer Science*, vol. 39, pp. 1163–1174, 1990.

[74] M. P. Lattimer, J. K. Hobbs, M. J. Hill, and P. J. Barham, "On the origin of the multiple endotherms in PEEK," *Polymer*, vol. 33, no. 18, pp. 3971–3973, Sep. 1992, doi: 10.1016/0032-3861(92)90391-9.

[75] K. N. Krueger and H. G. Zachmann, "Investigation of the melting behavior of poly(aryl ether ketones) by simultaneous measurements of SAXS and WAXS employing synchrotron radiation," *Macromolecules*, vol. 26, no. 19, pp. 5202–5208, Sep. 1993, doi: 10.1021/ma00071a035.

[76] Y. Lee, R. S. Porter, and J. S. Lin, "On the double-melting behavior of poly(ether ether ketone)," *Macromolecules*, vol. 22, no. 4, pp. 1756–1760, Apr. 1989, doi: 10.1021/ma00194a043.

[77] D. Bassett, R. Olley, and I. Alraheil, "On crystallization phenomena in PEEK☆," *Polymer*, vol. 29, no. 10, pp. 1745–1754, Oct. 1988, doi: 10.1016/0032-3861(88)90386-2.

[78] C. Fougnies, P. Damman, M. Dosière, and M. H. J. Koch, "Time-Resolved SAXS, WAXS, and DSC Study of Melting of Poly(aryl ether ether ketone) (PEEK) Annealed from the Amorphous State," *Macromolecules*, vol. 30, no. 5, pp. 1392–1399, Mar. 1997, doi: 10.1021/ma961151i.

[79] C. Fougnies, M. Dosière, M. H. J. Koch, and J. Roovers, "Morphological Study and Melting Behavior of Narrow Molecular Weight Fractions of Poly(aryl ether ether ketone) (PEEK) Annealed from the Glassy State," *Macromolecules*, vol. 31, no. 18, pp. 6266–6274, Sep. 1998, doi: 10.1021/ma980640a.

[80] X. Tardif *et al.*, "Experimental study of crystallization of PolyEtherEtherKetone (PEEK) over a large temperature range using a nano-calorimeter," *Polymer Testing*, vol. 36, pp. 10–19, Jun. 2014, doi: 10.1016/j.polymertesting.2014.03.013.

[81] A. M. Jonas, T. P. Russell, and D. Y. Yoon, "Synchrotron X-ray Scattering Studies of Crystallization of Poly(ether-ether-ketone) from the Glass and Structural Changes during Subsequent Heating-Cooling Processes," *Macromolecules*, vol. 28, no. 25, pp. 8491–8503, Dec. 1995, doi: 10.1021/ma00129a005.

[82] B. S. Hsiao, K. H. Gardner, D. Q. Wu, and B. Chu, "Time-resolved X-ray study of poly(aryl ether ether ketone) crystallization and melting behaviour: 1. Crystallization," *Polymer*, vol. 34, no. 19, pp. 3986–3995, Jan. 1993, doi: 10.1016/0032-3861(93)90658-W.

[83] C. Fougnies, P. Damman, D. Villers, M. Dosière, and M. H. J. Koch, "Time-Resolved SAXS, WAXS, and DSC Study of the Annealing of Poly(aryl ether ether ketone) (PEEK) from the Glassy State," *Macromolecules*, vol. 30, no. 5, pp. 1385–1391, Mar. 1997, doi: 10.1021/ma961150q.

[84] C. Fougnies, M. Dosière, M. H. J. Koch, and J. Roovers, "Cold Crystallization of Narrow Molecular Weight Fractions of PEEK," *Macromolecules*, vol. 32, no. 24, pp. 8133–8138, Nov. 1999, doi: 10.1021/ma9909206.

Cette thèse est accessible à l'adresse : https://theses.insa-lyon.fr/publication/2023ISAL0006/these.pdf
© [H. Willeman], [2023], INSA Lyon, tous droits réservés

[85] C. R. Choe and K. H. Lee, “Nonisothermal crystallization kinetics of poly(etheretherketone) (PEEK),” *Polymer Engineering & Science*, vol. 29, no. 12, pp. 801–805, 1989, doi: 10.1002/pen.760291208.

[86] Y. Lee and R. S. Porter, “Double-melting behavior of poly(ether ether ketone),” *Macromolecules*, vol. 20, no. 6, pp. 1336–1341, Nov. 1987, doi: 10.1021/ma00172a028.

[87] Y. Lee and R. S. Porter, “Effects of thermal history on crystallization of poly(ether ether ketone) (PEEK),” *Macromolecules*, vol. 21, no. 9, pp. 2770–2776, Sep. 1988, doi: 10.1021/ma00187a022.

[88] L. D. Landau and E. M. Lifshitz, *Statistical Physics*. Pergamon Press, 1969. Accessed: May 30, 2022. [Online]. Available: https://ia800702.us.archive.org/22/items/ost-physics-landaulifshitz-statisticalphysics/LandauLifshitz-StatisticalPhysics.pdf

[89] M. Avrami, “Kinetics of Phase Change. I General Theory,” *The Journal of Chemical Physics*, vol. 7, no. 12, pp. 1103–1112, Dec. 1939, doi: 10.1063/1.1750380.

[90] T. Ozawa, “Kinetics of non-isothermal crystallization,” *Polymer*, vol. 12, no. 3, pp. 150–158, Mar. 1971, doi: 10.1016/0032-3861(71)90041-3.

[91] J. I. Lauritzen and J. D. Hoffman, “Crystallization of bulk polymers with chain folding: theory of growth of lamellar spherulites,” *J. RES. NATL. BUR. STAN. SECT. A.*, vol. 65A, no. 4, Art. no. 4, Jul. 1961, doi: 10.6028/jres.065A.035.

[92] S. Z. D. Cheng and B. Lotz, “Enthalpic and entropic origins of nucleation barriers during polymer crystallization: the Hoffman–Lauritzen theory and beyond,” *Polymer*, vol. 46, no. 20, Art. no. 20, Sep. 2005, doi: 10.1016/j.polymer.2005.03.125.

[93] C. N. Velisaris and J. C. Seferis, “Crystallization kinetics of polyetheretherketone (peek) matrices,” *Polymer Engineering & Science*, vol. 26, no. 22, pp. 1574–1581, 1986, doi: 10.1002/pen.760262208.

[94] C. Bas, A. C. Grillet, F. Thimon, and N. D. Albérola, “Crystallization kinetics of poly(aryl ether ether ketone): Time-temperature-transformation and continuous-cooling-transformation diagrams,” *European Polymer Journal*, vol. 31, no. 10, pp. 911–921, Oct. 1995, doi: 10.1016/0014-3057(95)00060-7.

[95] J. Wang, M. Alvarez, W. Zhang, Z. Wu, Y. Li, and B. Chu, “Synchrotron small-angle x-ray scattering study of crystalline structures and isothermal crystallization kinetics of poly(aryl ether ether ketones),” *Macromolecules*, vol. 25, no. 25, pp. 6943–6951, Dec. 1992, doi: 10.1021/ma00051a035.

[96] J. J. C. Cruz-Pinto, J. A. Martins, and M. J. Oliveira, “The isothermal crystallization of engineering polymers ? POM and PEEK,” *Colloid Polym Sci*, vol. 272, no. 1, pp. 1–16, Jan. 1994, doi: 10.1007/BF00653305.

[97] J. M. Govers, “Structure development and long-term performance of Poly-ether-ether-ketone (PEEK).,” p. 46.

[98] W. Wang, J. M. Schultz, and B. S. Hsiao, “Dynamic Study of Crystallization- and Melting-Induced Phase Separation in PEEK/PEKK Blends,” *Macromolecules*, vol. 30, no. 16, pp. 4544–4550, Aug. 1997, doi: 10.1021/ma970092l.

Cette thèse est accessible à l'adresse : https://theses.insa-lyon.fr/publication/2023ISAL0006/these.pdf
© [H. Willeman], [2023], INSA Lyon, tous droits réservés

[99] S. A. Chelaghma *et al.*, “Identification of isothermal crystallization kinetics of poly(ether-ketone-ketone) based on spherulite growth measurements and enthalpic data,” *POLYMER CRYSTALLIZATION*, vol. 3, no. 4, p. e10141, 2020, doi: https://doi.org/10.1002/pcr2.10141.

[100] Y. Deslandes, F.-N. Sabir, and J. Roovers, “Effect of molecular weight on the spherulitic growth rate of poly(aryl ether ether ketone),” *Polymer*, vol. 32, no. 7, pp. 1267–1273, Jan. 1991, doi: 10.1016/0032-3861(91)90231-7.

[101] M. Day, Y. Deslandes, J. Roovers, and T. Suprunchuk, “Effect of molecular weight on the crystallization behaviour of poly(aryl ether ether ketone): a differential scanning calorimetry study,” *Polymer*, vol. 32, no. 7, pp. 1258–1266, Jan. 1991, doi: 10.1016/0032-3861(91)90230-G.

[102] M. C. Chien and R. A. Weiss, “Strain-induced crystallization behavior of poly(ether ether ketone) (PEEK),” *Polymer Engineering & Science*, vol. 28, no. 1, pp. 6–12, 1988, doi: 10.1002/pen.760280103.

[103] J. Seo, A. M. Gohn, R. P. Schaake, D. Parisi, A. M. Rhoades, and R. H. Colby, “Shear Flow-Induced Crystallization of Poly(ether ether ketone),” *Macromolecules*, vol. 53, no. 9, pp. 3472–3481, May 2020, doi: 10.1021/acs.macromol.9b02611.

[104] J. Seo *et al.*, “Flow-Induced Crystallization of Poly(ether ether ketone): Universal Aspects of Specific Work Revealed by Corroborative Rheology and X-ray Scattering Studies,” *Macromolecules*, p. acs.macromol.0c01840, Nov. 2020, doi: 10.1021/acs.macromol.0c01840.

[105] Solvay, “Technical DataSheet KT820.” [Online]. Available: www.solvay.com

[106] Solvay, “Technical Data Sheet KT880.” [Online]. Available: www.solvay.com

[107] R. Séguéla, “Temperature dependence of the melting enthalpy of poly (ethylene terephthalate) and poly(aryl-ether-ether-ketone),” *Polymer*, vol. 34, no. 8, pp. 1761–1764, Apr. 1993, doi: 10.1016/0032-3861(93)90338-B.

[108] S. Z. D. Cheng and B. Wunderlich, “Heat capacities and entropies of liquid, high-melting-point polymers containing phenylene groups (PEEK, PC, and PET),” *J. Polym. Sci. B Polym. Phys.*, vol. 24, no. 8, pp. 1755–1765, Aug. 1986, doi: 10.1002/polb.1986.090240811.

[109] A. L. Patterson, “The Scherrer Formula for X-Ray Particle Size Determination,” *Phys. Rev.*, vol. 56, no. 10, pp. 978–982, Nov. 1939, doi: 10.1103/PhysRev.56.978.

[110] B. Fillon, J. C. Wittmann, B. Lotz, and A. Thierry, “Self-nucleation and recrystallization of isotactic polypropylene (alpha phase) investigated by differential scanning calorimetry,” *Journal of Polymer Science Part B: Polymer Physics*, vol. 31, pp. 1383–1393, 1993.

[111] G. Urciuoli, O. Ruiz de Ballesteros, R. Cipullo, M. Trifuoggi, A. Giarra, and F. Auriemma, “Thermal Fractionation of Ethylene/1-Octene Multiblock Copolymers from Chain Shuttling Polymerization,” *Macromolecules*, p. acs.macromol.2c00773, Jun. 2022, doi: 10.1021/acs.macromol.2c00773.

[112] J. J. C. Cruz-Pinto, J. A. Martins, and M. J. Oliveira, “The isothermal crystallization of engineering polymers ? POM and PEEK,” *Colloid Polym Sci*, vol. 272, no. 1, Art. no. 1, Jan. 1994, doi: 10.1007/BF00653305.

Cette thèse est accessible à l'adresse : https://theses.insa-lyon.fr/publication/2023ISAL0006/these.pdf
© [H. Willeman], [2023], INSA Lyon, tous droits réservés

[113] C. Millot, “Multi-scale characterization of deformation mechanisms of bulk polyamide 6 under tensile stretching below and above the glass transition,” thesis, Lyon, INSA, 2015. Accessed: Jun. 05, 2019. [Online]. Available: http://www.theses.fr/2015ISAL0028

[114] L. D. Landau and E. M. Lifshitz, *Theory of Elasticity*, Moscou: Editions Mir. 1967.

[115] A. N. Gent, “Compression of Rubber Blocks,” *Rubber Chemistry and Technology*, vol. 67, no. 3, pp. 549–558, 1994.

[116] O. Reynolds, “On the theory of lubrication and its application to Mr. Beauchamp tower’s experiments, including an experimental determination of the viscosity of olive oil,” *The Philosophical Transactions of the Royal Society of London*, vol. 177, pp. 157–234, 1886.

[117] K. L. Johnson, *Contact Mechanics*, Cambridge University Press. 1985.

[118] K. Tashiro and H. Tadokoro, “Calculation of three-dimensional elastic constants of polymer crystals. 3. α and γ Forms of nylon 6,” *Macromolecules*, vol. 14, no. 3, pp. 781–785, May 1981, doi: 10.1021/ma50004a060.

[119] K. Miyasaka, T. Isomoto, H. Koganeya, K. Uehara, K. Ishikawa, and N. Ogata, “Nylon-6 α-phase crystal: Chain repeat distance and modulus in the chain direction at low temperature,” *Journal of Polymer Science: Polymer Physics Edition*, vol. 18, no. 5, pp. 1047–1052, 1980, doi: 10.1002/pol.1980.180180511.

[120] S. Dasgupta, W. B. Hammond, and W. A. Goddard, “Crystal Structures and Properties of Nylon Polymers from Theory,” *J. Am. Chem. Soc.*, vol. 118, no. 49, pp. 12291–12301, Jan. 1996, doi: 10.1021/ja944125d.

Cette thèse est accessible à l'adresse : https://theses.insa-lyon.fr/publication/2023ISAL0006/these.pdf
© [H. Willeman], [2023], INSA Lyon, tous droits réservés

Résumé en français

Introduction

Le poly éther éther cétone (PEEK) est un thermoplastique semi-cristallin dit de hautes performances, à haute Tg ($T_g \cong 150$°C). Pour élaborer une modélisation prédictive de ses propriétés mécaniques, il est nécessaire de partir d'une description aussi complète que possible de la structure et de la morphologie semi-cristalline à toutes les échelles, en relation avec les conditions de mise en œuvre et de cristallisation des échantillons, et cela tout au long de la déformation. Il s'agit en effet de pouvoir prédire comment le procédé affecte la structure et la morphologie, qui à leur tour vont déterminer les propriétés mécaniques finales des matériaux. L'objectif de cette thèse est d'établir le scénario multi-échelles de déformation du PEEK lorsqu'il est sollicité en traction. Pour cela, des échantillons de PEEK ont été étudiés lors d'expériences in situ de diffraction des rayons X lors de traction uniaxale en Synchrotron.

Chapitre 1. Etude bibliographique

Le premier chapitre de ce manuscrit présente une étude bibliographique comprenant une étude du PEEK, traitant de la structure du polymère, de sa cristallisation et de ses propriétés thermiques et mécaniques. Une dernière partie passe en revue les mécanismes connus de déformations des polymères semi-cristallins.

Les PEEK et autres polymères de la famille des aryl ether cétones sont caractérisés par une haute température de transition vitreuse Tg, une température de dégradation thermique très haute et une très bonne résistance aux solvants. Ces propriétés sont dues à sa structure comportant des groupements phényls, aryl et cétones. Le PEEK est un polymère semi-cristallin de structure cristallographique orthorhombique qui cristallise sous forme de sphérulites. La taille de ces sphérulites est fortement dépendante des conditions de cristallisation mais aussi d'autres paramètres comme la masse moléculaire du polymère.

Le phénomène de double pic de fusion est un phénomène largement étudié à propos de la cristallisation du PEEK. Deux hypothèses s'affrontent pour l'expliquer : une double population de cristaux ou une réorganisation pendant l'étape de chauffe du cycle DSC. La cinétique de cristallisation des polymères peut être étudiée avec différents modèles comme celui d'Avrami décrivant les modes de cristallisation d'un polymère en isotherme.

Son comportement mécanique dépend des conditions de traction : la température, la vitesse de déformation mais aussi de son poids moléculaire. Le PEEK présente une relaxation α autour de 150°C mais aussi une relaxation β à basses températures (entre -70 et 100°C), ce qui démontre que des mouvements locaux sont possibles à basses températures lorsque le polymère est à l'état vitreux. La présence de cette transition indique aussi que ce polymère peut être sujet au vieillissement physique. Des études ont montré l'impact du vieillissement physique de la phase amorphe de ce polymère sur ces propriétés mécaniques. Le PEEK a tendance à se rigidifier mais aussi à devenir plus fragile.

Les mécanismes de déformation des polymères semi-cristallins incluent dans le régime élastique principalement la déformation de la phase amorphe. Ces déformations peuvent s'effectuer par séparation des lamelles cristallines par extension des chaines de la phase amorphe, par cisaillement inter-lamelles ou par rotations des empilements lamellaires. Dans le domaine plastique, on peut retrouver des mécanismes de déformation irréversibles comme la formation de cavités, de craquelures ou de bandes de cisaillement.

Cette thèse est accessible à l'adresse : https://theses.insa-lyon.fr/publication/2023ISAL0006/these.pdf
© [H. Willeman], [2023], INSA Lyon, tous droits réservés

Chapitre 2. Matériaux et méthodes

L'étude des propriétés thermiques du PEEK et de la cristallisation du polymère a été menée par DSC. L'influence de différents paramètres de process et de cristallisation comme la température de fondu ou la vitesse de refroidissement a permis d'instaurer un protocole d'élaboration par thermocompression d'échantillons. La dégradation du polymère a été étudiée par TGA et FTIR. L'analyse mécanique dynamique (DMA) et des essais de traction nous ont permis de caractériser les propriétés mécaniques macroscopiques des échantillons réalisés.

Des essais réalisés en Synchrotron de traction uniaxiale couplés à des essais de diffraction des rayons X aux grands angles (WAXS) et aux petits angles (SAXS) nous ont permis d'accéder à l'évolution multi-échelles de la structure microscopique du matériau au long de la déformation. Ces analyses ont été complétées par un système digital de corrélation d'images afin d'accéder précisément au champ de déformation en chaque point de l'échantillon étiré. Cela permet la comparaison entre la déformation macroscopique mesurée sous le faisceau et les mesures microscopiques obtenues par rayons X.

Chapitre 3. Propriétés thermiques et structurales du PEEK

Les températures d'étude choisies dans ce travail sont soit inférieures, soit supérieures à Tg, dans la mesure où les mécanismes de plasticité et d'endommagement peuvent être très différents dans chacun de ces cas. Deux grades de masses moléculaires différentes fournis par Solvay ont été étudiés (KT820, haute M_w et KT880, basse M_w).

Tout d'abord, les conditions de cristallisation du PEEK ont été étudiées par DSC. La température d'oubli thermodynamique ainsi que la sensibilité aux vitesses de refroidissement ont été établies. Une étude de la cinétique de cristallisation a été menée par DSC pour accéder aux temps caractéristiques de nos polymères ainsi que par microscopie optique in-situ avec une platine chauffante afin d'observer les phénomènes de nucléation et croissance des sphérulites. Le grade de PEEK dont la masse moléculaire est la plus faible (KT880) cristallise environ 5 fois plus vite que le grade à haute masse moléculaire (KT820) et la taille de ses sphérulites est jusqu'à 10 fois plus grande. Ces mesures ont permis d'établir le diagramme TTS de nos matériaux et de comparer ces valeurs à la littérature. (chap III, fig 16)

Concernant la mise en œuvre de nos matériaux, le point clé était de s'assurer du caractère isotrope des morphologies initiales. Pour cela, le procédé de thermocompression a été choisi pour l'élaboration de nos échantillons. Les morphologies multi-échelle (morphologie des sphérulites, empilements lamellaires, longue période) et les structures cristallines de ces échantillons ont été caractérisées. Des observations par microscopies optique et électronique et des mesures de diffusion X aux petits angles (SAXS) et aux grands angles (WAXS) confirment l'isotropie initiale des échantillons thermocompressés.

Les propriétés mécaniques macroscopiques de nos matériaux ont été préliminairement caractérisés par DMA et par essais de traction. L'influence du grade de polymère, des températures de process, de la vitesse de sollicitation et de la température de l'essai a été étudiée. La différence de comportement pour des essais à température en dessous et au-dessus de la température de transition vitreuse souligne l'importance de l'état de la phase amorphe dans la réponse globale du matériau. Le phénomène de localisation de la déformation pendant les essais en traction a été suivi et quantifié par corrélation d'images. (chap III, fig 28)

Chapitre 4&5. Etude de la déformation microscopique dans le régime pre et post-yield

Enfin, des essais menés en Synchrotron de mesures SAXS et WAXD en temps réel sur des échantillons étirés in situ ont été combinées pour caractériser de façon quantitative les mécanismes de déformation

Cette thèse est accessible à l'adresse : https://theses.insa-lyon.fr/publication/2023ISAL0006/these.pdf
© [H. Willeman], [2023], INSA Lyon, tous droits réservés

locaux à l'échelle des empilements lamellaires (SAXS) et de la structure cristalline (WAXD), à la fois dans le régime élastique linéaire de déformation et dans le régime plastique, et jusqu'à la rupture des matériaux ou jusqu'à l'obtention d'un matériau fibrillaire fortement orienté. Ces essais ont été réalisés à deux températures, au-dessous et au-dessus de T_g afin de varier l'état de la phase amorphe, vitreux ou caoutchoutique. Plus spécifiquement, les résultats qui ont été obtenus dans ces mesures de diffusion/diffraction sont les suivants :

- la déformation locale dans les empilements lamellaires et les mailles cristallines en fonction de l'orientation. En comparant les résultats de ces deux mesures, on obtient une information sur les différences de module entre phase amorphe et phase cristalline, ainsi que sur les couplages mécaniques phase amorphe/phase cristalline. Cette mesure permet aussi de comparer la déformation aux échelles microscopiques avec la déformation à l'échelle macroscopique. Au-dessous de T_g, dans le régime élastique, la déformation des empilements lamellaires est égale à la déformation macroscopique alors que la déformation des plans cristallins est inférieure car ces entités sont plus rigides que la phase amorphe. Au-dessus de T_g, les déformations des empilements lamellaires et des plans cristallins sont inférieures à la déformation macroscopique. Cela peut s'expliquer par la présence de cisaillement, non détecté par les mesures de diffusion/diffraction. La déformation multi-échelles dans le PEEK dans les directions parallèle et perpendiculaire à la direction de traction est résumée dans les figures 29 et 30 du chapitre 5.

- l'évolution des distributions d'orientation des empilements lamellaires dans le régime élastique (avant la plasticité). Cette donnée est également un élément central pour la modélisation du comportement micromécanique, dans la mesure où elle permet d'accéder au mécanisme de couplage (ou transmission de contrainte) phase amorphe/phase cristalline. Les plans cristallins s'orientent globalement perpendiculairement à la traction de manière à aligner les chaines dans la direction de traction. Au-dessous de T_g, ce phénomène est logiquement accompagné de l'orientation des empilements lamellaires dans la direction de traction. Au-dessus de T_g les empilements lamellaires s'orientent à 45° par rapport à la direction de traction, ce qui confirme la présence de cisaillement dans les mécanismes de déformation à hautes températures.

- la réversibilité de la déformation macroscopique et microscopique dans le régime élastique ainsi que la déformation résiduelle pour un étirement au-dessus du yield. Lorsqu'un échantillon est étiré dans le régime linéaire de déformation, cette déformation est réversible à toutes les échelles. Lorsqu'il est étiré jusque dans le régime plastique, après le yield, une déformation résiduelle macroscopique de l'ordre de 3% est observée. Cependant, à l'échelle des empilements lamellaires, une déformation résiduelle est observée seulement pour les empilements soumis seulement à un effort de traction. Aucune déformation résiduelle n'est observée à l'échelle des plans cristallins. La déformation résiduelle macroscopique provient donc d'une déformation irréversible de la phase amorphe. (chap 5 fig 17)

- dans le régime de déformation plastique, la fragmentation lamellaire ainsi que la cavitation, ont été caractérisées. Le profil de diffusion centrale change en fonction de la température d'essai, ce qui montre un endommagement différent en fonction de l'état de la phase amorphe. A température ambiante, le profil de diffusion centrale est inhabituellement large, centré autour de la direction de traction. Ce profil peut provenir de petites entités, cristallites ou petits empilements lamellaires fragmentés, orientées de manière aléatoire. A 170°C, au-dessus de T_g, la diffusion centrale est étroite et centrée autour de la direction perpendiculaire à la direction de traction. L'endommagement de cet échantillon se fait donc par l'apparition de cavités orientés selon la direction de traction. (chap 5 fig 25&28)

En conclusion, un scénario global multi-échelles des mécanismes de déformation du PEEK est proposé. (chap 5, fig 31&32)

Cette thèse est accessible à l'adresse : https://theses.insa-lyon.fr/publication/2023ISAL0006/these.pdf
© [H. Willeman], [2023], INSA Lyon, tous droits réservés

FOLIO ADMINISTRATIF

THESE DE L'INSA LYON, MEMBRE DE L'UNIVERSITE DE LYON

NOM : WILLEMAN DATE de SOUTENANCE : 24/01/2023

Prénoms : Héloïse

TITRE : Caractérisation multi-échelle des mécanismes de déformation du poly-ether-ether-ketone (PEEK) en traction uniaxiale

NATURE : Doctorat Numéro d'ordre : 2023ISAL0006

Ecole doctorale : Matériaux de Lyon

Spécialité : Science des Matériaux

RESUME : L'objectif de cette thèse est d'établir le scénario multi-échelles de déformation du PEEK lorsqu'il est sollicité en traction uniaxiale. Préalablement à la mise en œuvre d'échantillons de deux grades commerciaux de PEEK, les propriétés thermiques et mécaniques de ces matériaux ont été caractérisées. La température d'oubli thermodynamique ainsi que la sensibilité aux vitesses de refroidissement ont été établies. Des éprouvettes de traction ont été obtenues à partir de plaques thermocompressées, procédé choisi pour obtenir des morphologies les plus isotropes possibles. Les propriétés mécaniques en traction ont ensuite été caractérisées au-dessus et au-dessous de la transition vitreuse de la phase amorphe (Tg). Grâce à un dispositif expérimental fabriqué sur mesure, des essais de traction à deux températures distinctes au-dessous et au-dessus de T_g ont été suivis par diffusion des rayons X aux petits (SAXS) et grands angles (WAXS) pour caractériser les déformations à l'échelle des empilements lamellaires et à l'échelle de la maille cristalline. Simultanément, le champ de déformation a été mesurée par corrélation d'images (DIC) afin de comparer la déformation macroscopique et microscopique. Pour les deux températures, les lamelles tendent à s'orienter perpendiculairement à la direction de traction (TD). Ce mécanisme d'orientation local (que nous appelons « modèle de réseau de chaînes ») est induit par la transmission des contraintes par les chaînes amorphes reliant les lamelles cristallines adjacentes. Au-dessus de T_g, l'allongement local est plus faible que l'allongement macroscopique dans les lamelles perpendiculaire à TD, ce qui implique que les lamelles inclinées doivent être cisaillées. L'évolution de la distribution d'orientation des lamelles appuie ce résultat. Une morphologie fortement orientée est finalement obtenue quelle que soit la température. Cependant, le profil d'endommagement est différent. En-dessous de T_g, le profil de diffusion centrale indique l'existence de petites entités (lamelles ou crystallites) orientées aléatoirement. A hautes température, le matériau est fibrillaire et présente des cavités.

MOTS-CLÉS : poly-ether-ether-ketone, WAXS, SAXS, traction in-situ, domaine élastique, domaine plastique

Laboratoire (s) de recherche :

IMP – INSA de LYON / CNRS (UMR 5223)

MATEIS – INSA de LYON / CNRS (UMR 5510)

Directeur de thèse : SOTTA Paul (IMP), LAME Olivier (MATEIS)

Président de jury : GAUCHER Valérie

Composition du jury : ALBOUY Pierre-Antoine, BIKARD Jérôme, BILLON Noëlle, GAUCHER Valérie, GOVAERT Leon, LAME Olivier, SOTTA Paul

Cette thèse est accessible à l'adresse : https://theses.insa-lyon.fr/publication/2023ISAL0006/these.pdf
© [H. Willeman], [2023], INSA Lyon, tous droits réservés